

Technische Universität Dresden

**Improved Organic Semiconductor Thin-Film
Formation through the Addition of Vibrations to the
Solution Shearing Method**

Cecilia Teixeira da Rocha

geboren am 12. Sept. 1990 in Brasilia, Brasil

der Fakultät Elektrotechnik und Informationstechnik der Technischen
Universität Dresden

zur Erlangung des akademischen Grades

Doktoringenieur

(Dr.-Ing.)

genehmigte Dissertation

Vorsitzender: Prof. Dr. Johann W. Bartha
Gutachter 1: Prof. Dr. Stefan C. B. Mannsfeld
Gutachter 2: Prof. Dr. Francisco Molina-Lopez

Tag der Einreichung: 13.09.2019
Tag der Verteidigung: 23.06.2020

Gutachter 3: Prof. Dr. sc. techn. habil. Dipl. Betriebswissenschaften Frank Ellinger

Publications

Articles:

- C. Teixeira da Rocha, G. Qu, X. Yang, R. Shivhare, M. Hamsch, Y. Diao, S.C.B. Mannsfeld, "Mitigating Meniscus Instabilities in Solution-Sheared Polymer Films for Organic Field-Effect Transistors," *ACS Applied Materials & Interfaces*, p. acsami.9b07832, Aug. 2019.
- K. Haase, C. Teixeira da Rocha, C. Hauenstein, Y. Zheng, M. Hamsch, and S. C. B. Mannsfeld, "High-Mobility, Solution-Processed Organic Field-Effect Transistors from C8-BTBT:Polystyrene Blends," *Advanced Electronic Materials*, vol. 4, no. 8, p. 1800076, Aug. 2018.
- C. Teixeira da Rocha, K. Haase, Y. Zheng, M. Löffler, M. Hamsch, and S. C. B. Mannsfeld, "Solution Coating of Small Molecule/Polymer Blends Enabling Ultralow Voltage and High-Mobility Organic Transistors," *Advanced Electronic Materials*, p. 1800141, May 2018.

Book Chapter:

- K. Haase, M. Hamsch, C. Teixeira da Rocha, J. Zessin, S.C.B. Mannsfeld, "Advances in solution processing of organic materials for devices", in *Handbook of organic materials for electronic and photonic devices*, 2nd ed., O. Ostroverkhova, Ed. Woodhead Publishing, p. 551-577, 2019.

Conference contributions:

- C. Teixeira da Rocha, G. Qu, X. Yang, R. Shivhare, M. Hamsch, Y. Diao, S. Mannsfeld, "Coating of smooth thin films on non-wetting substrates for organic field-effect transistors", 16th European Conference on Organized Films, Oral presentation and poster presentation, 2017.
- C. Teixeira da Rocha, M. Hamsch, M. Löffler, S. Mannsfeld, "Piezoshearing: a new solution-coating method for high-performance organic semiconductor thin films", 14th European Conference on Molecular Electronics, Dresden, Poster presentation, 2019.

Abstract

In this thesis, methods for improving charge carrier mobility and deposition conditions for the solution shearing of organic semiconductors for organic field-effect transistors (OFETs) are investigated. Electrical performance for OFETs is currently still limited by the charge carrier mobility, especially when high fabrication speeds are required. In this work, adaptations are made to the solution shearing method to enhance charge carrier mobility values and to increase the deposition speed and film uniformity of semiconductor films. The solution shearing method can be easily adapted to large-scale roll-to-roll fabrication, a low-cost and high throughput fabrication process. In this work, the fabrication of OFETs with both crystalline small-molecule and donor-acceptor polymer semiconductors as the active layer is performed, and significant improvements in charge carrier mobility and film formation are achieved.

Specifically, the crystalline small-molecule semiconductor TIPS-pentacene is blended with the inert dielectric polystyrene, and solution shearing parameters are optimized to obtain highly-aligned crystalline films. The thin film with optimized morphology is deposited on a very thin polymer dielectric film, demonstrating the feasibility of high-performance OFETs (effective mobility of $\sim 1.2 \text{ cm}^2 \text{ V}^{-1} \text{ s}^{-1}$) and an ultra-low operating voltage ($\sim 1 \text{ V}$) – at the time a record value.

To improve crystal growth, the solution shearing method is modified to add vibrations to the liquid during the coating process. The new coating method, named “piezoshearing”, allows the application of vibrations to the liquid during deposition through the attachment of a piezo actuator to the shearing blade. The piezoshearing is implemented to enhance crystal growth during the solution shearing of crystalline materials, and tests of piezoshearing for the material 2,7-Dioctyl[1]benzothieno[3,2-b][1]benzothiophene (C_8 -BTBT) demonstrate that substrate coverage can be increased due to induced stick-and-slip caused by the piezoshearing.

Due to the unfavorable wetting conditions of semiconducting donor-acceptor polymer solutions on the commonly used low surface energy OFET substrates, conventional solution shearing is problematic. With piezoshearing, film deposition can be significantly improved. In particular, through piezoshearing the so-called stick-and-slip instabilities are mitigated, allowing the doubling of the shearing speed, and the deposition of smooth and ultrathin films ($\sim 7 \text{ nm}$). In addition to enabling higher coating speeds, piezoshearing also lowers the polymer material consumption by up to $\sim 70\%$ in comparison to the conventional solution shearing method. For some materials, piezoshearing is also found to increase the charge carrier mobility in OFET devices by up to two orders of magnitude.

The piezoshearing is utilized for viscous polymer solutions, which are challenging to coat, and usually, result in non-uniform films. Three donor-acceptor polymer systems were tested, and morphology changes are observed for all materials when piezoshearing is applied. For one of the polymeric solutions, an increase in crystallinity is achieved, possibly accompanied by a change in the degree of alignment of the polymer chains. For two other polymer solutions with higher molecular weight chains, very smooth films were obtained with the piezoshearing – saving 30% of material. Without the application of vibrations, such materials yield very non-uniform films, with significant thickness variations, which is unsuitable for OFET devices.

In summary, this work leads to significant improvements in the solution shearing of organic semiconductor materials by adding vibrations in the kHz range to the deposition

process. The effects and benefits of utilizing the piezoshearing are demonstrated, and suggestions for further improvement and studies are made.

Contents

Contents	7
1 Introduction	11
Motivation	11
Outline	12
2 Theoretical Principles of Organic Electronic Materials and Devices	13
2.1 Organic Electronics	13
2.2 Organic Semiconductors	14
2.2.1 Charge Transport Mechanisms in Organic Semiconductors	16
2.3 Organic Field-effect Transistors	19
2.3.1 Operation	19
2.3.2 The Metal-Semiconductor Interface	22
2.3.3 The Dielectric	25
2.4 Film Morphology and Charge Transport in OFETs	27
2.4.1 Small Molecules	27
2.4.2 Semicrystalline Polymers	29
3 Solution Shearing and Control of Film Morphology	33
3.1 The Solution Shearing Method	34
3.1.1 Capillary Flow and the Pinned Contact Line	36
3.1.2 Marangoni Flow	36
3.1.3 Shear Flow	37
3.2 Film Formation in Solution Shearing	38
3.2.1 Small Molecules	38
3.2.2 Polymers	43
3.3 Stick-and-slip Instabilities	50
3.3.1 Contact Angle Hysteresis and Stick-and-slip	52
3.4 Vibration-assisted Thin-film Solution Fabrication Methods	53
3.4.1 Effects on a Liquid stemming from Vibration	53
3.4.2 Relevant Characteristics	57
3.4.3 Vibrations and Thin-film Formation	58
3.4.4 Combining the Solution Shearing and Vibrations	61
4 Experimental Methods	63
4.1 Device Fabrication	63
4.1.1 Substrate Preparation	63
4.1.2 Electrode Evaporation	65
4.2 Piezoshearing Setup	65
4.3 Thin-film Characterization	68
4.3.1 Cross-Polarized Optical Microscopy	68
4.3.2 Grazing Incidence Wide-Angle X-ray Scattering	71
4.4 Electrical characterization	77
4.4.1 Characterization	77
4.4.2 Mobility estimation and overestimation discussion	77

5	Alignment Improvement from Blending the Small molecule TIPS-pentacene with an inert Polymer	81
5.1	Introduction	81
5.2	Optimization of film morphology for TIPS-pentacene	82
5.2.1	Device Fabrication	82
5.2.2	Electrical Characterization	83
5.2.3	Film morphology characterization	86
5.3	Fabrication of Ultra-low-voltage Operation Devices	96
5.4	Figure of Merit of this Study	97
5.5	Summary	99
6	Piezoshearing of Crystalline Materials.....	101
6.1	Introduction	101
6.2	Piezoshearing of Pristine TIPS-pentacene	102
6.2.1	Film Fabrication	102
6.2.2	Thin-film Characterization	102
6.3	TIPS-pentacene blended with PS in Toluene: Better Performing Devices 104	
6.4	Piezoshearing of C ₈ -BTBT	105
6.5	Summary	107
7	Addressing Stick-and-Slip Instabilities in solution-sheared films for OFET devices	109
7.1	Introduction	109
7.2	Device Fabrication	110
7.3	The Effect of Piezoshearing on Stick-and-Slip Instabilities	111
7.3.1	Increasing Shearing Speed	111
7.3.2	Thin-film Characterization	114
7.3.3	Electrical Characterization	116
7.4	Energy Barriers and Overcoming them with Vibration	119
7.5	Acceleration Threshold for Mitigating Stick-and-slip	122
7.6	Summary	126
8	Piezoshearing of Viscous Polymer Solutions.....	127
8.1	Introduction	127
8.2	Device Fabrication	128
8.3	DPP4DE-TT and Film Morphology	129
8.4	DPP6DO-TT, DPP6DO-T, and Faraday Instabilities	137
8.4.1	Thin-film Characterization	141
8.5	Piezoshearing as a Parametric Oscillator System.....	145
8.5.1	Solid Friction	146
8.5.2	Viscosity	146
8.5.3	Transition Between Regimes.....	147
8.6	Summary	147
9	Conclusion and Outlook	149
	Conclusion	149
	Outlook	150
	Appendix	153
	A.1 OFET data for devices from Chapter 7	153
	Bibliography.....	161
	List of Figures	181
	List of Tables.....	193
	List of Abbreviations.....	195
	Acknowledgment	197

Erklärung zur Eröffnung des Promotionsverfahrens	199
---	------------

Chapter 1

1 Introduction

Motivation

Due to unique features such as flexibility, stretchability, and transparency, organic electronic applications open up a field of applications that the traditional silicon technology cannot supply. Applications such as flexible and stretchable sensors, flexible readers, and large-scale photovoltaic panels that adapt to curved surfaces are a few of the applications that can be achieved with organic electronic technologies. Such fields of applications benefit highly from the research and development of organic electronic materials.

If, in addition to the beneficial mechanical properties that organic electronic applications offer, roll-to-roll fabrication can be implemented to the fabrication of organic electronics, it would represent a significant lowering of costs and environmental impact in comparison to amorphous silicon technology. Amorphous silicon (a-Si) electronics have already been matched in performance by organic devices, and the fabrication of amorphous silicon technology requires high fabrication temperatures and chemical vapor deposition methods, which are undesirable.

One of the biggest challenges in the field of organic electronics is to produce high-performance devices through an economically feasible large-scale fabrication method. Meniscus-guided coating methods can be easily extended to roll-to-roll methods and are seen by the scientific community as one of the deposition methods with the highest potential for upscaling. The works with the highest impact in the last years are mainly approaching how to improve charge carrier mobility in organic field-effect transistors (OFETs) and how to do so in a manner relevant to the industry.

To approach the problem of simultaneously improving device performance and increasing deposition rates for large-scale fabrication of semiconductors for OFETs, in this work, a modification to the solution shearing method is proposed. We suggest the attachment of a piezo actuator to the shearing blade to induce vertical vibration on the meniscus during the shearing process. This method has been termed “piezoshearing”. It is proposed as a solution to stir the crystalline semiconductor during the deposition and enhance crystal growth. The size of crystal grains and domains are usually limited by the speed of crystal growth. It is then demonstrated that the piezoshearing is a solution for the

non-wetting problem of coating of semicrystalline polymeric semiconductors and at how it can change the film morphology.

Outline

The main goal of this work was to explore how to improve electrical performance and fabrication conditions of organic field-effect transistors through the solution shearing process. Among the desired OFET features are devices with high charge carrier mobility, high reproducibility, and commercially feasible fabrication rates. Initially, the effect of blending a small-molecule crystalline material with an insulating polymer is investigated. A modification to the solution shearing method that consists of applying vibration to the solution shearing blade is then implemented. The effects of this mechanism on the material deposition of crystalline materials and semicrystalline polymer materials are explored.

The theoretical background for organic electronic materials and OFETs are presented in Chapter 2, including the influence of the semiconductor morphology on the charge carrier mobility of devices. The relation between morphology and electrical performance and the current challenges of unraveling this relationship are discussed for crystalline small molecule materials and donor-acceptor semicrystalline polymers. Chapter 3 presents an overview of the solution shearing method and some fluid transport mechanisms that are part of the deposition process. A review of the most significant works that use such a method is presented, including a discussion on how modifications to the solution shearing process can tune morphology. An overview of how vibrations affect liquids is given, and a few works that have used vibration as a way to enhance morphology are discussed. In Chapter 4, some of the essential methods of characterization of organic semiconducting materials are presented, and how they are used in the development of this work. Details about device fabrication are included.

The experimental results of this work are presented throughout Chapters 5 to 8. Chapter 5 is dedicated to exploring the improvement of electrical characteristics for a blend of a crystalline semiconductor and an inert polymer. It is also demonstrated that such high charge carrier mobility performance can be extended to ultra-low-voltage-driven devices, by utilizing a very thin cross-linked polymer blend. In Chapter 6, attempts at utilizing the piezoshearing process to increase crystal growth in crystalline materials during solution shearing are presented. Both pristine crystalline materials and small-molecule: polymer blends are tested. In Chapter 7, piezoshearing is used on semicrystalline donor-acceptor polymers for improving deposition speeds. The partial-wetting problem of the deposition of polymers on a low surface energy substrate is approached, and piezoshearing shows positive effects, enabling an increase in the solution deposition speed. Finally, in Chapter 8, the effect of piezoshearing on the morphology of donor-acceptor thin films is investigated. Viscous polymers are used in this chapter to avoid non-wetting instabilities that can be caused by the piezoshearing. Chapter 9 presents a summary of the effects observed during piezoshearing, and what properties of the setup can be extended and improved

Chapter 2

2 Theoretical Principles of Organic Electronic Materials and Devices

2.1 Organic Electronics

Organic electronic materials have arisen as an alternative class of electrical devices with superior mechanical properties, such as flexibility, stretchability, self-healing, and transparency, in comparison to inorganic semiconductors. Such properties enable the development of applications that were before limited by the rigidity and brittleness of inorganic semiconductor technology.

Among some of these applications are flexible sensors for biomedical sensors, stretchable and self-healing electronic skin,[1], [2] solar panels and screens that can adapt to curved surfaces, electronic packaging, and other applications that are currently under development. Figure 2.1 displays a few applications in which organic electronic technology is used.

The first organic electronic properties were observed in 1977, by the Nobel laureates Alan Heeger, Alan G. MacDiarmid, and Hideki Shirakawa through the doping of polyacetylene. The possibility of processing electronics at lower costs with alternative materials has impeded further research towards the development of such materials.

In the case of field-effect transistor (FETs), organic devices are still far from competing with classical silicon devices. Crystal silicon devices have charge carrier mobility capacities up to $1350 \text{ cm}^2 \text{ V}^{-1}\text{s}^{-1}$ for electrons and $480 \text{ cm}^2 \text{ V}^{-1}\text{s}^{-1}$ for holes,[3] polycrystalline materials have mobility of around $100 \text{ cm}^2 \text{ V}^{-1}\text{s}^{-1}$, and amorphous silicon, of around $1 \text{ cm}^2 \text{ V}^{-1}\text{s}^{-1}$. Organic technology has recently reached mobilities above $10 \text{ cm}^2 \text{ V}^{-1}\text{s}^{-1}$, [4], [5] which can compete with amorphous silicon technology, but still presents mobility of around $0.2 \text{ cm}^2 \text{ V}^{-1}\text{s}^{-1}$ for large-scale production.[6]

In terms of processing, organic electronics have presented an option of fabricating devices at lower temperatures, with a more flexible technology that does not require extreme processing temperatures and ambient conditions, has a lower fabrication cost and there is the versatility of material synthesis. Organic electronic materials present the advantage of being soluble, opening the possibility for solution deposition. In the last years, roll-to-roll fabrication methods have been developed for large-scale fabrication of organic electronics and are currently viewed as the solution for the fabrication of such materials.

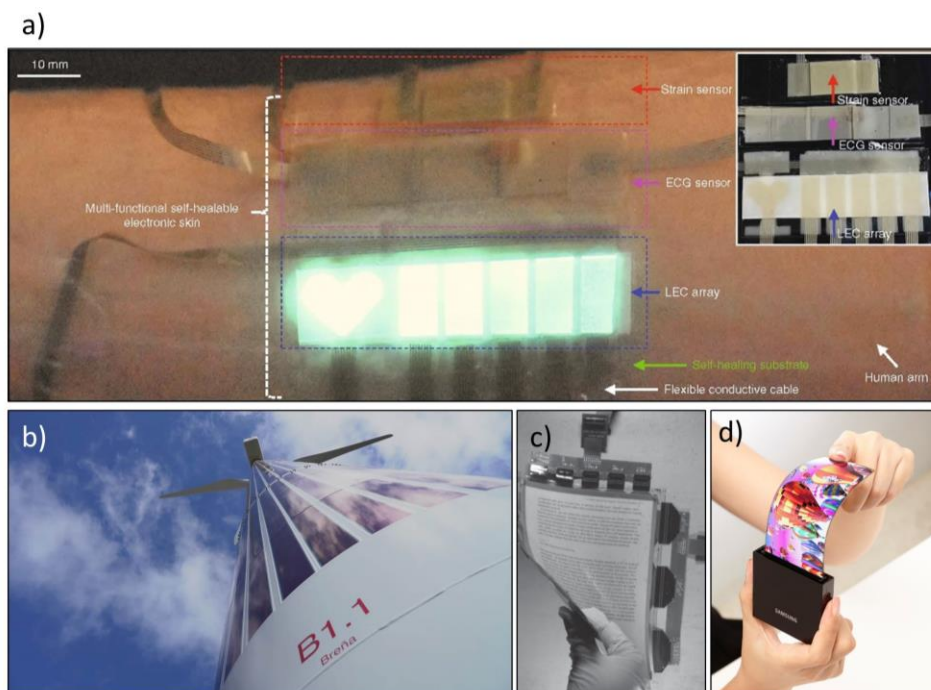


Figure 2.1: (a) Self-healable electronic skin device for health monitoring. Image reproduced from Ref.[2]. (b) Flexible solar panels from Heliatek on a windmill; (c) a flexible e-reader developed by Plastic Logic, and (d) a prototype of a flexible screen, by Samsung.

2.2 Organic Semiconductors

Semiconductors are the active layer materials in field-effect transistors. In the case of inorganic semiconductors, a minimum amount of energy is necessary for exciting electrons from an energy band filled with electrons – the valence band – to a band without electrons – the conduction band. Due to the strong covalent bonds present in an inorganic crystal, such as silicon or germanium, there are strong interactions between atomic orbitals, enabling a long-range delocalization of electrons. The electrons are delocalized in the valence band, and charge conduction occurs when the electrons are excited. The energy required for moving electrons from the valence band to the conduction band is equivalent to the energetic difference between the conductive band and the valence band; the difference is called the bandgap (E_g) of the semiconductor. The bandgap is a measure of the propensity of the material to conduct current.

For organic semiconductors (OSCs), the valence band and conduction band are less defined and do not present as many states as the inorganic counterparts do. The valence band is better characterized by the highest occupied molecular orbital (HOMO), and the conduction band by the lower unoccupied molecular orbital (LUMO). There is no long-range net delocalization, and energy needs to be introduced into the system for charge delocalization to occur. Such energies can come from electrical, mechanical, or photonic activation. For semiconductors, the bandgap ranges between 1 eV and 4 eV.

The main characteristic of metals is that their Fermi level (which defines the work function) lies within the conduction band. For insulators, the bandgap is too wide – over 4 eV – and charge transport does not occur.

While for inorganic semiconductors, covalent bonds hold the material together, the bonding present between organic semiconductor molecules is weak van der Waals forces. The organic semiconductor materials are characterized by aromatic π -bonds. Such π -bonds enable charge transport in the material when enough delocalization occurs. Figure 2.2a and b represent the wavefunction of the atomic orbitals s and p , respectively. The

shape corresponds to the probability of electrons to be localized in such regions. When two atoms are bonded along the axis of the cylindrical p orbital, molecular σ -orbitals (Figure 2.2c) are formed. When the orbitals are localized above and below the axis that connects the atoms, molecular π -orbitals are formed. σ -orbitals are close to the core of the atom and hold the atoms together. There is little electronic splitting among them, and filling such conduction band would require a high amount of energy in comparison to the π -orbitals. The π -orbitals are farther from the nuclei and require less energy for electronic splitting to occur. Figure 2.2e illustrates an energetic schematic of the π and π^* bands of ethane. π and π^* would correspond to the HOMO and LUMO values of the semiconductor, respectively. The electrical current in organic semiconductors is induced by electronic splitting and delocalization of these π -orbitals.[7], [8]

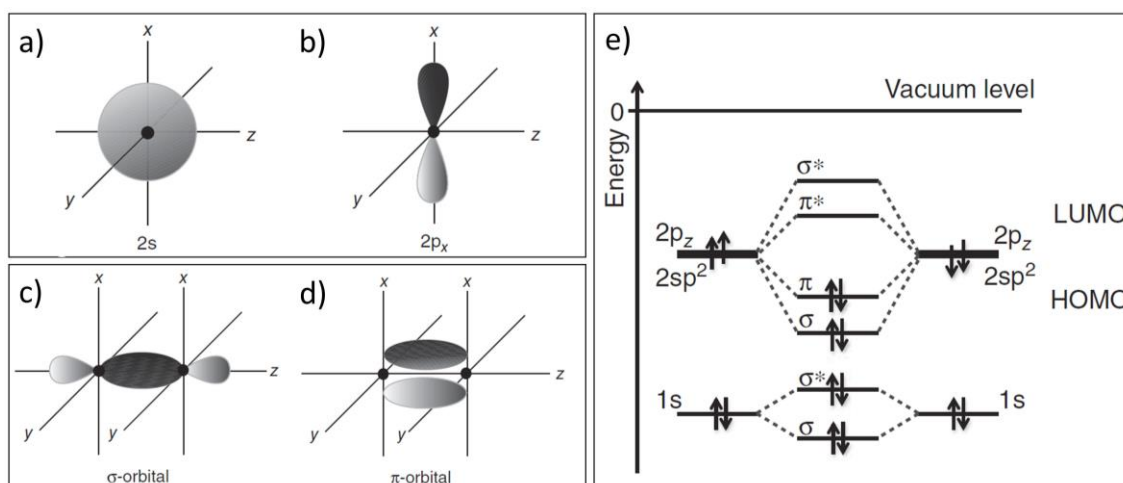


Figure 2.2: (a) The atomic s orbital and (b) p orbital. (c) The molecular σ orbital and (d) π orbitals resultant from the atomic overlap. (e) A simplified energetic diagram of σ and π orbitals for ethane. π corresponds to the bonding band and π^* to the antibonding. Images reproduced from Ref. [8].

There are two main classes of organic semiconductor materials, the small molecules, and the polymers. Currently, there are several small-molecule materials used that have demonstrated OFETs with high charge carrier mobility, such as the ones portrayed in Figure 2.3a. Currently, the class of polymer semiconductors most investigated is that of the donor-acceptor polymers. They consist of alternating moieties of electron donors and electron acceptors within the backbone chain of the polymer. Figure 2.3b illustrates this alternating polymer structure, and Figure 2.3d displays some of the most significant donor and acceptor components used for the synthesis of these materials. Such chemical structure enables intrachain transport, therefore requires less energy for activation, and these materials have a small bandgap. When the molecular structure is sufficiently ordered, interchain transport is expected to occur as well.

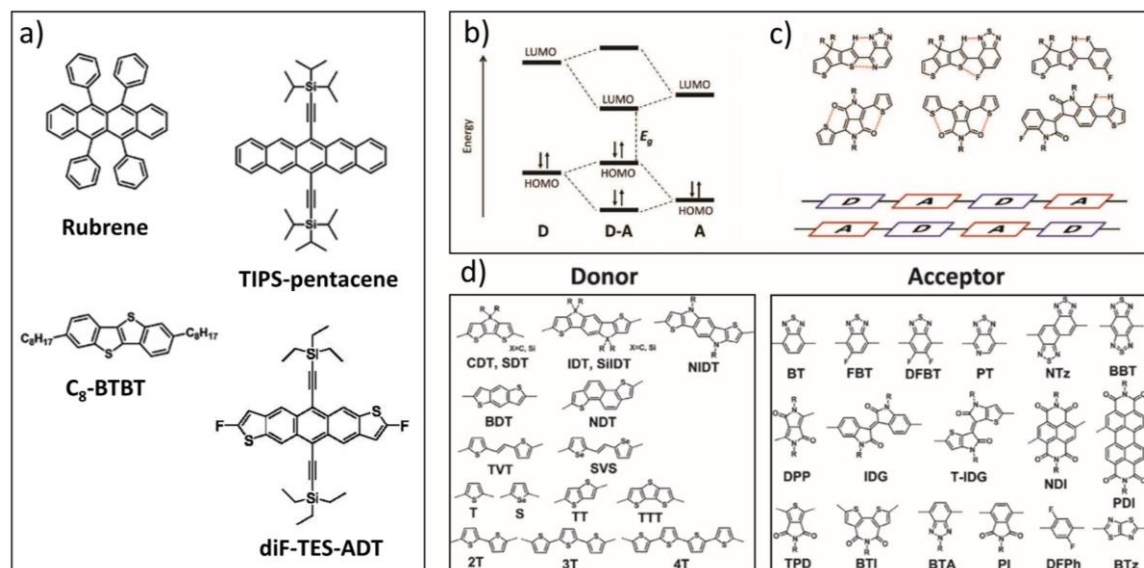


Figure 2.3: (a) Widely used small-molecule semiconductors. (b) A HOMO-LUMO representation of the donor and acceptor moieties in a D-A polymer, (c) a schematic representing how both moieties organize in a chain, and (d) the most used donor and acceptor units used for polymer synthesis. Figure reproduced from Ref. [9].

2.2.1 Charge Transport Mechanisms in Organic Semiconductors

One of the most significant quantifiers used to characterize a semiconductor is the charge carrier mobility. It determines the velocity of charge transport in a semiconductor. High mobility values are always sought, and are one of the main determinants of the speed of functioning of a device, and how much power needs to be supplied for a specific electrical current to be achieved.

In the case of inorganic materials, due to the net charge, the charge carrier mobility is a constant and is characterized by Equation (2.1):

$$\vec{v}_D = \mu \vec{E} \quad (2.1)$$

where v_D is the drift velocity of a charge when it is submitted to the influence of an electrical field E ; μ the charge carrier mobility. Charge transport in organic electronics is dominated by the semiclassical Marcus theory, which explains electron transfer in chemical reactions:

$$k_{ij} = \frac{2\pi}{\hbar} |V_{ij}|^2 \frac{1}{(4\pi\lambda k_B T)^{1/2}} e^{-(\Delta G^0 + \lambda)^2 / (4\lambda k_B T)} \quad (2.2)$$

where λ is the reorganization energy, ΔG^0 is the Gibbs free energy from the chemical reaction. This term is dependent on the energy required for hopping of an electron from one site to another. V_{ij} is the electronic coupling, which depends exponentially on the distance between sites:

$$|V_{ij}| = V_{(0)ij} \cdot e^{-\gamma_{ij} d_{ij}} \quad (2.3)$$

In Equation (2.3), d is the intermolecular separation. In a straightforward approach, the transfer integral, or electronic coupling, is determined by the geometry of its reactants, the distance between molecules, positioning among each other, and the bonding-

antibonding pattern of the molecular orbitals. Through the calculation of transfer integrals for dimers with density functional theory, coupled with theoretical Monte Carlo simulations, charge carrier mobility predictions can be made based on the molecular structure of a material.[7] In Figure 2.4, an example of charge carrier mobility predicted in terms of intermolecular distance is shown for tetracene. The wavefunctions in the HOMO and LUMO are displayed in Figure 2.4a, and the consequences of the distances on the electronic splitting and mobility are shown in Figure 2.4b and Figure 2.4c, respectively.

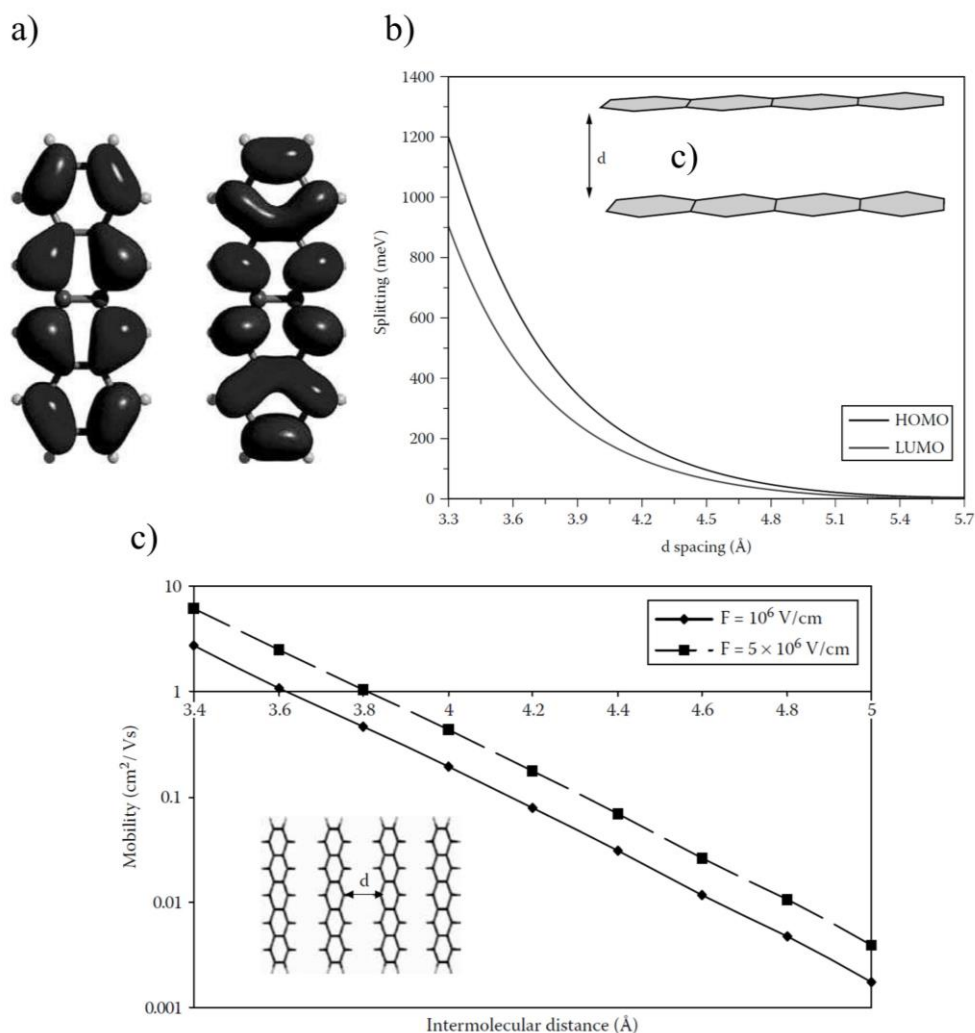


Figure 2.4: (a) Wavefunction of the HOMO and LUMO of tetracene; (b) the consequences of the electronic splitting when the distance between two cofacial tetracene dimers is increased. (c) Consequences of the increasing intermolecular distance on the charge carrier mobility. Image reproduced from Ref. [7].

The main goal of such studies is to relate charge carrier mobility to the mesoscale structural order of organic semiconductors. Therefore, the manner in which the semiconductor molecules are organized within a thin film is of crucial importance for tuning charge transfer in a thin film morphology.[7]

Band Transport

Band transport occurs in highly ordered materials, where charges are highly delocalized, and require low energies for charge transport. Once the temperature of the material increases, scattering increases, and charge carrier mobility decreases. This is the

case for most inorganic materials and for a few highly purified small-molecule crystalline materials.[7]

Band theory can be described by the Drude model, where charge carriers are free to move unless scattered by phonons (lattice vibrations). The mean drift velocity suggested by this model is the one in Equation (2.4), and the charge carrier mobility can be approximated by Equation (2.5):

$$\langle v_x \rangle = \frac{q\tau}{m^*} = \mu F_x \quad (2.4)$$

$$\mu = \frac{q\tau}{m^*} = \frac{q\lambda}{m^*v_{th}} \quad (2.5)$$

where q is the elemental charge, m^* the effective mass, τ is the mean free time between two collisions, and $v_{th} = \sqrt{\frac{3kt}{m^*}}$ is the electron thermal velocity.

In general, when temperature increases, lattice vibrations increase, causing charge transport and mobility to decrease:

$$\mu(T) \propto T^{-n} \quad (2.6)$$

The decreasing mobility with increasing temperature is one of the signature characteristics of band transport and is often used by groups to claim band-like transport in organic crystalline materials. This is not proved and remains unresolved.[7]

Polarons, Hopping, and Marcus model

In organic semiconductors, charges are significantly more localized than in the case of materials that present band transport. Such localization can occur due to weak van der Waals forces, the possibility of polarization, and structural disorder. There is so far no global model for charge transport in organic semiconductors, but a few models that are considered to partly describe behavior observed so far.

One of the models to be considered is the polaronic nature of the charge carriers. For organic materials, there is strong electron-phonon coupling, which results in the formation of polarons. A charge injected in a polymer film interacts with the molecular vibrations and leads to the formation of localized polarons, surrounded by a deformed molecular region that causes electronic relaxation. Polaron hopping occurs when the charge is transferred from an ionized site of a molecule to another site due to the deformation of molecules and enough applied energy. This leads to charge transfer from site to site in a molecule, and between molecules for some materials (e.g., poly(3-hexylthiophene-2,5-diyl) (P3HT)). Therefore, an electrical current is generated. Temperature increase enables polaron hopping and therefore increases charge carrier mobility.[7], [10], [11]

If the system is at a sufficient temperature, the charge transport in semiconductor materials is also expected to be governed by the Marcus theory for chemical reactions, described in the previous section. Marcus theory presents mobility as a thermally activated process (an Arrhenius type), where the charge carrier mobility is derived from Equation (2.2) and given by:

$$\mu = \frac{e \cdot a^2}{k \cdot T} \cdot v \cdot e^{-\frac{E_p}{2kT}} \quad (2.7)$$

where a is the hopping distance, and ν is the attempt frequency. The model is thermally activated despite the absence of disorder. The model of the density of states takes into account the disorder ubiquitous to organic semiconductors. Such disorder originates from local conformations, impurities, defects, and dipolar disorder that causes the broadening of the electronic density of states. The broader the density of states, the more delocalized are the charges. It also a thermally activated process; for charge transfer to different states, specific activation energy is required.[7], [10]

2.3 Organic Field-effect Transistors

2.3.1 Operation

The organic field-effect transistor is a three-terminal-voltage device in which a current can be generated by controlling the physical properties of the device and the combination of voltages applied to it. It is one of the most crucial components of modern electronics, and it is one of the most-studied components in the field of organic electronics.

The simplified architecture of a field-effect transistor is a parallel-plate capacitor, with a semiconducting layer in between and contacts for controlling current flow through the semiconductor. The basic architecture of a transistor is shown in Figure 2.5. The architecture shown here is that of a bottom-gate top-contact transistor (BGTC). Other OFET architectures are shown in Figure 2.6b, c, and d. The examples shown in Figure 2.6 are all for a p-type semiconductor. The gate-voltage in relation to the source contact is given in this work by V_g , and the drain voltage in relation to the source is given by V_d .

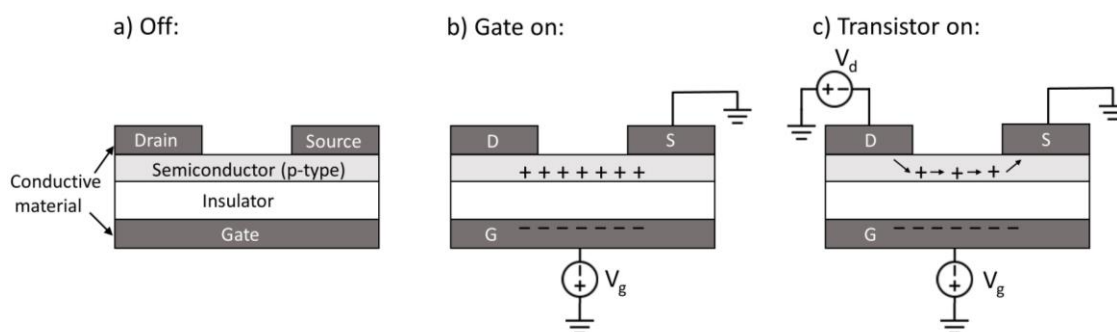


Figure 2.5: (a) Schematic a field-effect transistor. Schematics of (b) charge accumulated in the channel of the semiconductor when a gate voltage is applied; (c) drain current flowing in the transistor channel.

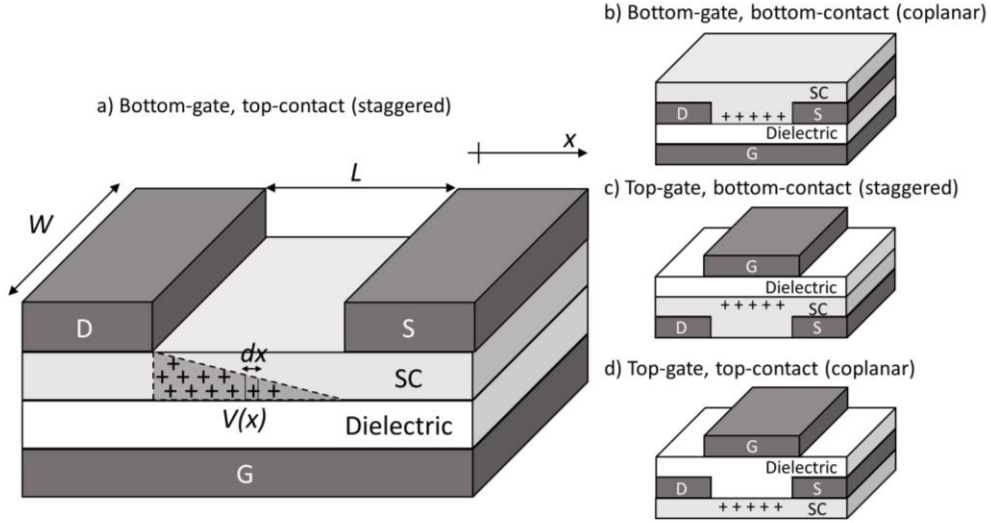


Figure 2.6: (a) Schematic of a bottom-gate, top contact architecture with a gradual charge channel. Schematics of (b) bottom-gate, bottom-contact, (c) top-gate, bottom-contact, and (d) top-gate, top-contact.

Differently from the classical MOSFET, the OFET operates in the accumulation mode. At the interface of the contact with the semiconductor, charges are “injected” in the semiconductor film. For a particular metal, if the semiconductor tends to create electrons in the semiconductor film, it is named an “n-type” material. If the semiconductor tends to create holes, it is named a “p-type” material. The characteristic equations for OFETs can be derived from the charge dQ accumulated in a small length dx at a position x in the channel of the transistor, that will have a voltage value of $V(x)$ (Figure 2.6a):

$$dQ = C_i \left((V_g - V_{th}) - V(x) \right) \cdot W \cdot dx \quad (2.8)$$

From the definition of electrical current:

$$I = \frac{dQ}{dt} \quad (2.9)$$

Therefore:

$$I = \frac{dQ}{dt} = C_i W \left((V_g - V_{th}) - V(x) \right) \cdot \frac{dx}{dt} \quad (2.10)$$

The drift velocity from a particle under the effect of an electrical field:

$$\frac{dx}{dt} = v = \mu E_x = \mu \frac{dV}{dx} \quad (2.11)$$

Replacing Equation (2.11) in Equation (2.10):

$$I = \frac{dQ}{dt} = C_i W \left((V_g - V_{th}) - V(x) \right) \cdot \mu \frac{dV}{dx} \quad (2.12)$$

Both sides of the equation are integrated for dx :

$$\int_0^L I dx = \int_0^{V_d} C_i W ((V_g - V_{th}) - V(x)) \cdot \mu \frac{dV}{dx} \quad (2.13)$$

Resulting in:

$$I_d \cdot L = \mu C_i W ((V_g - V_{th}) V_d - \frac{V_d^2}{2}) \quad (2.14)$$

If the drain voltages considered are small, the device is operating in the linear regime, then $V_d \ll (V_g - V_{th})$, and the linear equation can be given by:

$$I_d^{lin} = \mu C_i \frac{W}{L} (V_g - V_{th}) V_d \quad (2.15)$$

When drain voltage increases and $V_d = V_g - V_{th}$, the device channel suffers a pinch-off and reaches saturation, the Equation (2.14) can then be rewritten as:

$$I_d^{sat} = \mu C_i \frac{W}{2L} (V_g - V_{th})^2 \quad (2.16)$$

The saturation regime is reached when, ideally, the drain current does not increase with the drain voltage increase.

This model can be used under the assumption that the gate capacitance is uniform across the channel, there is only drift current, and the charge carrier mobility μ does not depend on the gate voltage.

The current as a function of varying V_g and constant V_d is given by the transfer curve of the device (Figure 2.7a and b). For transfer curves in the linear regime, small values of V_d are used (Figure 2.7a); while in the saturation regime, large values of V_d are used (Figure 2.7b). The current as a function of V_d and constant V_g is the output curve (Figure 2.7c). Extracting such curves is a necessary characterization procedure of OFETs. Through them, values such as charge carrier mobility (μ), the threshold voltage (V_{th}) and current on and off ratio ($I_{on/off}$) can be extracted. These are the most important figures of merit of an OFET device. A high charge carrier mobility is necessary for increasing the switching speed of transistors, and consequently faster circuits. The threshold voltage is preferably small, so the power requirements for supplying a circuit are as low as possible, and the $I_{on/off}$ current ratio should be as large as possible. The on-state and off-state should be as far apart from each other as possible for the reliability of a switching circuit.

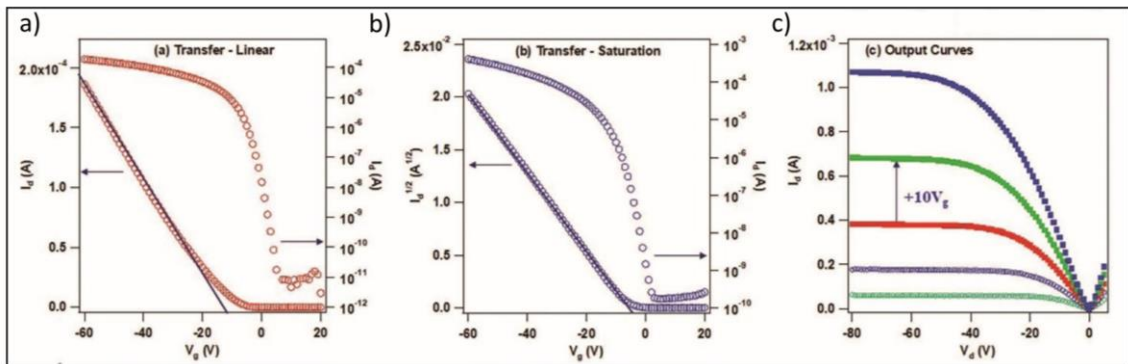


Figure 2.7: Example of (a) a transfer curve in the linear regime of a transistor, (b) the transfer curve of a transistor in saturation and the equivalent square root for mobility calculation, and (c) the output curve of a transistor with increasing V_g -value-steps of +10 V. Image reproduced from Ref. [9].

For mobility extraction from a device, either the linear mobility or the saturation mobility can be used. From Equation (2.15), linear mobility is given by:

$$\mu_{lin} = \frac{\partial I_{d,lin}}{\partial V_d} \frac{L}{WC_i(V_g - V_{th})} \quad (2.17)$$

From Equation (2.16), the saturation mobility is given by:

$$\mu_{sat} = \frac{2L}{WC_i} \left(\frac{\partial \sqrt{I_{d,sat}}}{\partial V_g} \right)^2 \quad (2.18)$$

It is good practice to calculate both values, and the values extracted for the linear and saturation charge carrier mobility should be comparable.[12] The method of mobility extraction used in this work is explained with more detail in the Experimental Methods, in Chapter 4.

The threshold voltage of OFETs depends on the gate dielectric and dielectric thickness, traps in the dielectric or in the semiconductor, and on the contacts as well. Devices that turn on gradually are not uncommon, adding a degree of complexity to the extraction of the threshold voltage. A turn-on voltage, which has a lower value than the threshold voltage, needs then to be considered.[13]

2.3.2 The Metal-Semiconductor Interface

An essential aspect of the OFET is the quality of the charge injection from the contacts to the semiconductor. Weak charge injection can lead to lower drain current, being a central bottleneck in the device performance. The efficacy of charge injection in the metal-semiconductor interface in OFET depends highly on the chosen combination of materials, the quality of the interface between the contacts and semiconductors, and can be tuned by using interlayers. Limited charge injection has been shown to lower device performance by orders of magnitude, and mitigating contact resistance is currently a considerable challenge in the field of organic electronics. [14]

Contact injection can be understood through an energy diagram, as illustrated in Figure 2.8. Considering the Fermi level (E_F) as the probability of a charge occupying either the conducting band or the valence band. For this example, a p-type material is used, and the Fermi level is shifted to closer to the valence band (Figure 2.8a). Once the metal and semiconductor come into contact, a barrier Φ_b between the work function of the metal and the valence band appears (Figure 2.8b). The magnitude of such a barrier will depend on the material combination and their respective energy levels. Once a minimum voltage is applied, charges can be injected into the semiconductor (Figure 2.8c).

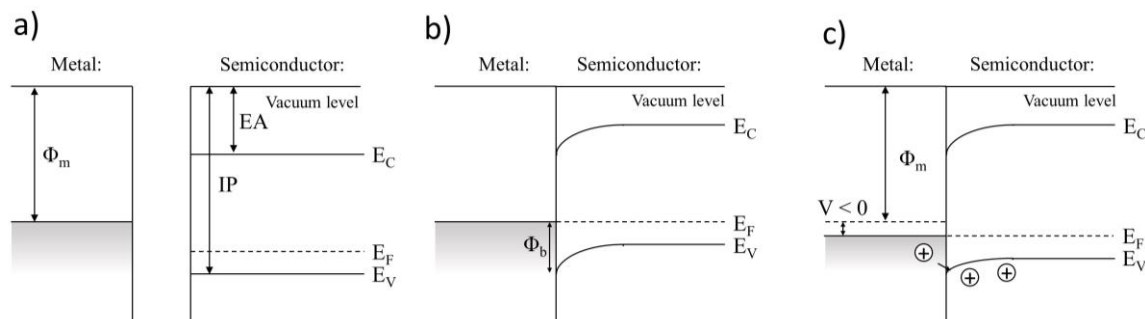


Figure 2.8: Schematic of the behavior of a metal-semiconductor junction for a p-type semiconductor. (a) The energy levels of a metal and a semiconductor interface when the interfaces are apart. Φ_m is the work function of the metal, EA the electron affinity of the semiconductor, IP the ionization potential, E_C the conduction band, E_V the valence band, and E_F the Fermi level. (b) When both surfaces are in contact, band bending occurs to maintain the Fermi level of the semiconductor at the same level of the metal's work function at the contact region. Therefore, a potential barrier of height Φ_b is formed. When a negative voltage is applied to the junction, the barrier is lowered by a factor dependent on the voltage applied.

An Ohmic contact is always desired for OFET contacts; it is the ideal junction, presents the smallest possible contact resistance, and therefore, the best conditions for high-performance devices. A representation of such a junction is shown in Figure 2.9a. It is a challenge to obtain such contacts. What occurs more in the OFET fabrication process is, however, the Schottky junction (Figure 2.9b). It is present in almost all electronic devices to some extent. It occurs when a barrier, such as Φ_b is present. If surface states are not considered, the barrier height for a junction is given by:

$$\Phi_b = \Phi_m - IP \quad (2.19)$$

$$\Phi_b = EA - \Phi_m \quad (2.20)$$

where Equation (2.19) is for hole injection, and (2.20) is for electron injection.

There are two mechanisms through which charge injection in Schottky contacts occurs: through tunneling and thermionic emission. Thermionic emission occurs when enough energy is introduced to the system, and the charges can overcome the potential barrier Φ_b . Tunneling occurs when the depletion layer at the interface is thin enough, and charges can tunnel through to the semiconductor (Figure 2.9b). For both mechanisms, the current density through the junction can be modeled by the Shockley diode equation:

$$J = J_0 \left(e^{\frac{qV_a}{kT}} - 1 \right) \quad (2.21)$$

where V_a is the voltage applied to the terminals, and J_0 is closely related to the potential barrier. The resultant contact resistance of both mechanisms is an exponential function of the potential barrier Φ_b . Therefore, the contact resistance is highly dependent on the potential barrier, making it one of the main parameters for contact engineering.[14]

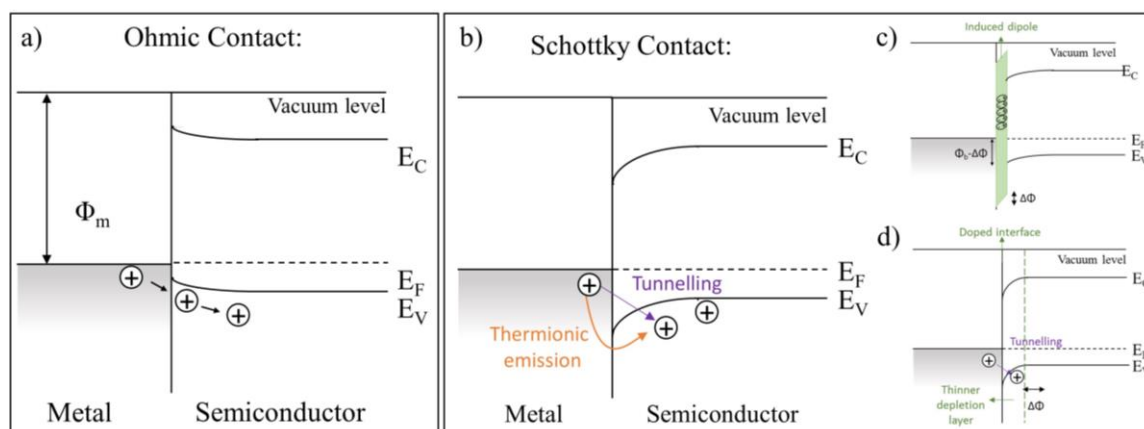


Figure 2.9: Schematic of the energy levels for an (a) Ohmic contact, and a (b) Schottky contact. (c) Schematic of the potential barrier lowering due to the insertion of an intermediate dipole layer. (d) The thinning of the depletion layer of a Schottky barrier through interface doping.

One of the strategies for avoiding a substantial potential barrier Φ_b is to make an appropriate choice of metal and semiconductor. It is essential to point out that the same material can have different work functions depending on surface roughness, ambient conditions, and even small amounts of contaminants.[14]–[16] Figure 2.10 displays the work function value for gold in different works, and the bandgap for some of the semiconductors used in this work.

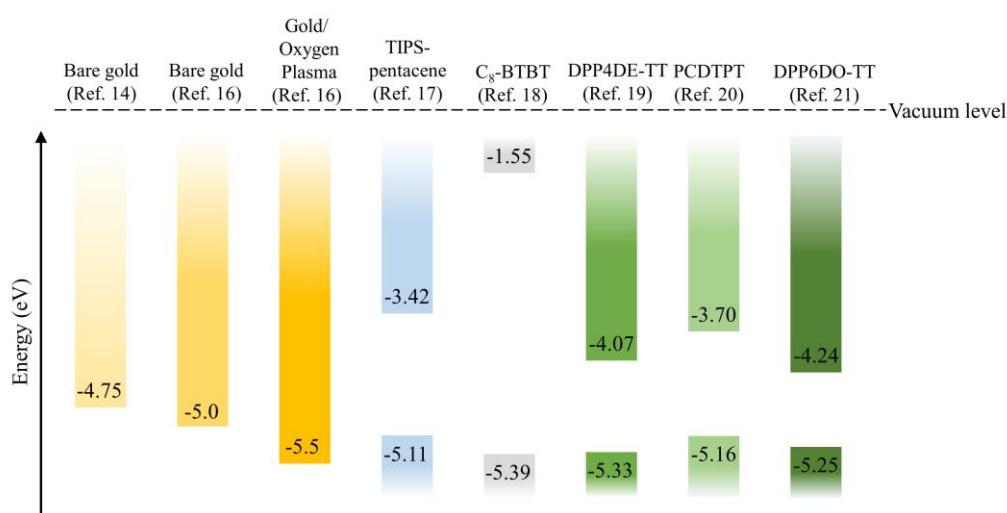


Figure 2.10: Work function for gold (Au) reported in different publications and under different cleaning condition. HOMO-LUMO values for semiconductors used in this work. The values from this image are taken from published works that utilize the same materials.[14], [16]–[21]

Metal contacts are so far the most widely used contacts for OFET fabrication. However, the use of non-metallic contacts is considered an alternative. Conductive polymers or graphene-based contacts are some of the potential materials. PEDOT:PSS (poly(3,4-ethylenedioxythiophene): polystyrene sulfonate) is one of the most commonly used materials for this. The advantage of these materials is that during the deposition process, the semiconductor layer (in case of top-contact architectures) is not as damaged as during the deposition of metallic electrodes – which is usually done through thermal evaporation. In addition to this, they offer the possibility of transparency of the electrodes. The limitations of these are, however, the deposition process and conductivity. For the case of graphene, the sheets need to be manually transferred, and for PEDOT:PSS, conductivity is still not comparable to metals. Although improving conductivity of such materials is a work in progress, they are far from competing with metallic contacts.[14], [22]–[24]

The metallic contacts can also be fine-tuned through interlayers. Very thin layers of oxide, for example, molybdenum oxide (MoO_x), have shown to change the work function of the contacts and enhance charge injection in OFETs.[25] The insertion of a layer can also act as a “buffering layer” during the metal deposition. It also offers the advantage of protecting the semiconductor from the diffusion of metal into the surface or surface disorder during the metallization process. The thickness of such interlayers has to be limited to a few nanometers. Too thick layers may have the opposite effect by adding an injection barrier or pinning the Fermi level.[14]

Although making an appropriate choice of metal-semiconductor to decrease the potential barrier, the potential barrier can be significantly higher in reality. The interface can be vulnerable to additional surface states, which can derive from structural disorder during fabrication, adding dipoles that shift the energy barriers or that pin the Fermi level. This is often due to poor quality contacts, destruction of the surface where the contacts are deposited, or diffusion of material into the semiconductor.[14] Such factors can lead to an increase in the potential barrier, and consequently to higher contact resistance. There are a few mechanisms that can be used, however, to overcome such injection problems.

Some approaches include the insertion of an intermediate layer to induce an additional dipole at the interface, and the doping of the interface. The insertion of a dipole between the contact layer and the semiconductor layer with an appropriate Self-Assembled Monolayer (SAM), for example, can form a dipole, decreasing the potential barrier Φ_b , as shown in Figure 2.9c. SAMs are an excellent way of introducing dipoles and at the same time maintaining an extremely low thickness that does not hinder charge injection. This facilitates thermionic emission and tunneling. The doping of the interface with a rich p-type or n-type material can decrease the depletion region of the potential barrier. The depletion region becomes thinner, facilitating charge tunneling (Figure 2.9d). The method is effective but has the drawback that if charge diffusion occurs in the semiconductor, such a treatment could increase the $I_{\text{on/off}}$ ratio of the device due to additional charge carriers permanently present in the conduction region of the device. Among the factors for improving contact resistance for OFETs is also changing the device architecture. When measuring contact resistance, in addition to the resistance at the interface, there can be bulk contact resistance.

There are a few methods recently used for evaluating contact injection in OFETs. The two-terminal measurement currently used for OFETs is useful to determine the mobility attained for devices but does not necessarily represent the intrinsic mobility of the semiconductor. For a better understanding of the effects of the quality of the contacts, methods such as TLM and four-point-probe measurements can be applied.[12], [26]

As is discussed in Chapter 4, contact resistance of an OFET can mask the actual quality of the semiconductor. Due to the slow turn-on of the device, it makes it appear as if there is a high charge carrier mobility for low gate voltages. Therefore, taking into account the effects of contact resistance in the electrical characteristics of a device is vital in evaluating the quality of charge carrier mobility.

2.3.3 The Dielectric

The dielectric used in an OFET has a critical role in its operation and performance. A general requirement for the dielectric layer is that it should have the highest possible capacitance, and enable very low operating voltages for the devices. Considering the capacitance of parallel plates given by:

$$C_i = \frac{\epsilon_0 k A}{d} \quad (2.22)$$

where k is the relative dielectric constant of a material, d the thickness of the dielectric, A the area of the parallel plates, and ϵ_0 is the dielectric constant of the vacuum. For a high drain current in the OFET, a high capacitance is required. This can be reached by either a low film thickness or by using a material with a high- k dielectric constant. Therefore, materials and processing conditions should be optimized for the lowest possible thickness without compromising the insulating character of the dielectric.

For the case of very low film thicknesses, one of the main challenges is high leakage currents. This can occur due to pinholes in the film, which are more likely to happen the thinner the layer is. The dielectric surface should also be smooth to enable a proper semiconductor-dielectric interface, where charge transport occurs. It should also not contain mobile charges or ions, so as to not create additional traps in the transport layer. Defects and microroughness the interface can create traps and significantly hinder device performance.[27] On top of these requirements, low-cost and reproducibility are requirements for upscaling in fabrication.

Dielectric materials can be generally classified into low- k and high- k materials. The dielectric constant is a measure of electrical polarizability of a material. Electrical polarizability refers to what degree dipoles in a material are created once an electrical field is applied to it. High- k dielectric materials are strongly polarizable, while low- k materials are weakly polarizable. A highly polarizable material is capable of inducing more charge at its surface, therefore inducing higher currents at lower voltages if used for OFETs. The polarization of material, however, has a response time. A certain degree of polarizability is limited to a certain switching frequency, leading to slow turn-on and turn-off of the device. Therefore, there is a trade-off between the switching frequency and device performance that is to be balanced-out depending on the desired application. A manner of balancing switching speed and current intensities is to use a combination of high- k and low- k dielectrics.[28]

Inorganic Materials

Si/SiO₂ wafers are often used in research due to its ready availability and convenience. SiO₂ acts as a suitable dielectric for a wide range of materials. It is mainly used in research where the investigation of new materials or processing conditions of the semiconductor are the focus. Due to its low dielectric constant, however ($k = 3.9$), voltages required for operating devices are often above 20 V, making this a good material only for laboratory research, and not tangible applications.

Other inorganic oxide materials have been used, such as aluminum oxides (AlO_x). SAM treatment on an ultrathin aluminum oxide layer has been shown to yield a capacitance of 800 nF cm⁻² for a film thickness of 5.3 nm, and devices with an operating voltage of 3 V.[29], [30]

Organic Materials

Besides the required electrical performance, it is desired that the dielectric be flexible, transparent, and have a low fabrication cost. The use of polymeric dielectrics deposited through solution-processing is currently considered the best choice for achieving this. Works have shown that OFETs with organic polymers as dielectrics can yield high charge carrier mobility while operating at low voltages.[31]–[33]

Some of the most common polymer dielectric materials are (poly(methyl methacrylate) (PMMA), polystyrene (PS), poly(4-vinyl phenol) (PVP), poly(alpha-methyl styrene) (PaMS), and poly(perfluorobutenylvinylether) (CYTOP).[34]–[36] These can often be dissolved into solvents orthogonal to the semiconductor solvents, allowing devices completely solution-processed.[32], [33] In the last few years, focus has been put on cross-linked polymers. The cross-linking of the polymer can be done at low temperatures (~100 °C), ensure insolubility of the dielectric layer, and increases the robustness of the film.[37] Such polymer blends have been used recently in combination with solution shearing and yielded films down to 11.4 nm and a capacitance of 280 nF cm⁻², demonstrating the high potential of such materials.[38]

In the case of bottom-contact architectures, the dielectric can influence the morphology of the semiconductor significantly. Rough surfaces can hinder the growth of large crystal domains and can change the nucleation density of polycrystalline materials.[27], [39]

2.4 Film Morphology and Charge Transport in OFETs

It is widely known that the charge carrier mobility of OFETs depends on several aspects of the semiconductor. Among these aspects is the electrical nature of the semiconducting material, and the structural order of the semiconducting materials. In general, films with a high degree of structural order are preferred. In this section, it is discussed how the morphology of different types of organic semiconductors, i.e., crystalline materials and polymers, influence the charge transport in an OFET fabricated with such materials.

2.4.1 Small Molecules

The performance of a thin film depends highly on the structural order of the film, both on the molecular scale, up to the microscale. It is known that charge transfer depends on the molecular stacking of the crystalline material, on the size of the crystal grains, and alignment with the transport direction, up to the scale of a device, which can have a channel length of over 100 μm. For devices to be reproducible, such structural order needs to be uniform over a large area. This is especially difficult in the growth of organic crystals, due to the weak van der Waals forces that hold them together. They are also, therefore, very prone to having their structure affected by defects during growth.[40], [41]

In the case of the molecular arrangement structure in a film, it is essential that it is formed in a manner favorable to charge delocalization and charge transfer.[42] The most common packing motifs for small molecules are the slip-stacked (or brick wall, face-to-face), and the herringbone. A schematic of both morphologies is shown in Figure 2.11b to the lower right. Examples of materials that pack in the slip-stacked motif are TIPS-pentacene, 6,13-bis(triethylsilylethynyl) pentacene, and 2,8-Difluoro-5,11-bis(triethylsilylethynyl)anthradithiophene (diF-TES-ADT).[43], [44] For the herringbone motif, some examples of materials are pentacene, rubrene, C₁₀-DNTT (2,9-didecyldinaphtho[2,3-b:20,30-f]thieno[3,2-b]thiophene), and C₈-BTBT.[40], [45]

The organization of crystalline grains and domains in a thin film is believed to be one of the main determinants of the charge transport in crystalline thin films. Figure 2.11a shows an illustrative schematic of how grains and domains are related in the film structure. Considering that on a device scale, there can be several crystalline domains, grain boundaries and domain boundaries are believed to be significant hindrances for charge

transport. In order to obtain a bandlike transport mechanism, large crystalline domains are desired.[46] Each crystalline grain is treated as having the intrinsic mobility of a single crystal and therefore the intrinsic mobility of a material. Grain boundaries and domain boundaries are expected to slow down charge transport due to trapping, and therefore higher energy required to overcome such boundaries. Currently, the composite mobility model is well accepted and appears to describe well such behavior:[41], [47]–[49]

$$\frac{L_G + L_{GB}}{\mu} = \frac{L_G}{\mu_G} + \frac{L_{GB}}{\mu_{GB}} \quad (2.23)$$

where L_G is the size of the grain, and L_{GB} is the size of the grain boundary. Therefore, even a small grain boundary is enough to decrease the charge carrier mobility significantly, and the active channel of an OFET usually consists of multiple grain domains.

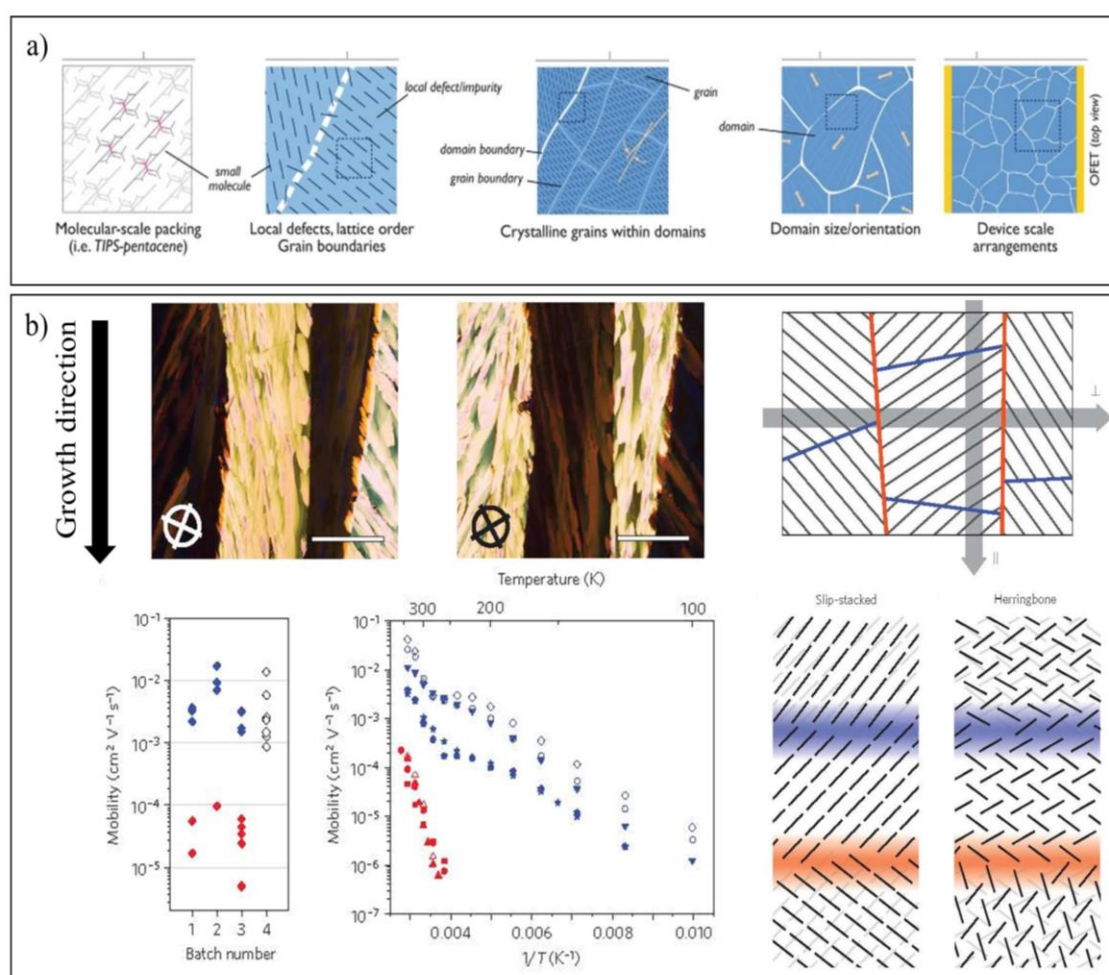


Figure 2.11: (a) Different scales and morphology features for organic crystalline thin films. Image reproduced from Ref. [40]. (b) Study of the influence of crystalline grains and boundaries of the small-molecule PDI8 on the charge carrier mobility of the transistors. The schematics to the right show the orientation of the crystal structures in a film. Images reproduced from Ref. [42].

In the work of Rivnay et al., the influence of the domain and grain boundaries is studied for an anisotropic film of the small-molecule *N,N'*-bis(*n*-octyl)-(1,7&1,6)-dicyanoperylene-3,4:9,10-bis(dicarboximide) (PDI8-CN₂). They argue that if a material has a slip-stacked packing motif (cofacial), the charge transport will be more strongly affected by boundaries than herringbone stacking (Figure 2.11b to the lower right). They

that for OFETs in which charge transport occurs along grain boundaries, the charge carrier mobility is significantly higher than for when charge transfer occurs along domain boundaries. Grain boundaries have only small angle shifts between the cofacial stacks, while domain boundaries have large angles between the core of the small molecule, hindering charge transfer more strongly.[42]

2.4.2 Semicrystalline Polymers

The understanding of how the morphology of a polymer thin film affects charge carrier mobility is still fairly limited. There are several studies that indicate what features are important and morphology trends that favor increased charge carrier mobility. However, the degree to which each type of morphology in polymeric conformation affects charge carrier mobility is not quantitatively understood.[50], [51]

It is understood that for common donor-acceptor polymer systems, intrachain transport is faster than interchain transport. Figure 2.12 illustrates the preferred charge transport directions. Due to the alternating donor and acceptor moieties along the polymer backbone, smaller distances and smaller activation energies are required for a charge to travel along (intrachain transport) the backbone than perpendicular to it, moving to another chain (interchain transport). Therefore, polymer alignment along the backbone is desired, and several works have shown that polymer thin films with aligned backbones in relation to the charge transport direction present good charge carrier mobility.[52]–[54] Factors that impact the intrachain delocalization are the chemical structure and processing conditions of the polymer. Different donor-acceptor moieties, different side chains, and more planar backbones can be achieved through organic synthesis of the semiconductors.[21], [55]–[58] It has been shown in a recent work that by changing solution shearing parameters, planarization of the polymer's backbone can be induced.[59]

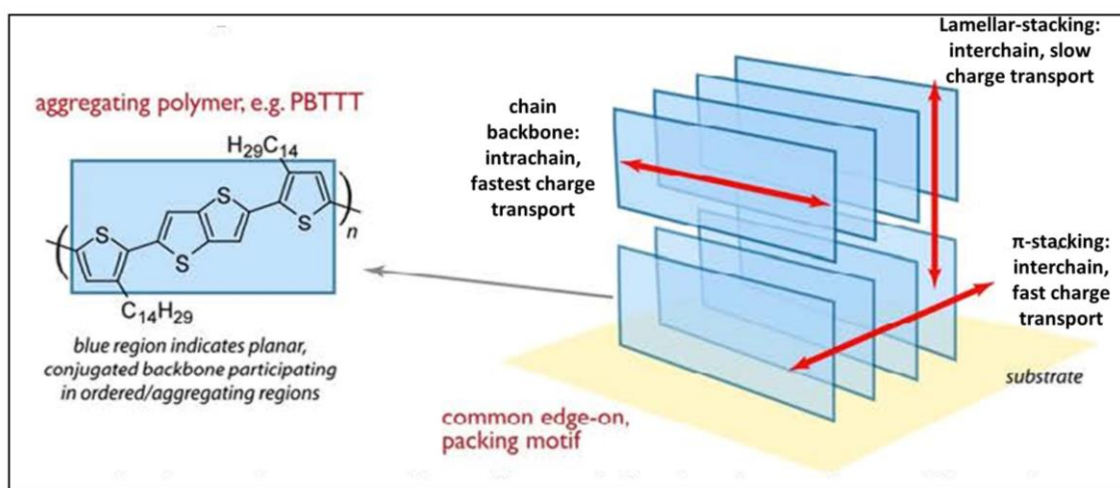


Figure 2.12: Typical charge carrier paths in semicrystalline polymer semiconductors. Image reproduced and adjusted from Ref. [51]

It is known that nanoscale disorder and the mesoscale material connectivity are relevant for device fabrication.[50], [60] So although the electronic delocalization along the backbone is important, the connection between chains and crystalline domains is important as well. Several groups state that high molecular weight (M_w) polymers have a high potential of achieving charge carrier mobility due to the higher chance of the existence of a percolation path along the channel of a device if the polymer chain can be aligned.[61] For low molecular weights, it is believed that due to lower chain lengths, tie-chains are

necessary for connecting one polymer chain to another and creating a percolation path.[50] However, the high M_w polymers are more prone to conformational disorder, such as higher chain entanglement in comparison to their lower M_w counterparts, hindering chain alignment.[50], [62] Figure 2.13b illustrates the potential charge carrier mobilities that could be achieved if a polymer chain would be ideally stretched from one electrode to the other.

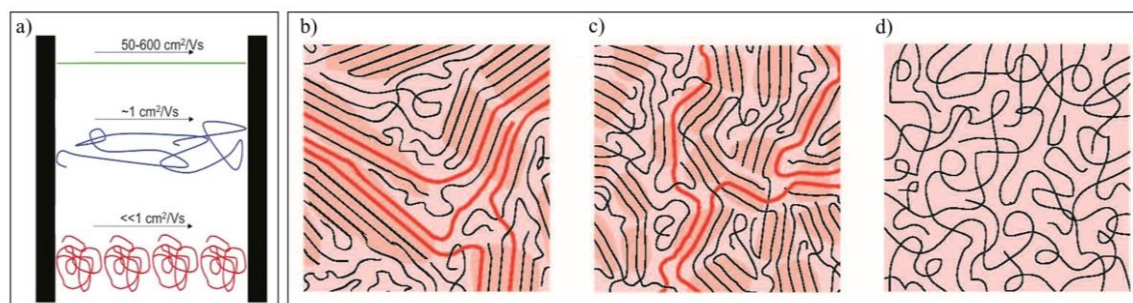


Figure 2.13: (a) Potential charge carrier mobilities depending on the degree of disorder of a polymer semiconductor. Image reproduced from Ref. [Grozema].⁴¹ (b) A semicrystalline polymer, (c) small disordered aggregates, and (d) a completely amorphous polymer. The ordered regions are highlighted by orange, the entangled black lines are the amorphous regions of the polymer, and the red chains are connecting ordered regions. Image reproduced from Ref. [51].

This is where interchain transport plays a role. Semicrystalline semiconducting polymers are highly desired due to the belief that interchain transport is enhanced in such ordered structures. Semicrystalline polymer solutions and films consist of various domains, from amorphous to crystalline populations, with varying degrees of size and density. Figure 2.13 illustrates film morphologies with different degrees of crystalline populations. Such crystalline populations are believed to facilitate charge transport between backbones of different polymer chains, allowing a higher chance of a percolation path being formed along the transport channel of an OFET channel. In amorphous regions, mostly intrachain percolation paths are expected. Once reaching a limit, if there are crystalline domains, interchain transport is therefore permitted. It has a similar role to what tie-chains are believed to have.[50] Some works suggest that the distance between the polymer backbone is also vital for charge delocalization in the interchain direction.[21] The resulting charge carrier mobility of such films is then a combination of both intra and interchain transport.[51]

Therefore, altogether, it is highly desired to have in OSC films high in-plane polymer alignment, and good crystallinity. Both these characteristics are highly sought during the fabrication process. There are, however, a few trade-offs. One of them is the belief that high M_w materials yield better intrachain transport than low M_w materials; but at the same time, in-plane alignment is more difficult due to higher chain entanglement, and crystalline formation also depends on the disentanglement for cofacial conformation. Recent works have shown that depending on the processing method, low- M_w polymers can have a higher charge carrier mobility due to better crystalline formation.[63]

With regard to the out-of-plane orientation of the polymer backbone, it is not yet a consensus of how vital the edge-on morphology is. From previous works, it was believed the edge-on morphology to be necessary at the semiconductor-dielectric interface of the device. [64] However, later works have shown that although this can contribute to increasing the charge carrier mobility, films with predominantly face-on orientation can yield comparable charge carrier mobility values.[21], [65]

Determining how each morphology characteristic affects the final charge carrier transport is especially challenging due to the various parameters that change in consequence of changing one parameter of the experiment. When changing, for example,

the molecular weight of the polymer, either viscosity or concentration change as well. As a consequence, film morphology formation will change depending on which parameter is chosen to be fixed. Deconvoluting to which percentage a thin film is crystalline or amorphous is also a challenge. Ideally, a single-crystal and a fully amorphous polymer need to be compared. It is conceptually unfeasible to fabricate single-crystal polymeric film to precisely determine this. A work that has attempted in doing so is the work of Noriega et al., that utilizes P3HT at different degrees of regioregularity.[51]

Chapter 3

3 Solution Shearing and Control of Film Morphology

Historically, vacuum evaporation, sublimation, and vapor deposition were the methods mostly used. These methods are, however, costly to upscale and economically unfeasible due to low fabrication speeds. Fast output, low-cost, and high-performance fabrication methods must be developed if organic electronic technologies are to be extended to large-scale production. It is currently believed that solution deposition methods are the most realistic option for upscaling the fabrication of organic electronic materials for commercial use.[66]–[68]

The solution processing methods that exist currently can be grouped into two big categories: one in which the liquid is deposited and left to dry on the substrate, and the deposition methods in which the dried film is formed during the deposition process. The primary solution deposition methods currently used are shown as schematics in Figure 3.1.

Methods in which the semiconductor is left to dry on the substrate are shown in the top row of Figure 3.1. These methods consist of drop-casting and printing techniques. Drop-casting is the deposition of a liquid on a substrate through drops and waiting for the solvent to evaporate. Additional processes such as annealing and capillary engineering of a drop-casted sample can be implemented.[66], [67] Printing techniques are a form of drop-casting, but with a higher degree of control of size, deposition rate, and deposition location in comparison to the drop-casting. Printing techniques have been shown to output semiconductor morphologies for high-performance OFET devices, such as in the work of Minemawari et al., where engineering of the liquid drying of C₈-BTBT after inkjet printing provided single-crystalline deposits.[71] Although electrical results are excellent, the deposition speed is still considered to be on the slow side and far from the desirable if it were to be used commercially.

For the case in which the film is wholly formed during the deposition process, there are the spin-coating and the meniscus-guided coating methods, as seen in the bottom row of Figure 3.1. The spin-coating method yields uniform films for small substrates, but thickness variations can become quite significant for large areas. Besides being very wasteful, if spin-coating were to be implemented for large-scale fabrication, it would require either a long time for fabrication or an absurd number of spin-coaters.

Among the challenges regarding upscaling of thin crystalline films are the broad particle size distribution, batch-to-batch variation, lack of control of polymorphs, and impurities.[72] The controlled drying process of the film that occurs during meniscus-guided coating (MGC) deposition allows the film growth to depend more on external processing factors, instead of the self-assembling of the material itself, solving part of the upscaling issues, such as batch-to-batch variations and control of polymorphs.

MGC methods are currently viewed as the most feasible deposition method for upscaling fabrication speeds and that have the highest commercial potential. Morphology of the thin film is controlled with MGC methods through the evaporation of the solvent at the contact line of a receding meniscus. Due to the sharp wedge shape close to the contact line of the meniscus, the film is expected to start forming there, and with the evaporation rate controlled, film growth can be controlled as well. Evaporation rate can be then controlled by the speed of the receding meniscus, the concentration of the solution, or the temperature of the substrate. Some of the most commonly used MGC methods are the dip-coating, bar-coating, and solution shearing methods. In this work, we make use of the solution shearing method and analyze how to improve semiconductor morphology through modifications in the shear-coater.

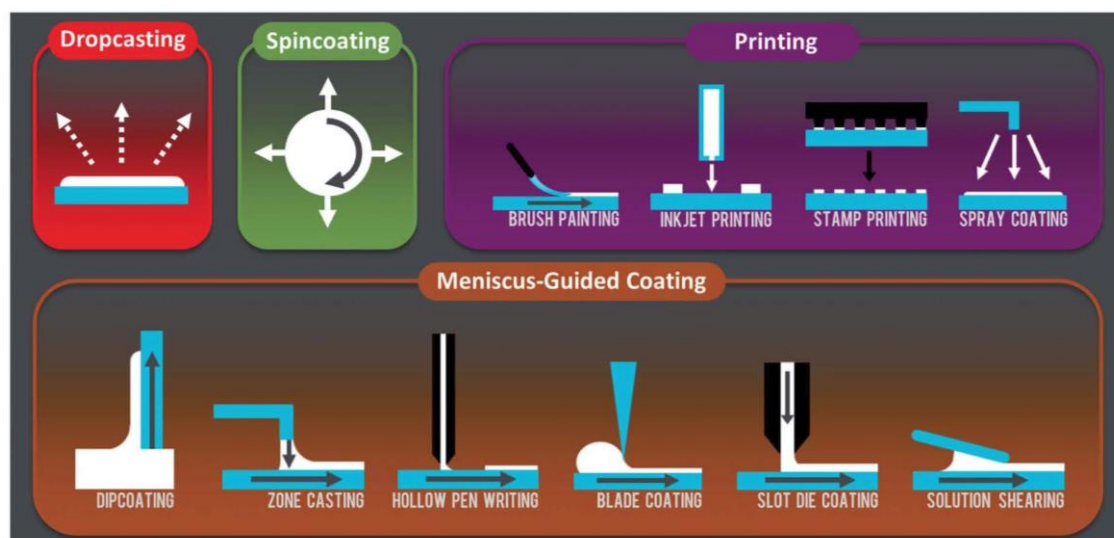


Figure 3.1: Schematic illustrations of solution deposition methods. Image reproduced from Ref. [73].

3.1 The Solution Shearing Method

Solution shearing is a recently developed method of solution coating that has shown great promise in providing access to a wide range of film formation conditions, ranging from near equilibrium to highly kinetically controlled deposition. The simplicity of setup and the flexibility to test a wide range of parameters has made it one of the favorite solution deposition methods in the field of organic electronic materials in the last years. It is also relatively fast, relatively easy to scale to large-area fabrication and has a very low material consumption compared to other commonly used laboratory deposition methods like spincoating.

The solution shearing method has first been reported by Becerril et al. in 2008 and used with the intention of depositing crystalline small-molecule films more uniformly. In addition to that, charge carrier mobility values of solution-sheared films are improved in an order of magnitude.[74]

Later, the work of Le Berre et al., in their experiments with a colloidal system of phospholipids, identified two solution shearing regimes: the evaporation regime and the

Landau-Levich regime. The significantly different regimes depend on the shearing speed and on two competing forces: the evaporative force of the meniscus and the viscous drag out of the meniscus that impedes it from following the receding blade. In the evaporation regime, the evaporation force is predominant, and films dry at the contact line (Figure 3.2a). In the Landau-Levich regime, the blade is too fast for the evaporation rate, and a stretched wet film is left on the substrate after the deposition is done (Figure 3.2b).

The two regimes can be identified by how the thickness of the film changes when coating speed is increased. In the evaporation regime, the higher the shearing speed, the thinner is the film deposited. In the Landau-Levich regime, the higher the shearing speed, the higher the film thickness. The graph in Figure 3.2c shows the relation between film thickness and shearing speed for both of the regimes.

The transition speed v^* in Figure 3.2c is determined by the speed at which the solution meniscus cannot follow the blade anymore due to viscosity. Thickness at v^* is the minimum thickness that can be obtained from this solution at these shearing conditions. Factors such as the type of solute and solvent, solution concentration and temperature of the substrate are factors that can change the transition speed and the minimum film thickness achievable.

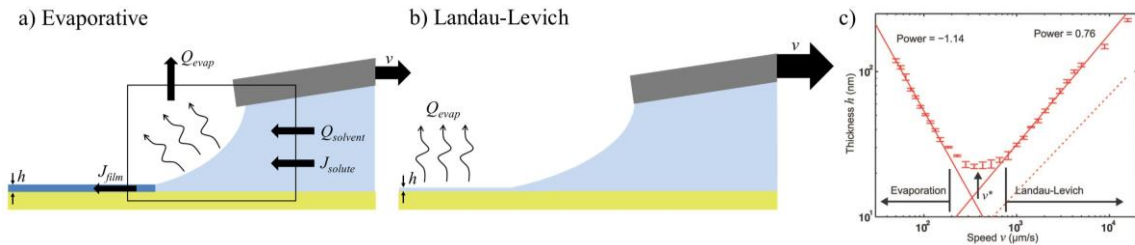


Figure 3.2: Schematic of the (a) evaporation regime and the (b) the Landau-Levich regime. (c) Graph of the film thickness as a function of the shearing speed, showing both the evaporation and Landau-Levich regimes. The Figures (a) and (b) are adapted, and (c) are reproduced from Ref. [75].

The **Landau-Levich regime** occurs when the shearing speed is high, and the solution does not evaporate at the same rate as the meniscus is receding. The occurrence and resulting film thickness of the Landau-Levich regime depend on the capillary characteristics of the system. Therefore, it depends on the viscosity, the surface tension of the liquid, and on which substrate the liquid is being deposited. Liquids with high viscosity and low surface tension are more prone to “sticking” to the substrate and leaving behind wet films. This depends as well on the substrate being coated. Surface modifications can be used to promote the wetting of the liquid on the substrate, yielding films for liquids not prone to wetting. Although the Landau-Levich regime has been used for the deposition of semiconductors in the field of organic electronics,[76]–[78] it is not the most used regime due to the lack of control of the drying of the solvent.

The **evaporation regime** is treated as a steady-state condition, where all the solvent from the solution sheared evaporates at the contact line, forming a film at the meniscus front while the blade is casting. The evaporation rate of the film can be calculated from a mass balance equation, where all the material entering the contact line evaporates at the contact line or become part of the deposited film. The equilibrium equation of material gives Equation (3.1):

$$h = \frac{C \cdot Q_{evap}}{L \cdot v \cdot \rho} \quad (3.1)$$

where h is the film thickness, C the concentration of the solution, Q_{evap} the evaporation rate of the solvent, L the width of the meniscus, v the coating speed, and ρ the

density of the film.[75] With this relation, the film thickness obtained from the coating can be predicted, or the evaporation rate of a film with known film thickness can be estimated. In this section, we approach and briefly describe a few fluid transport mechanisms that can occur during the solution shearing process, and appear throughout this work.

3.1.1 Capillary Flow and the Pinned Contact Line.

Deegan et al. have explained the “coffee ring effect” through the presence of a capillary flow that occurs in a drop with a pinned contact line.[79] The coffee ring effect is characterized by a stain of solute deposited at the borders of an evaporating drop system (Figure 3.3a). The condition for it to occur is that an evaporative system has a pinned contact line and a non-zero contact angle.[79], [80]

Due to the sharp shape of the drop closer to the contact line, the solvent evaporation flux there is higher. Once evaporation occurs, and solute concentration at the pinned contact line increases, the liquid from the interior of the drop moves toward the edges of the drop to make up for the liquid lost by evaporation. The liquid flow outwards transports the solute to the edges of the drop, and when supersaturation at the edge is reached, the solute is deposited there, forming a ring around the drop.[80]

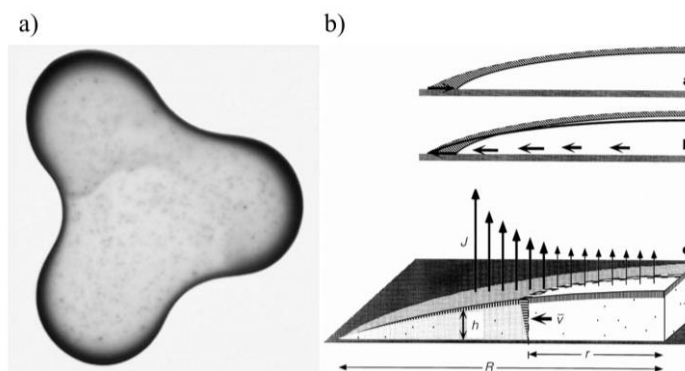


Figure 3.3: (a) The coffee ring effect: a higher concentration of solute is deposited at the borders of the evaporating drop. (b) The stronger evaporating flux at the edges of the drop and the pinned contact line promotes an outwards flow close to the substrate, and carry the solute from the center of the drop to the contact line. Images reproduced from Ref. [79].

3.1.2 Marangoni Flow

The Marangoni flow promotes a liquid flow close to the air-liquid surface of the drop due to a gradient in surface tension. The surface tension of a liquid is submitted to a gradient when there is a concentration or a temperature gradient.[81] The direction of the Marangoni flow will depend on the direction the gradient is positive along the droplet surface. The thermal and solutal Marangoni numbers are defined by:

$$Ma_T = \left(\frac{d\gamma}{dT} \right) * \frac{d_0 \Delta T}{\mu \alpha} \quad (3.2)$$

$$Ma_C = \left(\frac{d\gamma}{dC} \right) * \frac{d_0 \Delta C}{\mu D_{AB}} \quad (3.3)$$

ΔT and ΔC are the thermal and concentration differences, respectively, between the values at the contact line of the drop and the apex of the drop. σ is the surface tension, μ is the viscosity, α the thermal diffusivity, and D_{AB} the mass diffusivity of the solution.[82]

In the case of a temperature gradient, for example, if the substrate is heated, the temperature close to the contact line will have a higher temperature than at the apex of the drop. The higher temperature lowers the surface tension of the liquid close to the contact line.[82] Other characteristics of the liquid will determine, however, in which direction will the flow move. These factors include viscosity and thermal diffusivity of the liquid.

For most of the liquids, the surface tension tends to increase with solute concentration. The Marangoni flow due to a concentration gradient is more complex and depends on the nature of the solute and solvent.[83], [84] Factors such as viscosity, volatility, and mass diffusivity should be considered.[82], [84]

Although there are a few models for predicting the Marangoni flows direction, it is usually not a straightforward process and occurs simultaneously with other effects. The resulting flow dynamics in a system and the resulting deposit will depend on the combination of different flow mechanisms. A schematic of this is shown in Figure 3.4. Marangoni flow can be used to induce additional circulation of an evaporative system and change deposited patterns. In the work of Majumdar et al., for example, they allege to counteract the coffee ring effect with a Marangoni flow induced with ethanol vapor and obtain very uniform droplet deposition, as seen in Figure 3.4e.

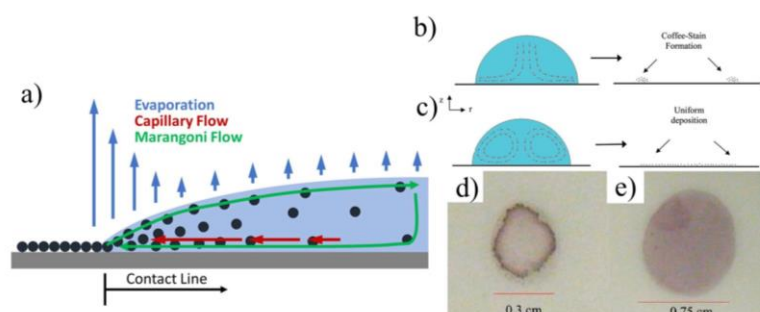


Figure 3.4: (a) Capillaries and Marangoni flows in a sessile evaporation droplet. Image reproduced from Ref. [85]. (b) An evaporating drop with its natural flow and the (d) consequent coffee ring effect. (c) An induced Marangoni flow (e) resulting in a uniform deposit. Images (b-e) are reproduced from Ref. [86].

3.1.3 Shear Flow

Shear flow occurs when there is stress applied in the direction parallel to a wall bordering a liquid. The shear flow is proportional to the speed of the moving wall, the liquid's viscosity, and inversely proportional to the thickness of the liquid's cross-section.

In the case of the solution shearing, there can be shear stress applied with the variation of the shearing conditions, such as the height of the blade, the shearing speed, or the ink formulation. In a recent work of Park et al., they are able to create different degrees of shear flow by modifying the coating speed of a conjugated polymer. Different flows promote different meniscus shapes and different strain. Such work has shown to yield different morphologies depending on the combination of shear rate and the residence time of the material in the liquid. From Figure 3.5, the shear rate appears to be minimum in the evaporation regime, and maximum for the Landau-Levich regime.

This is one of the few works to approach and attempt to simulate the flow mechanisms during solution shearing. A better understanding of such mechanisms is crucial for further developing the deposition method for large-scale deposition. The work of Park et al. has shown it beneficial for uniformity and morphology to be able to control

shear flow during large-scale deposition.[87] There could be better control of film morphology and possibly flow engineering for the desired film morphology for a particular material. For example, flow-induced characterization has been intensely explored for flexible polymers, but such knowledge is not necessarily extendable to organic electronic materials.[88]

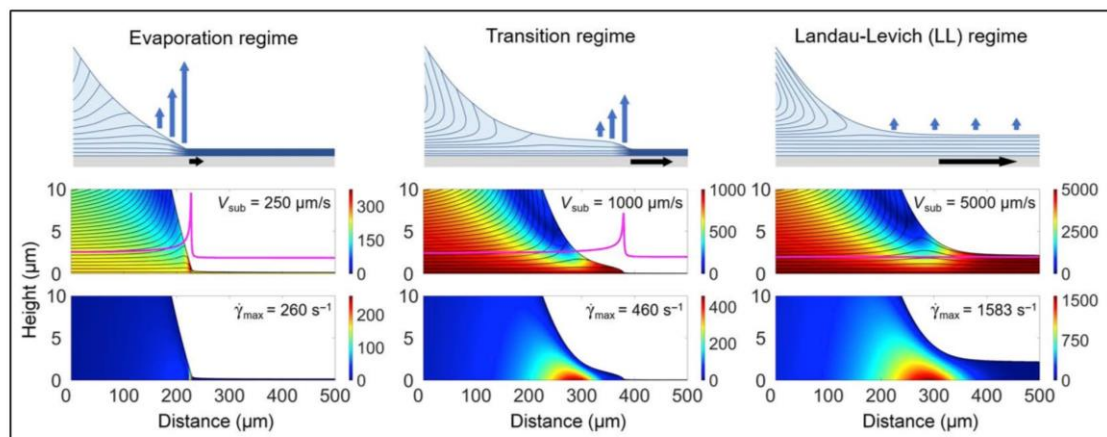


Figure 3.5: Simulation of shear flow in a receding meniscus at the different solution shearing regimes. The top row shows the evaporation flux and flow field. The middle row, the flow field and corresponding coating speeds; and the bottom row corresponds to the strain rate applied. The image is reproduced from Ref. [59].

3.2 Film Formation in Solution Shearing

Although the solution shearing of molecules and polymers happen under a similar experimental setup, the effect of the shearing on the resulting films and the behavior of the semiconducting small molecules and polymers is significantly different and has different purposes in both cases.

3.2.1 Small Molecules

Small-molecule materials tend to form crystalline films when processed from solution, being even possible to fabricate single-crystalline structures. The idea behind the shear-coating of OSC of small molecules is the better control of nucleation and crystal growth through the evaporation of solvent at the contact line. Crystallization is considered one of the most challenging processes to scale-up;[72] this makes the meniscus-guided coating method quite interesting for large-scale applications if it manages to control crystal morphology precisely.

According to the classical nucleation theory,[72], [89] there are two main crystallization processes: **nucleation** and **crystal growth**. The resulting crystalline formation depends on the predominant process during the crystallization and how these are combined. Films in which nucleation tends to be predominant are likely to be more fine-grained and have a higher grain density than crystals in which the crystal-growth process is predominant. Therefore, the particle size and distribution depends on the balance between the nucleation and crystal growth mode.

From both processes, nucleation is considered the one more difficult to control. It is the formation of a solid phase due to supersaturation of the solution; which is in a non-equilibrium regime, and several additional factors can play a role in the onset nucleation.[72] The solid formation acts as a “seed”, controlling the further deposition of the surrounding molecules. Nucleation-driven processes are often challenging to scale up

due to the risk of significant batch-to-batch variations, a broad particle size distribution and possible lack of control of solvates and polymorphs.

The nucleation during the solution shearing is expected to occur first at the air-liquid interface of the contact line of the meniscus, where supersaturation is reached first due to shallow liquid thickness.[90] We believe the solution shearing method to be a reasonably good fabrication method for controlling nucleation due to the very thin and localized region (contact line) at which it occurs.

The deposits from the solution tend to crystallize in a similar arrangement to the seed if the deposition rate is “appropriate enough”. How ordered the film will grow depends on processing conditions, such as temperature, pressure, and evaporation time.[72] For large crystal grains, a continuing balance at the evaporative front should be maintained to avoid secondary nucleation points.[72] It is a general rule though that more ordered films, the longer they need to be formed, while shorter formation times tend to yield disordered films.[72] The fabrication time of crystalline materials is a general challenge to the field of organic electronics, considering that the more ordered the films, the better the expected charge carrier mobility for OFET devices.

According to the classical nucleation theory, when a solution reaches supersaturation, combined with order fluctuations, clusters of organized molecules (nuclei) can be formed. The clusters already have the shape of the mature crystal, and the further crystal growth happens around the nuclei. A “non-classical” perspective of crystal nucleation argues that nucleation happens in a two-step process and that clusters are liquid-like and tend to stay so while further molecule aggregation occurs.

A schematic of both processes is presented in Figure 3.6. Depending on the material and the crystallization process, the classical or “non-classical” approach is more appropriate.[89] The detailed discussion regarding the difference of both approaches is out of the scope of this work, but assists in explaining why a receding meniscus is especially favorable for well-aligned crystal growth.

Among the factors that influence the crystal nucleation rate is the thermodynamics, which involves the volume, shape, and surface energy of the liquid. The kinetics of the crystal nucleation depends on how the attachments and detachments of the molecules occur, and the clusters are organized.

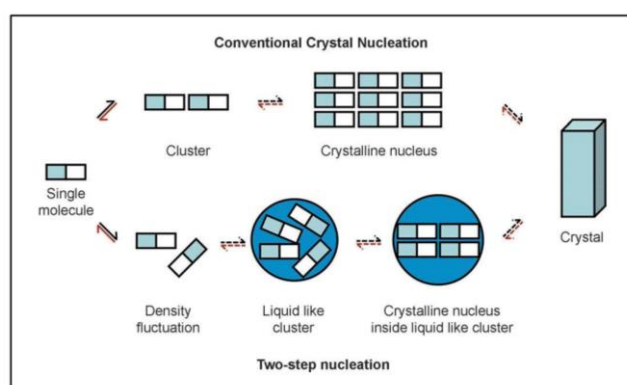


Figure 3.6: Schematics of the two crystal nucleation models in solution. Image reproduced from Ref. [89].

The solution shearing of organic thin-film materials tends to have great potential of formation of highly ordered crystalline films due to the small bulk size of the liquid at the contact line and stronger influence of the surface energy, making the nucleation energy necessary easy to reach.[72], [89]

Although the nucleation plays a part important part in the determination of polymorph available in the sample, the crystal growth process of the material might be the biggest responsible for large grains and polymorphs and in which quantity they are

available in the crystal.[72], [89] After nucleation occurs once, continuous crystal growth is desired as the dominant phase, to yield larger grains and fewer grain boundaries.[41], [72] Single-crystal growth is often required to be a slow process and obtaining large crystalline domains in solution processing quite challenging. For good quality crystal growth, the supersaturation of the solution should continuously be under control.[72]

The evaporation regime of the solution shearing method fits very well the purpose of growing crystalline films with large domains. By adjusting the deposition temperature, solution concentration, and shearing speed, it is possible to control with accuracy the nucleation and crystal growth of small molecules. The work of Giri et al. has shown that the solution shearing method enables the morphology control and crystal growth of the small molecule 6,13-Bis(triisopropylsilylethynyl)pentacene (TIPS-pentacene).[91] They have claimed average gate-voltage-dependent charge carrier mobilities of $4.2 \text{ cm}^2 \text{ V}^{-1} \text{ s}^{-1}$ and opened new possibilities for the fabrication of organic semiconductor devices through solution-coating.

For organic electronics, it is well known that film morphology and molecular packing in the film are fundamental factors that govern the observed charge carrier transport. Through the control of crystallization and the tuning of the molecular packing, significant improvements in the electronic properties have previously been observed.[91], [92] It is commonly accepted that films with high crystallinity are favorable for charge carrier transport due to the high degree of structural coherence (resulting in a low energetic spread of the transport levels) and a low density of grain boundaries which are also known to significantly hinder charge transport.[41], [48] The molecular packing of the material itself has also been shown to affect the electrical characteristics of organic semiconducting films strongly, specifically when multiple polymorphs of the active material exist that differ in their degrees of π orbital overlap. The control of the polymorphism in such materials becomes vital for accessing higher charge carrier mobilities.[93]

Figure 3.7a-g portrays the solution shearing method used for TIPS-pentacene, the morphology changes, and how molecular packing has been modified through confining metastable polymorphs of this material.[91] Such an effect is believed to occur due to vertical confinement during the crystallization of the meniscus, possible due to the very low thickness of the meniscus.[94] Figure 3.7h illustrates such a mechanism.

It has been demonstrated for benchmark materials such as (TIPS-Pentacene),[91], [92], [94]–[96] 2,7-Dioctyl[1]benzothieno[3,2-b][1]benzothiophene (C_8 -BTBT)[97], [98] and 2,8-Difluoro-5,11-bis(triethylsilylethynyl)anthradithiophene (diF-TES-ADT)[44] that films with high fractions of non-equilibrium polymorphs can be obtained by proper tuning of the fabrication parameters such as the speed of deposition,[91] solution concentration,[92] annealing,[44], [95] addition of polymers[97] or even the application of an external electrical field during processing.[98]

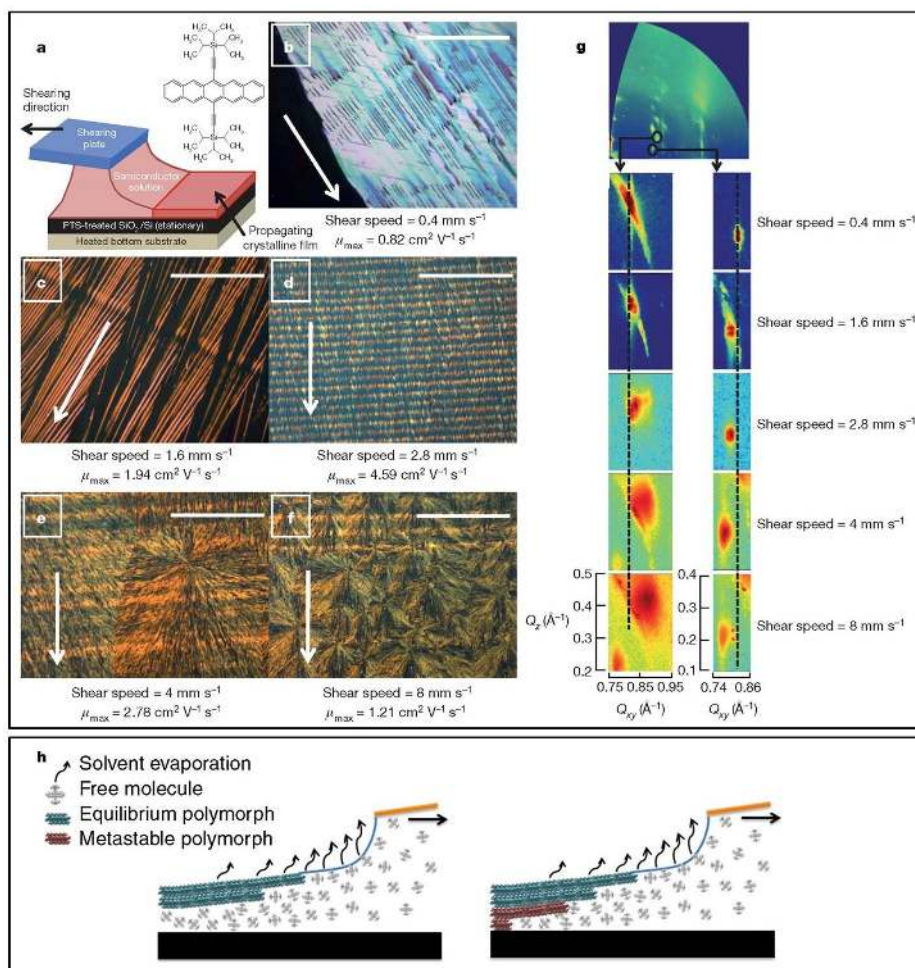


Figure 3.7: (a) Solution shearing method from the work of Giri et al. and (b-f) the respective films sheared with varying speed. (g) The corresponding polymorphs present in the films. These images are reproduced from Ref. [91]. (h) Schematic of the formation of TIPS-Pentacene polymorphs in the films through vertical confinement during the solution shearing process. This image is reproduced from Ref. [94].

Modifications in the solution shearing process of small-molecule OSCs

Although the solution shearing method has shown to be highly flexible and provide suitable OFET devices with morphology control, it can be seen in the work of Giri et al. that there is a limit to which morphology can be controlled with only temperature, concentration and deposition speed. The devices with maximum charge carrier mobilities are given by an optimal combination of the thickness (high mobility polymorph) and continuous macrostructure of crystalline structures on the substrate. The crystal growth mode of the TIPS-pentacene is limited by nucleation due to the high shearing speed. Due to such limitations, several works have branched out from the solution shearing method attempting to improve charge carrier mobility of devices through modification of the solution shearing method. In this section, the most significant works for the small-molecule materials are highlighted.

The work of Janneck et al. has proposed a model for predicting the optimal shearing speed necessary for the equilibrium steady state mass-balance of the meniscus. They argue this is the optimal growth situation for OSC solutions in their work with C₈-BTBT, for a wide range of solvents tested. Here it is shown that the critical speed, the speed at which the mass entering the meniscus is precisely the same being outputted, is the condition under which there is the most continuous crystal growth of semiconductors. These conditions are consequently the speeds at which maximum charge carrier mobilities are obtained.

Although the shearing speeds calculated in the work of Janneck et al. are significantly low, it has been shown to work for a wide range of solvents and various temperature conditions.[99]

One of the most notable works with solution shearing of semiconducting small molecules is the work of Diao et al. Through the structuring of the shearing blade, they are able to shear nearly single-crystalline large-area films of TIPS-pentacene and trimethylsilyl-substituted quarterthiophene (4T-TMS). The rationale behind the structuring of the blade is the increase of flow in the semiconducting meniscus through recirculation. As can be seen in Figure 3.8a, the microstructures have an architecture which enables recirculation and re-stirring of the organics semiconductor in order to inhibit nucleation of the material and improve more continuous crystal growth. In Figure 3.8a at the right, are microscopy images of the films sheared with and without micropillars. Significantly continuous crystals are achieved for films sheared with the FLUENCE method. In combination with the patterning for the substrate, which selects the crystalline domain formed in the shearing direction (making use of the coffee ring effect principle), the work of Diao et al. has demonstrated a very successful method of printing single-crystalline films.[92]

The use of multi-menisci for crystal growth has been shown in the works of Kim et al.[100] (Figure 3.8b) and Xiao et al. (Figure 3.8c),[101] both utilizing derivations of the micropillars. With the intent of creating multiple menisci formations during the shearing process, the first group has used pattern rubber substrates and the second, micropillars. They believe the multiple menisci and different capillary forces applied to the semiconducting system to be the main reason for increased charge carrier mobility. This is a way of taking advantage of the capillary flow in the meniscus, by only changing the shape of the contact line of the meniscus in order to induce nucleation at the desired sites.

Other works that have modified the shearing method of crystalline semiconducting materials involve patterning the substrate. Besides the crystal selection used in the FLUENCE method, the utilization of patterns of wetting and dewetting areas on the substrate has enabled the control of crystal growth in the work of Giri et al. Lateral confinement of the crystal growth can be beneficial for film formation and charge carrier mobility for OFET devices.[102] However, there is a limit in crystal size below which the performance regresses.[102]

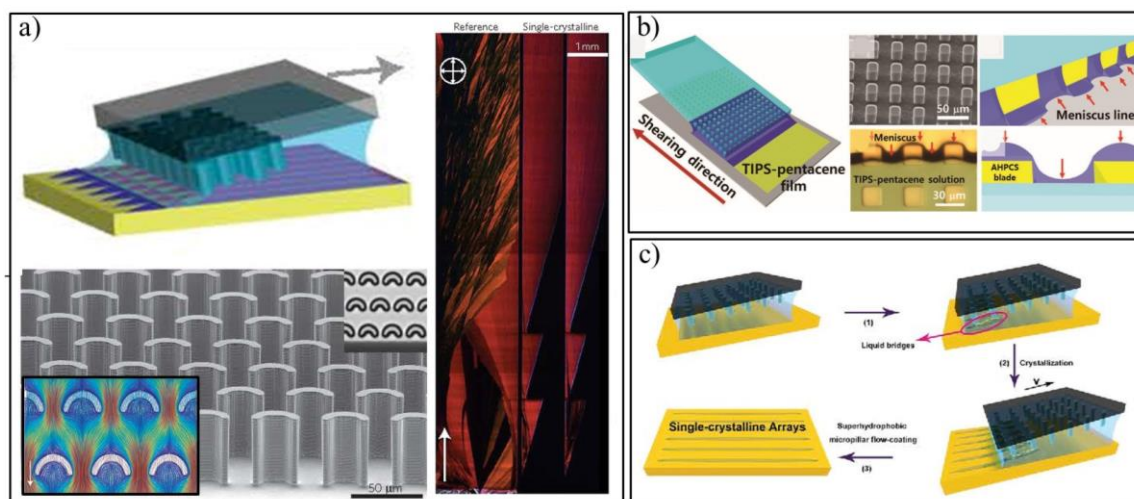


Figure 3.8: (a) The solution shearing setup for the FLUENCE method with the microstructured blade and patterned substrate. The images are reproduced from Ref. [92] (b) The flexible patterned blade from Kim et al. and details of the multiple menisci. Images reproduced from Ref. [100]. (c) A schematic showing the micropillar, and the single-crystal arrays from the work of Xiao et al. Images reproduced from Ref. [101].

The change in the formulation of the sheared semiconductors is another option for improving device quality. The semiconductor blends utilizing a dielectric polymer as a binder for the films, described by Niazi et al., [103], [104] and the works of Anthopoulos, [105], [106] involving the blends of both small-molecule and semiconducting polymers. Both types of polymers have shown benefits and have shown to improve the solution shearing method. The blends of small molecules and polymers will be discussed in Chapter 5.

Blends of solvents with different boiling points have also been used in solution shearing and given good results. The work of Zhang et al. with bar-coating assumes there is a change in Marangoni flow, leading to more continuous films (Figure 3.9). Although the Marangoni effect of the solvent blend cannot be proved, it seems to be an effective way of mitigating discontinuity and new nucleation sites of small molecules. [107]

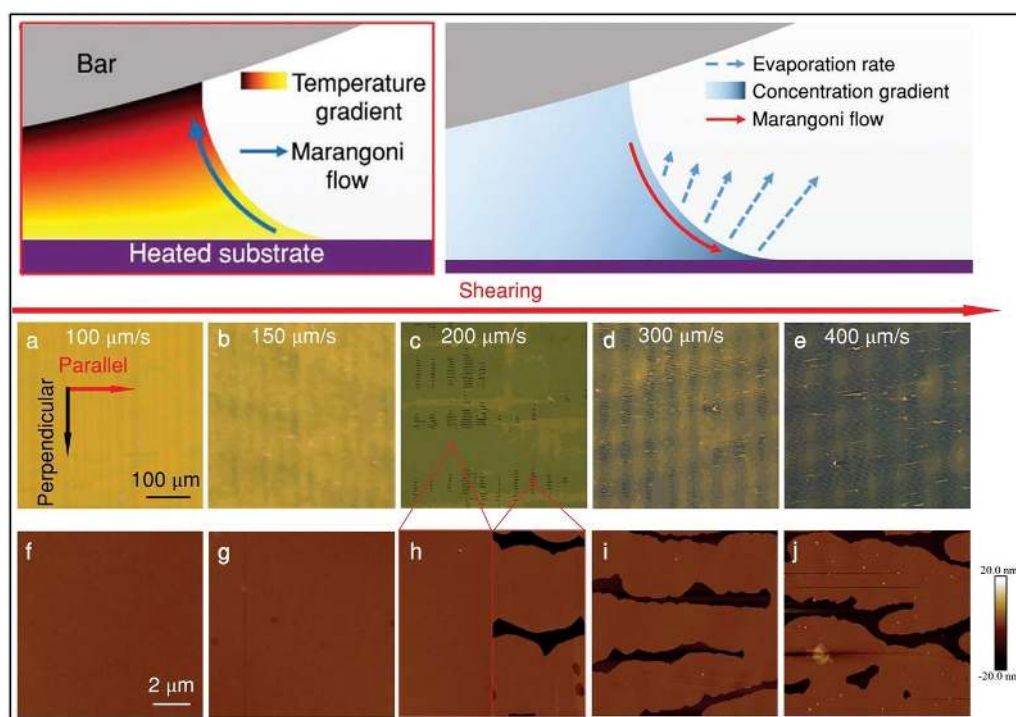


Figure 3.9: The meniscus at the top left is the simulated backward flow Marangoni from the thermal gradient of the substrate. The meniscus at the top right is the expected Marangoni flow towards the contact line, believed to be caused by the solvent blending. (a-e) Are the resulting polarized optical microscopy images of the films deposited by using the solvent blend, and (f-j) are the corresponding atomic force microscopy (AFM) images. The images above are reproduced from Ref. [107].

3.2.2 Polymers

Most of the high-performance devices reported in the literature are based on crystalline small-molecule thin films. They have been widely used due to the knowledge that active layers with high crystallinity, large domains and a small density of grain boundaries are highly beneficial for charge carrier mobility and have the highest potential of obtaining transport speeds comparable to the classical silicon devices. In the last years, however, organic polymer materials have risen as materials with great potential, and significant performance improvements have been achieved.

With the synthesis of donor-acceptor copolymers, the field of polymer OFETs has recently gained more momentum. With intrachain carrier mobility as a transport path in addition to the interchain charge transfer, they have opened many doors for the study and optimization of devices. Several works focus attempts of charge transport improvement on

the molecular structure of these polymers, with the intent of changing the π - π stacking distances or modifying the sidechains to obtain more favorable film formation. However, only in the last years have groups attempted in enhancing performance through adapting of the deposition method of such materials.

The crystallization process for polymer materials happens in a different way and in a significantly more sophisticated manner than crystallization in small-molecule materials. For the case of homopolymers, crystallization in a solution can be divided into three stages: aggregation, extension (or coalescence), and crystal growth. Such phases are presented in the schematic of Figure 3.10.

In the aggregation phase, “baby nuclei” appear due to the folding of parts of the polymer chain. While each small molecule can only participate in one nucleation process, there can be several aggregation processes starting at different locations of the polymer chain. (Figure 3.10b).[108] The aggregations happen through the folding of the polymer on itself, and with the time given to self-assemble, has the length of the crystal precursor L_0 . During the extension (or coalescence) phase, the length is extended to its limit L^* , which will define the final length of the crystallite formations (Figure 3.10c).[109] These crystallites will act as a nucleus for crystallite growth, and new chains will aggregate to it during the growth phase (Figure 3.10d).[110] For the case of copolymers, it should be added that π -stacking interaction might also promote aggregation even in the solution phase.[111]

Due to the different crystallization mechanism in polymers, and desired amorphous chain alignment, the film formation mechanism that is the most effective for small-molecule materials is not the same as for the polymers. While the formation of thin crystalline films depends mainly on the control of nucleation rates and crystal growth, morphology changes for polymer films might depend more on the fluid transport mechanism of the MGC process. The long times necessary for disentanglement of polymers and organized self-assembly require perhaps stronger flow control mechanisms and further understanding of self-assembly during the deposition process.[111]

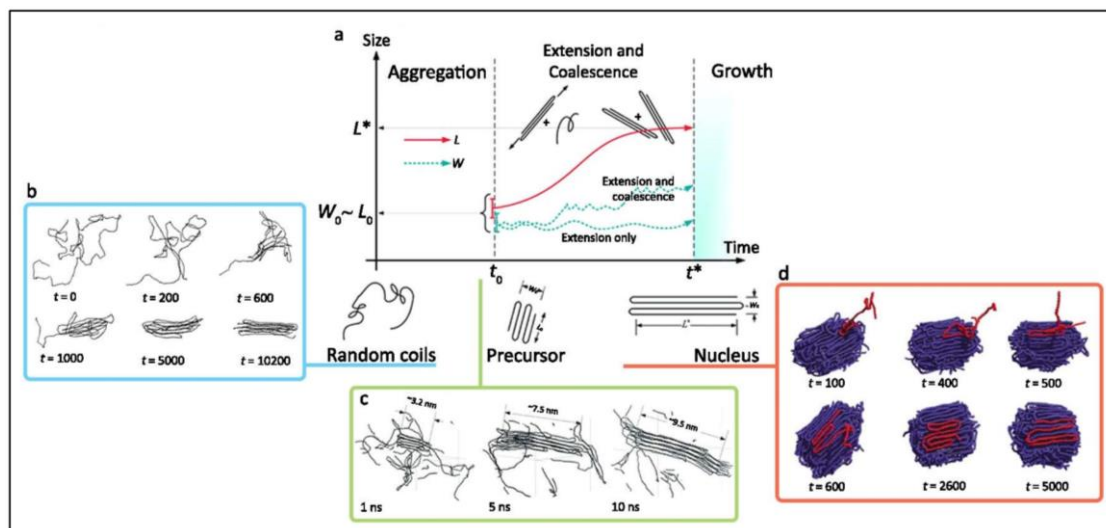


Figure 3.10: (a) Schematic of the crystal growth process in homopolymers in solution. (b) Illustration of the aggregation phase; (b) the extension – or coalescence – phase, and (c) the crystal growth phase. Illustration adapted from Ref. [111].

Most of the works that have used a MGC method for deposition of polymers have used the coating method in the evaporation regime. While the Landau-Levich regime would be desired due to the high deposition rates, the drying time of the film after the deposition is expected to allow the polymer chains to relax and undo any effect of shear stress that has been applied to them. This is, however, highly beneficial for OPV

fabrication, since in-plane anisotropy is desired. For OFETs, which in-plane alignment is desired, however, not so much. In addition, if speeds are increased too much in the Landau-Levich regime, thick films hinder charge carrier mobility for OFETs as well.

Therefore, most of the existing works operate in the evaporation regime.[21], [53], [112], [113] With a small gap between the substrate and blade and an angle applied to the blade, shear flow is expected to increase by the confinement of the liquid when it moves from a larger area under the printer head to the meniscus front (lower height). Because tilt angles are often quite meager, it might not have a significant enough shear stress, and the shear stress applied is then mostly due to the speed component.

The speed during the coating is, however, limited to the evaporation regime. It is also limited by wetting conditions and meniscus instabilities such as stick-and-slip. In this case, the shape of the meniscus adds another degree of difficulty of understanding the transport mechanisms in the deposition and how this collaborates to the final film morphology. There are multiple phenomena that occur in the semiconductor meniscus during the film deposition process. A few of them are the shear strain caused by the speed and the pressure from the back of the meniscus, the capillary flow of a dynamic contact line, both occurring in combination with effects from Marangoni flow.

In Figure 3.11, the mechanisms present during the solution shearing process for polymer semiconductors are sketched. There are notions of how these mechanisms influence the final film morphology. It is believed most of the morphology is determined at the point where the semiconductor enters the meniscus front. The quantity of parameters for MGC of polymers is so vast, and results vary from material to material, that a global understanding of how coating parameters influence the resulting film, and how extendable these results are to other systems is still far from being achieved.[111]

With the increasing number of works that show the electrical potential of aligned polymers, the organic electronic community has begun to recognize the importance of a more thorough understanding of fluid mechanics and rheology in the application for organic electronics. Research on the mechanical and structural properties of common polymeric materials is quite well understood, and there is an abundant quantity of works. The application and translation of such mechanisms to the field of organic semiconductors are, however, only at its beginning.

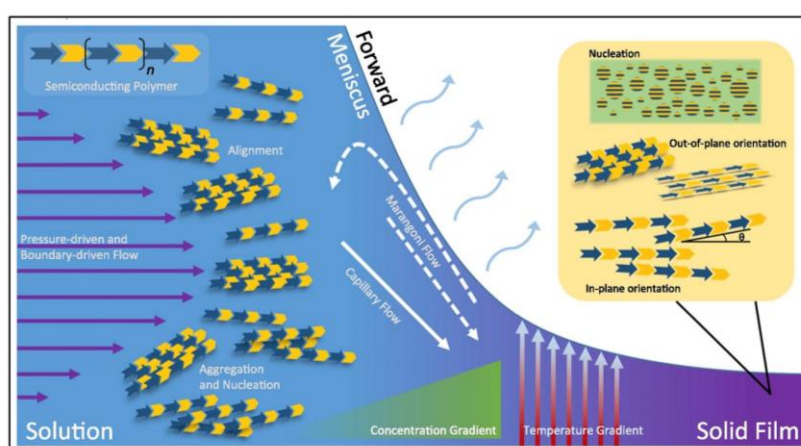


Figure 3.11: Schematic of flow fluid transport mechanism, such as flows; and polymer conformation mechanisms during solution shearing. Image reproduced from Ref. [111].

Further theoretical and simulation work is suggested as the main enablers for improvement and further development of the field.[111] Due to the vast range of parameters for the fabrication and optimization of film morphology, theoretical work would be of great use. In this section, a few MGC processing methods used for controlling

the morphology of polymeric films are approached. Among these approaches are the post-processing alignment methods, the ink formulation pre-processing due to the deposition, modified geometries for MGC methods, and substrate patterning.

In previous works, **post-processing** methods have been shown to improve device performance significantly. In the work of Park et al. and Kim et al., they use the dipping of polymeric thin films in moderate solvents and believe lower molecular weight portions of the polymer to be removed, improving morphology quality,[114] and a more significant number of P3HT aggregates to be formed, respectively.[115] Stretching is a standard method for chain alignment in homopolymers,[116] and has been observed quite early for the case of organic electronics, in poly(3-octylthiophene) thin films. The stretching of a thin film (< 100 nm) induced anisotropy in the charge carrier mobility to a degree of over 4 times.[117], [118] In more recent work with P3HT, an anisotropy of 9-fold is reached.[119]

Annealing has been shown to be effective in improving thin-film crystallinity and out-of-plane alignment. For annealing to be effective, however, the necessary temperatures are often usually higher than 200 °C. This has shown to improve the microstructure organization of film morphologies significantly and boost charge carrier mobility. Formation of nanofibrils and improved crystallinity films have been observed obtained through annealing.[63], [120]–[123] This is, however, a limitation for fabrication on flexible substrates, which often do not tolerate such a high temperature.[124]

One of the most effective methods for controlling polymer alignment is the **pre-processing** of the semiconductor solution. Coating solutions that have already aggregates, crystal seeds or nanofibers have shown to act as precursors for highly aligned films. In the work of Bielecka et al. an aging time of months induces polymer aggregation of P3HT and increase charge carrier mobility values in two orders.[125] In the works of Chu et al., exposure to UV-light and aging is used for aggregation of P3HT in nanofibers, and such nanofibers are aligned during the blade-coating process, yielding highly aligned and high-performance charge-carrier mobility (Figure 3.12a).[126] Chang et al. tune the aggregation through the exposure time of the solution and explain the effect of UV-light as delocalizing the π -electrons of the thiophene rings along the backbone, increasing its rigidity. The decreased rigidity is expected to decrease the solubility and increase the molecular assembly. The results of this study are shown in Figure 3.12d.[127] In the work of Chang et al., the formation of nanowires of P3HT through embedding the semiconductor in a polystyrene matrix also had improved in-plane alignment morphology.[128]

Aiyar et al. have shown that submitting a solution of P3HT/chloroform to ultrasonic oscillations is capable of disentangling polymer chains and promoting favorable self-assembly conditions. When such solutions are coated by dip-coating and spin-coating, large rod-like aggregates are observed in the morphology, and charge carrier mobility improved. This is tested, and morphology changes due to ultrasonic oscillations are effective for polymers with two different regioregularities and for both the spin-coating and dip-coating method.[129]

Another ink formulation of the solution is to use a solvent-antisolvent blend to induce aggregation in the solution. Such formulations work, so that poor solvents tend to induce polymer conformation to reach minimum chain free energy and make them adhere to smaller formats.[130] In the work of Chang et al., methanol is used in a solution of PDPPF-DTT and chloroform as a non-solvent for films coated by slot die coating. Polymer aggregation is tuned by changing the methanol concentration, and alignment is optimized through the deposition speed. Molecular packing and crystallinity of the films are improved, and mobility is raised from an average of $1.3 \text{ cm}^2 \text{ V}^{-1}\text{s}^{-1}$ to $3.7 \text{ cm}^2 \text{ V}^{-1}\text{s}^{-1}$. In the work of Park et al., the increased aggregation of a P3HT/chloroform solution from adding the non-solvent acetonitrile improved charge carrier mobility values in spin-coated thin

films by a factor of 20. This is associated with the increased 2D ordering of the polymer and higher tendency of the material to adopt an edge-on packing.[131]

It is essential to notice here that the choice of solvent is a challenge ahead of expanding roll-to-roll methods to polymeric semiconductors. Due to poor solubility of such materials, usually chlorinated solvents are used for laboratory tests. This is a significant limitation in fabrication upscaling due to the hazardous nature of such materials for workers and the environment.[66], [111], [130]

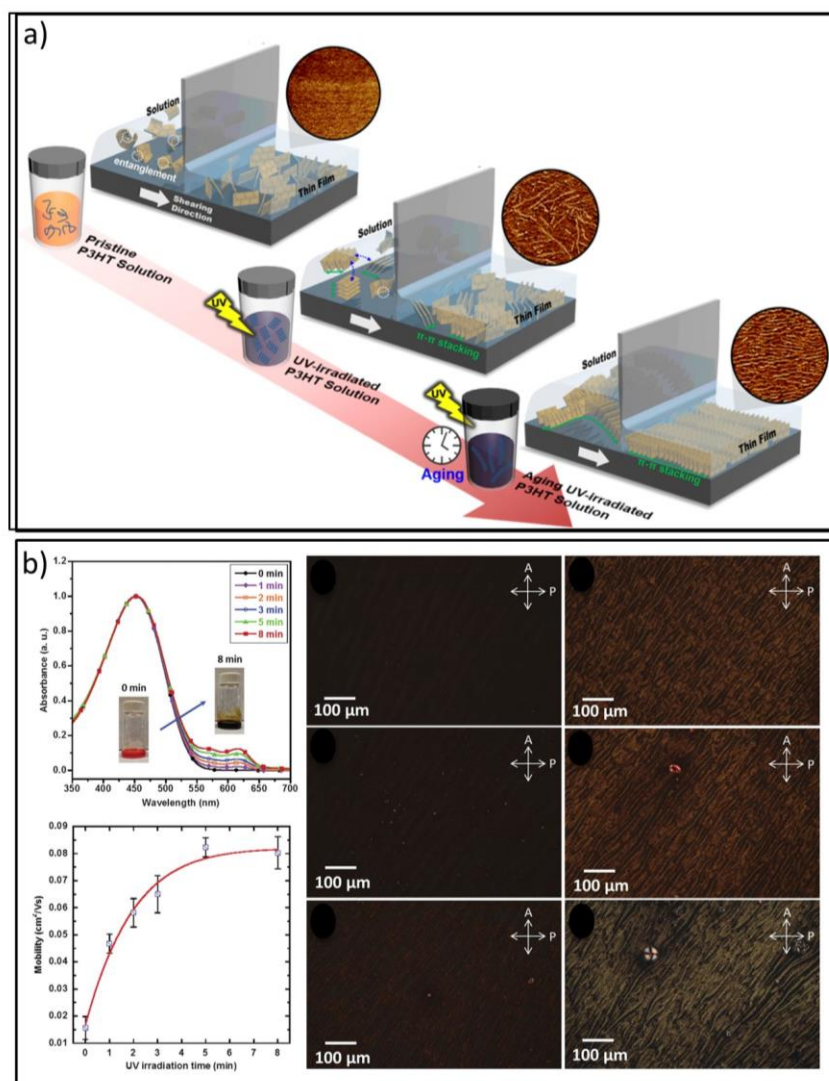


Figure 3.12: (a-c) UV-light exposure and aging process of the P3HT solution slot-die coated. Image reproduced from Ref. [126]. (d) Effect of UV radiation on the P3HT solution, charge carrier mobility, and birefringence of the P3HT film as a function of the time exposed to UV-light. Image reproduced from Ref. [127].

A few aspects of film morphology can be tuned only through the standard MGC method parameters, such as speed, solvent choice, and temperature. High boiling temperature solvents have been preferred for the coating of polymer films for OFETs. This allows more time for chain disentanglement and formation of favorable morphologies in relation to in-plane anisotropy.[21], [132] The work of Park et al. has also shown that for specific polymers, different morphologies can be reached by changing the shearing regime. This is also done by changing the shearing speed.[59]

Substrate patterning has also been used for the solution shearing of polymers. The result of the solution shearing of a polymer depends on the combined effects of the film

formation that starts at the liquid-air interface (top surface of the film), and the film formation that starts at the liquid-substrate (bottom surface of the film).[52], [53] If the alignment is induced from the substrate strongly enough, it should be able to predominate the film formation and be the defining morphology at the region of the film where the charge transport occurs. Patterning of substrates has been shown to have a significant impact on the morphology of copolymer thin films. The copolymer poly [4-(4,4-dihexadecyl-4H-cyclopenta[1,2-b:5,4-b'] dithiophen-2-yl)- *alt* - [1,2,5] thiadiazolo[3,4-c] pyridine] (PCDTPT) has been shown to have charge carrier mobility up to $5 \text{ cm}^2 \text{ V}^{-1} \text{ s}^{-1}$ if solution-sheared on a nanogrooved patterned substrate.[52], [123] In the work of Patel et al., it is shown with near-edge X-ray absorption fine structure (NEXAFS) highly anisotropic bottom surface of the polymer film, induced by growth on nanogrooved substrates (Figure 3.13a).[133] The work of Wu et al. have also shown the effect of such grooves in mobility, and how the nanogrooves predominate the bottom surface morphology of films. The effect of the grooves is so significant, it turns out to be determinant for charge carrier mobility in bottom-gate transistors (Figure 3.13b).[52] This work suggests that the grooves, with a nanometric scale, are capable of aligning both crystalline and amorphous phases of the polymer. The nanogrooves can be combined with other deposition methods, such as in the work of Lin et al., with the “Chinese brush”, that creates multiple meniscus-shaped curves at the contact line (Figure 3.13c),[54] and the very slow drying process used by Tseng et al. to obtain very high charge carrier mobility values.[122]

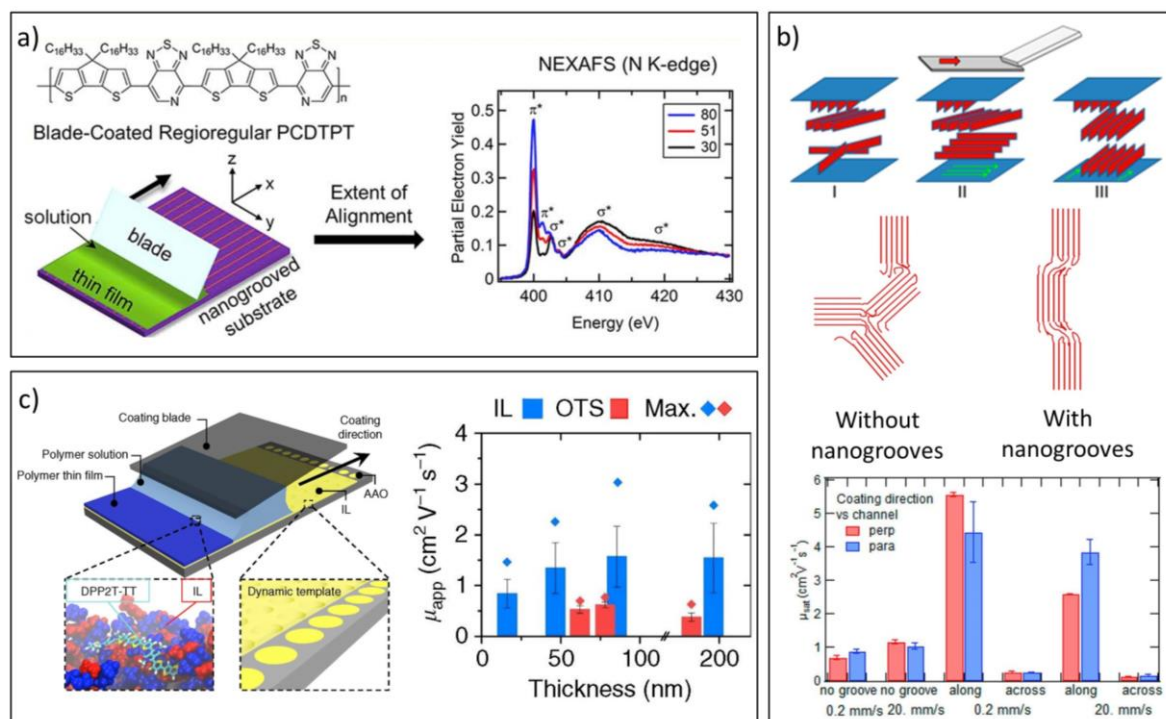


Figure 3.13: (a) The solution shearing of PCDTPT on a nanogrooved substrate promotes alignment on the film surface, which is detected by NEXAFS. Image reproduced from Ref. [133]. (b) An in-situ study of the polymer alignment during the solution shearing over nanogrooves unravels the change in alignment for different depths of the film. They show significant charge carrier mobility differences and suggest what causes such a mobility boost. Images reproduced from Ref. [52]. (c) A dynamic template allows the higher crystalline quality of polymeric films, improving charge carrier mobility of OFET devices. Images reproduced from Ref. [134].

The novel ionic-liquid (IL) technique presented in the work of Mohammadi et al. also shows how modifying substrate can enhance favorable film formation in polymeric films. Using a substrate that allows reconfigurability of the polymer organization, and promotes ion- π interaction between the substrate and the polymer, increased polymer

alignment and crystallinity is observed. This reflects in increased charge carrier mobility as well (Figure 3.13c).[134]

An effective method of controlling morphology is also the **modification of the shearing blade**. In the work of Diao et al., the crystallinity of all-polymer solar cells is significantly improved, along with favorable phase separation of the bulk heterojunction. The blade modified with micropillars is designed to induce extensional flow in the ink, to uncoil the polymer chains and allow them to more efficiently cofacially aggregate. (Figure 3.14a). The blade is expected to enhance extensional flow in the system.[135] A similar approach has been used recently in the work of Xu et al. for a large-scale output method for stretchable polymeric OFETs. Patterned blades are used for aligning the structures polymers and have proven to be very effective.[68] Although the patterned-blade solutions are effective for polymer aligning, the patterning processing of the blade is non-trivial, and the technological limitation of the micropillars is still not down to the necessary dimensions to ideally uncoil the polymers (hundreds of nanometers).

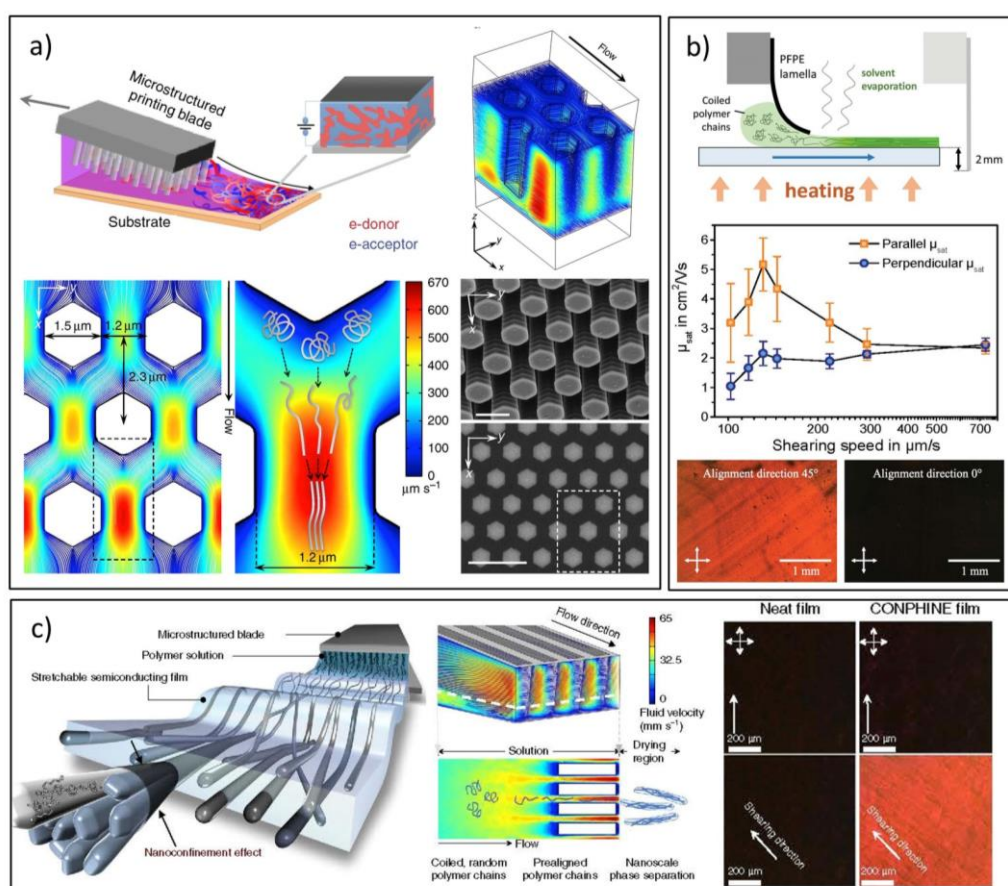


Figure 3.14: (a) Illustration of the FLUENCE method: a shearing blade with micropillars is used for enhancing the crystallinity of all-polymer solar cells. Images reproduced from Ref. [Diao].[92] (b) The coating method using a flexible lamella for a higher shear force during the deposition of the co-polymer DPP-BTz, resulting in highly anisotropic thin films. Images are reproduced from Ref. [136]. (c) The CONPHINE method for aligning polymer lamellas for stretchable semiconducting films. Images are reproduced from Ref. [68].

Another very effective and simple method is the use of the flexible coating blade in the work of Schott et al. on poly[[2,5-bis(2-octadecyl)-2,3,5,6-tetrahydro-3,6-diketopyrrolo[3,4-c] pyrrole-1,4-diyl]-alt-(2-octylonyl)-2,1,3 benzotriazole] (DPP-BTz). The flexible lamella used as a blade conforms to the substrate and applies a higher shear force than that of only a liquid meniscus coated by a rigid blade (Figure 3.14c). It has shown to be an effective method in controlling the degree of alignment of the co-polymer DPP-

BTz. In-plane anisotropy is highly increased, and maximum saturation mobility claimed to be as high as $6.7 \text{ cm}^2 \text{ V}^{-1} \text{ s}^{-1}$ (Figure 3.14c).[136]

3.3 Stick-and-slip Instabilities

The stick-and-slip instability is an additional characteristic of the solution shearing of polymeric semiconductors. Because most polymer solutions present some viscosity, the stretching and release of the meniscus provide either dewetting or films with significant thickness variations in the form of undulations. This instability hinders speed deposition and can be detrimental to devices that require high uniformity.[111]

Film instabilities that may occur during solution deposition have been studied and employed in recent works, most prominently with the intention to precisely control solute deposition to create micro-patterned surfaces.[137]–[143] While the goal may so far have been to exploit the deposition inhomogeneities for gratings and surface patterns, understanding their origin is also of great importance to avoid undesired instabilities such as those appearing during the solution shearing of electronic device films where a continuous and homogeneous film morphology is required.

Several types of patterns have been observed in the literature such as dots,[137] lines,[137], [139]–[141], [143] and meshes[137], [140], [142, p.] when colloidal or polymeric systems are solution sheared.[137], [138] These have been described as instabilities that occur at the evaporating contact line (CL) of a receding meniscus during solution deposition.[75], [85], [137], [144], [145] Among these instabilities are Rayleigh dewetting instabilities,[137] stick-and-slip,[137], [139], [141], [146], [147] and fingering instabilities.[137], [140] Several research groups have investigated the cause and correlation of such patterns to the coating parameters as well as how the combination of multiple instabilities affects the resulting deposited solute. The variables that usually contribute to the occurrence of instabilities are the deposition surface (surface energy and roughness),[137], [140], [148], [149] the concentration of the solute,[137], [139], [147], [150] the solution viscosity,[144] and the deposition speed.[137], [138], [141] Examples of patterned deposits making use of the stick-and-slip instability studied in some of these works are reproduced in Figure 3.15.

Functionalized surfaces are commonly used for the deposition of organic semiconductors during the fabrication process of organic field-effect transistors (OFETs). Many past works have shown that especially substrates treated with octadecyltrichlorosilane or octadecyltrimethoxysilane (ODTS) yield better performance for OFETs in general.[21], [50], [151]–[158] This is usually attributed to either a higher charge carrier density caused by the dipole-induced built-in electrical field from the monolayer,[151], [152] an increased molecular ordering,[21], [50], [153]–[156] or the reduction of electronic trap states as for example caused by water.[157] Although it is challenging to cast a uniform film over substrates with low surface energies, ODTS-treated substrates are still preferred over plain SiO_2 substrates when depositing polymer thin films for device fabrication. However, due to the low surface energy of the ODTS-functionalized substrates, dewetting of the solution commonly occurs, leading to meniscus instabilities such as stick-and-slip especially when solution shearing speeds are increased, and in extreme cases, absence of solute deposition on the substrate. The stick-and-slip instability is thus one of the main obstacles to an increase of the fabrication throughput of polymer-based OFET devices.

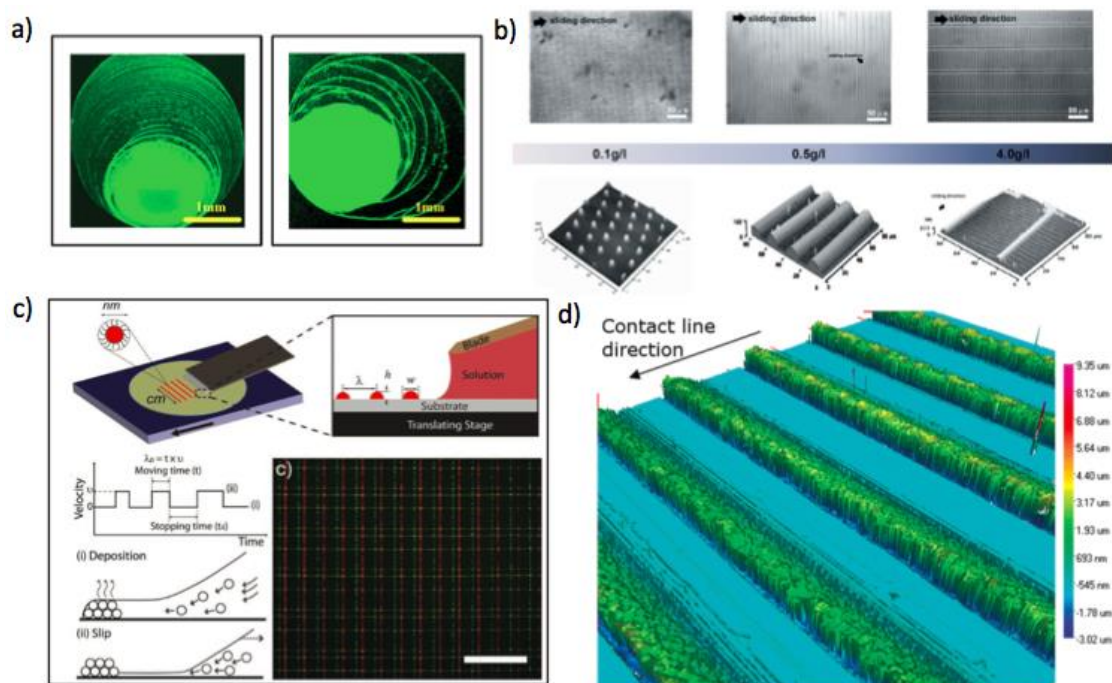


Figure 3.15: (a) DNA stain patterns formed from aqueous solution at a concentration of $50 \mu\text{g ml}^{-1}$ (left) and $20 \mu\text{g ml}^{-1}$. (b) Polystyrene patterns formed from the shearing of a chloroform solution at different shearing speeds. (c) Method for manipulating stick-and-slip for nanoparticle deposition; scale bar: $200 \mu\text{m}$. (d) Deposition of silica particles through dip-coating of a colloidal suspension. Images reproduced from Refs. [137], [139], [141], [150], respectively.

The stick-and-slip phenomenon originates from the instability at the contact line of the meniscus, attributed mainly to low surface energy substrates that appear incapable of maintaining a prolonged and stable meniscus during the coating process.[146], [148], [159], [160] It is associated with continuous cycles of pinning and de-pinning of the contact line and has been observed for a diverse range of solutions.[135], [137], [141], [146], [147], [150], [161] The pinning/de-pinning cycles can be described as follows: solvent evaporation at the contact line causes the concentration and the viscosity to increase, pinning the contact line to the substrate when the viscosity exceeds a certain threshold. The pinned contact line subsequently promotes capillary flows towards the pinned contact line leading to solute deposits at the pinning point.[138], [150] This deposition of solute at the border of the contact line is termed “coffee ring effect”.[79] The building pulling force on the meniscus due to the continued motion of the blade eventually leads to a de-pinning and a very fast subsequent slip of the contact line until it reaches a position closer to equilibrium. Figure 3.16a-d illustrates such a process in an evaporating sessile drop.

The stick-and-slip phenomenon manifests in thin films as periodic thickness variations and produces films with undulations or “wire” deposits (Figure 3.16e, f), the latter being a kinetic border case of the thickness undulations. When the concentration in the slipping meniscus is too low or the slip speed too high to adhere to the surface, as a result, no film is deposited between the pinning locations, thus forming only “wires”. The work of Ge et al. has described the transition from a film to a wire morphology as a result of a shift in the balance between the liquid’s surface tension and the interface energy to the substrate that occurs at higher coating speeds.[146]

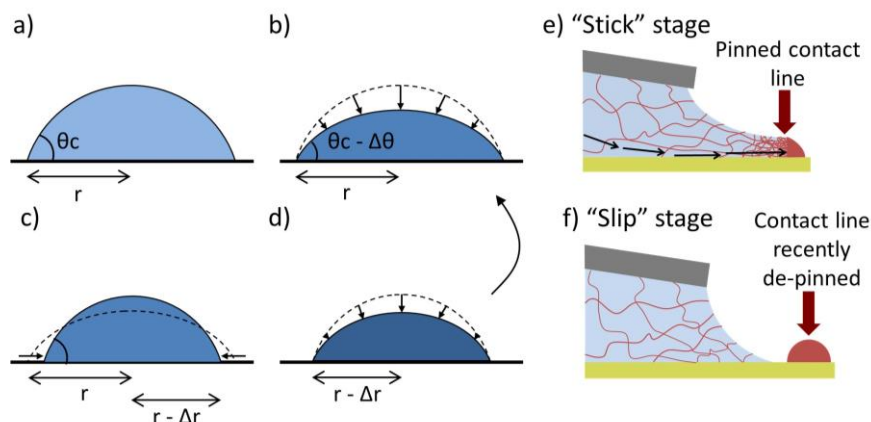


Figure 3.16: Schematic of the stick-and-slip motion of the contact line. (a) Initial evaporation condition; (b) contact angle and drop height decrease due to evaporation until reaching a limit contact angle; (c) slip occurs due to high free surface energy; (d) new pinned contact line. Schematic adapted from Ref. [148]. (e) the equivalent pinned contact line (“stick”) for a receding meniscus during solution coating; (f) a deposited wire and the meniscus after the “slip” process.

3.3.1 Contact Angle Hysteresis and Stick-and-slip

From literature, it is well known that a contact line that has enough defects (due to substrate non-uniformities or uneven solute distribution in the solution) can be pinned at metastable energy states, which is a cause for contact angle hysteresis.[162]–[165] The contact angle hysteresis is the difference between the biggest and the smallest contact angle a liquid on a substrate can have. The apparent contact angle can then assume any value between the receding and advancing contact angle, hindering precise characterization of a system’s wettability.[166], [167] The higher the contact angle hysteresis of a system, the higher the range of contact angles the system can assume. Therefore, a system with a high contact angle hysteresis can stay “stuck” for a longer time, and stick-and-slip instabilities are more likely to occur. A system with large contact angle hysteresis could have a significant $\Delta\theta$ (Figure 3.17b) before the “slip” occurs.

Contact angle hysteresis arises from both the chemical and physical properties of the system.[148], [149], [167] Among the chemical properties are the heterogeneity of the surface, or the modification of the surface due to interaction with the liquid, such as swelling.[148], [167] Physical reasons for the hysteresis are surface roughness, asperities, and surface defects.[148], [149], [162], [163], [168]

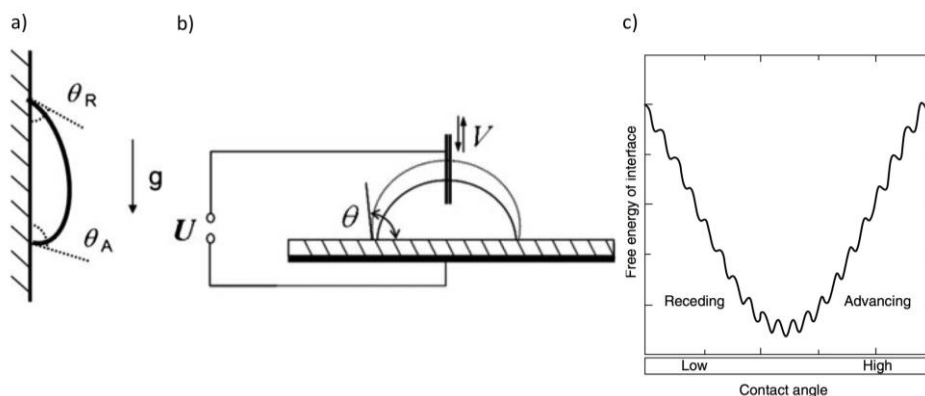


Figure 3.17: (a) A drop stuck at its critical advancing contact angle (θ_A) and critical receding contact angle (θ_R). In addition to tilting a drop, (b) slowly pumping liquid in or out of a drop enables the measurement of the critical contact angles. Images are reproduced from Ref. [167]. (c) A qualitative graph representing the apparent contact angles of a meniscus and its metastable states. Image (c) is reproduced from Ref. [169]

In Chapter 7 of this work, a solution for such a hindrance in film deposition is developed, and the understanding of definitions such as stick-and-slip and contact angle hysteresis is crucial.

3.4 Vibration-assisted Thin-film Solution Fabrication Methods

Acoustics, i.e., the emission of mechanical waves through a medium (gaseous, liquid or solid), has a wide field of unexplored aspects that are currently still under investigation and not completely understood.[170], [171] There is a large number of works involving vibration and liquids, including different solutions, vibration geometries, and applications in various fields.

In this work, the use of vibration of the shearing blade with the piezoshearing method is proposed to attempt improving film morphology of the semiconducting layer for organic field-effect devices. It is a novel method, and to the best of our knowledge, there are no works that are directly related to it, or that have a good understanding of such a complex setup as the one presented in this work. In this section, a few effects that occur when applying vibration to a liquid body are assembled, and a few cases in which vibration is used to improve thin film for organic electronic applications. It is not clear if all these effects occur in our shearing system, but signs of them have been observed, and they are factors that should be considered when examining the results of our piezoshearing process.

3.4.1 Effects on a Liquid stemming from Vibration

The transport mechanisms in liquids are a rich field of study, with a broad range of varying conditions and effects. When considering the vibration of liquids, several aspects are to be taken into account: surface wave propagation, wave reflections, the liquid medium to be analyzed, and the boundary conditions. However, it is out of the scope of our work to analyze these effects in detail. These would require a robust and detailed theoretical understanding of fluid transport and dynamics, which is not the focus of our work.

In this section, some common effects of vibration application on liquids are discussed; effects that have been observed in our experiments, and how these are related to our piezoshearing setup. The experimental factors of the setup that can influence such effects are also discussed. A few elements to be considered when treating a dynamic vibrating system are cited. Effects that can arise in liquid suffering the effect of vibration are traveling or standing surface waves, atomization, acoustic streaming, cavitation, microstreaming, and acoustophoresis.

Different methods of applying a vibrating force to liquid are possible, depending on the nature of the liquid and the desired effects. Acoustic (~20 kHz) and ultrasound (~20 kHz to 100 kHz) vibrations have been used as an ultrasonic probe, a vibrating substrate, a loudspeaker close to the liquid, or interdigitated transducers for generating surface acoustic waves (SAW). Figure 3.18 shows schematic illustrations of effects the vibration of a substrate or an ultrasonic probe can have on a liquid.

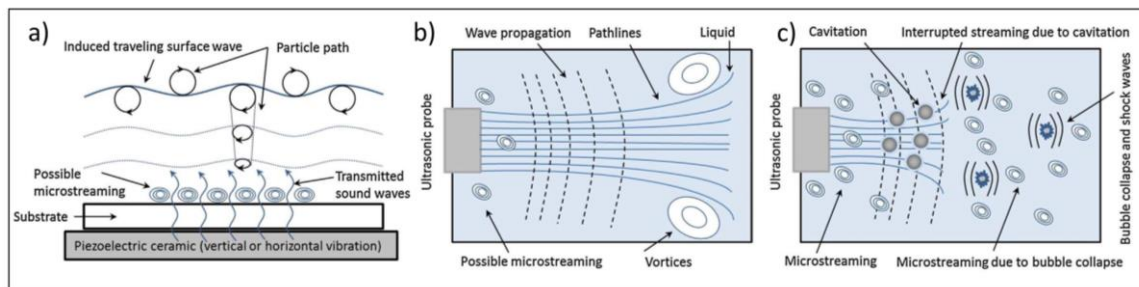


Figure 3.18: (a) Surface waves and microstreaming induced by a vibrating substrate and (b) acoustic streaming caused by an ultrasonic probe. Figures are reproduced from Ref. [172].

Surface waves

The pressure variation of the vibration can induce surface waves that propagate along the surface of the liquid body. These are a combination of both longitudinal and a transversal wave propagating into the liquid. Surface waves can occur at any frequency and can be traveling or standing waves - in the case it is confined by boundaries.

The existence of surface waves in our experimental setup is considered. The resulting propagating surface waves of a system depend on a wide range of factors, such as the liquid in which they are propagating, surface tension, and especially boundary conditions. A small meniscus or a pinned contact line have been shown to have a significant effect on the reflection of surface waves,[173], [174] and the conditions under which our semiconducting liquids are pinned vary considerably, as will be discussed further.

In the case of our receding meniscus setup, we expect the boundary of the liquid to be determined by the combination of the OSC at the contact line and the surface energy of the substrate. In the case where the contact line is pinned, and vibration power (or amplitude) is low, the boundary might be considered fixed. One of the boundary conditions of our setup – at the three-phase contact line - is discussed further in Chapter 8, in which the pinning and depinning of the contact line and how the vibration can change such a boundary is studied. The observation of surface waves is a fairly complex process and has an additional factor of difficulty added when our liquid meniscus is in constant motion.

Faraday instabilities: standing waves were observed by Faraday in 1831 in a sheet of liquid when vibration is applied to the substrate and became a topic studied by many afterward. Standing waves on a liquid are observed for several materials and shown to produce a wide range of patterns. The patterns observed in these liquids are found to oscillate at a frequency of half the frequency of the external excitation source. This is often what authors in the field use as a determining characteristic of a Faraday Instability. We believe this effect to be present in one of our experimental setups, which is described in Chapter 8.[170], [171], [175]–[178]

Atomization

This is observed when the vibration power applied to the liquid is high, and droplets are ejected from the liquid body. These can appear as droplets at the surface or as a mist. Existing works describe such an effect, and it is seen as a product of two possible mechanisms: increase of surface wave instabilities until the detachment of droplets; and/or the cavitation formation with subsequent collapse at the surface of the liquid, which ejects the droplets from the bulk of the liquid.[179]–[182] Traces of such effect for a few experimental setups.

Acoustic Streaming (or circulation)

Acoustic streaming is generated by an external oscillating source, which causes variation of positive and negative pressures, and therefore a steady flow in the liquid.[183] The pressure variation acts as a longitudinal wave into the medium, which intensity tends to dissipate when distance increases from the source of vibration.

The power of the streaming is directly proportional to the power of the vibration (or to the amplitude of vibration squared).[183], [184] Therefore, the higher the power, the higher the net motion set into the liquid. It is important to note that although this relation is linear, the net motion (velocity) that propagates into the liquid is much weaker than the velocity of the fluid once the wave passes through it.[183] The resulting flow is an overlap of the propagating flow and the new sound waves that are introduced into the system.

The closer the portion of the liquid is to the vibration source, the higher the flow is induced.[184], [185] Viscous forces of the liquid act both as an attenuator and a propeller for acoustic streaming. On the one hand, the wave propagation dissipation is higher when viscosity is significant, and therefore, the velocity of a portion of liquid at a certain distance from the source is smaller. On the other hand, a more significant velocity gradient in space is induced, generating a larger flow.[183], [184]

As derived by Leonhard Euler in 1757, acceleration in a fluid can appear even if the velocity field is constant with time, but varies with space. Therefore, a velocity gradient in space is enough to create acceleration and therefore flow.[183] Flow in response to oscillation is exclusive to fluids, due to their deformation when subjected to shear stress.

From the work of Eckart[184] on flow induced in a liquid through a sound beam, it is argued the geometrical characteristic of the experiment to be of high importance. According to him, the larger the proportion a sound beam reaches in a liquid body, the larger the area of the liquid that has its flow enhanced. The velocity induced is directly proportional to the distance from the vibrating source. On the other hand, there is a more considerable reflection from boundaries, such as walls (in our case, the substrate), when propagation from the source reaches the wall. Figure 3.20 from the work of Eckart et al. illustrates the possibilities and consequences of the relative reach of the beam in comparison to the size of the container or liquid body. Considering our sound beam as the vibrating of piezoblade, our sound beam is significantly smaller than the cross-section of the liquid body under the blade. The distance of the blade from the substrate in our work can vary from 20 μm (at the meniscus front) to 800 μm (back of the meniscus), approximately, while the maximum displacement the blade can vibrate is 2.2 μm . Although the maximum displacement of the blade is not necessarily equivalent to the size of the acoustic beam in the work of Eckart, the dimension is rather small when compared to the dimension of the liquid coated. Therefore, according to Eckart, Figure 3.20a, a significant flow enhancement could possibly be obtained close to the blade, where velocity is maximum, but the flow would remain in the region only close to the blade and not necessarily propagate to the areas of the liquid closer to the substrate. In Chapter 8, the main differences in the film morphology are indeed detected on the top surface of the films coated with piezoshearing.

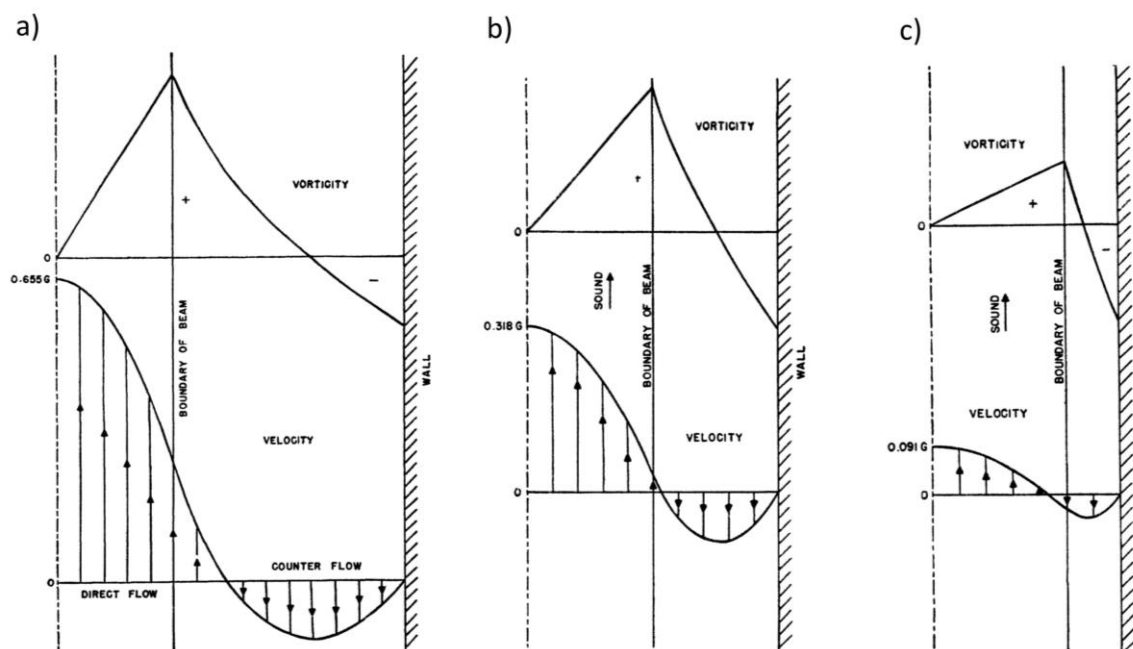


Figure 3.19: Depictions of solutions for flow, counterflow, and vorticity caused by acoustic oscillations. These are the intensity of flows expected when (a) the sound beam is narrow in relation to the width of the liquid (distance from center to the wall); (b) the beam is approximately half of the width, and when the (c) beam occupies a significantly large portion of the width. Images reproduced from [184].

The presence of cavitation decreases the pressure gradient in the liquid in the locations close to the source of vibration and therefore damps the flow in regions far from the source.

Cavitation

Cavitation occurs due to positive and negative pressure applied to the liquid. Bubbles are formed, and these can either stay in the liquid or collapse. The collapse of bubbles can cause shockwaves and turbulence in the liquid, inducing another source of circulation called microstreaming. Microstreaming can occur due to bubble collapse or due to mild oscillations.

Cavitation is often used for cleaning due to the high energy that the shockwaves the bubbles release when the collapse occurs. The formation of such bubbles depends highly on the frequency and vibration power applied to the liquid.[172]

Microstreaming

Besides the acoustic streaming, which occurs along a large portion of the liquid body, there is also the microstreaming, which is classified as high flow intensity in a small scale, as a consequence of microbubbles formed in the liquid.[183] Depending on the overall experimental setup, if cavitation occurs, it can either decrease streaming if it collapses at the peak of flow or can create additional localized flows around them, termed microstreaming.

3.4.2 Relevant Characteristics

Factors of the liquid system that should be considered when approaching vibration in a liquid are nature, volume, geometry, surface tension, and viscosity of the liquid. These factors are crucial to determine how the liquid will react to vibration. It will determine what frequencies and intensities it will respond to, and what effects will the vibration have on the liquid body.

The resonance frequency of the liquid is the frequency to which the liquid responds the strongest. This occurs when the vibration frequency is close to the natural frequency of the system. The resonance frequency of a liquid volume depends on several physical parameters of the meniscus - the composition, viscosity, surface tension, and geometry of the liquid. The natural frequency of a free drop has been studied by several works since Kelvin (1890) and Rayleigh (1894). According to the work of Lamb (1932),[186] the oscillating frequency of an inviscid free droplet is given by:

$$\omega_n^2 = \frac{n(n-1)(n+1)(n+2)}{(n+1)\rho^i + n\rho^e} \frac{\sigma}{R^3} \quad (3.4)$$

Where n is the number of the harmonic, σ the surface tension between two fluids, R the drop radius, and ρ^i and ρ^e the density of the internal and external fluid, respectively. Such formula is applicable to inviscid liquids or liquids with lower viscosity. Later, such calculations have been extended by Miller and Scriven (1968) and Prosperetti (1980) to viscous liquids. A liquid with similar characteristics, but increased viscosity is expected to have a lower resonance frequency. The work of Strani and Sabetta (1984) used these results to extend the solution of low viscosity for a drop placed on a substrate instead of a free droplet.[187] The support of the droplet by a substrate is expected to raise the natural frequency of the system.

We observe here that the physical characteristics of the liquid play a significant role in the resulting effect. This is one of the limitations of the current setup of the solution shearing and piezoshearing methods. Considering solvent evaporation and that there is no constant supply of material for dispensing, the natural frequency of the meniscus is likely to change during the shearing process, and therefore the response of the liquid to a particular frequency can change throughout the shearing process.

In the work of Picard et al., the addition of material generates new eigenmodes and is transient with time. In this work, they observe that the resonance frequency is controlled by the composition of the bulk of the meniscus, the surface tension, and the boundary conditions. Also, the resonance frequency of the system changes with the curvature of the meniscus. Therefore, the constant pinning and depinning of the contact line in the polymeric systems used in our work adds another factor of difficulty to the determination of a resonance frequency.[188]

In addition to influencing the resonance frequency of a system, viscosity adds a damping factor to the meniscus. The energy introduced into the liquid is damped by the viscosity, and power transmitted decays. This is why viscous liquids require a higher amount of energy for effects to be observed.[177], [189], [190] Viscous films are also more likely to have a no-slip condition in relation to a solid substrate, which affects the contact line, and therefore reflection or dissipation of surface waves.[191]

3.4.3 Vibrations and Thin-film Formation

In the section above a number of effects that can be observed when applying vibration to a liquid are cited, and how the characteristics of the liquids matter. If these effects are to be extended to thin-film fabrication, it is crucial to include the influence of solvent evaporation coupled with the vibration in the fabrication process. In this section, a few works that have used vibration to improve the quality of thin films are cited. This has been done by either treating the solution before deposition or applying vibration directly to the system during film formation.[172]

The effects that arise in the liquid are dependent on the material, the dimension of the liquid body, the vibration frequency and amplitude used, and how the vibration is applied to the liquid. Therefore, the effects the vibration have over a small quantity of liquid used for deposition can be significantly different from those observed for a bulk liquid. Due to the top and bottom confinement of the liquid in the case of thin films, dewetting and instabilities are more likely to appear than in liquid bulk. If streaming in the large scale happens to be induced, film breakage could also occur. Surface waves and microstreaming are the most likely effects to be observed for the case of thin-film deposition.[172]

Most of the works of vibration and thin films use either a setup of a vibrating substrate through a piezo actuator or through loudspeakers, inducing SAW (Surface Acoustic Waves). The work of Diemer et al. is one of the first to apply vibration to an evaporating solution during film formation. The setup used is a petri dish mounted between two speakers, both in a vertical direction in relation to the petri dish, with a drying semiconductor of a solution of diF-TES-ADT/chlorobenzene on a substrate inside the petri dish. A low frequency of 100 Hz is applied, and device performance increased for several crystalline materials. The improvement is explained by the vibration lowering the global energy potential of the system and reducing trap density at the dielectric/semiconductor interface. The setup used in this work is shown in Figure 3.20a.

Later, works have used the vibration of the substrate while the film is still wet for obtaining a smoother thin film. The works of Wang et al., Zabihi et al., and Chen et al., use a vibrating substrate to improve PEDOT:PSS thin films after spray-coating or spin-coating deposition.[192]–[194] Figure 3.20b displays the application of ultrasonic vibration of the substrate after application of PEDOT:PSS through spray coating at a frequency of 15 kHz.[193] The result of the vibration on the final thin films is a significant decrease in the film thickness and film roughness. The vibration parameters varied are the vibration time and power intensity. For short times or low power intensity, more uniform films are yielded, possibly allowing the material to rearrange and coalesce, although evaporation rates seem to be higher during the vibration of the substrate.[195] If the power is too high or the time during which the vibration is applied is too long, the film appears to break and increase thickness. For the thinner and smoother films, the conductivity of the PEDOT:PSS films was increased for all cases in which the effect of vibration is tested. These trends are observed for vibration applied after different deposition methods, and for solutions with different additives, such as surfactants[192] or blending with another conductive material such as graphene.[194] It has also been shown that ultrasonic vibration (40 kHz) at low power (5 W) can enhance wetting and spreading of a film, while high power vibration (50 W) can provoke de-wetting and film rupture for PEDOT:PSS solvent blends.[196]

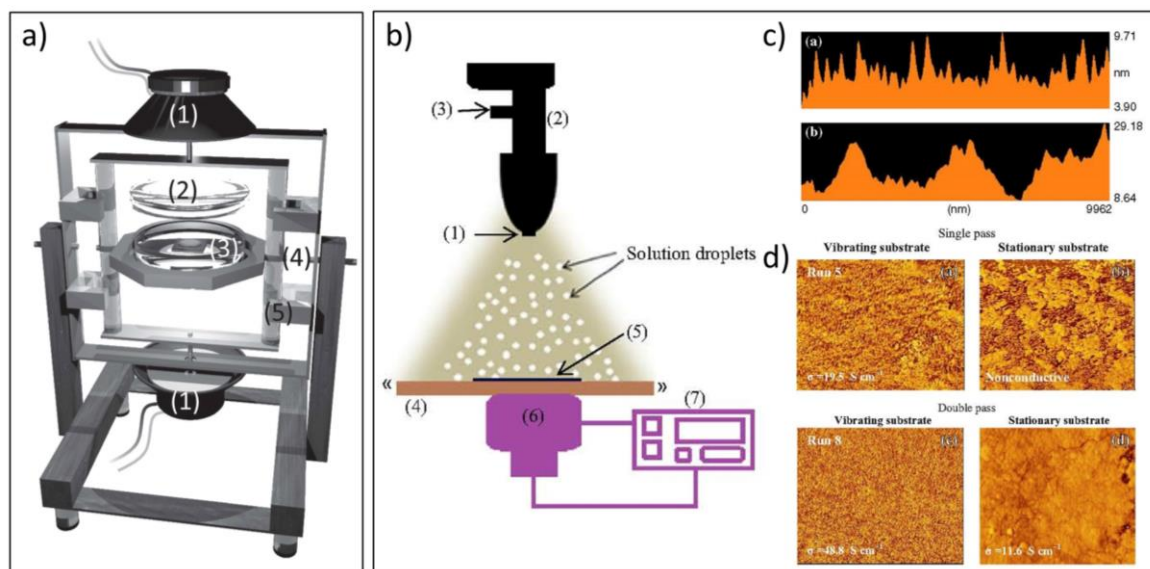


Figure 3.20: (a) The setup with speakers used in the work of Diemer et al. Image is reproduced from Ref. [197]. (b) The setup used in the work of Zabihi et al. for vibration during spray-coating deposition. (c) The profile and (d) AFM images of the films PEDOT:PSS films deposited with and without vibration of the substrate. Images reproduced from Ref. [193].

It has been observed that for semicrystalline polymers such as P3HT, the vibration motion from ultrasonic oscillation can enhance the crystallinity of thin films and decrease chain entanglement, producing beneficial effects in both OFET and solar cell devices. In the work of Kim et al., [198] ultrasonic vibrations are combined with a cosolvent system to induce aggregation of P3HT into well-packed crystalline P3HT nanowires. In the work of Zhao et al., crystallinity and ordering of P3HT in nanofibrils is promoted through ultrasonic oscillation, and for higher molecular weights. The group believes the ultrasonic vibration to decrease the polymer entanglement and permit self-assembly of fibrils through a more thermodynamically stable conformation. [199] Using this approach, Aiyar et al. have used the sonication method for preparing P3HT OFET devices and have observed it has a significant effect on the thin film crystallinity, and therefore on the charge carrier mobility in OFET devices (Figure 3.21a). They have found that the effectiveness of the oscillation on the film morphology depends on the regioregularity of the material and the solvent-polymer interaction. [62], [129] Kondo et al. have attempted to apply vibration to a substrate in a vial in an ultrasound bath during the solvent evaporation of drop-casted devices of P3HT and have observed somewhat of a change in charge carrier mobility. [200]

The works cited above have utilized ultrasonic vibration at the frequency of a standard ultrasonication bath of 40 kHz. The mechanism that controls the polymer conformation in such works is the cavitation collapse - when the bubbles formed by vibration hit the vial in which the solution is deposited. [201] As has been discussed in the previous section, the bubble collapse is expected to release a high quantity of energy, enabling such morphological changes. All these works show how the treatment of the solution before the deposition is beneficial for film formation, and have the benefit of the spacial mobility of the polymer chains in the solution, facilitating order transformations.

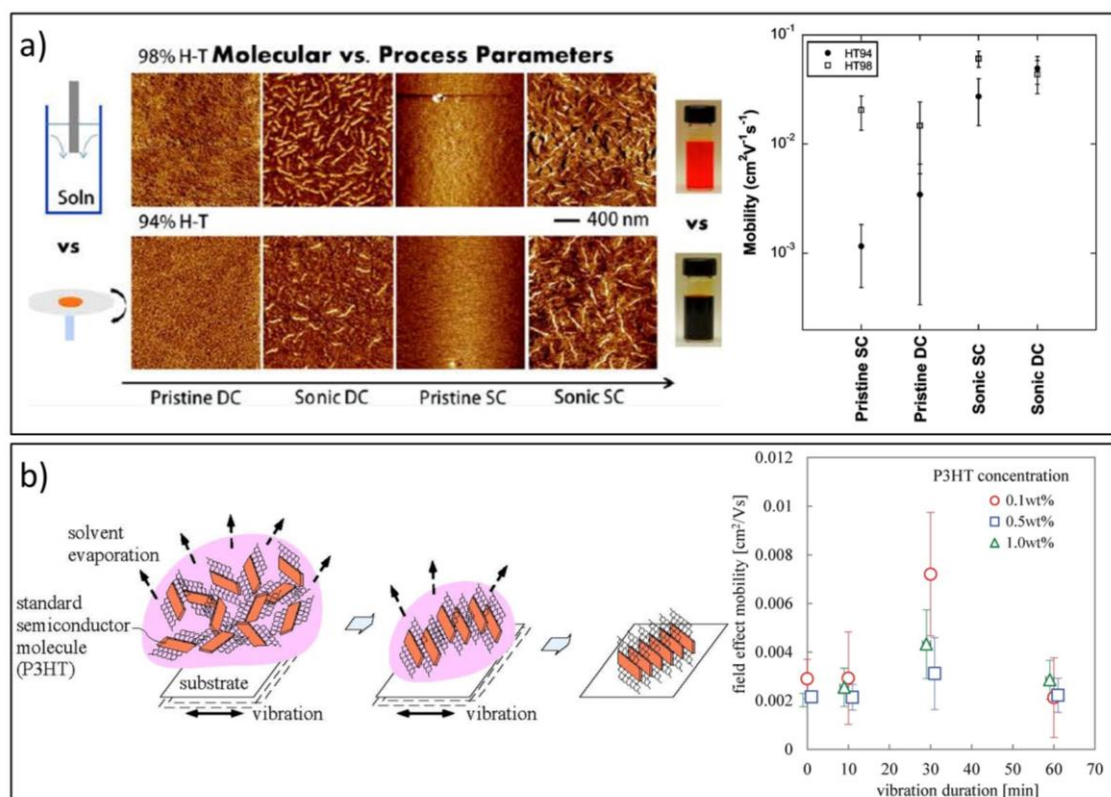


Figure 3.21: (a) At the left, AFM images of films coated through drop-casting (DC), spin-coating (SC), for a P3HT/chloroform solution with (Sonic) and without (Pristine) ultrasonication before the deposition. At the right are the charge carrier mobility values for the corresponding OFETs. Images reproduced from Ref. [129]. (b) Schematic shown in the work of Kondo et al., for the expected self-assembly behavior of P3HT when the solution is vibrated during solvent evaporation, after drop-casting. At the right are the resulting charge carrier mobility values for devices with different solution concentrations fabricated using this method. The images are reproduced from Ref. [200].

Recently, the work of Habibi et al. has implemented ultrasonic vibration to both the solution of P3HT/dichlorobenzene before spin-coating, and the substrate of an OFET after spin-coating of a wet film of P3HT/dichlorobenzene during solvent evaporation. The application time of vibration for both cases is the same, and the results are comparable. Figure 3.22 displays the procedures and the results of this work. Applying the vibration during the deposition of the material reduces the fabrication time substantially.[202]

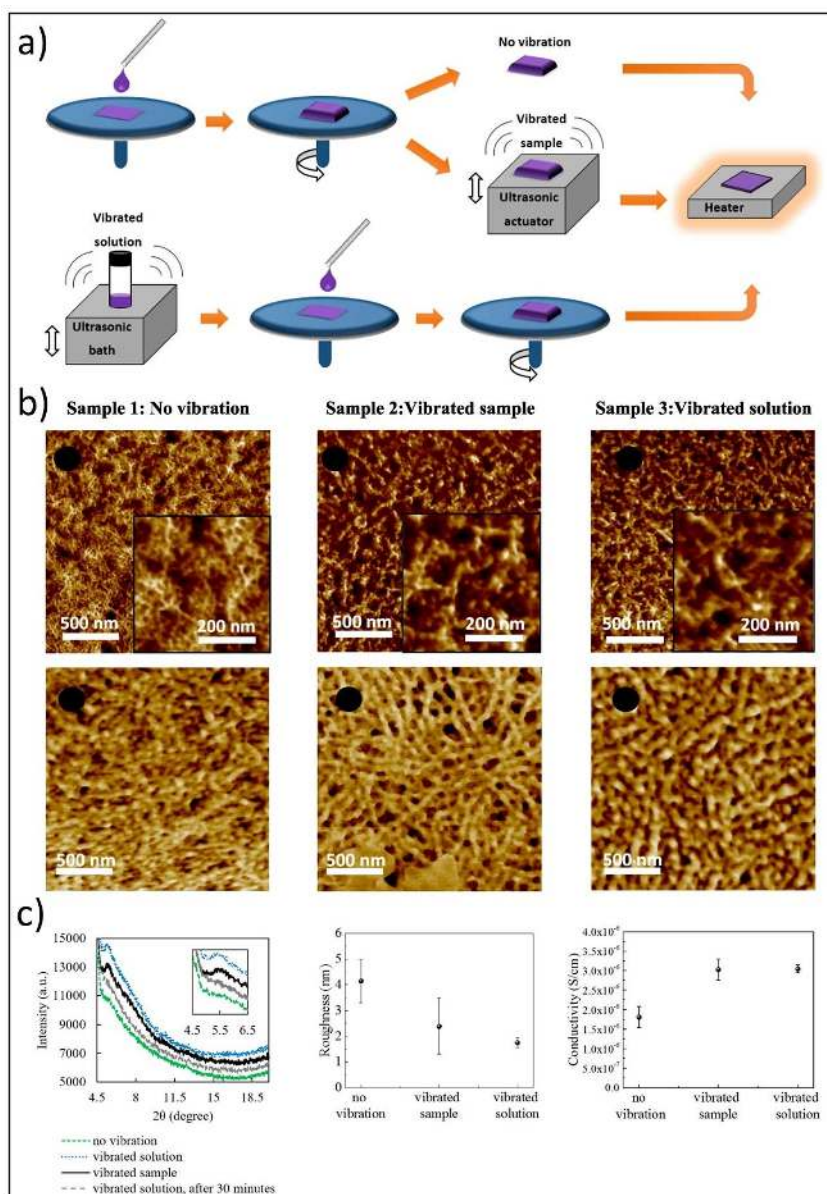


Figure 3.22: (a) Schematic of the experiment for comparing the vibration of the spin-coated film and the vibration of the solution before spin-coating. (b) Resulting AFM surfaces. (c) X-ray diffraction patterns, the roughness of film, and conductivity for the experiment in (a). Images reproduced from Ref. [202]

3.4.4 Combining the Solution Shearing and Vibrations

The acoustic waves are generated by a vibrating body, which, due to mechanical displacement, causes the surrounding medium to be displaced and a wave to be propagated in the longitudinal direction. In the case of the piezoshearing, the transducer is the piezo crystal, which propagates a wave through the liquid and the air above it.

The proposal of the project of the piezoshearing is commenced with the idea of inducing more continuous crystal growth during solution shearing of small-molecule materials. The use of flow in the previous work of Diao et al. has enabled single-crystalline thin films, but at a high cost for fabricating the shearing blade. The vibration of the blade is motivated by the belief that the vibration of the liquid during deposition would induce stirring flows at the evaporation front of the meniscus, enabling the more continuous crystal growth of organic semiconductors in a similar manner.

The rationale for why this should work is the fact that the coated films are so thin that the nanoconfinement effect would enable change at the morphology formed at the liquid surface to extend all the way to the bottom of the thin films, where the charge transport layer of the bottom-gate devices occurs. Previous works in microfluidics have shown vibrations to induce mixing, which would have a stirring effect in a single solution.[203]–[206] One example is the work of Oberti et al. shows that vibrating a microchannel at 100 Hz with two fluids going through a laminar flow is enough to mix the two fluids effectively. They associate the mixing to vortices created due to the vibration.[204] The application of piezoshearing for the solution shearing of small-molecule crystalline materials is studied in Chapter 7 and has presented unexpected effects on the resulting coated film.

Based on the numerous works using ultrasound sonication for polymers such as P3HT, we believe that vibration applied during the solution shearing of semiconducting polymers would be highly favorable to film morphology for the fabrication of OFET devices. This would eliminate the procedure of sonicating the liquid, and at the same time, use a deposition method easily scalable to large-area deposition. Viscous solutions of semicrystalline polymers are used in Chapter 9 to test the effect of vibration on the film morphology. Viscous polymer solutions are chosen to decrease the probability of film breakage or dewetting, so morphology changes could be more easily observed. Most of the works in acoustic vibration of liquids are done in a vertical direction to the medium; which is also the case of our piezoshearing setup. Some have, although done works with horizontal vibration. Although vertical vibration can increase chances of instabilities in the liquid, the vibration at low amplitudes can have a stirring effect.[207]

During the experiments performed in this work, piezoshearing was also found to be very useful in improving the wetting conditions of donor-acceptor copolymers (Chapter 7). The stick-and-slip instability is typical during the coating of polymer solutions on a partially-wetting substrate, and it is demonstrated here that the instability can be mitigated with the piezoshearing setup. This is attributed to the depinning of the contact line. Such a contact line is a boundary to the liquid and the effects such as surface waves and other instabilities will depend on whether the contact line is pinned or not.

For the case of our piezoshearing setup, it is treated as a small liquid body, confined from the bottom by the substrate and from the top by the air-liquid surface of the meniscus. Therefore possible effects observed are expected to be limited to microstreaming, surface waves, and acoustophoresis.[207] Because it includes a liquid body under the blade and not only a few nanometers of the film, we believe additional effects, such as large-scale streaming can occur in the meniscus.

For the works that study the effect of vibration on a liquid, a quantifier of the energy introduced into the system is the acceleration of the vibration. To describe the “turning on” of a particular effect on the liquid, a threshold acceleration can be calculated. The acceleration for a sine wave vibration is a function of the frequency and displacement, as described by Equation (3.5). [175], [179], [189], [208], [209] In chapters 7 and 8 this parameter is used for comparison of the amount of energy used for a specific shearing condition. It is a way of including both the frequency and displacement amplitude in one parameter.

$$\alpha = 2 \cdot \pi^2 \cdot f^2 \cdot Dpp \quad (3.5)$$

Chapter 4

4 Experimental Methods

4.1 Device Fabrication

Unless specified otherwise, the architecture utilized in this work is the bottom-gate, top-contact architecture (Figure 4.1e). A highly doped silicon (Si) wafer is used as the gate, and a 300 nm-thick, thermally grown layer of SiO₂ is used as the dielectric. This architecture is commonly used to test the quality of the semiconducting layer.

Figure 4.1 depicts a simplified workflow of the fabrication process of the organic field-effect devices used in the majority of this work.

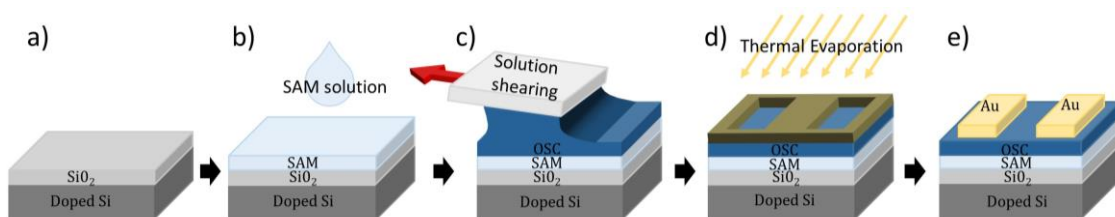


Figure 4.1: Fabrication process of OFET devices for this work: (a) a Si/SiO₂ wafer is used as the substrate, (b) the surface is cleaned and treated with SAMs, (c) the organic semiconductor is deposited through solution shearing – or piezoshearing, (d) the electrodes are deposited through thermal evaporation, and (e) the final device has a bottom-gate top-contact architecture.

4.1.1 Substrate Preparation

Before utilizing the Si/SiO₂ wafers, they are thoroughly cleaned. They are sonicated for 10 minutes in acetone, and 10 minutes in isopropanol and blow-dried a nitrogen flow.

To control the wettability and coverage of the substrate during the coating process of the active layer, different surface treatments are utilized, mainly with self-assembled monolayers (SAMs). The most commonly used surface treatments used throughout this work are the phenyltrichlorosilane (PTCS) and octadecyltrimethoxysilane – or

octadecyltrichlorosilane(ODTS). The last both materials are expected to have the same product as a monolayer, but the processing procedure is different.

Such monolayer formation procedures are widely used by works that fabricate OFETs and use meniscus-guided-coating apparatuses. The **PTCS** treatment is used for the deposition of small molecules in Chapters 5 and 6. For proper film formation of crystalline materials on the surface, a surface with high energy is required. The PTCS allows the coating of films down to nanometers, in comparison to no film deposition without the monolayer. The procedure is described in previously published works.[91], [92]

In our experiments, the PTCS treatment is performed immediately after the cleaning procedure. For proper PTCS-treated surfaces, high-quality cleaning is required, and non-uniformities on the surface of the substrate will result in defects in the monolayer and difficulties depositing the semiconductor. Therefore, the wafer cutting is done even before the cleaning process to ensure there are silicon particles on the surface. The 3wt% solution of PTCS in toluene is prepared inside the glovebox to avoid reaction of the chlorine molecules among each other before the substrates are deposited in the solution. The substrates are treated for oxygen plasma for 2 minutes (gas flow at 1.0 on scale and 98% power) and then immediately immersed in the PTCS solution. The solution is tightly covered with aluminum foil and left overnight on a hot plate at 140 °C. The temperature of the hot plate is calibrated, so the temperature of the solution (100 ml) would be 90 °C. It should be immersed in the solution for around 15 hours. It is essential to seal the container properly, otherwise solvent might evaporate and the samples damaged. It is also crucial that the surfaces of the substrate remain free and not touching, otherwise multiple layers of PTCS will be deposited, and the solution deposition hindered.

After the immersion in the PTCS solution, the substrates are sonicated for 2 minutes in toluene and gently swabbed to remove any additional layers. A successful PTCS treatment will yield a contact angle of 72-75° for a droplet of water. If the PTCS treatment is not successful, it is improbable that any crystalline material, such as small molecules, will be deposited through solution shearing.

The deposition of the **ODTS** monolayer on the substrate decreases the free energy of the surface, lowering wettability and film deposition. This is used for the solution shearing blade, and substrates of OFETs coated with polymeric materials, investigated in Chapters 7 and 8. The reason for using this surface treatment is discussed in Chapter 7.

The procedure for the ODTS surface treatment used in this thesis is the one described in the work of Ito et al.[156] The entire Si/SiO₂ wafer is rinsed with acetone and isopropanol and exposed to UV-ozone light for 10 minutes. The wafer is then rinsed with deionized water (DI water) and dried with a nitrogen gun. A solution of 13 μl of octadecyltrimethoxysilane in 10 ml of trichloroethylene (1 mM) is spin-coated on the wafer for 30 seconds, at 3000 min⁻¹. For the cross-linking of the monolayers to the substrate, the wafer is stored overnight in a desiccator with a small quantity of ammonium hydroxide (30%). After the wafer is removed from the desiccator, it is sonicated in toluene for 30 minutes and swabbed to remove any additional deposited layers. To ensure the treatment is successful, the contact angle of water on the surface is measured. A successful treatment yields a very hydrophobic surface, with a contact angle of 106°- 108° for a drop of water.

For contact angle measurements, a custom-built stand with a diffused-light background was used. A drop of 3-5 μl of deionized water is gently deposited on the surface, and a picture is taken. Utilizing the macro “Contact Angle” from the open-source software ImageJ, the contact angle of the droplet on the substrate was acquired. For this measurement, it is crucial that deionized water is used; plain water will have contaminants and yield different behavior. The drop should not exceed 5 μl; otherwise, gravity might exert influence on the measurement.

4.1.2 Electrode Evaporation

Unless otherwise stated, the contacts utilized in this work are gold (Au), thermally evaporated at a rate of 1.5 \AA s^{-1} to a final thickness of approximately 50 nm. Shadow masks with a variety of channel dimensions are used and are specified in each chapter. The evaporation is done under high vacuum 10^{-7} mbar in a custom-built chamber (Organicube, from Dreebit GmbH).

Before electrical measurements, the SiO_2 layer is scratched until the Si substrate is reached for contacting the gate. The semiconductor around the source-drain is gently removed to ensure no current leakage through the edges of the substrate.

4.2 Piezoshearing Setup

A piezo crystal actuator was used for the vibration of the blade. The piezo crystal is a stack of PZT material between two conducting plates. When a voltage is applied to the terminals, it expands proportionally to the voltage applied and has a response of microseconds. Therefore, the amplitude and frequency of the vibration can be controlled through an alternating signal generator.

The piezo actuator is embedded in the solution-shearing setup, as illustrated in Figure 4.2a. A hydrophobic blade (size $1.6 \times 1.6 \text{ cm}$) treated with ODTs is used for the piezoshearing assembly. The piezo crystal (model PA4GE, Thorlabs) is attached to an aluminum holder through a temperature-cured epoxy (323LP-T from EPO-TEK). Both the surface of the aluminum holder and the back of the blade are sandpapered to increase abrasiveness of the surface and facilitate adhesion. The aluminum holder is put on a hot plate at $130 \text{ }^\circ\text{C}$ and the epoxy snap-cured with temperature for both the holder-crystal and the crystal-blade bond, followed by a curing step for one hour at $130 \text{ }^\circ\text{C}$ for each bond. After curing, the capacitance of the piezo crystal is re-measured to ensure that there is no damage from the heating. The aluminum holder is screwed to the moving linear stage of the shear-coater. The same piezo crystal is used for all the samples described in a single chapter to avoid possible displacement variations between crystals.

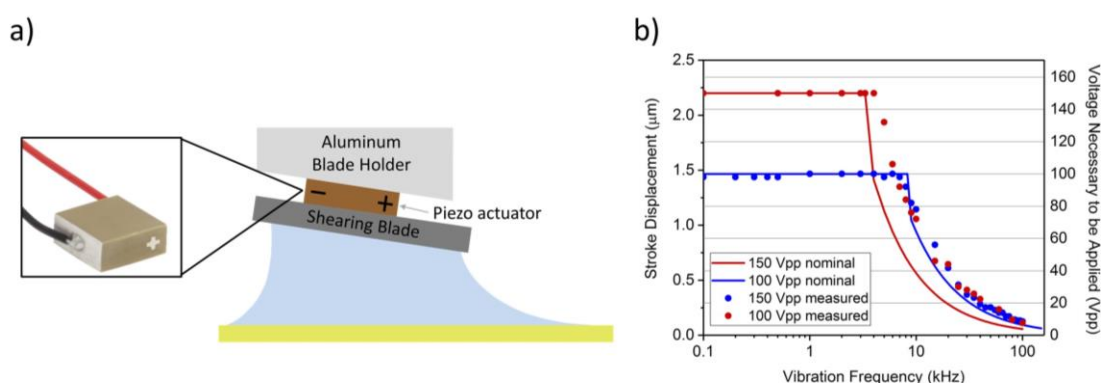


Figure 4.2: Figure 4.2: (a) Schematic of how the piezo crystal is embedded in the solution shearing system, and a figure of the PA4GE model, used throughout this work; (b) maximum displacement applicable to the piezo actuator, depending on the frequency applied. These include both the nominal value, which is calculated from the nominal I_{ave} and nominal capacitance of the piezo actuator, and the maximum voltage reached experimentally with our setup.

Several designs for the configuration of the piezoshearing blade were tested, aiming for a configuration that could be easily mounted and dismantled from the printer. This is desirable for cleaning purposes. Some of our design included fixing the whole holding

apparatus of the head by vacuum. However, due to the high roughness of the surface of the piezo crystal and limited surfaces to which the piezo actuator could be attached firmly, the design with the fixed blade is preferred.

The piezo crystal behaves like a capacitor, and therefore acts a low-pass filter. For the long-term dynamic operation, the average current supplied to the actuator is a crucial factor and limits the displacement that can be achieved at each vibrating frequency. From the average current that our amplifier can provide, the maximum displacement achievable can be calculated:

$$I_{ave} = f \times C \times V_{pp} \quad (4.1)$$

Therefore, the vibrating frequency is limited by the maximum current we can supply, and is given by:

$$F_{max} = \frac{I_{ave}}{(C \times V_{pp})} \quad (4.2)$$

For frequencies higher than these, lower voltages can be applied, with a maximum voltage value determined by:

$$V_{pp_{max}} = \frac{f}{(I_{ave} \times C)} \quad (4.3)$$

Therefore, the higher the frequency, the smaller the displacement, and piezo actuators with the smallest possible capacitance are preferred. To maximize the frequency range, a piezo crystal with the smallest possible capacitance possible, that would have an appropriate size to be stably attached to the blade was selected. A square piezo chip (PA4GE), with side dimensions of 7 mm and 2 mm thickness, which has a nominal capacitance of 390 nF was used. The resulting voltage/frequency range that can be applied to the piezo actuator is displayed in Figure 4.2b. The two curves display the two maximum output configuration options from the voltage amplifier utilized.

To amplify the voltage signal used as the input for the piezo actuator, the amplifier MX200 from PiezoDrive was utilized. It has a gain of 20 V V⁻¹, and the maximum voltage V_{pp} it can supply can be either 100 V or 150 V, depending on the configuration selected. In Figure 4.2, the maximum displacement for these two configurations is displayed. Both voltage setups are used, according to the requirements of the experiments. Figure 4.3a displays the amplifier MX200 and its respective pinning schematic (Figure 4.3b). The table in Figure 4.3c shows the possible configurations that can be selected for the maximum output supplied by the amplifier. The maximum voltage our piezo actuator tolerates is 150 V; therefore, the 200 V configuration is not utilized. The configuration is changed manually on the amplifier with jumpers that connect LK1 and LK2 (Figure 4.3c).

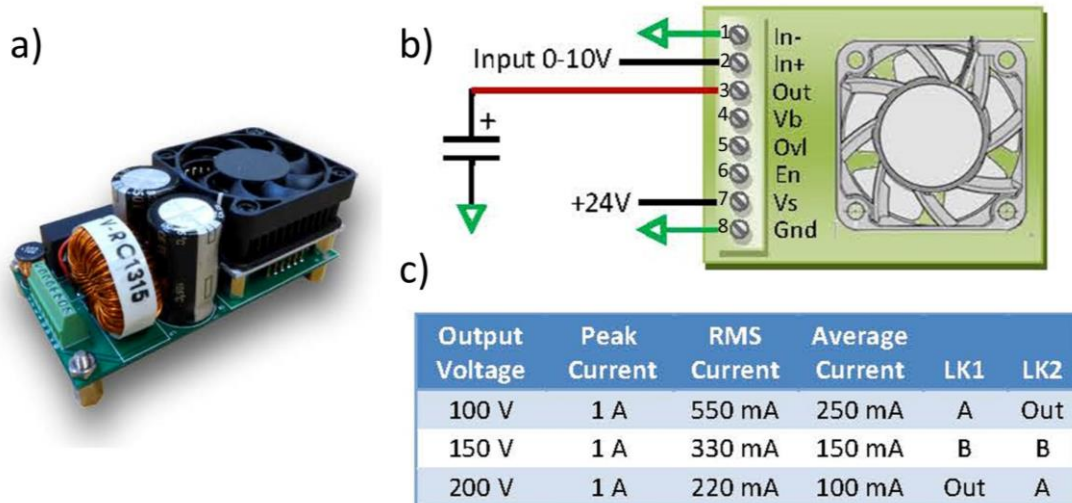


Figure 4.3: (a) The amplifier MX200, from PiezoDrive; (b) schematic of the circuit configuration used for our setup; (c) output voltage configuration options for the MX200 amplifier and its respective current values. The output voltage configurations of 100 V and 150 V are used to calculate the maximum displacement of the crystal displayed in Figure 4.2b.

Figure 4.4 displays the complete circuit schematic of the piezoshearing setup. The function generator used is from Kuman, 60 kHz, and an oscilloscope is attached to the input of the piezo crystal to ensure the correct signal is being applied. To test whether the frequency of displacement of the actuator is equivalent to the frequency of the applied waveform, a phone application to detect sound frequencies is utilized. A frequency up to 15 kHz was tested, and the frequency detected by the application was equivalent to the frequency applied to the piezo crystal.

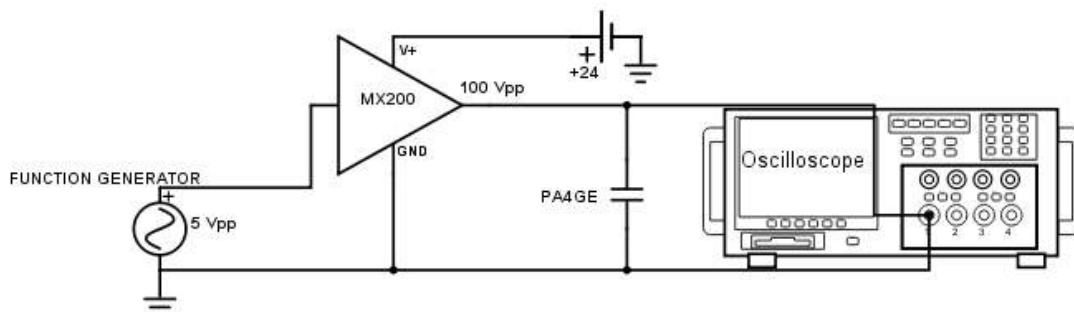


Figure 4.4: Circuit Schematic for the Piezoshearing setup.

Throughout this work, the displacement of the crystal will be referred to by the peak-to-peak voltage applied, V_{pp} . Once the piezo crystal is embedded is attached to the blade and holder, the system is quite stable. The blade was then used for hundreds of samples, and results are repeatable. The biggest issue is if the silicon blade is broken, the piezo crystal cannot be re-used, and another blade needs to be fabricated. Although results from one blade are reproducible, it appears that results yielded from different blades to vary. We believe the bonding process to be one of the main influencing factors. If there is any epoxy running on to the side of the crystal, it can constraint the maximum displacement.

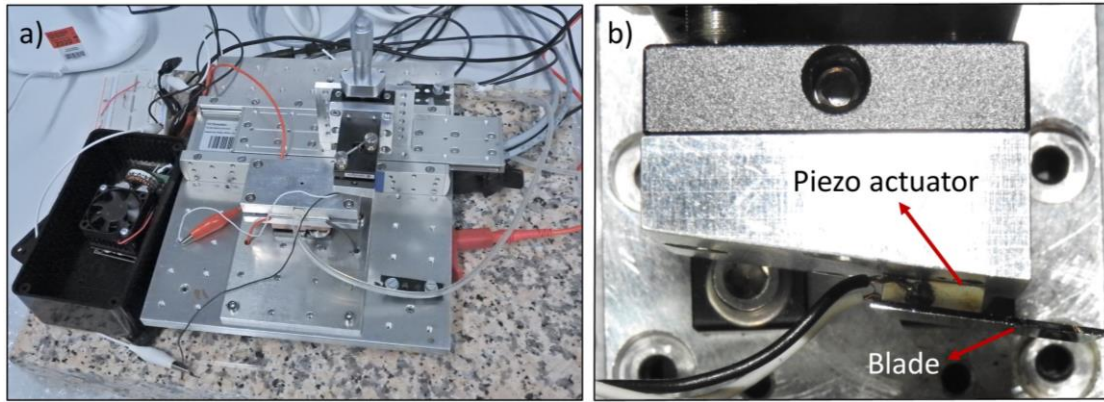


Figure 4.5: (a) Final experimental setup for the piezoshearing. (b) Piezoshearing blade.

4.3 Thin-film Characterization

4.3.1 Cross-Polarized Optical Microscopy

It is common to use cross-polarized optical microscopy (CPOM) for characterization of anisotropic materials. Non-cubic crystallite structures and polymers with significant chain alignment can be optically significantly anisotropic, and linear polarized optical microscopy is a straightforward and useful technique in evaluating this qualitatively. Due to the birefringence of such materials, a significant contrast can be observed when changing the in-plane position of a thin film.

Optical birefringence is an indication of the presence of anisotropy in the structural formation of the material. Birefringence is given by the difference between refractive indexes when light is incident on the material from in different directions. The birefringence is given by:

$$\Delta n = |n_1 - n_2| \quad (4.4)$$

where n_1 and n_2 are the refractive indexes for the different positions of the material being analyzed, and are orthogonal to each other. Non-crystalline materials, most liquids and gases, and cubic structures have only one refractive index.[210]

The light waves can be decomposed into an electrical (E) and a magnetic component (B), both sinusoidal and oscillating in space and time. They are perpendicular to each other and have the same amplitude and phase (Figure 4.6a). For convenience, only the electric field vector (E vector) is usually depicted in schematics. Such rays can be filtered using a polarizer, a filter with a linear transmission axis. Figure 4.6b shows a schematic illustration of linear polarizers. One of the filters is termed “polarizer”, and the other “analyzer”. When overlapped, the angle between the transmission axis of the filters determines the amount of light transmitted. Figure 4.6b depicts the resulting light transmitted by changing the angle between the polarizer and the analyzer. When increasing the angle between the transmission axis of the polarizer and analyzer, the total light transmitted decreases, until they are perpendicular – then they are said to be cross-polarized, and light transmission is minimum.[211]

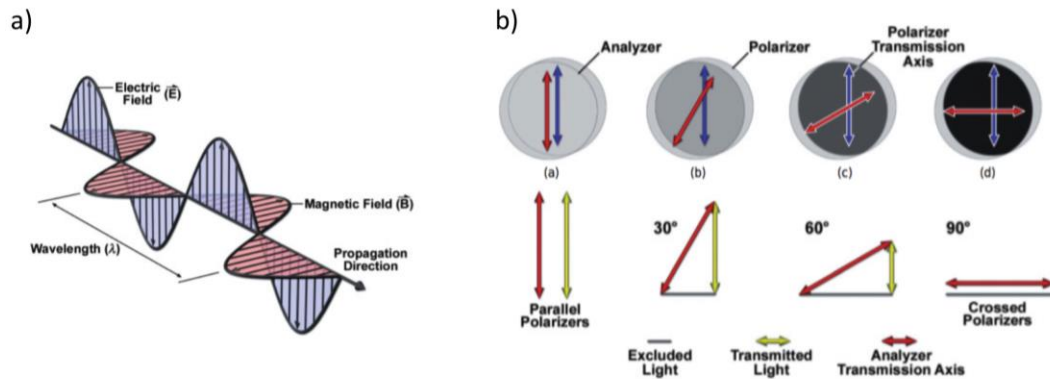


Figure 4.6: (a) Representation of light as an electromagnetic wave. The electrical (E) and magnetic (B) components are orthogonal to each other, with the same amplitude and phase, and oscillate in time and space. For simplicity, only the electrical component is shown for schematics of light rays. (b) Schematic of light transmission when crossed polarizers are overlapped with different angles between the respective transmission axis. The larger the angle between the axis', the least light is transmitted. Both images reproduced from Ref. [211].

A birefringent material is a material capable of splitting incident light into two different components: the ordinary (O ray) and extraordinary (E ray), which can follow different paths. The ray splitting occurs due to the organized molecular structure of the material, and to the direction of the incident rays in relation to the optic axis of the material being analyzed. By definition, the optic axis is the only direction in a crystal where a ray of light does not suffer double refraction.[211]

Figure 4.7 is a schematic illustrating the light incidence with different angles in relation to the optic axis of a crystal. When the incident ray is parallel (Figure 4.7c) to the optic axis of the material, there is no splitting of light. When it is perpendicular to the optic axis (Figure 4.7b), the beam is split into O and E rays, but they follow the same path in the crystal. When the incident ray is neither parallel nor perpendicular to the optic axis, there is ray splitting into O ray, E ray, and the path of these diverge (Figure 4.7a). The path length between these rays varies depending on the incident angle and is observed to have different intensities. The highest transmitted intensity occurs when the path length between O and E ray is maximized, which is always when the optic axis is 45° from the polarizer. This always occurs at 45° because O and E are always normal to each other. The position of the optic axis in relation to the position of the crystalline material will depend on the lattice structure of the material.

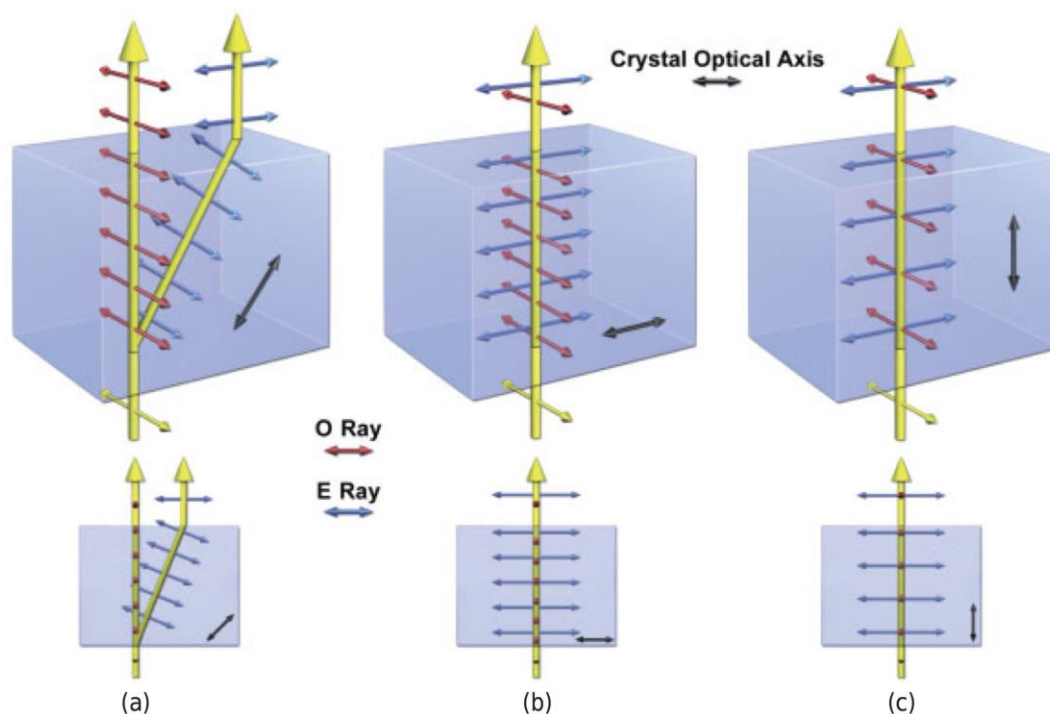


Figure 4.7: Illustration of ray splitting on a crystal structure, with different incident angles in relation to the optic axis of the crystal. The optic axis of the crystal is the black double arrows; the O Rays are the pink arrows, and the E rays are the blue arrows. The incident ray is (a) oblique, (b) perpendicular, and (c) parallel to the optic axis. This image is reproduced from Ref. [211].

Through cross-polarized microscopy, it can be determined for crystalline materials whether there are crystalline films on a substrate, an estimation of where the optical axis of the materials is, and an approximate relation to its lattice. Moreover, it enables the observations of whether the crystallites on a sample have different orientations. Therefore, a qualitative evaluation can be made, on whether there are many or few grain boundaries.

Polarized microscopy is commonly used for crystalline OFETs fabricated from small molecules.[91], [92], [212], [213] Although polarized microscopy has been used for quite a long time in the field of polymers in general,[116], [210], [214]–[216] only in the last years have groups in the field of organic electronics started using it as a thin-film characterization method for polymeric semiconductor alignment for devices. [53], [54], [128], [217], [218] This is now possible due to the novel polymer materials capable of chain alignment and crystallization.

For polymeric films, if there are a high number of chains aligned, the refractive index will be different parallel and perpendicular to the backbone.[210], [211] If the polymers are randomly oriented, the material should have only one refractive index and no significant birefringence. The intensity of the birefringence will depend on the thickness of the film, the degree of organization of the polymer chains – both in-plane and out-of-plane, and whether there is more than one phase of the material.[116] The higher the number of aligned chains, the higher the intensity of the birefringence, and therefore, it is possible to estimate the direction of the backbone.[210] Older works on polymer crystallization have shown that different birefringence can be due to a different out-of-plane structural organization.[214] For the case of polymer thin films, it means that different degrees of crystallization can also appear as a change in the birefringence.[116]

This method is utilized for the characterization of all the polymeric materials studied in this work. In Chapter 7, polarized microscopy is used in the thin-film characterization. However, due to the ultralow thickness of the films, not much

birefringence is detected. In Chapter 8 a quantitative analysis of the birefringence intensity is done, and it is used as a guide to evaluating how the piezoshearing affects the polymer films, and which piezoshearing parameters result in more significant differences.

Figure 4.8 shows a schematic of the polarizer and analyzer in relation to the crystalline samples. After passing through the analyzer, the sample presents birefringence: two different colors are observed- black and gray- when the incident angle of the light ray goes from 0° to 45° .

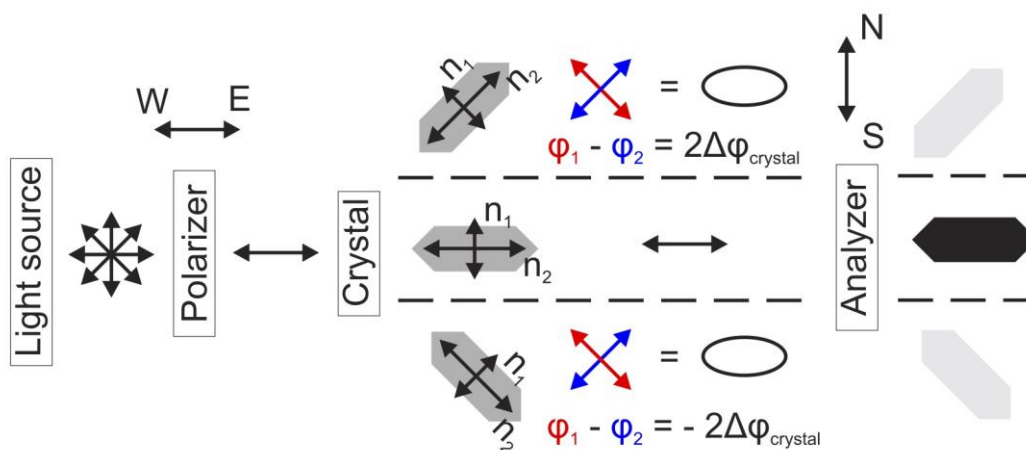


Figure 4.8: Schematic of cross-polarized microscopy and a crystal sample. From the different optical colors observed after passing through the analyzer, it can be concluded there is birefringence. This figure is reproduced from Ref. [219].

4.3.2 Grazing Incidence Wide-Angle X-ray Scattering

In addition to large domains with minimized grain boundaries at a device scale, the film structure at the molecular level is also crucial for achieving devices with good charge carrier mobility. The intermolecular charge transfer depends highly on the molecular structure and packing of the thin film and is a determining factor in the charge delocalization, therefore, resulting performance of the semiconductor. Structure distances, packing angles, and anisotropy of organized formation in a film are features wished to know in order to optimize and characterize organic films.[40], [220], [221]

X-ray scattering is currently widely used in the field of organic electronics for characterizing the morphology of thin films. The scale of characterization goes from sub-nanometer to the micrometer range. Depending on the X-ray setup, different scales and degrees of details of morphology characteristics can be extracted. In smaller scales (0.1 - 1 nm), molecular packing can be determined, while at larger scales (micrometers), grain boundaries and phase separation can be characterized. Figure 4.9 illustrates the full range of scales of domains that can be characterized for semiconductor films. It shows an example of a dual-material system, as used for organic photovoltaics, and for a one-material system, such as OFETs.[40]

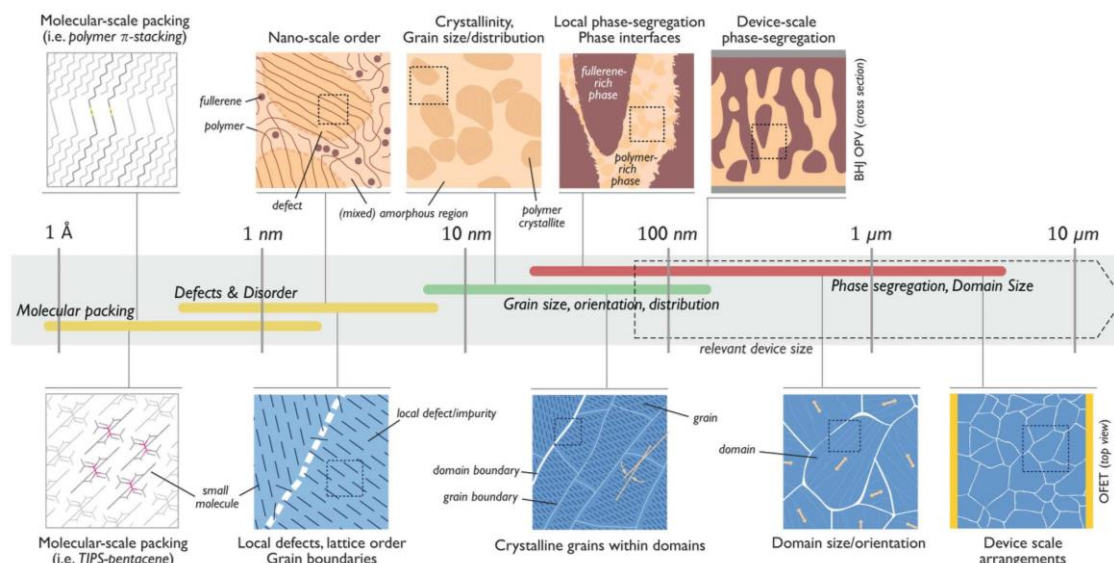


Figure 4.9: Schematic illustration of the different lengths scales of X-ray characterization and the particular traits that can be detected in the thin-film morphology analysis. The top row shows a system for a blended material, such as used in photovoltaic systems, and the bottom row shows a one material system, such as used in OFETs. Image reproduced from Ref. [40].

In the course of this study, X-ray measurements are used to characterize mainly molecular organization structures and packing, and how charge transfer can be improved with changing molecular morphology. Because organic thin films do not scatter so strongly, lab-scale X-ray beams are usually not sufficient for characterization; therefore, synchrotron methods are utilized. The high beam intensity from a synchrotron enables the detection of these very weak scattering samples. The structures analyzed are in the 0.1-1 nm range and are usually measured utilizing grazing incidence wide-angle x-ray scattering (GIWAXS). This is the most commonly used X-ray characterization method used for organic semiconductors - Figure 4.10 displays such a setup.

Through GIWAXS, characteristics of both in-plane and out-of-plane molecular packing can be obtained; that is, along the plane of the substrate and in the normal direction to the substrate, respectively. However, the in-plane data collected is more reliable for setup reasons and more interesting for the analysis of thin films. In our experiments, a 2D-detector is used for collecting the data. A shallow incident grazing angle (α in Figure 4.10) in relation to the plane is used, to characterize the thin film and not the dielectric substrate. For this, the incident grazing angle used is above the critical angle of the thin film, but below the critical angle of the dielectric. For our experiments, if not stated otherwise, the incident angle used is of 0.13° .

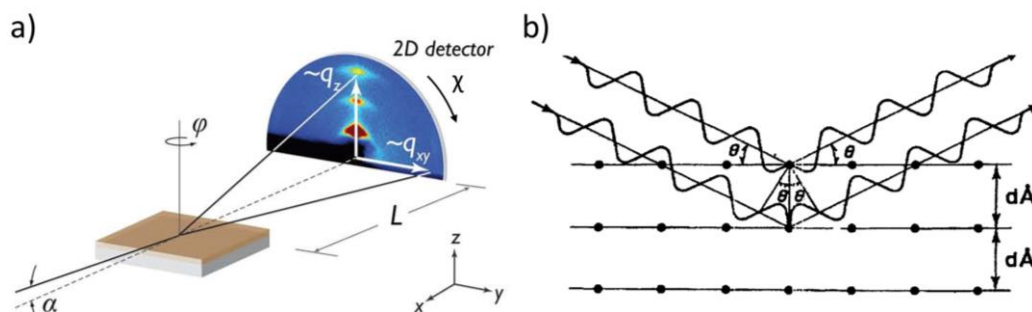


Figure 4.10: (a) 2D-detector GIWAXS setup, as utilized for the characterization of our films. Image reproduced from Ref. [40]. (b) Incident beam on atomic planes when Bragg's law is fulfilled, and diffraction occurs. Image reproduced from Ref. [222].

Although quantitative data is crucial for a thorough understanding of a direct relation between charge transport quality and morphology, GIWAXS data is most customarily used as a qualitative method for comparing films. Features such as lattice spacing, a relative comparison of the degree of ordering of films, and anisotropy of favorable morphology for effective charge carrier transport are analyzed in this work.

The intensity of the peaks detected depends on the thickness, length of the film, time of exposure to the beam, and beam intensity. It will be proportional to the volume of structures reached by the beam. Therefore, a more ordered film would have peaks with a higher intensity and a narrower full-width half maximum (FWHM).

The incident angle at which diffraction occurs is determined by the spacing between the planes of the film, and the direction of the diffracted film is determined by the orientation of the planes. For diffraction to occur, constructive interference is required, and therefore, the Bragg condition must be fulfilled:

$$n\lambda = 2d \sin\theta \quad (4.5)$$

And the magnitude of the scattering vector is:

$$q = \left(\frac{4\pi}{\lambda}\right) \sin\theta \quad (4.6)$$

Therefore, the distance between planes can be calculated as:

$$d_{hkl} = \frac{2\pi}{q} \quad (4.7)$$

where h, k, l are miller indexes and refer to the planes of a lattice. Therefore, plane distance values d_{hkl} can be calculated with the known incidence wavelength λ and the scattering vector q measured through GIWAXS.

For small molecules, such as TIPS-pentacene, which is polycrystalline and is used in this work, the scattering patterns show the distance between molecular planes, and consequently the packing it arranges once forming a film. Therefore, GIWAXS is also a method used to determine the packing structure for crystalline materials. For characterization of unknown packing structures, ideally, a single crystal sample is necessary, or energy minimizing algorithms are used on polycrystalline thin films. For the case of TIPS-pentacene, its structure has been characterized for the first time for thin films already in 2011[43] and has been thoroughly studied,[91], [92], [95] enabling us to compare our measurements with existing polymorphs of this material.

Comparison of whether films are more or less ordered for crystalline materials can also be made, ideally for a wide angle of φ (Figure 4.10a) for reliable sampling. Very aligned films tend to have very narrow peaks (low FWHM) and high intensity, and disorganized films tend to have broad peaks (high FWHM) and lower intensity due to the crystal structures oriented in a wide range of directions.[40]

For organic polymers, due to the flexibility of the backbone and the alkyl branches, characterization of polymer semiconductors is more limited in comparison to small-molecule materials. In the case of semicrystalline polymers, thin films usually consist of mixed regions of amorphous and crystalline domains to different degrees, and only the organized (aligned and/or crystalline) domains can generate strong enough peaks during a GIWAXS scan.

The peaks observed from the diffraction of semicrystalline polymer thin films are those of the π - π stacking (010), which provides the distance between the backbones of the polymer; and the alkyl stacking (001), which corresponds to the width of the polymer.[40] The π - π peaks are usually localized at $q = 1.4 - 1.8 \text{ \AA}^{-1}$, and alkyl peaks at lower values. These peaks provide a general idea of whether the backbone of the polymer is “face-on” or “edge-on”. Films with predominant edge-on characteristics have a π - π peak at q_{xy} axis, while face-on packing tends to have stronger peaks closer to the q_z axis.[220], [221] In Figure 4.11, examples of thin films with stacking preference in the (a) edge-on position and in the (b) face-on position are shown. Although it is possible to observe a preferential stacking position of the backbone in a film, peak intensities closer to q_{xy} and closer to q_z cannot be directly compared. Due to the specular geometry of the setup, the area of the detector closer to q_z is highly distorted.[40]

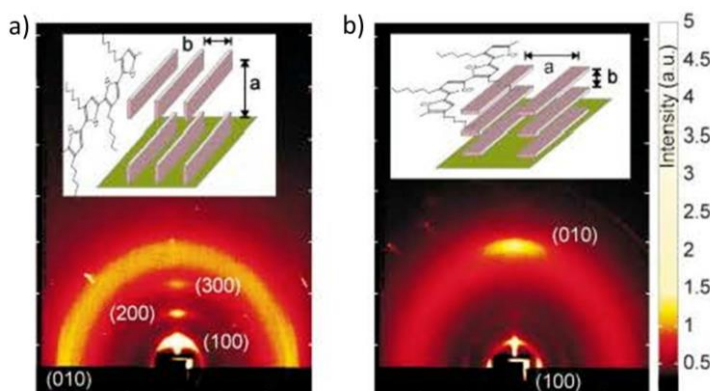


Figure 4.11: Different out-of-plane stacking preferences for the polymer P3HT and the respective diffraction imprints. For the edge-on (a) stacking preference, a strong (010) peak is observed at q_{xy} , and a strong (100) peak is observed close to the q_z axis. For the face-on stacking preference, a strong (010) peak is present close to q_z , and a strong (001) peak is close to the q_{xy} . Image reproduced from Ref. [221].

Out-of-plane polymer orientation:

GIWAXS also allows us to obtain a notion of the general degree of organization of the film. If films are highly disorganized, the peaks can extend to a wide range of the polar angle χ , as displayed in Figure 4.12a. In the case of somewhat organized films, such as the ones of Figure 4.12b and c, χ is limited to a smaller range, depending on the degree of alignment and preferential packing position. The breadth of these peaks allows a qualitative comparison between different processing conditions and how these affect the resulting film morphology.

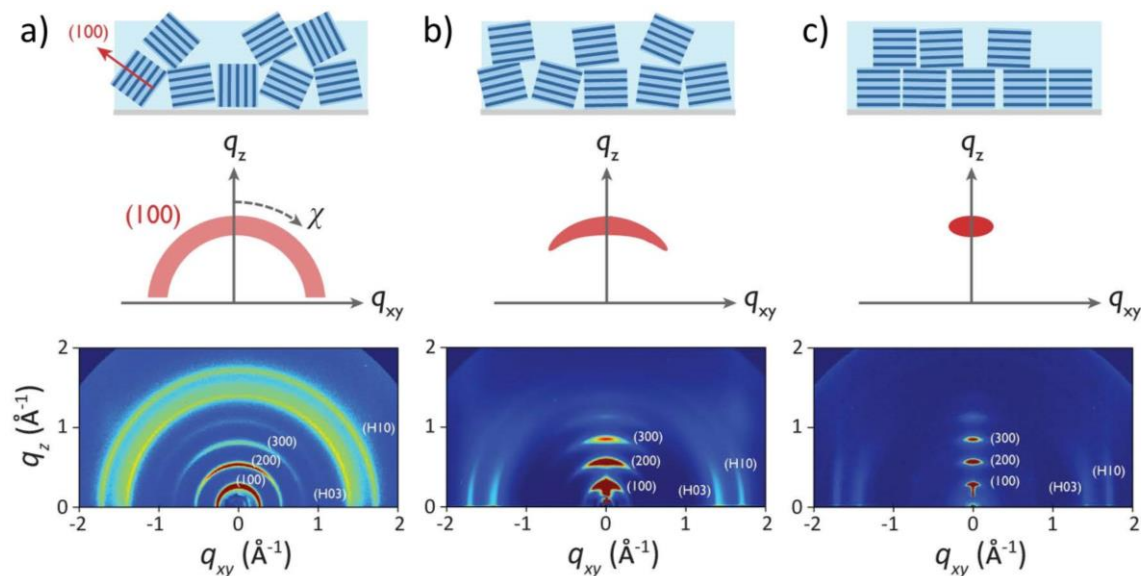


Figure 4.12: (a) Films with randomly oriented crystallites tend to have a diffraction pattern of rings. When the out-of-plane alignment of crystallite populations is increased, rings are limited to arches, as displayed in (b) and (c). The images displayed in the bottom row are for the polymer PBTTT and are the resulting diffraction patterns from processing through a solid-state press (a), spin coating (b) and annealing after spin coating (c). The image is reproduced from Ref. [40].

In-plane polymer orientation:

If films have an edge-on stacking preference, in-plane texture for films can also be analyzed. Anisotropy of alignment in the thin film plane is of significant importance in achieving high-performance devices. If the films are anisotropic with the favorable charge transport direction parallel to the channel of the transistor, higher are the chances that there is a percolation path between the device's electrodes.

To observe the in-plane texture of films, the substrate can be rotated in an angle ϕ , around the normal axis (Figure 4.13a).[40], [223] The angle ϕ at which diffraction intensity is higher is the direction in which the film tends to align. If films are isotropic, such as in the example of Figure 4.13a, the peak intensity detected for every angle of ϕ will be similar. If the films are anisotropic, such as in Figure 4.13b, a significant peak intensity increase at localized angles of ϕ is observed.

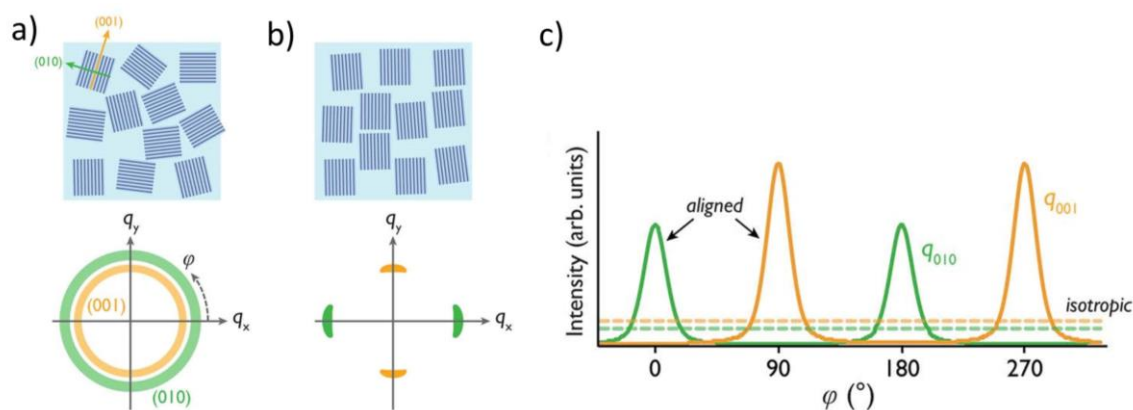


Figure 4.13: Illustration of the top view of films and their respective diffraction patterns for varying ϕ for (a) isotropic films and (b) anisotropic films. (c) Resulting peaks for (001) and (010) peaks in an aligned film.

In Chapter 8, in-plane polymer alignment is characterized. Considering that a full rotation around φ is very time-consuming and there are a limited number of synchrotron setups that have such a feature, only angles $\varphi = 0^\circ$ and $\varphi = 90^\circ$ are characterized. This means directions parallel to the shearing direction and perpendicular to the shearing direction, respectively. Only these angles are characterized because it is known beforehand from CPOM that the polymer aligns either parallel or perpendicular to the shearing direction.

A different incident angle can be used for evaluating different depths of the film. For our study with viscous polymer solutions in Chapter 8, thick films are obtained, and it has been shown in previous works that there can be an alignment gradient along the height of the film. Usually, an incident angle of around 0.13° is utilized, which is above the critical angle of the thin film, therefore allowing to capture characteristics from the bulk of the thin film. In Chapter 8, an additional incident angle, smaller than the critical angle, is used for capturing near-surface film features. When utilizing incident angles below the critical angle, the penetration in the film is minimal, due to an “evanescent wave” traveling almost parallel to the surface of the thin film. A penetration depth of approximately 5 nm is approximated for most thin films.[224], [225]

The relative degree of crystallinity:

Taking into account that semicrystalline polymer thin films are composed of both amorphous and crystalline regions, to different degrees, it is interesting to know what is the relative grade of organization of a film and how this optimized morphology is achieved through controlling processing conditions. A parameter that would assist in the evaluation of the degree of organization (DoC) is the degree of crystallinity of a film. It is the relative quantity of crystallite populations within a film, compared to a film of the same material that is wholly formed of crystallites.

Because obtaining a polymer film that is entirely crystalline is so far unfeasible, the relative degree of crystallinity (rDoC) is a more appropriate comparison parameter. Instead of comparing the degree of crystallinity of a film to another film 100% crystalline, films of the same material are compared among each other.

Considering that the intensity of the peaks diffracted is directly proportional to the crystal population sampled, integration of all the peak intensities could provide a measure of the degree of crystallinity of the film. For such integration, pole figures are utilized. A pole figure is the sum of the intensity acquired for a chosen peak from every possible orientation in a thin film. To take into account the distortion of the peak intensities due to the geometry of the setup, the peak intensities need to be corrected for small values of the polar angle χ . The higher χ , the lower the intensity captured. Therefore, the DoC is proportional to the integration of the poles:

$$DoC \propto \frac{\Delta\beta\Delta\theta}{2\pi} [I_{peak} - I_{baseline}] + \int_0^{\pi/2} \sin(\chi) I(\chi) d\chi \quad (4.8)$$

This method is used in the case of no in-plane texture. The degree of crystallinity is assumed to be the same in any direction scanned for the sample. In our analysis in Chapter 8, it is known that the films are highly anisotropic in the in-plane direction. In the case of an anisotropic film, the pole figure should be integrated for all directions of φ , therefore from $\varphi = 0^\circ$ to $\varphi = 90^\circ$:

$$rDoC \propto \int_0^{\pi/2} \int_0^{\pi/2} \sin(\chi) I(\chi, \varphi) d\chi d\varphi \quad (4.9)$$

Although the ideal measurement would be a scan of the sample rotated around φ or a sufficient amount of scans between these angles, this is quite time-consuming and beam time is limited. In Chapter 8, where the pole figures are calculated as a way to compare the degree of crystallinity of different films, the poles in the in-plane directions $\varphi = 0^\circ$ and $\varphi = 90^\circ$ are integrated. It is known from CPOM characterization and previous works that these are the in-plane angles of maximum and minimum scattering intensity, and therefore, the pole figures for the in-plane angles $0^\circ < \varphi < 90^\circ$ will all fall between these values. It should be noted, however, that for these calculations to be applicable, the assumption that there is no change in the packing of the polymer should be made. If there would be a different stacking structure in the film, the scattering intensity caused by these structures could be mistaken for a higher number of crystallite populations of the first structure.

For the calculation of the poles in Chapter 8, the (010) pi-pi stacking peak from 10° cake segments of χ is extracted, from $13^\circ < \chi < 83^\circ$. The factor $\sin(\chi)$ is used for the angle in the middle of each cake section. All the values are normalized for film thickness. The 2D scattering data in this work are analyzed using the WxDiff[226] software.

4.4 Electrical characterization

4.4.1 Characterization

Unless specified otherwise, all devices are electrically characterized by a Keysight B1500 semiconductor analyzer. For the saturation mobility, the transfer curve I_d - V_g is measured with a V_g sweep from 40 to -100 at a constant drain voltage $V_d = -100$ V. For the output curves I_d - V_d , the drain voltage is swept from 0 to -100 V at gate voltages of 0, -20, -40, -60, -80 and -100 V.

To contact the gate, the SiO_2 is scratched through until the Si is reached. To avoid leakage current through the edges of the substrate, the regions with the electrodes are isolated through the removal of the semiconductor around it.

4.4.2 Mobility estimation and overestimation discussion

Throughout the course of this doctoral work, significant changes have occurred in the evaluation of the electrical performance of organic semiconductors in the field of organic electronics. In the OFET field, the value of the charge carrier mobility is used as one of the main quantifiers of the quality of a new material or fabrication method. It has been for years a standard in the determination of the effectiveness of device improvement process in the field. In early-published works the strictness in the method of calculation of mobility for OFETs has been overlooked and works alleging high charge carrier mobility values are now claimed to be overestimated. In the last three years, works alleging high charge carrier mobility values have been reviewed by researchers attempting to explain the causes for the gate-voltage-dependent mobility values. Several works on the matter have arisen, and it is currently an essential topic in the OFET community. It is crucial to include in this work a discussion regarding the recent changes in the mobility evaluation and possible causes for them.

From the original gradual channel approximation model, the charge carrier mobility of the semiconductor used in the Equations (2.17) and (2.18) is only considered a valid quantifier of the quality for the semiconductor material if the values are independent of the

number of charge carrier density. Therefore, the mobility is expected to be independent of the V_g , or to be constant in a wide range of voltages for V_g .

The charge carrier mobility for organic materials is a combined result of intrinsic and extrinsic characteristics of the organic materials, such as grain boundaries, impurities, carrier trapping, dielectric inhomogeneities, and contact limitations. The V_g -dependent mobility can be induced by a diverse range of factors and can be a misleading factor in the comparison of intrinsic semiconductor quality when extrinsic factors of the semiconductor are not taken into account.

Figure 4.14 compiles some characteristic transfer curves that have been reported over the last years, including cases where gate-voltage dependent mobility occurs. The work of Choi et al. terms them the S-shape curve (a), superlinear curve (b), sublinear curve (c), the hump non-linearity (or double-slope) (d), and ideal shape with large V_{th} , (e) and an ideal curve according to the gradual channel approximation model (e).

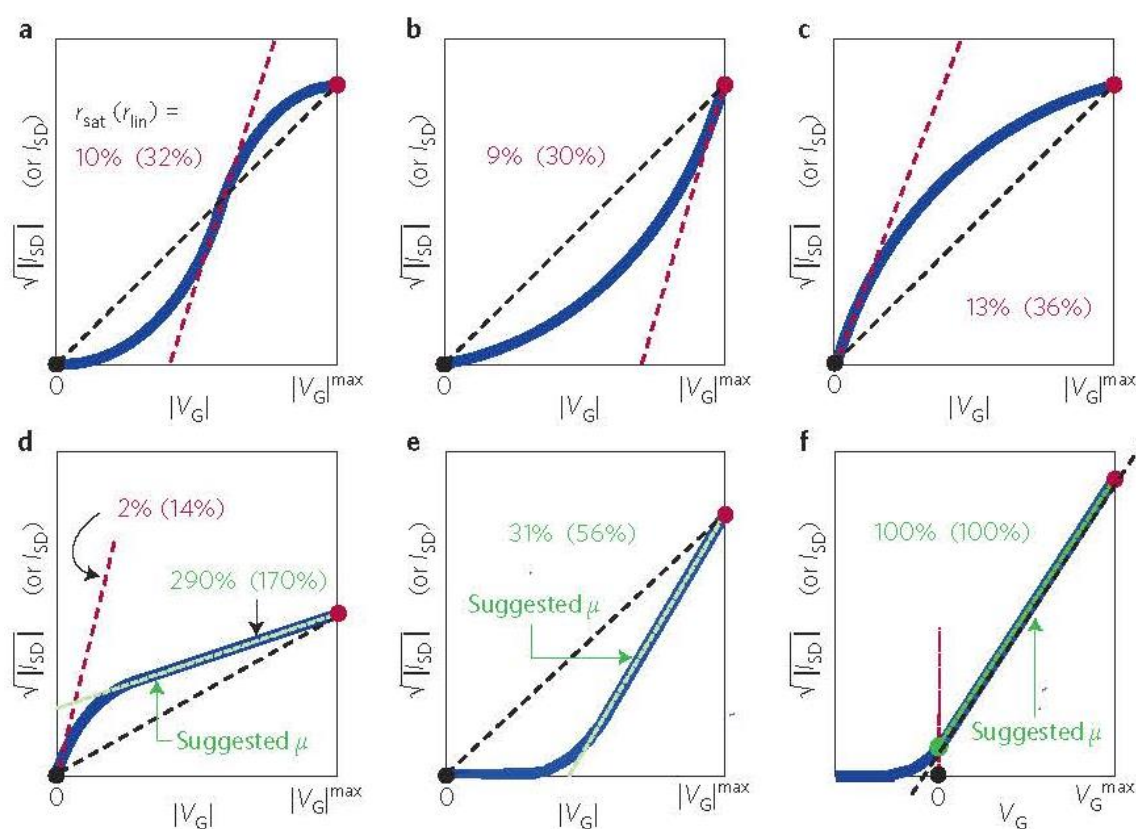


Figure 4.14: Common plots of transfer functions for OFET devices. The Ideal model is in (f). The black dashed lines are the equivalent plot, and the red lines are the values often reported and that are considered to be overestimated. The green lines in (d-f) are the suggested values and the respective reliability factor r . The black dot represents the origin and the red dot the maximum current. Image reproduced from Ref. [12].

The nonideality of mobility increasing with gate-voltage (Figure 4.14b) is associated with carrier-dependent mobility. Disorder in the semiconductor can cause charge localization, and therefore, higher energy required for charge delocalization and transport to occur for in the material.[227], [228]

The nonideality resembling a bump (Figure 4.14d) is often observed in works claiming high charge carrier mobility and is still not completely understood. It is currently associated with two main factors: i) contact resistance and ii) minor charge carrier trapping in donor-acceptor materials. In the case of contact resistance, the contact limitation requires a larger voltage to inject carriers, and once this is achieved, the current is expected to rise very rapidly, giving the impression of a high charge carrier mobility.

The work of Bittle et al. shows a case in which the V_g -dependent mobility changes abruptly due to a Schottky contact, yielding devices with transfer curves with the bump nonideality. Through simulation of a Schottky barrier, they have shown that an increasing contact resistance with gate bias fits well such nonideality observed in a single-crystal device. The work of Uemura et al. is in agreement with the latter work and goes further and highlights important papers in the field of OFETs that are now considered to be overestimated due to contact resistance. Besides the shape of the transfer function, another indication that this is the cause for the mobility dependence is the shape of the output curves in the linear regime.[26] Close to the origin the current should not be dependent on the drain voltage. Such nonideality is quite common, especially for D-A polymers.[21] The work of Phan et al. alleges that the double-slope mobility can also be due to the charge trapping of minor charge carriers in donor-acceptor materials.[229] The presence of a high V_{th} , such as the one in Figure 4.14e, can be indicative of limitations with carrier injection or a high density of deep traps.[12]

The black dashed lines in figures (a-e) are equivalent to the ideal $\sqrt{I_{d,sat}}$ curves of the gradual channel approximation if such devices would have the same maximum current and voltage and a constant charge carrier mobility. The red dashed lines are the gate voltage ranges where the mobilities are often calculated and reported from, due to the high slope value, and therefore, high mobility values. The green lines in Figure 4.14d and Figure 4.14e are the suggested voltage ranges where mobility can be calculated for. In this work, it is also suggested that a reliability factor be reported for the method used for calculation. The reliability factor r is calculated as the ratio between the slope of the black dashed line (ideal transistor case) and the slope used for the calculation of the claimed mobility. It represents the ratio of ideal conductivity to the maximum reported. It facilitates the fast evaluation for the reader of how close the reported mobility is to the ideal Shockley behavior. These are the values expressed in percentages for the graphs in Figure 4.14 out of the brackets, and the values inside the brackets are the ratio for the slope used for the linear mobility calculation. The reliability factor should be used in conjunction with other measurements methods, such as the gated four-probe measurement or Hall effect measurements.

Considering that our studies work towards the improvement of charge carrier mobility, it is crucial to take into account conservative reporting standards for evaluating our fabrication methods. Reports such as the one from Choi et al.,[12] suggest the report of mobility in a standard way that takes into account the nonidealities of the OFET device in comparison with the ideal Shockley mobility.

In this work, the OFET devices have different degrees of mobility dependence on the gate voltage. Several materials are used, and for simplification of comparison of mobility values, the effective mobility is reported. With the exception of the earlier study on TIPS-pentacene (Chapter 5), the other charge carrier mobilities reported correspond to the effective mobility, and the plot of the mobility as a function of gate-voltage are shown.

Chapter 5

5 Alignment Improvement from Blending the Small molecule TIPS-pentacene with an inert Polymer

5.1 Introduction

It has previously been demonstrated for benchmark materials such as TIPS-pentacene,[91], [92], [95], [96] C₈-BTBT,[97], [98] and 2,8-Difluoro-5,11-bis(triethylsilylethynyl)anthradithiophene (diF-TES-ADT)[44] that films with high fractions of non-equilibrium polymorphs can be obtained by proper tuning of the fabrication parameters such as the speed of deposition,[91] solution concentration,[92] annealing,[44], [95] addition of polymers[97] or even the application of an external electrical field during processing.[98]

For TIPS-pentacene, which was not known to have mobility over 1 cm² V⁻¹ s⁻¹ before it was solution-sheared, average mobility as high as 8.1 cm² V⁻¹ s⁻¹ has been obtained through careful flow engineering.[92] However, the FLUENCE method developed to achieve such high mobility values[92] does require a non-trivial micro-structuring of the silicon coating blade and a chemical micro-patterning of the substrate to achieve these mobilities. Therefore, one of the motivations for this work is to develop a more accessible to scale-up and less technologically difficult method to achieve comparable performance as this state-of-the-art solution shearing derivative method.

Here, a much easier method of fabrication of high-performance and low-power consumption devices, that is scalable to large areas is demonstrated. In our experiments, the deposition of blended films of the small-molecule TIPS-pentacene and the inert dielectric polymer polystyrene is fine-tuned by solution-shearing. It has previously been shown that mixing small-molecule semiconductors with dielectric polymers leads to easier processing, better control of the solution viscosity, and greater uniformity throughout the film.[103], [104], [230]–[233]

These types of blends have now been utilized for several years, but it has been only in the last couple of years that researchers started to use them with the solution-shearing method.[103], [104] This resulted in devices with excellent performance, for example for a blend of TIPS-pentacene and poly(α -methyl styrene) (PaMS) saturation charge carrier

82 Alignment Improvement from Blending the Small molecule TIPS-pentacene with an inert Polymer

mobilities of $4.6 \text{ cm}^2 \text{ V}^{-1} \text{ s}^{-1}$ for bottom-gate bottom-contact devices[104] and similar blends with diF-TES-ADT average mobilities over $3 \text{ cm}^2 \text{ V}^{-1} \text{ s}^{-1}$ are reported.[103] All of these devices use SiO_2 as the dielectric resulting in operating voltages $> 10 \text{ V}$, which is not suitable for applications like mobile or wearable electronics where the power consumption is one of the most critical parameters.

In this work, a fabrication approach to realize high mobility bottom-gate top-contact OFETs with a solution-sheared blend of TIPS-pentacene and polystyrene (PS) is presented. The optimized devices with a SiO_2 dielectric layer achieved average maximum mobility of $8.3 \text{ cm}^2 \text{ V}^{-1} \text{ s}^{-1}$. This is amongst the highest reported values for OFETs based on TIPS-pentacene.[92] The optimization of TIPS-pentacene:PS blends is initially described, regarding the molecular weight of polystyrene and the shearing speed with the resulting films being characterized by optical microscopy, electrical measurements, grazing incidence X-ray scattering (GIWAXS), atomic force microscopy (AFM), and scanning electron microscopy (SEM). Hereby, it is shown that for maximum mobility, a ribbon-like morphology and a vertical phase separation between the semiconductor and the dielectric are essential. Furthermore, it is shown that our fabrication process can be easily transferred to low-voltage transistors using a cross-linked PVP:HDA dielectric layer instead of the SiO_2 . The resulting devices achieved mobility values of up to $4.2 \text{ cm}^2 \text{ V}^{-1} \text{ s}^{-1}$ at an operating voltage of -1 V , which is to the best of our knowledge among the highest ever reported mobilities at such a low voltage, and the highest at the time the study was implemented.[234]

5.2 Optimization of film morphology for TIPS-pentacene

5.2.1 Device Fabrication

This study starts with the fabrication and characterization of high charge carrier mobility OFETs through solution shearing with the small molecule semiconductor TIPS-pentacene blended with different molecular weights of polystyrene. Phenyltrichlorosilane, octadecyltrimethoxysilane, polyvinylphenol, 4,4'-(hexafluoroisopropylidene)diphthalic anhydride and polystyrene with different molecular weights were purchased from Sigma-Aldrich. 6,13-Bis(triisopropylsilylethynyl)pentacene was purchased from Ossila Limited and used as received without any further purification.

In this chapter, two different bottom-gate top-contact device architectures have been used. The first one uses 300 nm-thick thermally grown SiO_2 as the dielectric and is treated with PTCS for improved wetting conditions of the substrate. The second type of devices utilizes a cross-linked PVP:HDA (poly(4-vinylphenol): 4,4'-(hexafluoroisopropylidene) diphthalic anhydride) layer. The PVP:HDA films were deposited on silicon wafers with native oxide and prepared at 10:1 weight ratio with PVP at a concentration of 20 mg ml^{-1} . $1 \mu\text{l ml}^{-1}$ of TEA was added to the solution. The preparation of the solution and deposition is described in detail in a previous publication.¹⁵ This dielectric has the advantage of enabling low voltage transistor operation.^{6,15,16}

For the TIPS-pentacene:PS blend, both materials were dissolved in toluene at a concentration of 8 mg ml^{-1} , stirred at 1000 min^{-1} at $60 \text{ }^\circ\text{C}$ for an hour, blended at a ratio of 1:1 and subsequently stirred at 1000 min^{-1} at $60 \text{ }^\circ\text{C}$ for another hour. The solution was cooled down to $35 \text{ }^\circ\text{C}$ while stirring at 1000 min^{-1} right before the shearing to ensure proper blending of the small molecule and polymer, and discard effects of the solution being heated to $60 \text{ }^\circ\text{C}$. The neat solution was left at a concentration of 8 mg ml^{-1} and used immediately after preparation. All the semiconducting solutions were prepared right before

the shearing process of each experiment to ensure repeatability. The substrate temperature for the shearing of the TIPS-pentacene:PS blends was 90 °C. The blade angle utilized was 8° with a gap of 100 µm between the edge of the blade and the substrate. After the shearing, the substrates were immediately removed to ensure no changes in phase separation that could be caused by the further annealing of the sample. For bottom-gate, top-contact transistors 50 nm-thick Au electrodes were thermally evaporated onto the semiconductor to finish the devices.

Unless specified otherwise, the electrical characterization of the TIPS-pentacene was carried out always on the same day, right after the printing and subsequent evaporation of electrodes. The whole process of OSC deposition, electrode evaporation, and electrical characterization happened in a time window of 8 hours to avoid as much as possible the influence of the ambient conditions on the performance of the semiconductor or change in the contacts.

5.2.2 Electrical Characterization

In Figure 5.1a, the maximum saturation mobilities for devices using SiO₂ as the dielectric with different molecular weights of polystyrene sheared at different speeds are shown. The maximum saturation mobility value is described further in this chapter. Through the adjustment of speed and molecular weight of the insulating polymer polystyrene, it is possible able to obtain an average maximum saturation hole mobility of 8.3 cm² V⁻¹ s⁻¹. The transfer curve of a typical device is shown in Figure 5.1b and the speed-dependent threshold voltages, On/Off ratios and maximum saturation currents are shown in

Figure 5.2. In Figure 5.1a, it can be observed that for devices with higher molecular weight polymers, the mobility is higher than for pristine and low molecular weight ($M_w = 2$ kDa). The optimum molecular weight and shearing speed is found to be at 2 mm s⁻¹ for the blend with $M_w = 20$ kDa. This high mobility is attributed to several combined factors: the excellent coverage of the substrate and smoothness of the film due to the blending with the polymer; the uniformity of the film in the larger scale, and a higher mobility polymorph present in the very thin films to print highly aligned crystalline structures parallel to the charge transport channel. All these aspects of the optimized films will be discussed throughout this chapter.

One can notice that for the best devices (Figure 5.3a) there is current hysteresis in the transfer curve, in which there is a lower back sweep current. Hysteresis is often observed for organic devices and seldom reported. It can have diverse causes, such as effects of trapping and slow-moving components in the semiconductor (e.g., ions), charge injection from the semiconductor into the dielectric, and possibly charge injection from the gate through the dielectric.[235]

Due to the present hysteresis in the OFET transfer curves, both the maximum and minimum mobility values are plotted, for both forward and backward sweep. The curves are swept, and slopes used for calculated as indicated in Figure 5.3a. The maximum and minimum mobilities for sweeping in both directions in all devices are presented in Figure 5.3b, c, and d. It can be observed that the trend regarding mobility related to shearing speed and molecular weight of the blends is maintained, in both optimistic and conservative case scenarios of mobility estimation.

84 Alignment Improvement from Blending the Small molecule TIPS-pentacene with an inert Polymer

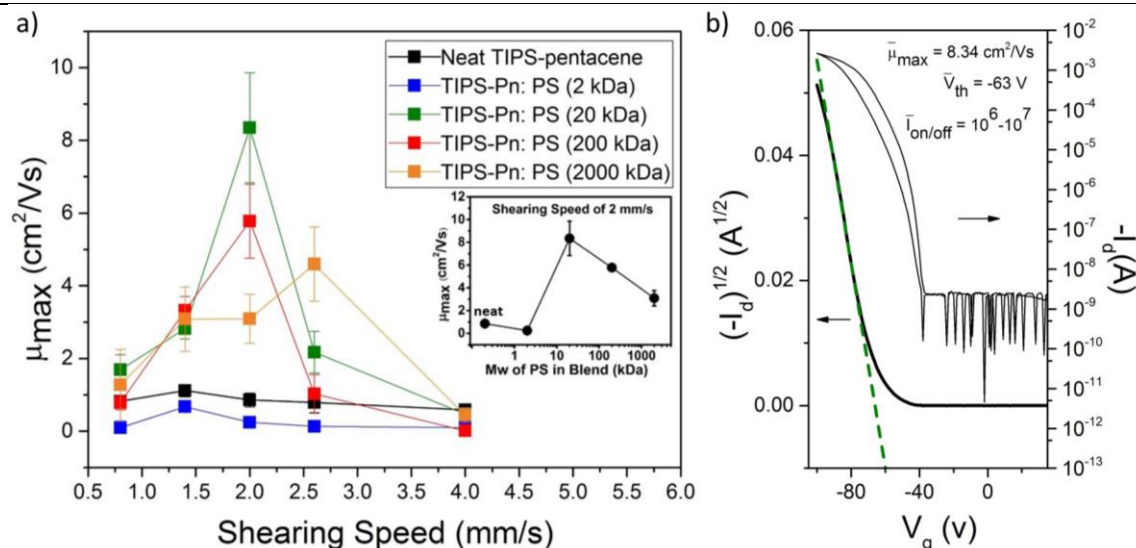


Figure 5.1: (a) Shearing speed-dependent maximum saturation charge carrier mobility of neat TIPS-pentacene and blends with different molecular weight polystyrene (blend ratio 1:1 by volume). The inset shows the molecular weight dependent mobility of the blends at a shearing speed of 2 mm s^{-1} . (b) Transfer characteristics of a typical device with TIPS-pentacene:PS blend ($M_w = 20 \text{ kDa}$ and ratio 1:1). Image reproduced from Ref. [234].

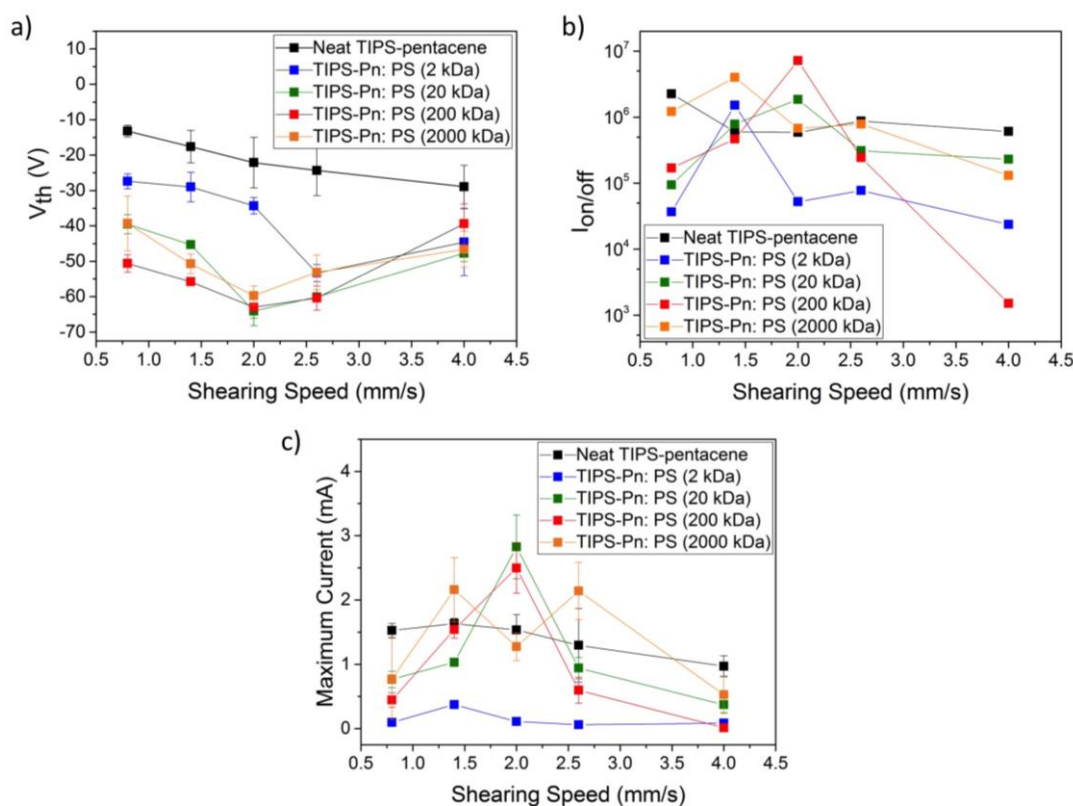


Figure 5.2: (a) The threshold voltage, (b) Ion/off ratio and (c) maximum values of drain current for TIPS-pentacene:PS blend films (ratio 1:1) with different polystyrene molecular weights sheared at different speeds. The large error bars in (b) are omitted. Image reproduced from Ref. [234].

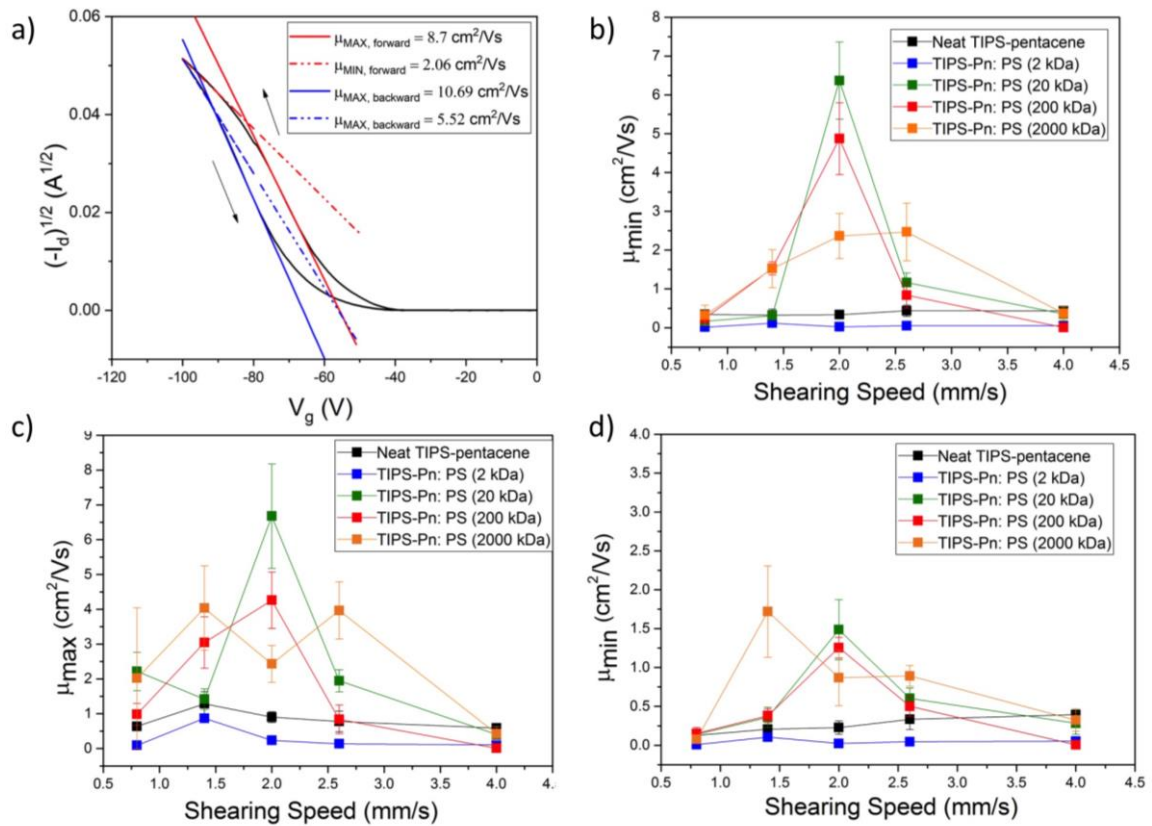


Figure 5.3: (a) Transfer curve for a typical device sheared at 2 mm s^{-1} with a 20 kDa blend. (b) minimum mobility values for backward sweep measurement, (c) maximum values of mobility for the forward sweep measurements, and (d) minimum values of mobility for the forward sweep. Image reproduced from Ref. [234].

From Figure 5.4, two trends for the intensity of hysteresis are observed. It is possible to notice thicker films to have a more considerable hysteresis, and blends to have more hysteresis than pristine films, although blended films are much thinner. Therefore, there seems to be more than one mechanism causing such current differences. The hysteresis here is taken as the voltage difference ΔV_g for constant current (approximately half of the maximum current reached by the device). Lower back sweep currents are often related to charge-trapping in the semiconductor channel.[235] This is associated with mobile charges trapped in the channel, charge injection from the semiconductor into the dielectric, slow reaction of charge carriers or mobile ions in the semiconductor.

Taking into account that thicker films have more significant hysteresis than thinner films, it might be that these are due to bulk trapping mechanisms. However, to so far our best knowledge, there is no systematic study of the effect of thickness on the current hysteresis of devices. It should also be taken into account that different thickness is accompanied by different morphologies, which complicates to determine whether the reason for such a hysteresis is exclusively due to thickness. The causes for hysteresis are multiple, and a way of deconvoluting the underlying cause would be evaluating how the hysteresis changes with different sweeping rates.

86 Alignment Improvement from Blending the Small molecule TIPS-pentacene with an inert Polymer

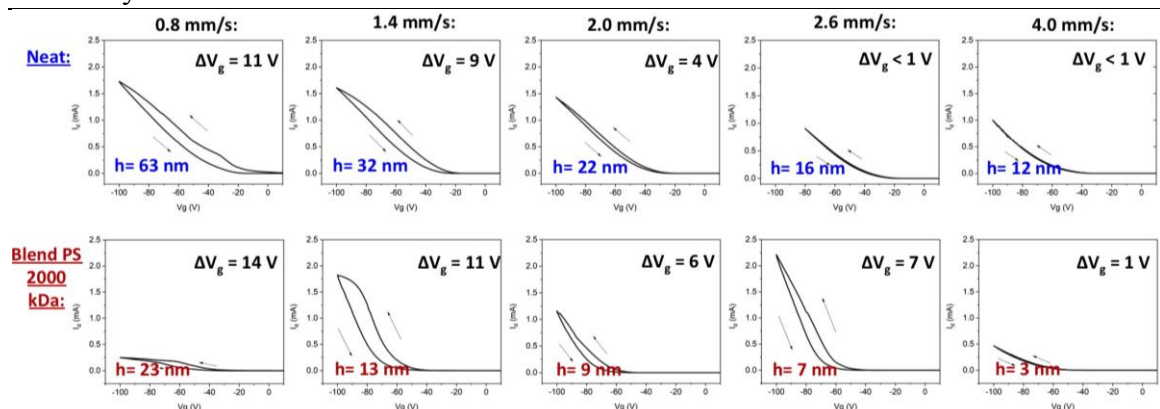


Figure 5.4: Top row: neat TIPS-pentacene films with increasing speed from left to right; and lower row: blended films of TIPS-pentacene:PS 2000 kDa with increasing shearing speeds. The size of the hysteresis for each plot is given by ΔV_g .

From Figure 5.4, it can also be observed that although the semiconductor layer of the film fabricated with blends of TIPS-pentacene:PS 2000 kDa is significantly thinner, the hysteresis is higher than for the pristine films. Considering that the polystyrene might act as a dielectric as well for the blended films, we speculate it possible to exist an overlapping hysteresis mechanism due to charge trapping in the latter.[235]

Molecular Weight (kDa)	Speed (mm/s)	Devices (#)	Mobility										On/Off ratio		Threshold Voltage				Maximum Current	
			Forward					Backward					Average	Std. Dev	Forward		Backward		Average (A)	Std. Dev (A)
			Average (cm ² /Vs)	Std. Dev (cm ² /Vs)	Maximum (cm ² /Vs)	Std. Dev (cm ² /Vs)	Average (cm ² /Vs)	Std. Dev (cm ² /Vs)	Maximum (cm ² /Vs)	Std. Dev (cm ² /Vs)	Average (V)	Std. Dev (V)			Average (V)	Std. Dev (V)				
Neat	0.8	10	0.38	0.05	0.64	0.09	0.58	0.06	0.82	0.13	2.25E+06	4.50E+06	10.30	5.55	-13.20	1.66	1.52E-03	1.10E-04		
Neat	1.4	10	0.75	0.17	1.29	0.35	0.72	0.09	1.12	0.17	6.02E+05	4.09E+05	-11.40	9.58	-17.60	4.59	1.63E-03	8.07E-05		
Neat	2.0	9	0.56	0.11	0.90	0.16	0.60	0.13	0.86	0.19	5.88E+05	7.74E+05	-11.33	9.09	-22.11	7.16	1.53E-03	2.40E-04		
Neat	2.6	15	0.52	0.16	0.78	0.30	0.57	0.18	0.79	0.28	8.73E+05	1.76E+06	-22.20	6.80	-24.33	7.13	1.30E-03	5.72E-04		
Neat	4.0	12	0.49	0.04	0.59	0.06	0.51	0.05	0.59	0.07	6.08E+05	7.35E+05	-25.83	6.63	-28.92	6.09	9.71E-04	1.63E-04		
2	0.8	10	0.05	0.02	0.09	0.04	0.05	0.02	0.10	0.03	3.68E+04	3.39E+04	11.10	11.00	-27.40	2.11	9.63E-05	2.54E-05		
2	1.4	10	0.49	0.04	0.87	0.08	0.40	0.04	0.67	0.08	1.52E+06	3.65E+06	-26.70	4.94	-29.00	4.17	3.74E-04	3.32E-05		
2	2.0	10	0.13	0.05	0.24	0.10	0.13	0.03	0.24	0.06	5.25E+04	3.10E+04	-33.80	2.52	-34.30	2.33	1.11E-04	1.77E-05		
2	2.6	10	0.09	0.04	0.14	0.06	0.09	0.04	0.13	0.06	7.75E+04	1.85E+05	-50.80	5.13	-53.30	2.45	6.06E-05	1.90E-05		
2	4.0	10	0.08	0.01	0.10	0.01	0.08	0.02	0.10	0.02	2.37E+04	4.12E+03	-41.10	11.41	-44.60	9.47	8.38E-05	1.27E-05		
20	0.8	10	1.18	0.30	2.22	0.55	0.93	0.23	1.69	0.42	9.43E+04	2.49E+04	-1.80	5.19	-39.50	2.69	7.66E-04	1.28E-04		
20	1.4	10	0.89	0.20	1.42	0.30	1.57	0.16	2.82	0.29	7.85E+05	1.24E+06	6.30	7.68	-45.30	0.90	1.03E-03	6.55E-05		
20	2.0	25	4.08	0.74	6.68	1.50	7.36	1.22	8.35	1.51	2.17E+06	2.23E+06	-53.42	3.06	-64.08	4.09	2.83E-03	4.96E-04		
20	2.6	10	1.27	0.18	1.95	0.32	1.67	0.37	2.17	0.57	3.11E+05	2.20E+05	-53.60	2.97	-60.10	0.70	9.41E-04	1.65E-04		
20	4.0	10	0.34	0.14	0.40	0.13	0.41	0.17	0.47	0.17	2.30E+05	3.11E+05	-44.55	3.65	-47.73	2.34	3.72E-04	1.18E-04		
200	0.8	10	0.57	0.18	0.98	0.31	0.51	0.12	0.78	0.20	1.70E+05	2.51E+05	-20.00	10.27	-50.60	2.46	4.45E-04	1.12E-04		
200	1.4	10	1.71	0.37	3.04	0.74	2.43	0.24	3.32	0.38	4.66E+05	8.28E+04	-45.20	1.60	-55.80	0.40	1.54E-03	1.30E-04		
200	2.0	10	2.76	0.36	4.26	0.81	5.33	0.96	5.78	1.02	7.19E+06	8.50E+06	-51.90	1.22	-63.00	0.00	2.50E-03	3.92E-04		
200	2.6	10	0.67	0.26	0.84	0.41	0.93	0.42	1.03	0.53	2.44E+05	3.45E+05	-51.50	7.88	-60.40	3.41	5.95E-04	2.02E-04		
200	4.0	10	0.01	0.01	0.01	0.01	0.01	0.01	0.01	0.01	1.52E+03	1.05E+03	-62.80	19.00	-67.10	17.60	1.26E-05	1.40E-05		
2000	0.8	10	1.05	1.02	2.02	2.03	0.80	0.60	1.28	0.98	1.22E+06	2.95E+06	-21.70	14.94	-39.30	7.73	7.70E-04	6.31E-04		
2000	1.4	10	2.88	0.78	4.04	1.21	2.30	0.67	3.08	0.89	3.99E+06	9.44E+06	-42.40	7.10	-50.70	2.79	2.16E-03	4.98E-04		
2000	2.0	15	1.65	0.38	2.43	0.53	2.73	0.58	3.09	0.68	6.78E+05	5.75E+05	-49.13	6.83	-59.73	2.74	1.27E-03	2.13E-04		
2000	2.6	15	2.43	0.42	3.97	0.82	3.53	0.79	4.60	1.02	7.85E+05	2.90E+05	-44.93	5.52	-53.13	4.88	2.14E-03	4.46E-04		
2000	4.0	10	0.37	0.17	0.43	0.20	0.41	0.19	0.44	0.20	1.31E+05	1.06E+05	-42.70	5.76	-46.60	5.04	5.26E-04	2.94E-04		

Table 5.1: Electrical characteristics of shear-coated TIPS-pentacene:PS devices.

5.2.3 Film morphology characterization

In general, two morphology regimes for the TIPS-pentacene films fabricated in this study can be observed: one with large crystalline ribbons (high anisotropy), and a spherulitic one (more isotropic). The ribbon-like regime is related to lower shearing speeds and the spherulitic morphology to higher speeds; this has been observed for TIPS-pentacene before.[91], [104] In Figure 5.5 the ribbon-like crystalline structure is only observed for the pristine films and blends with $M_w \geq 20$ kDa, while the films with blends of $M_w = 2$ kDa present a spherulitic morphology for the whole range of tested speeds.

For the blends with $M_w \geq 20$ kDa, it can be observed that the speed at which the morphology transitions to the spherulitic regime occurs, increases with the polymer weight in the blend, i.e., is higher for $M_w = 2000$ kDa than for 200 kDa. Figure 5.5s shows that the

film morphology of the blend of $M_w = 2000$ kDa still has a ribbon-like structure at a shearing speed of 2.6 mm s^{-1} , whilst at the same speed, the films with M_w of 20 kDa and 200 kDa have already transitioned into a spherulitic morphology (Figure 5.5k and o). This is associated with the higher viscosity of the 2000 kDa M_w polymer. Figure 5.6 displays the shear rate-dependent viscosities of a solution of PS in toluene, at the same concentration (4 mg ml^{-1}) and temperature ($90 \text{ }^\circ\text{C}$) as of the sheared films. The viscosity of the solution tends to increase with the polymer's molecular weight, but the viscosity is significantly higher for the 2000 kDa PS. Furthermore, a shear-thinning aspect for the 2000 kDa PS is observed.

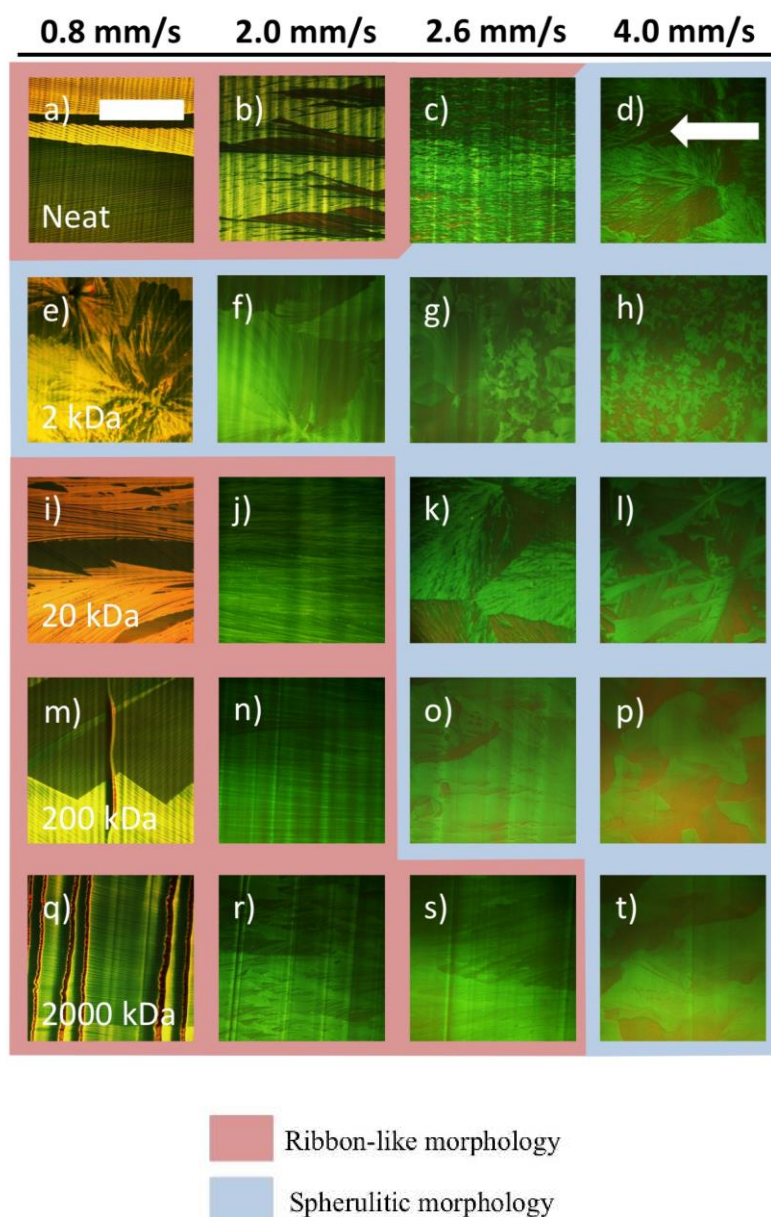


Figure 5.5: Optical microscope images of (a-d) pristine TIPS-pentacene and blends with polystyrene with a molecular weight of (e-g) 2 kDa, (i-l) 20 kDa, (m-p) 200 kDa, and (q-t) 2000 kDa. The white arrow indicates the shearing direction. Scale bar: $200 \mu\text{m}$. Image reproduced from Ref. [234].

If $\dot{\gamma} = v/h$ is taken as the shear rate, where v is the speed of the moving blade and h the substrate-blade gap ($100 \mu\text{m}$). The expected shear rate during solution shearing of the films should not be significantly above 40 s^{-1} , considering the range of speeds tested in this work.

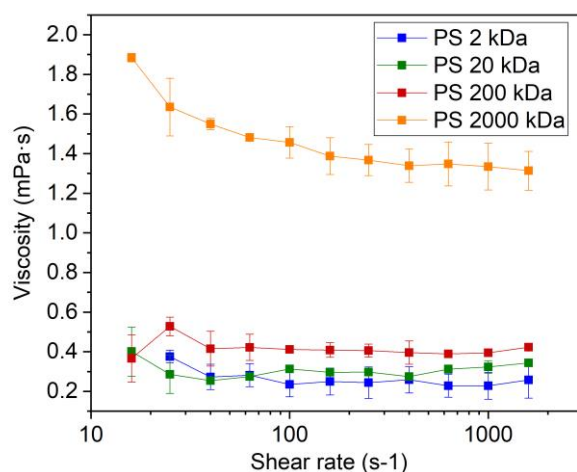


Figure 5.6: Shear-rate dependent viscosities for PS:toluene solutions, with the equivalent PS concentration as in the semiconducting solution. Measurements are carried out at 90 °C, to resemble as much as possible the solution shearing process.

Furthermore, in the blends with $M_w \geq 20$ kDa, there are undulations, which are more pronounced for the high molecular weight blends due to higher viscosity (see Figure 5.5j, n, and r). The undulations are perpendicular to the shearing direction and are often associated with stick-and-slip phenomena.[139], [143] It is known that viscosity over a critical value at the contact line is enough to trigger a pinning-depinning cycle, therefore stick-and-slip.[150] They appear to induce nucleation of the TIPS-pentacene, disrupting the continuous crystal growth of the ribbons. This can be seen clearly in Figure 5.5r, where the crystalline domains are smaller, and the direction of growth of the structures are more scattered. It is believed these undulations to be the main reason for which the films with $M_w \geq 200$ kDa have lower values of charge carrier mobility in comparison to the blend with $M_w = 20$ kDa. Also, for the blends of $M_w \geq 200$ kDa, the undulations become more pronounced as the shearing speed is decreased.

The very low charge carrier mobility of the $M_w = 2$ kDa films is likely due to the fact that the morphology is always spherulitic regardless of the shearing speed. Similar behavior has previously been observed,[76], [236] for example, by Galindo et al. where the small-molecule DB-TTF is blended with PS of $M_w = 3$ kDa. The morphology of the resulting bar-coated films is mostly spherulitic, isotropic, and presenting large smooth domains. It is speculated this could be due to higher miscibility of polymer and semiconductor, especially when utilizing low molecular weight polymers, which prevents the formation of vertically phase-separated, highly crystalline TIPS-pentacene layers. This will be further discussed below.

From the atomic force microscopy (AFM) images in Figure 5.7, it can be seen that the blended films also present better coverage of the substrate. All the blended films present nearly full coverage of the substrate and significant lower roughness, while the pristine film has gaps, as can be observed in Figure 5.8. In Figure 5.8, a cross-section of the pristine film shows the steep edge of the crystalline structure in relation to the substrate. It is equivalent to the total thickness of the pristine film, which is shown further on.

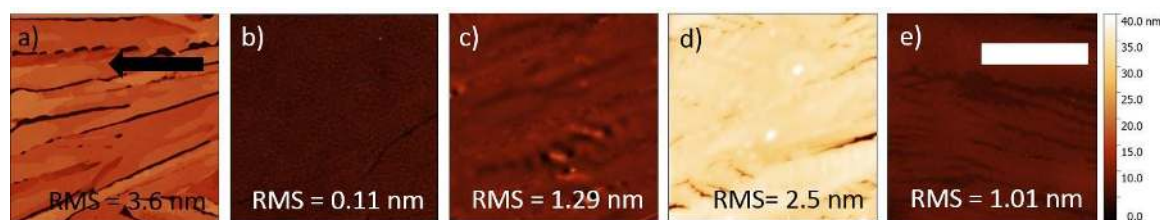


Figure 5.7: Atomic force microscopy images of film surfaces for (a) neat TIPS-pentacene films (shearing speed of 2.6 mm s^{-1}), films blended with (b) PS $M_w = 2 \text{ kDa}$ (2 mm s^{-1}), (c) PS $M_w = 20 \text{ kDa}$ (2 mm s^{-1}), (d) PS $M_w = 200 \text{ kDa}$ (2 mm s^{-1}), and (e) PS $M_w = 2000 \text{ kDa}$ (2.6 mm s^{-1}). Scale bar: $5 \mu\text{m}$. Image reproduced from Ref. [234].

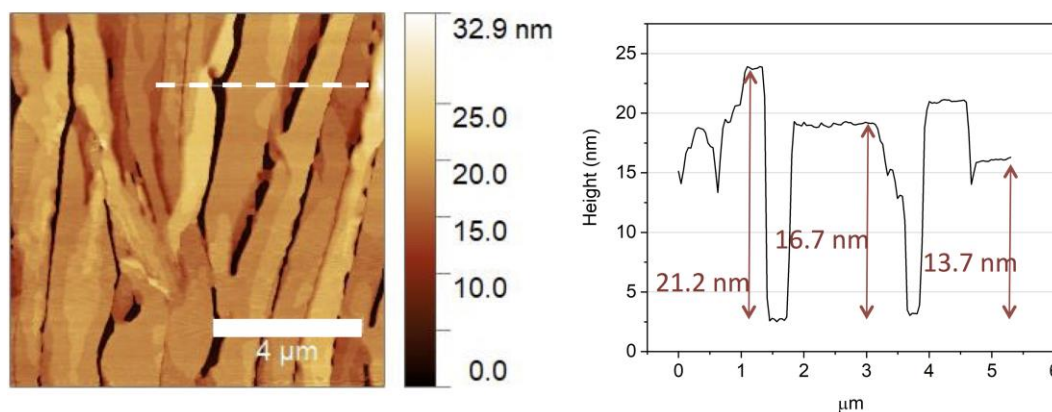


Figure 5.8: AFM scan for a film of neat TIPS-pentacene. The cross-section shows gaps with the same height as the nominal film thickness, $16.6 \pm 3.4 \text{ nm}$, and indicating exposed substrate between crystallite formations.

The coating conditions presented in Figure 5.5 are all using a TIPS-pentacene:PS ratio of 1:1 by weight. Different blending ratios have been tested for blends of PS ($M_w = 20 \text{ kDa}$) and the best charge carrier mobility values obtained are at a blending ratio of 1:1. Figure 5.9 shows the effect of blending different ratios of TIPS-pentacene and PS ($M_w = 20 \text{ kDa}$) over the charge carrier mobility and film morphology. For blends containing a larger ratio of TIPS-pentacene than PS, the films present a ribbon-like morphology even when the PS percentage is drastically reduced, such as in the case of 33% PS (Figure 5.9b). The films have, though, less continuous crystalline growth, with more nucleation sites. We believe the higher number of nucleation sites and a lower degree of alignment in crystallite growth in relation to the shearing direction to be the main reason for lower charge carrier mobilities in these films. For the films with a larger ratio of PS than TIPS-pentacene, even a small increase in the PS percentage, such as in for the case of 55% PS (Figure 5.9i), is enough to disrupt the formation of the ribbon-like morphology and transition into the spherulitic regime, reducing the charge carrier mobility drastically. We speculate this trend to be similar for blends of $M_w \geq 20$. A similar trend in charge carrier mobility has been observed previously for diF-TES-ADT:PS blends.[103]

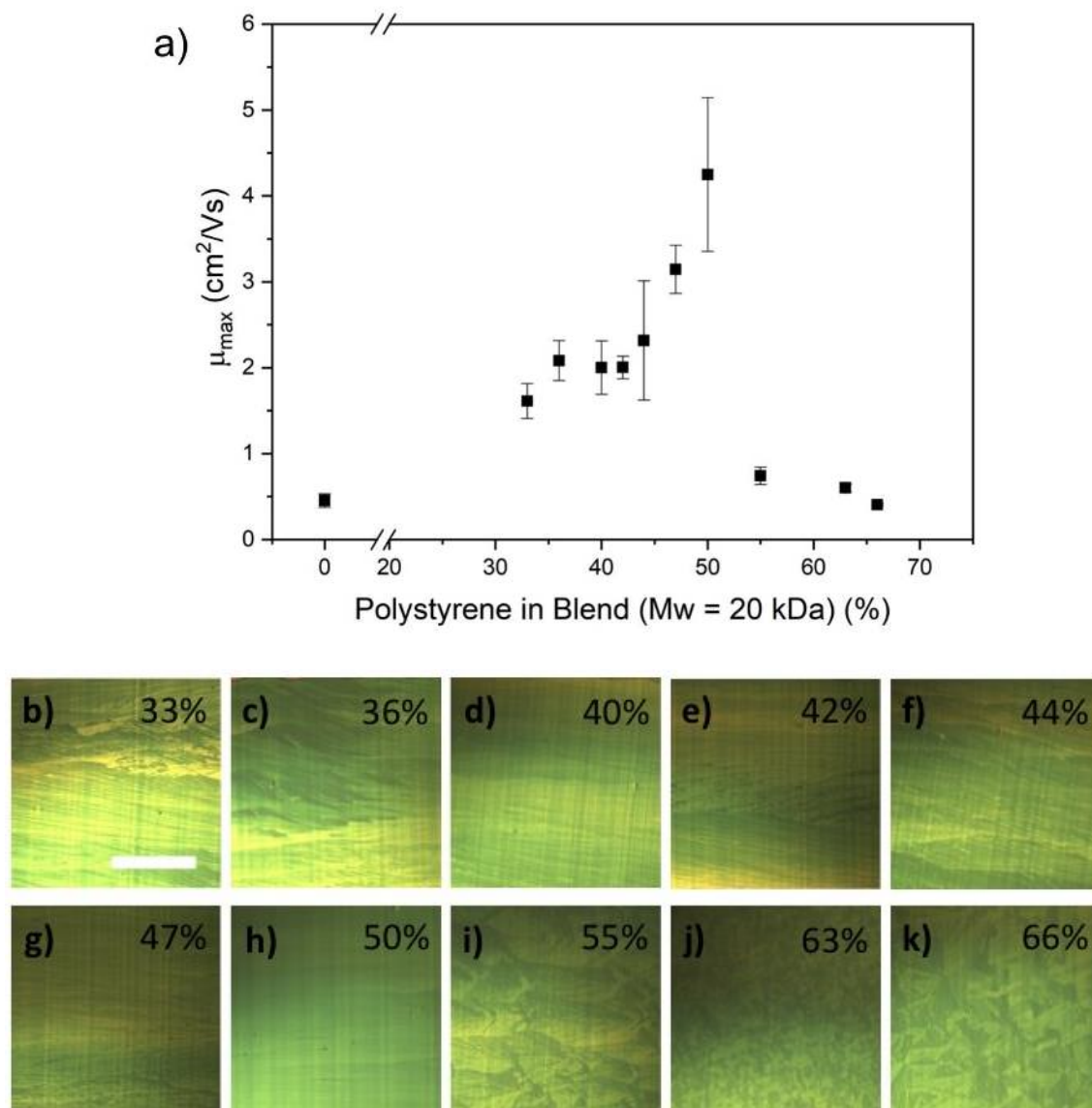


Figure 5.9: (a) Charge carrier mobility of TIPS-pentacene:PS with different blending ratios at a shearing speed of 2.2 s⁻¹. Microscopy images for blends containing (b) 33%, (c) 36%, (d) 40%, (e) 42%, (f) 44%, (g) 47%, (h) 50%, (i) 55%, (j) 63%, (k) 66% weight of polystyrene. Scale bar: 500 μm . Image reproduced from Ref. [234].

Although the films with blending ratio of 1:1 present the highest charge carrier mobility in comparison to the samples with different blending ratio, the absolute values of charge carrier mobility for the devices in Figure 5.9 are lower in comparison to the samples presented previously as a result of these samples being measured under different time conditions. The electrodes in this experiment are deposited 24 h, and devices measured 48 h after the shearing of the films, opposed to the whole fabrication process, which has been done in a time interval of 8 hours for all samples in Table 1, and Figure 5.1, Figure 5.2, and Figure 5.3. Samples are stored in ambient air.

In order for the blended films of small-molecule and inert polymer to yield high charge carrier mobilities, it is necessary to achieve a favorable phase separation in which the semiconducting small-molecule can form a continuous crystalline film. It has been shown in several cases [103], [104], [230], [233], [237]–[239] that this vertical stratification of the materials allows the small-molecule layer to have a thin, crystalline film with big and well-connected domains towards the air interface. This is believed to be the case for

our group of high M_w films – and one of the reasons for the very high charge carrier mobilities. In our samples, vertical phase separation in the films with polystyrene of molecular weights of 20 kDa is observed, leading us to believe a similar phase separation is present for the films with 200 kDa and 2000 kDa. The cross-section scanning electron microscopy (SEM) image of the blend film with $M_w = 20$ kDa is presented in Figure 5.10 and clearly shows the phase separation. The film with PS of $M_w = 20$ kDa is chosen due to its high charge carrier mobility and to the less likeliness for it to vertically phase separate, in comparison to films of $M_w = 200$ kDa and $M_w = 2000$ kDa. Because of very similar morphologies among blends with polymer molecular weights ≥ 20 kDa, these films are all expected to exhibit a vertical stratification as visible in Figure 5.10. The likeliness of such a vertical phase separation is further corroborated for blends of $M_w = 20$, 200 and 2000 kDa when the top layer of TIPS-pentacene is selectively dissolved with hexane. After removing the top layer of TIPS-pentacene, a remaining buried layer of PS is present in all films with high molecular weight blends, also strongly suggesting that there is phase separation for all the blends with a $M_w \geq 20$ kDa. This is consistent with previous reports on solution-shearing of small molecules and insulating polymer blends of high molecular weight.[103], [104] Micrographs of the films before and after dissolving the TIPS-pentacene layer are given in Figure 5.11. Once the TIPS-pentacene is removed, the ripples in the polymer films caused by a stick-and-slip motion are still visible, reinforcing that these undulations in the polymer layer are responsible for defects in the crystal growth of the top TIPS-pentacene layer.

The image below was made by Dr. Markus Löffler at the Dresden Center for Nanoanalysis (DCN). Details of the imaging have been described in our publication.[234]

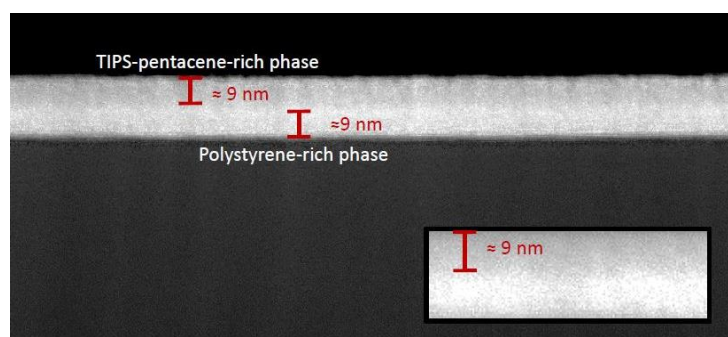


Figure 5.10: Scanning electron microscopy image of the cross-section of a TIPS-pentacene:PS blended films of ($M_w = 20$ kDa and shearing speed of 2 mm s^{-1}). Image reproduced from Ref. [234].

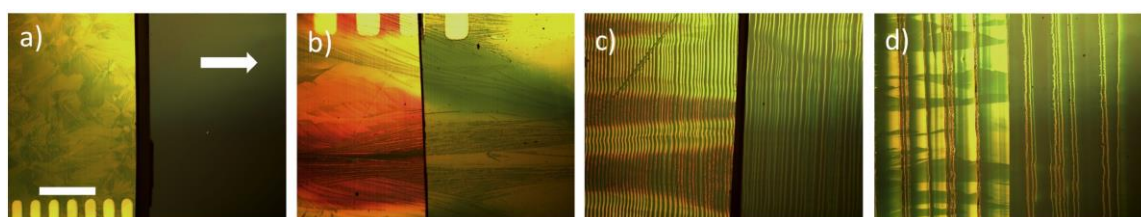


Figure 5.11: Optical microscopy images of the film before (left) and after (right) removing the TIPS-pentacene with hexane for blends of polystyrene of (a) 2 kDa, (b) 20 kDa, (c) 200 kDa and (d) 2000 kDa. Scale bar: 500 μm . Images reproduced from Ref. [234].

In previous studies, it was shown that this phase separation is influenced by the type of polymer,[232], [238], [240] the polymer molecular weight,[230] the solvent,[232], [239] the contact surface area[103], [233], [241] and spin coating speed.[241] Even though the mechanism of phase separation that occurs for spin-coated films is not necessarily applicable to shear-coated films, it has also been previously observed in spin-coated experiments[230] that higher molecular weight blends yield more pronounced phase separation than those with lower molecular weight polymers. Another aspect to consider

92 Alignment Improvement from Blending the Small molecule TIPS-pentacene with an inert Polymer

is that the stratification of the TIPS-pentacene towards the air interface also enables the fabrication of high-performance top-gate devices. A previous study has shown a case where top-gated devices present even higher charge carrier mobility as opposed to bottom-gate devices due to a higher quantity of TIPS-pentacene at the air interface when using a spin-coated blend of TIPS-pentacene: poly(triarylamine).[233]

It is believed that the samples with a lower molecular weight, such as the ones discussed above, show less vertical phase separation, such as the ones discussed above. No clear indication for a vertical phase separation for the 2 kDa blends is found in the corresponding scanning electron microscopy (SEM) images, and the attempt to dissolve the layer of the TIPS-pentacene removed the whole film, leaving the silicon substrate bare (Figure 5.11a). In the AFM phase image and the surface SEM image of the film blended with 2 kDa (Figure 5.12), it is possible to see separate domains, which could potentially be from two different materials or domains with different relative fractions of TIPS-pentacene and polystyrene, indicating a lateral phase separation. This suggests that the TIPS-pentacene is embedded in the polymer matrix and does not crystallize towards the air surface, and not forming a crystalline film of the semiconducting small molecule as the higher molecular weight blends do. This would be consistent with the fact that the blended films with PS $M_w = 2$ kDa have lower mobility values than even the pristine semiconductor films. Embedding of the semiconductor in the polymer matrix has also been observed in previous works involving the blending of small molecules with low molecular weight polymers.[242]

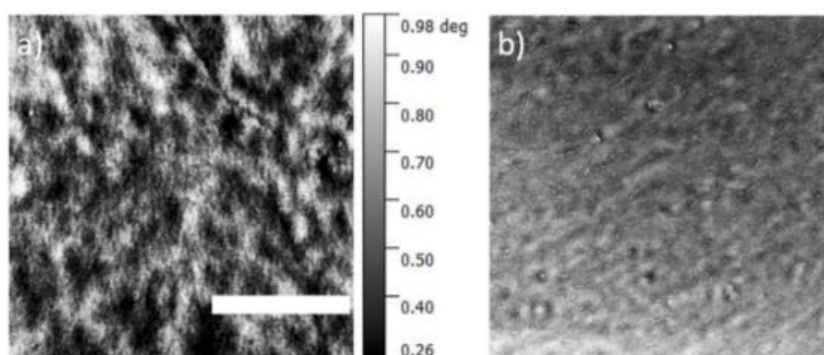


Figure 5.12: (a) Phase image from sample blended with 2 kDa and a (b) SEM image of the film surface. The scale bar applies to both images and has a length of 4 μm . Image reproduced from Ref. [234].

In Figure 5.13, the dependence of the blended film thickness on the shearing speed is plotted. It can be seen that the thickness of the films gradually decreases as the molecular weight increases. It can be observed that the thickest films are obtained for the neat material, and the thinnest films are obtained for blends with a PS molecular weight of 2000 kDa. Additionally, the higher the PS molecular weight, the less pronounced is the dependence of thickness on the shearing speed. This is another property that can be beneficial for the fabrication of large-area films through printing: with more viscous materials, there is a higher tolerance to small fabrication variances or errors. For the pristine materials, a rather small speed variation is likely to cause a significant change in film thickness.

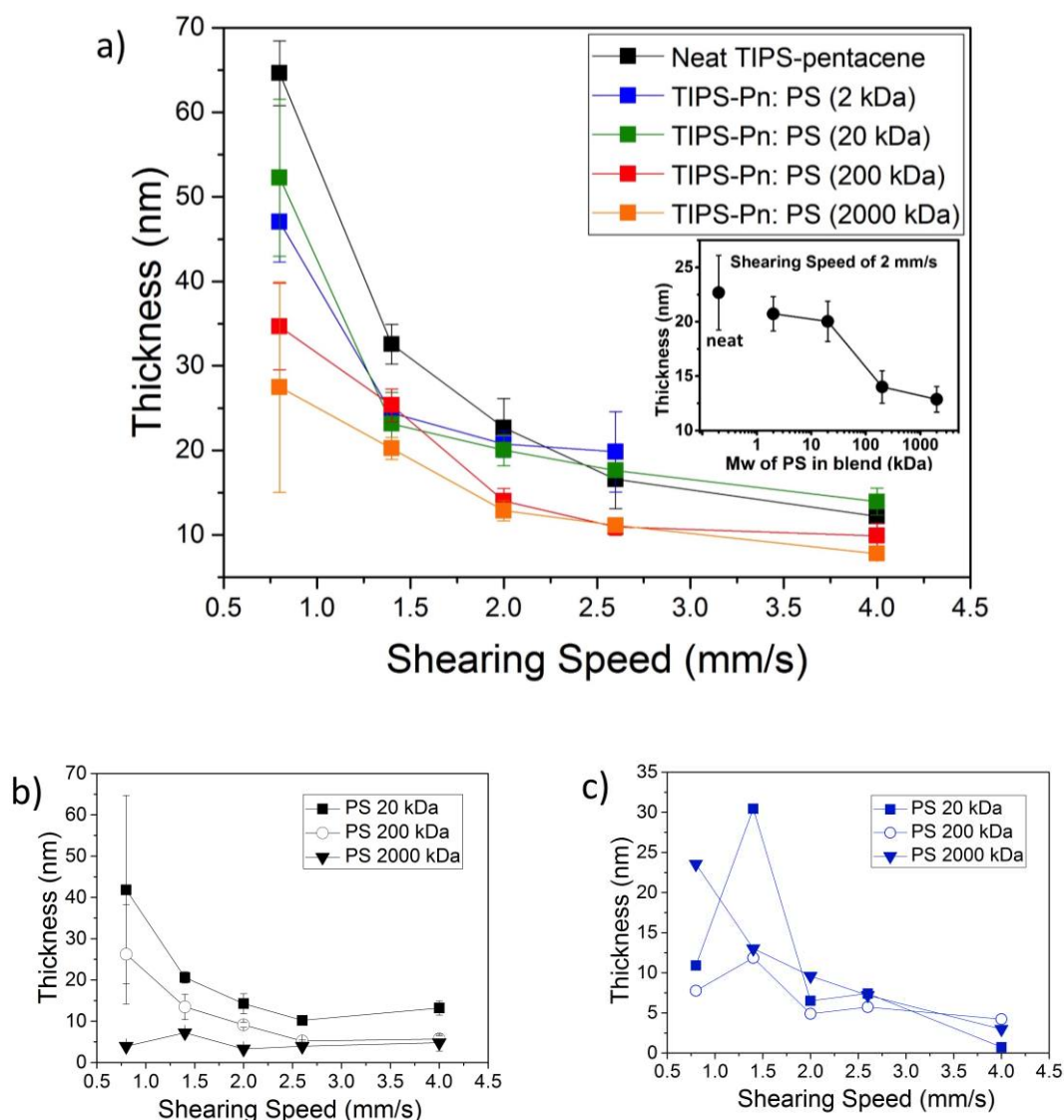


Figure 5.13: (a) Shearing speed-dependent film thickness of TIPS-pentacene:PS blends with different molecular weights. (b) The thickness of the PS layer buried in the film (measured after dissolving the TIPS-pentacene layer with hexane); (c) thickness of the TIPS-pentacene layer formed at the interface of air due to phase separation. This thickness was obtained from subtracting the thickness of the buried PS layer from the total film thickness. Image reproduced from Ref. [234].

To obtain an approximate thickness of each layer of the phase-separated films, the TIPS-pentacene layer is first removed with solvent - and subsequently, the thickness of the PS layer buried underneath with AFM is measured. In Figure 5.14a, b and c, the measured thickness of the PS layer, and the calculated thickness of the TIPS-pentacene layer can be seen, respectively. It is clear that the polymer makes up the majority of the thickness of the layer. This is also shown in Figure 5.14; for the films in the group of high M_w films (where vertical stratification is observed), the polymer layer measured is thicker than the layer of TIPS-pentacene, except for the case of 2000 kDa, where the opposite is observed.

It has been shown before that achieving high mobility in TIPS-pentacene devices is tightly linked to being able to control the polymorphism of the material by the processing conditions.[92], [94], [95] Specifically, it was shown that in TIPS-pentacene thin films, the fraction of the high mobility-polymorph (type IIb)[92], [95] in the TIPS-pentacene films relative to the lower mobility, equilibrium phase-polymorph (type I) strongly depends on the film thickness.[92] Based on grazing incidence X-ray scattering data (Figure 5.15), the same trend also for the blended films discussed here can be confirmed. Blended films with

94 Alignment Improvement from Blending the Small molecule TIPS-pentacene with an inert Polymer

high M_w (e.g., 200 kDa) show an evident signature of the high-mobility polymorph II when sheared at 2 mm s^{-1} (thickness $< 15 \text{ nm}$) whereas pristine samples sheared at the same speed (thickness $> 20 \text{ nm}$) still show predominantly polymorph type I.

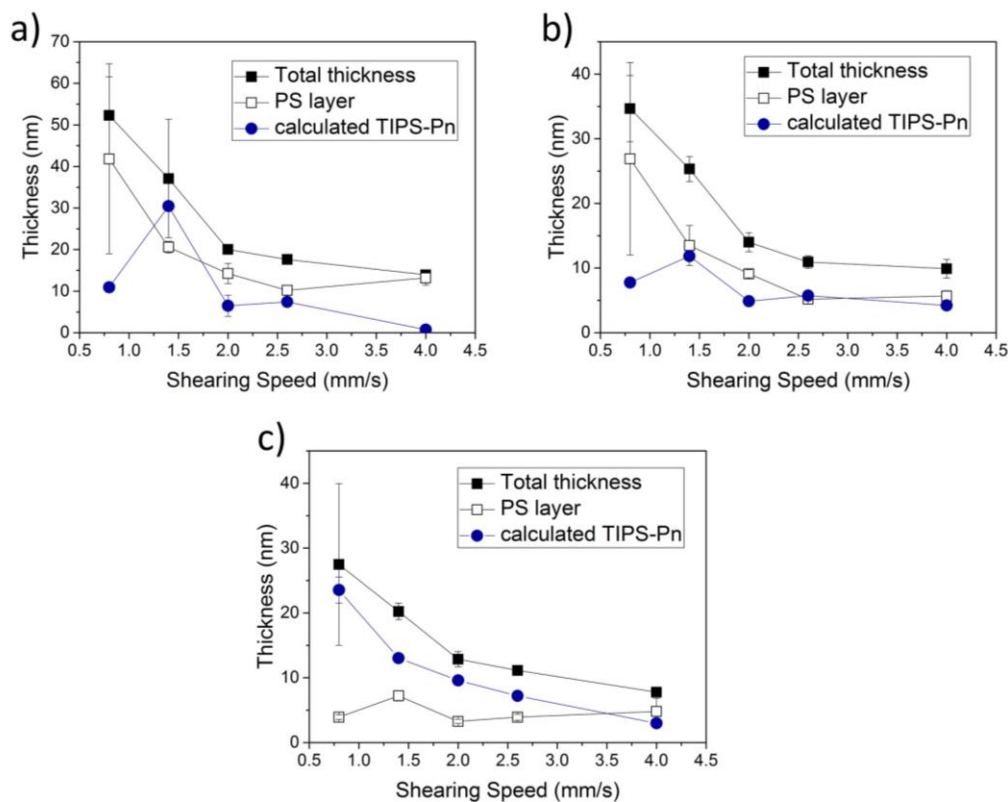


Figure 5.14: Film thicknesses of TIPS-pentacene:PS blends with (a) $M_w = 20 \text{ kDa}$, (b) $M_w = 200 \text{ kDa}$, and (c) $M_w = 2000 \text{ kDa}$ sheared at different speeds. The thicknesses for the blends and polystyrene are measured, and the TIPS-pentacene thicknesses are calculated by subtracting the other two. Images reproduced from Ref. [234].

Figure 5.15 shows the in-plane projections of the (10) and (01) Bragg rods (background-corrected, noise filtered, and Gaussian fitted. These data suggest that similar to what was previously found for neat films of TIPS-pentacene, the polymorph composition in the blends also strongly depends on the film thickness. In the thicker blended films with 200 kDa PS, i.e., sheared at low speeds (1 mm s^{-1}), the predominant signature is that of the equilibrium polymorph I. Films sheared at higher speeds such as 2 mm s^{-1} show a clear signature of polymorph II shifted to larger q_{xy} values. In fact, in the 4 mm s^{-1} -sheared samples, phase III is already predominantly detected, which was previously shown to only exist at RT in ultrathin films. Still, it should be noted that to accurately map all the polymorphs present in the film a full rotation of the samples would be necessary which could not be done here.[91], [95]

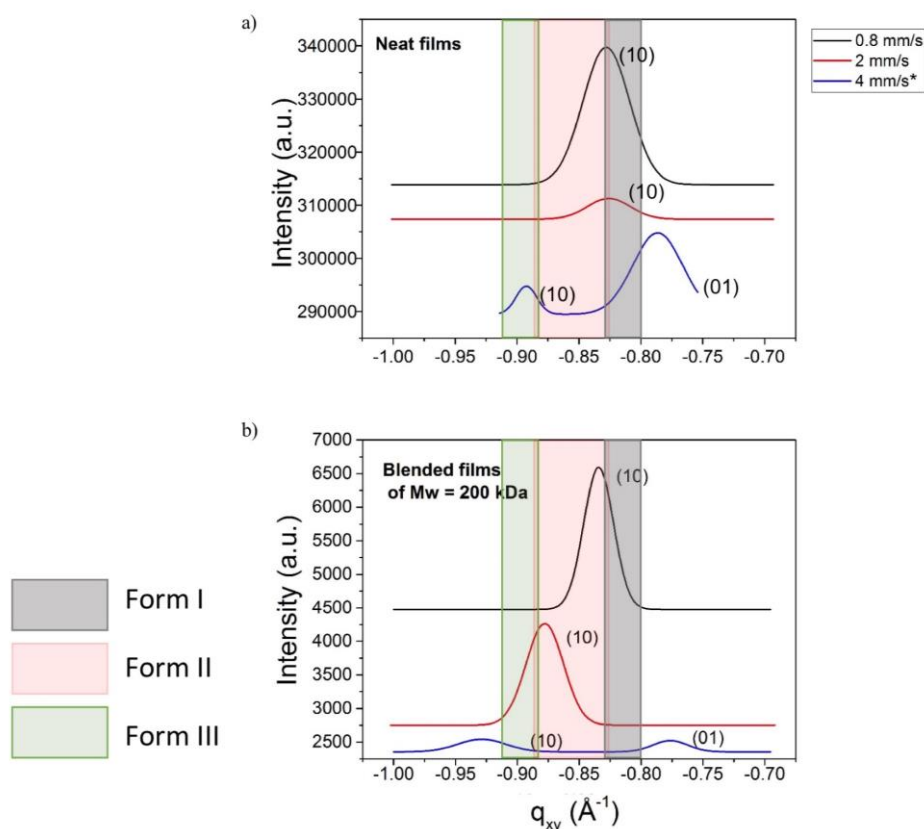


Figure 5.15: GIWAXS data for films (background-subtracted, Gaussian fits, scaled and offset) of (a) neat semiconductor and (b) blend of $M_w = 200$ kDa films. The peaks are background-corrected, noise filtered, and Gaussian fitted. The colors in the legends represent the ranges of the peak positions for the different polymorphs forms of TIPS-pentacene mapped out in previous works.[92], [95] One can observe the more visible peak shift of the 200 kDa films starting at 2 mm s^{-1} due to the significant thickness difference between the neat films and the films of high molecular weight. This is consistent with previous observations of the nanoconfinement effect for TIPS-pentacene.[92], [94], [95] Image reproduced from Ref. [234].

Since the in-plane charge transport in TIPS-pentacene is expected to be anisotropic,[243] it is essential to test in which way the shearing of blends creates in-plane crystallographic textures in the film. In order to test the anisotropy of the electrical device performance and to see if the blending or the molecular weight of PS in the blend has an influence on the thin film texture, special electrode layouts that enable us to measure transistors at different azimuthal angles (with steps of 15°) relative to the shearing direction are used (Figure 5.16).[244] From Figure 5.16, it is possible to observe that for the films sheared with the neat semiconductor and the higher molecular weights, the crystal growth and charge carrier mobility is highly anisotropic. For the best sample, sheared at 20 kDa the anisotropy is even more evident due to the high alignment of the crystalline ribbons of the film. However, films sheared with the 2 kDa PS blends are significantly more isotropic, which is consistent with the spherulitic morphology of the film. This isotropy has also been previously observed[95] in blended films with low molecular weight polymers.

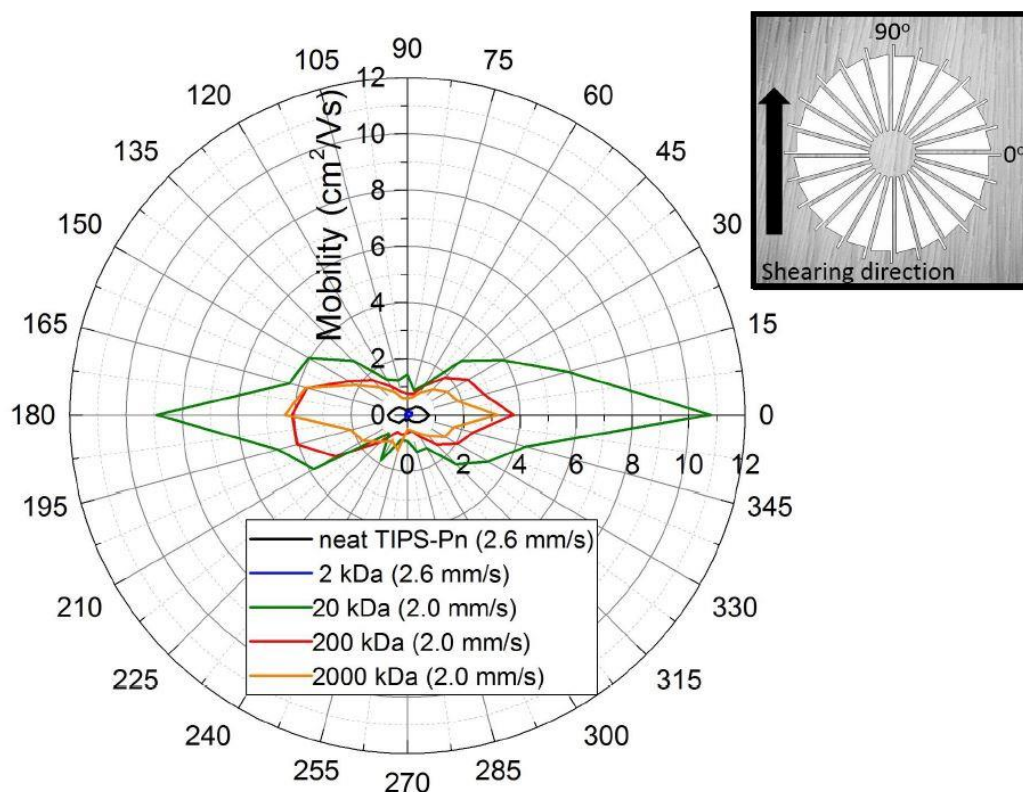


Figure 5.16: Maximum saturation charge carrier mobility as a function of orientation for the best sample of each blend. The inset shows the electrode geometry and the shearing direction. Image reproduced from Ref. [234].

5.3 Fabrication of Ultra-low-voltage Operation Devices

Despite its prominent use in literature, devices based on TIPS-pentacene are usually produced on thicker dielectrics—most commonly SiO₂ wafers—with the resulting devices requiring very high voltages of up to -100 V.[91], [92], [98], [101] Although the charge carrier mobility of the devices shown so far is very high, the voltage necessary to operate them is unrealistically high since even a simple circuit would require a large amount of power. Here it is demonstrated that devices fabricated with the solution-sheared blend of TIPS-pentacene:PS can operate at very low voltages by using the cross-linked polymer dielectric PVP:HDA instead of SiO₂. This dielectric layer has been described in previous works, and it has been shown that it is possible to achieve low-voltage transistors in conjuncture with organic semiconductors.[245], [246] In our work we are able to obtain devices with average maximum mobility of 4.2 cm² V⁻¹ s⁻¹ and a threshold voltage of only -380 mV for shear coated films of TIPS-pentacene:PS with M_w = 20 kDa. Figure 5.17b and c show the representative transfer and output characteristics of a typical device. The film morphology based on an optical micrograph of one of these samples is presented in Figure 5.17a and shows the preferential ribbon-like structure similar to the films prepared on SiO₂. The device performance for the neat TIPS-pentacene on PVP:HDA dielectric is also superior to devices that used SiO₂ dielectric, where the highest mobilities are measured to be around 1 cm² V⁻¹ s⁻¹ (Figure 5.18). Devices operated at ultra-low voltages (V_g < -1 V), have been reported previously[245], [247] but only achieved relatively low mobilities, such as 0.3 cm² V⁻¹ s⁻¹ for DDFTF-based transistors. On the other hand high-performance

devices with charge carrier mobilities $\geq 1 \text{ cm}^2 \text{ V}^{-1} \text{ s}^{-1}$ have been reported for operation voltages below 20 V.[29], [248]–[254] The devices that are closest in terms of mobility and threshold voltage to the transistors presented in this work operate at voltages in the range of 3 – 5 V.[29], [250] The mobility of $4.2 \text{ cm}^2 \text{ V}^{-1} \text{ s}^{-1}$ for the devices using the blend is to the best of our knowledge, one of the highest values for an ultra-low voltage, solution-processed OFET reported so far. It is currently only surpassed by the recent work of Haase et al.,[38] with the coating of C₈-BTBT on a solution-sheared dielectric film of PVP:HDA.

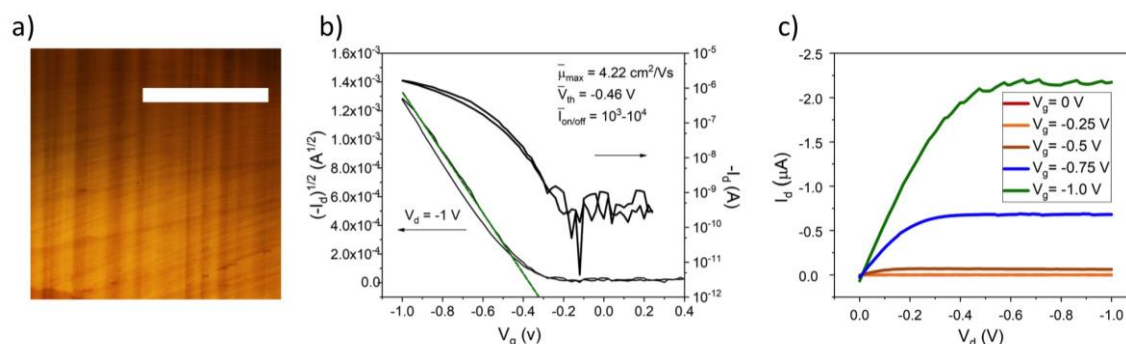


Figure 5.17: (a) Optical micrograph of TIPS-pentacene:PS (20 kDa) sheared over the PVP:HDA dielectric layer. Scale bar: 200 μm ; (b) transfer and (c) output characteristics of low voltage operating devices. The films are sheared with a blend of TIPS- pentacene:PS (20 kDa) at a speed of 2 mm s^{-1} . Image reproduced from Ref. [234].

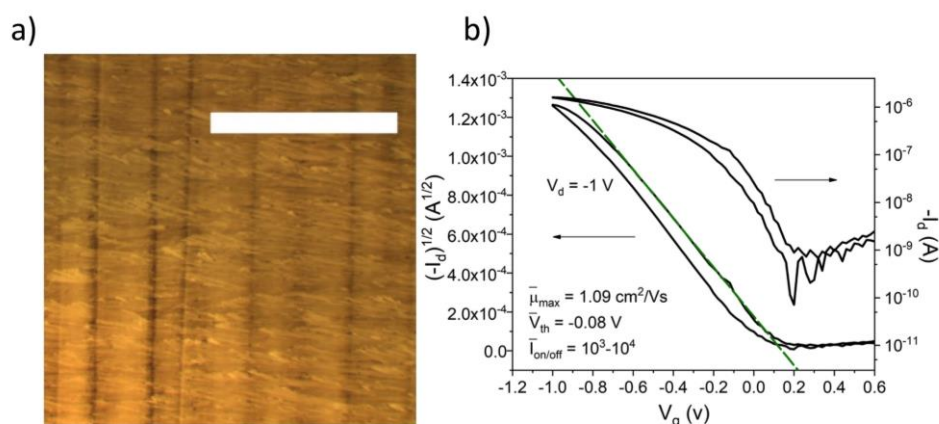


Figure 5.18: (a) Optical microscopy image and (b) transfer characteristics of the neat TIPS-pentacene sheared over the PVP:HDA dielectric layer. Scale bar: 200 μm . Image reproduced from Ref. [234].

5.4 Figure of Merit of this Study

At the time of the publication of this study,[234] the values reported for our TIPS-pentacene devices were record-breaking; comparable to an elaborate work published with a complicated fabrication method – the FLUENCE method. It was also the work with the lowest driving voltage combined with the highest charge carrier mobility. As has been shown in recent studies and works providing explanations for gate-voltage-dependent charge carrier mobilities, it is, however, challenging to compare existing fabrication methods. Different authors report charge carrier mobility values using differing criteria. In this section, the electrical characteristics of these works are assessed using a more recent approach, which suggests reporting the charge carrier mobility for each gate voltage, and the calculation of effective mobility.[12]

Various reasons for overestimation of charge carrier-mobility that have been suggested by recent works are high contact resistance,[12], [26], [255] trapping of minority carriers,[229] and possibly reasons not yet detected. In the case of the electrical curves present in this work, the substantial mobility peak at low voltages is an indication high of contact resistance.[26], [255]

As has been shown in Figure 5.3a, due to hysteresis and different “slopes” in the transfer curve, it is possible to calculate different charge carrier mobility values. In the case of our best devices, mobility can vary from $2.06 \text{ cm}^2 \text{ V}^{-1}\text{s}^{-1}$ to $10.69 \text{ cm}^2 \text{ V}^{-1}\text{s}^{-1}$, depending on which voltage range is chosen for mobility calculation. In Figure 5.19f, typical mobility values as a function of gate voltage are depicted for typical devices coated at the best conditions. Dependence of the charge carrier mobility on the gate voltage is observed. It is found that the devices on PVP:HDA present significantly smaller hysteresis, which we speculate could be due to the better quality of the dielectric.[235] The transfer graphs from the previous works[91], [92], [98], [101], [103] are extracted and plotted according to device dimensions described in each publication and can be observed in Figure 5.19. With the exception of the work of Niazi et al., most of the previous works reporting high charge carrier mobilities have a strong gate-voltage-dependence and report no hysteresis.

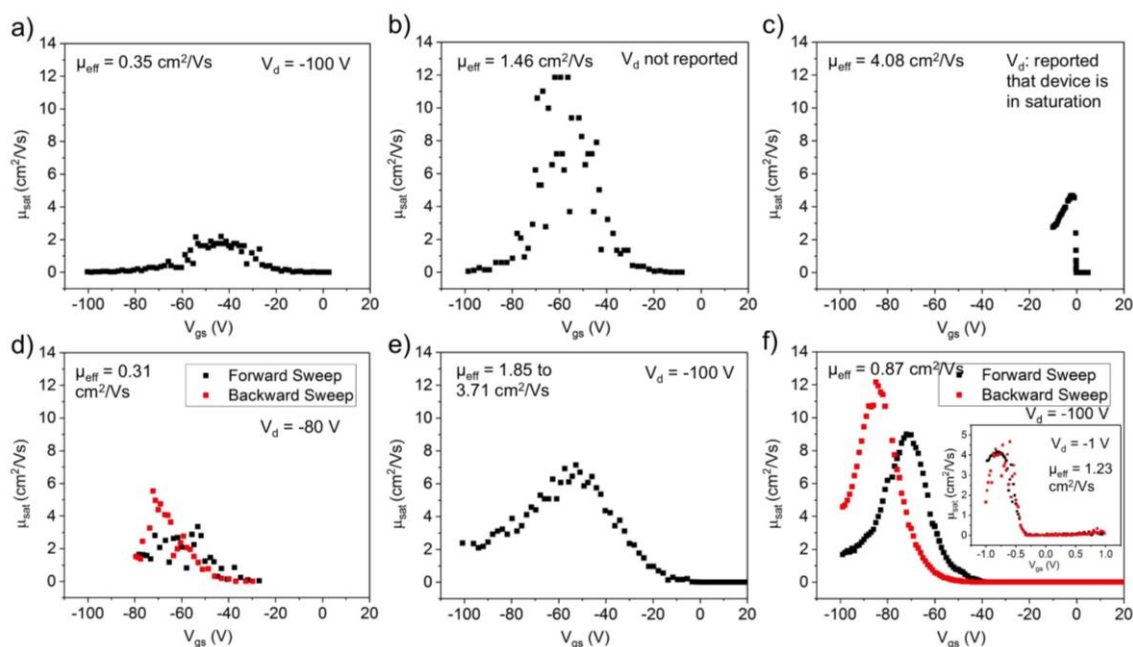


Figure 5.19: Mobility plots extracted from data from the works of (a) Giri et al. (2011),[91] (b) Diao et al. (2013),[92] (c) Niazi et al.(2016),[104] (d) Molina-Lopez et al. (2017)[98] (e) Xiao et al. (2017),[101] (f) and from our group (2018).

The degree of gate-voltage-dependence varies widely from work to work, and comparison is quite challenging. As has been discussed earlier in Chapter 4, the method suggested by the work of Choi et al., of reporting the effective mobility, facilitates comparison of device quality. In Figure 5.19, the effective mobility values (μ_{eff}), according to the device dimensions specified in the respective publications, are displayed. If a 300-nm-thick layer of SiO_2 is used as the dielectric, the capacitance value is corrected to 11.5 nF cm^{-2} , as also suggested by the work of Choi et al. It can be observed that the devices with the highest effective mobility are from the work of Niazi et al. The $\mu_{\text{eff}} = 4.08 \text{ cm}^2 \text{ V}^{-1}\text{s}^{-1}$ is very close to the value reported in the publication, however only very low voltages have been measured, and the mobility estimation is possibly problematic. We speculate that improved contact resistance could be a defining factor of the quality of these devices, considering that this is the only work that uses bottom-contact architecture. The “peak” in

the mobility value when the device turns on, characteristic of significant contact resistance, is not so prominent.

Comparing the effective mobility of devices fabricated with TIPS-pentacene, we conclude that our mobility is possibly significantly lower than the one initially calculated. However, it still remains among one of the highest values reported when compared to other works under the same mobility calculation criteria.

In Figure 5.20, a comparative graph of voltage operation versus charge carrier mobility is displayed. A combination of high mobility and low driving voltage is the most desired scenario. Moreover, for this mobility, our devices were at the time of publication of this work, record-breaking. They were later surpassed by C₈-BTBT devices with solution-coated thin-film dielectrics in the work of Haase et al.[38]

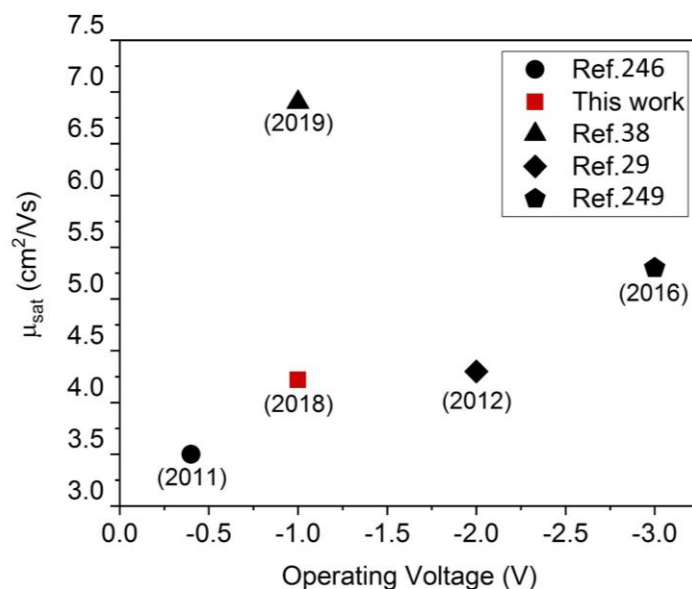


Figure 5.20: Graph depicting the charge carrier mobility of OFETs and their respective operation voltages. The year in brackets corresponds to the year of publication.

5.5 Summary

In summary, it has been in this chapter reported the detailed characterization of high-performance TIPS-pentacene:polystyrene OFET devices fabricated by solution shearing, which reached average maximum mobility of $8.3 \text{ cm}^2 \text{ V}^{-1} \text{ s}^{-1}$, and effective mobility of $\mu_{\text{eff}} = 1.23 \text{ cm}^2 \text{ V}^{-1} \text{ s}^{-1}$. This is amongst one of the highest mobilities for solution-processed devices based on TIPS-pentacene. The improved performance of the devices from the blend over the neat semiconductor is attributed to more preferential molecular packing due to a confinement effect caused by the vertical phase separation in the blend films and very continuous crystalline ribbons grown in the shearing direction. Furthermore, it has been shown here that by replacing the SiO₂ dielectric with a solution-processable and cross-linkable PVP:HDA layer it is possible to maintain the preferred morphology and achieved high mobility field-effect transistors ($\mu = 4.2 \text{ cm}^2 \text{ V}^{-1} \text{ s}^{-1}$, $\mu_{\text{eff}} = 1.23 \text{ cm}^2 \text{ V}^{-1} \text{ s}^{-1}$) operating at ultra-low voltages ($< 1 \text{ V}$).

Chapter 6

6 Piezoshearing of Crystalline Materials

6.1 Introduction

For this chapter, the vibrations are applied during the solution shearing of crystalline materials to attempt improving the crystal growth. It is speculated the vibration can cause a stirring of the semiconductor close to the contact line and slow down secondary nucleation, aiming to achieve larger crystalline domains.

As discussed in Chapter 3, the vibration of liquids can improve the circulation of liquid, which can have the effect of mixing or stirring. The results of stirring a liquid during crystallization are diverse and often unpredictable. Stirring is often used in large-scale processes for seed growing. The stirring of a solution can cause effects on the crystal growth rate such as a change in the mass transfer rate around the growing crystal, and minimize local supersaturation at the point of addition, enhancing crystal growth and suppressing nucleation. [72] This is the effect expected to be achieved in this chapter.

As nucleation and crystal growth occur at the air-liquid interface, we believe the stirring of the OSC to be necessary only at the liquid surface. Due to the very low film thickness, the crystalline morphology formed at the top surface is expected to reach down to the substrate[94]

As mentioned in Chapter 3, previous works demonstrate that using transducers to mix liquids for microfluidic applications through vibrations[256], [257] or ultrasonic propagation[206] is very effective. Industrial applications have also shown the use of vibration for mixing liquids in a cuvette,[258] homogenization of a slurry for deposition,[259] and mitigation of nozzle clogging in inkjet printers.[260] Although in industrial crystallization such stirring is usually done with propellers[72], [261] and to the best of our knowledge, vibration is not commonly used method, we believe it to have the potential for improving crystal growth in our system.

In this chapter, thin films of TIPS-pentacene, a blend of TIPS-pentacene and PS, and C₈-BTBT are deposited from solution by the described piezoshearing method.

6.2 Piezoshearing of Pristine TIPS-pentacene

For the initial tests, the semiconductor TIPS-pentacene is chosen due to the rich amount of information available on it. Optimized coating conditions for solution shearing have been presented in previous works,[91], [92] polymorphs have been mapped out,[95] and the devices present reasonable charge carrier mobility.[91], [92]

In general, setups that yield very thin films, with ribbon-like morphology and that can be coated at very slow speeds, are chosen. It is believed that the low coating speed to be an essential factor for allowing more continuous crystal growth. Slower shearing allows the molecules in the meniscus to assemble to the film in a more ordered form, instead of creating new nucleation sites, and therefore, more grain boundaries, which hinder charge carrier mobility. It is also speculated that higher coating speeds would require higher frequencies for producing the same effect, and our setup is limited in displacement for high vibration frequencies.

6.2.1 Film Fabrication

For the film fabrication, a low concentration of TIPS-pentacene in toluene (1 mg ml^{-1}) is used, and a coating temperature of $90 \text{ }^\circ\text{C}$. Volumes from $50 \text{ }\mu\text{l}$ to $80 \text{ }\mu\text{l}$ are used for coating a substrate of an approximate size of $1.6 \text{ cm} \times 3 \text{ cm}$. The volume used depended on the coating speed. Coating speeds vary from 0.2 mm s^{-1} to 1 mm s^{-1} . The gap between the substrate and the edge of the blade is of $100 \text{ }\mu\text{m}$.

6.2.2 Thin-film Characterization

Figure 6.1 displays the effect of a constant displacement amplitude at different vibration frequencies and various shearing speeds. The vibration amplitude used for the piezosheared films was of 20 Vpp . Through an increase of vibration frequency, the energy introduced into the system increases, in direct relation to the acceleration of the actuator. The acceleration values for each piezoshearing condition is displayed in Figure 6.1.

Figure 6.2, the corresponding thicknesses for such films are shown. For films with thickness above 25 nm , cracks appear. For films coated at lower speeds (Figure 6.1a-c), large cracks are observed. The cracking is associated with different cooling rates between the substrate and the organic film, and thicker films are more prone to cracking under stress. Therefore, films at lower thicknesses are likely to be better for devices of TIPS-pentacene and have the additional advantage of being more prone to polymorphism due to nanoconfinement.[95]

Compared to films produced constant low speeds from Figure 6.1, (i.e., the column of coating speed at 0.2 mm s^{-1} or 0.4 mm s^{-1}), the stick-and-slip seems to increase when increasing the vibration frequency. Consequently, the crystals start to grow in lines of varying width. It is believed the wide parts of the crystalline stripes to be a consequence of the contact line staying pinned for a longer time (stick phase), enabling more extensive crystal formation, and the thin lines to be due to fast contact line movement when the contact line depins (slip phase). The change in the stick-and-slip cycle and resulting pattern depends on how susceptible the liquid is to a particular vibration frequency, and whether the vibration amplitude is enough to change the depinning behavior of a contact line. Since the stick-and-slip seems to increase with increasing frequency, it is speculated that the resonance frequency (or one of its harmonics) is closer to 15 kHz than to 5 kHz .

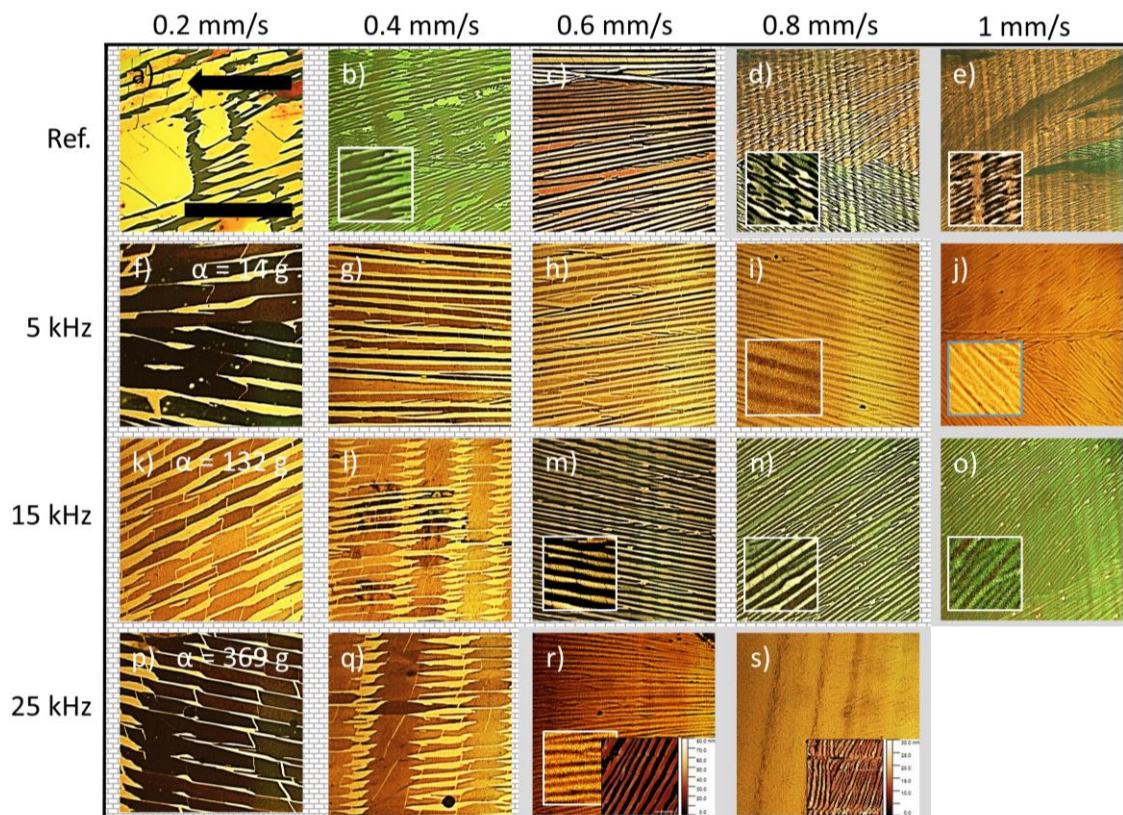


Figure 6.1: Microscopy images of TIPS-pentacene films coated from a toluene solution with a substrate temperature of 90 °C with the (a-e) standard shearing method; and with vibration with a constant amplitude, and frequencies of (f-j) 5 kHz, (k-o) of 15 kHz, and (p-s) of 25 kHz, and a constant displacement voltage of 20 Vpp. Scale bar in (a): 100 μm . Size of AFM images in insets (r) and (s) is of 40 μm .

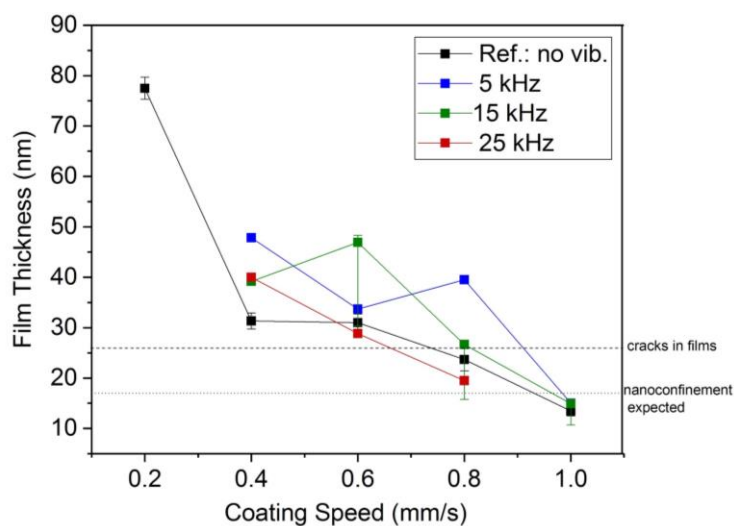


Figure 6.2: Thickness for the shearing conditions displayed in Figure 6.1.

The vibration appears to change the dynamic of the contact line, and therefore, the film formation time at the evaporation front. For the cases in which the film becomes thicker than the reference sample (Figure 6.1i and n), cracks appear. For the speed of 1 mm s^{-1} , the films appear to be thinner (Figure 6.1j and o) and present no visible (or less) cracks and also less variation of the crystallite width. Therefore, there seems to be a decrease in stick-and-slip for higher coating speeds (0.8 and 1.0 mm s^{-1}).

In Chapter 7, similar aspects are observed, and the mitigation or increase of the stick-and-slip phenomena at a receding contact line is explained with more detail. To obtain continuous crystalline growth for crystalline materials, low thickness films have to be

coupled with a slow receding contact line speed that does not present stick-and-slip phenomena. In this experiment, the only sample that seems to fulfill the requirements is the film in Figure 6.2o.

Figure 6.3 displays the mobilities for the higher shearing speeds ($> 0.6 \text{ mm s}^{-1}$) and the samples piezosheared at 15 kHz. In Figure 6.3g and h, there is significant mobility decrease. This is associated with the cracking of the crystalline ribbons. In Figure 6.3i, variations might occur, but the gate-voltage-dependence of the mobility makes it difficult to evaluate this. Effective saturation mobility, however, does not change.

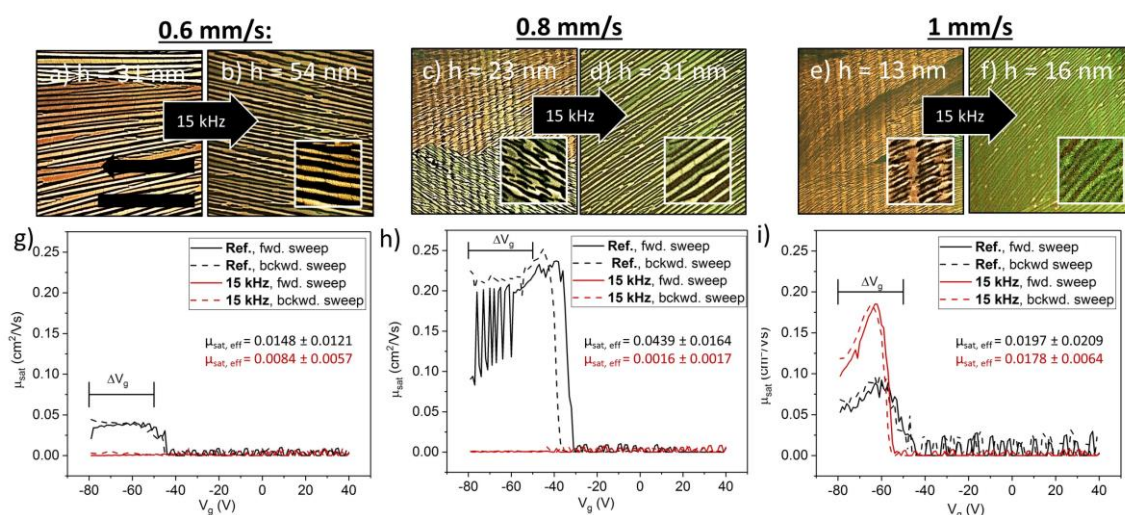


Figure 6.3: (a-f) Microscopy images from films sheared without vibration, and with vibration at 15 kHz; and (g-i) their corresponding charge carrier mobility as a function of the gate voltage. The effective saturation charge carrier mobility is also displayed. The black arrow represents the shearing direction. Scale bar in (a): 100 μm .

From Figure 6.3, it is possible to conclude that the charge carrier mobilities of such devices are rather low when compared to the devices of TIPS-pentacene:PS reported in Chapter 5. To continue the investigation of the piezoshearing of crystalline materials, the optimized blend of TIPS-pentacene:PS is used.

6.3 TIPS-pentacene blended with PS in Toluene: Better Performing Devices

The films fabricated in this section are the optimized films, as described in Chapter 5. The polystyrene with $M_w = 20 \text{ kDa}$ is used, and blended with TIPS-pentacene (8 mg ml⁻¹, 1:1 ratio of material), according to the description in section 5.2.1. The coating speed used is 2 mm s^{-1} .

The films are piezosheared with varying frequency and constant amplitude. A wide range of frequencies is tested (20 kHz - 100 kHz), and the displacement amplitude used is 8 Vpp. The results and the equivalent acceleration values from the vibration of the actuator are displayed in Figure 6.4. No apparent improvement in the film morphology is observed. The most significant effect observed is the appearance of stick-and-slip at 40 kHz and 85 kHz (Figs. 6.4c and f, respectively) and new nucleation sites at 80 kHz (Figure 6.4e). The stick-and-slip has been observed in the coating of the neat material, and films with more nucleation sites have also been observed in a few different frequency/ amplitude configurations. Both effects, however, tend to be detrimental for charge transport. If the stick-and-slip becomes too extreme, it might cause new nucleation sites, like the ones in Figure 6.4f.

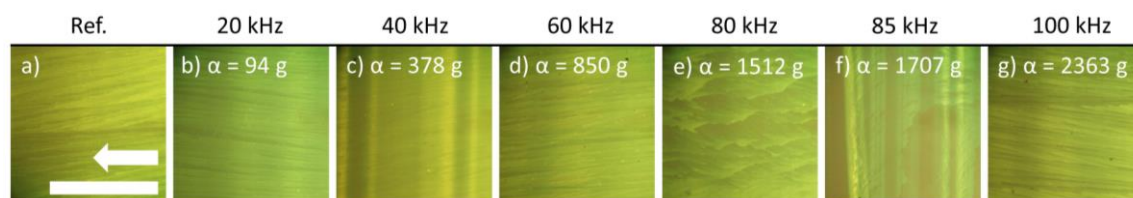


Figure 6.4: (a) Reference film for TIPS-pentacene:PS blend, and (b-g) piezosheared samples. The white arrow indicates the shearing direction. Scale bar: 100 μm .

Due to the complex TIPS-pentacene:PS phase separation, and that both materials respond differently to each vibration frequency/amplitude, a different crystalline semiconductor is chosen for the next study. In the following section, the small-molecule C₈-BTBT is studied, to test whether the vibration can enhance the coverage of the film.

6.4 Piezoshearing of C₈-BTBT

The small-molecule semiconductor C₈-BTBT has shown in the last years outstanding charge carrier mobility. Single-crystalline ribbon-like structures have shown charge carrier mobility with values of up to 8 cm² V⁻¹s⁻¹. [5] Although the ribbon-like films have high charge carrier mobility, the coverage of the substrate is not complete.

From the work of Haase et al., [5] it is possible to observe that ultrathin films of C₈-BTBT are only possible to be obtained with incomplete coverage of the substrate. In this work, they have thoroughly attempted to increase coverage by changing parameters, and the ribbon-like films remain the best morphology in terms of electrical performance. From the same work, it has been discovered that blending the semiconductor with the inert dielectric polystyrene improves coverage, and charge carrier mobility is increased up to 12 cm² V⁻¹s⁻¹. Janneck et al. suggest the evaporation of C₈-BTBT for epitaxial growth to improve film coverage. [262]

In this section on improving film coverage of the pristine C₈-BTBT material through the piezoshearing is attempted. We are convinced the vibration is able to stabilize the contact line and possibly redistribute the semiconductor into a continuous layer, instead of forming ribbon-like structures.

In this section, preliminary results for such a study are presented. The films are fabricated with the optimized shearing setup described in the work of Haase et al. Small changes regarding shearing speed and temperature are implemented due to weather conditions. A solution of 4 mg ml⁻¹ of C₈-BTBT in toluene is coated at 225 $\mu\text{m s}^{-1}$ at a temperature of 35 °C. A wide range of frequencies (5 kHz – 100 kHz) at several amplitudes is tested.

Figure 6.5 and Figure 6.6 display the preliminary results of such experiments. It is found that a beneficial effect is observed in the film morphology at a vibration frequency of 60 kHz. A microscopy image of the reference film is shown in Figure 6.5a, and a microscopy image of the piezosheared film is shown in Figure 6.5b. The black arrows in the image highlight some stick-and-slip features that appear in the film. In these regions, the film presents a region of a film with a larger coverage area. The work of Haase et al. describes that regions with better coverage directly impact the charge carrier mobility, but are challenging to obtain and occur only in some areas of a film.

As a consequence of the stick-and-slip, the thickness of the film can also increase. For the other vibrating parameters tested, the film can have quite thick regions where the stick-and-slip occurs, and this can be fairly detrimental to charge carrier mobility. However, for this vibration condition of 60 kHz, the stick-and-slip is very subtle and does not increase the thickness as much as to hinder charge carrier mobility significantly. In Figure 6.5c, the

effective saturation charge carrier mobilities for these samples are displayed.[12] Both samples are measured the day after fabrication, and four days after fabrication, after being stored in air. Effective mobility improved from $1.56 \pm 0.11 \text{ cm}^2 \text{ V}^{-1}\text{s}^{-1}$ to $2.11 \pm 0.29 \text{ cm}^2 \text{ V}^{-1}\text{s}^{-1}$ on day one, and from $0.19 \pm 0.03 \text{ cm}^2 \text{ V}^{-1}\text{s}^{-1}$ to $0.49 \pm 0.10 \text{ cm}^2 \text{ V}^{-1}\text{s}^{-1}$ on day four. The charge carrier mobility is expected to be significantly higher if the devices are measured immediately after fabrication.

Figure 6.6 displays AFM images of the reference sample and the piezosheared sample. It shows how the morphology changes in the area closer to the closer film regions in the piezosheared sample. The ribbons are narrower, have similar height as the reference sample, and there is material between the nanoribbons. The ribbon-like structure can still be observed in the closed-film region.

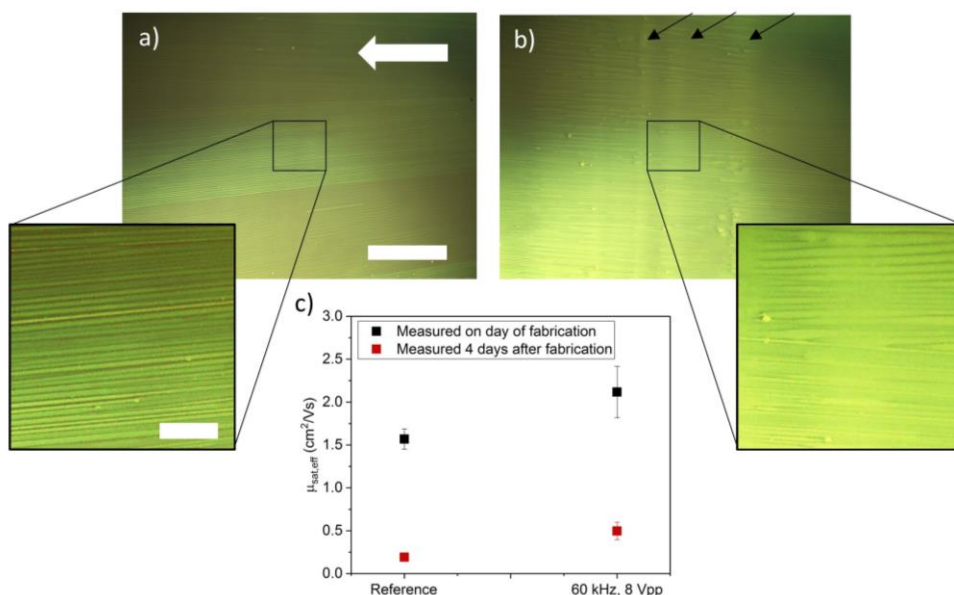


Figure 6.5: (a) Microscopy image of a reference film and (b) of a film piezosheared at a frequency of 60 kHz and a displacement of 8 Vpp. The white arrow indicates the shearing direction. (c) Effective saturation charge carrier mobility values are equivalent to film in (a) and (b). Scale bar in (a) is $500 \mu\text{m}$, and in the inset is $100 \mu\text{m}$.

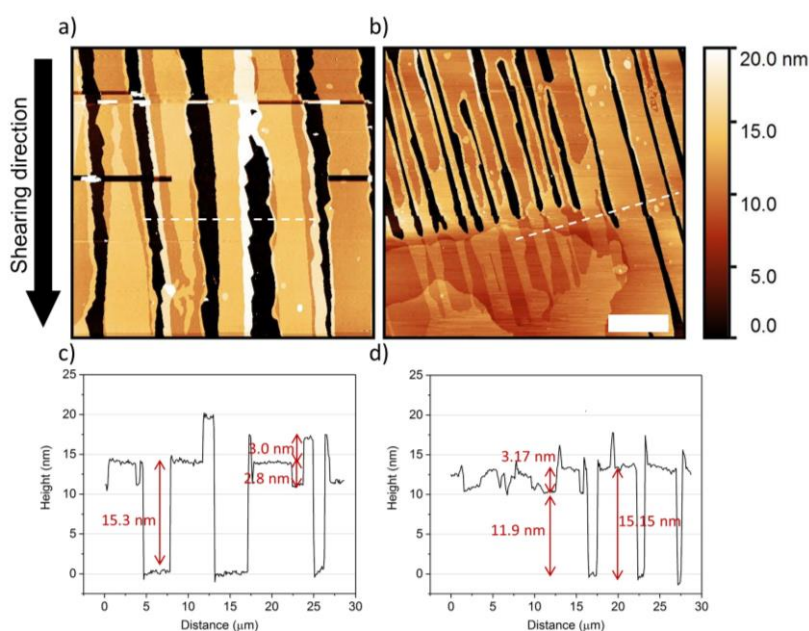


Figure 6.6: (a) Reference film for C₈-BTBT, and (b) piezosheared sample with at a frequency of 60 kHz, and an amplitude of 8 Vpp. The white arrow indicated the shearing speed. (c) and (d) are the cross-sections of the dashed white line indicated in (a) and (b), respectively. Scale bar: $100 \mu\text{m}$.

We believe that by fine-tuning the vibration frequencies, a stick-and-slip frequency can be established in a manner that the regions with increased coverage are neighboring, forming one complete film and that the thickness is still low enough not to hinder charge carrier mobility. The results for this setup are found to be repeatable, but the different substrate coverage is noted mainly towards the end of the coated film. We believe this occurs due to the smaller volume of liquid, or to the necessary building-up of the vibration in the meniscus. Often vibration in a liquid has been observed to require a certain number of pulses for the liquid to reach a stable condition.[179], [208], [209]

The results presented here are only preliminary, and thorough investigation would be needed to better understand the effect of the vibration in the crystallization process of C₈-BTBT.

6.5 Summary

In this chapter, the effect of the piezoshearing for crystalline small-molecules has been tested. From the three semiconductor systems tested, it seems as if the piezoshearing changes the dynamic of the meniscus and the contact line, but the stirring effect expected from the vibration is not easily distinguishable.

In general, the evaluation of data of the small-molecule materials is somewhat challenging. Due to the delicate procedure that is growing crystalline thin films, additional external factors can significantly influence film formation. Substrate size, semiconductor volume, blade height, and ambient conditions, such as temperature and humidity, are enough to change the morphology of the thin. Therefore, evaluating whether morphology differences are due to sample-to-sample and batch-to-batch differences or due to the piezoshearing is rather tricky.

Although further investigation can be done for the piezoshearing of small-molecule crystalline materials, the focus of this work has shifted towards polymeric semiconductors. As described in Chapter 5 and by the work of Haase et al., the solution shearing of the crystalline small-molecules seems unquestionably more straightforward and provides excellent results in terms of device performance.

Chapter 7

7 Addressing Stick-and-Slip Instabilities in solution-sheared films for OFET devices

7.1 Introduction

As discussed in Chapter 3, stick-and-slip instabilities are present in a wide range of solution systems and hinder uniformity issues. While undulations in semiconductor films so far seem not to have been identified as a major issue for device fabrication or performance, the formation of wires is a crippling issue for devices that require continuous films and significantly increase device-to-device performance variations.

In this chapter, a solution that stabilizes the contact line during the solution shearing is presented by subjecting the shearing blade to high-frequency vibrations. The critical speed for a particular solution concentration is shifted to higher values, resulting in the formation of complete films at shearing speeds that without vibrations would have consisted only of wires. It is hypothesized that the vibration introduces enough mechanical energy into the system to constantly “move” the contact line to a state closer to the equilibrium contact line position. In that sense, the additional mechanical energy can be thought of as helping the meniscus to overcome the energetic barrier for unpinning.

The work of Garoff and Decker that investigated a vibrating vertical meniscus provides a very similar description. They found that when introducing energy into the meniscus in the form of vibrations and above a certain threshold, it became possible to move the contact line to a lower energy state closer to the minimum global energy contact angle.[263] If enough energy is introduced into the meniscus to overcome the energy barriers that separate these metastable states, the contact line can be moved to a lower energy state, which would be closer to the intrinsic contact angle value. The intrinsic contact angle is considered to be the most stable contact angle, i.e., the position which presents the global energy minimum.[163], [266]

In addition to discussing a vertical contact line on a plane[263] or tube,[264] previous works have shown that using a large enough vibration amplitude can mitigate contact angle hysteresis in sessile drops.[265], [267] This means that vibrations can also

be used as a mechanical solution for measuring the most stable contact angle.[166], [265], [267]–[270] By studying methods through which one can obtain a contact angle with lower global equilibrium energy, Rodriguez-Valverde et al. have shown that the vibration of water droplets on smooth PDMS surfaces can move the contact line to a more stable contact angle, independent of the contact angle of the droplet before vibration. In these experiments, a sine wave function with the resonance frequency of the droplet is used, and the amplitude is shown not to be an essential factor, as long as it is over a specific minimum threshold value.[267] The work of Meiron et al. demonstrated that if enough kinetic energy is applied to a sessile drop via vibration, it is possible to depin and move the contact line to a position closer to the most stable contact angle, even on very rough surfaces.[166] Additionally, they have shown that if the applied amplitude is too high, the contact line of the drop is deformed.

Here the effect of the piezoshearing process is investigated; it can increase shearing speeds more than two times in comparison to the standard method. The shearing speed is raised by stabilization of the contact line that in turn decreases the stick-and-slip effect during the coating process. Through this method, the maximum coating speed, the film uniformity, and the charge carrier mobility of the films can be increased up to two orders of magnitude. In this study, the use of piezoshearing and its effects on solution-sheared films and OFETs of poly(diketopyrrolopyrrole-co-thiophene-co-thieno[3,2-b]thiophene-co-thiophene) (DPP4DE-TT) and poly [4-(4,4-dihexadecyl-4H-cyclopenta[1,2-b:5,4-b'] dithiophen-2-yl)- *alt* - [1,2,5] thiadiazolo[3,4-c] pyridine] (PCDTPT) is discussed. In addition, a more detailed explanation of why more uniform films are obtained is provided.

7.2 Device Fabrication

The polymer PCDTPT ($M_w = 75$ kDa, PDI = 2.5) was purchased from 1-Material and used without any further purification. The polymer DPP4DE-TT ($M_w = 108$ kDa, PDI = 6.8) was synthesized following a previously published procedure[19] and also used without any further purification. The polymer was received from the collaborating group Diao Research Group, at the University of Illinois at Urbana-Champaign.

All the polymer materials were dissolved at a concentration of 5 mg ml^{-1} in either chloroform (CF) or chlorobenzene (CB) and stirred at 500 min^{-1} at 25°C for at least two hours before shearing. The blade angle utilized was 8° with a gap of $20 \text{ }\mu\text{m}$ between the edge of the blade and the substrate. For bottom-gate, top-contact transistors, 50 nm thick Au electrodes were thermally evaporated onto the semiconductor to finish the devices.

The silicon substrates and the shearing blade were treated for hydrophobicity with octadecyltrimethoxysilane (ODTS).

Grazing incidence wide-angle X-ray scattering measurements were performed at ID 03 surface diffraction beamline of the European synchrotron radiation facility (ESRF), Grenoble. The beam energy for the measurements was 12 keV , and a point detector was used to capture the scattering signal. Two-dimensional reciprocal maps were obtained by stitching together the point detector signal at all the scattering angles. The grazing incidence angle for all measurements was 0.12° , and the beam exposure time onto the samples was around 600 seconds. The 2D scattering data were analyzed using the WxDiff⁶⁸ software.

The PCDTPT devices were measured under ambient conditions, and the DPP4DE-TT devices were measured in air, but under a constant flow of nitrogen.

The menisci during solution shearing were imaged using a camera IDT NX4-S1, at a frame rate of 800 FPS, 10x magnification and frame size of 760×320 pixels. The circles were fit to the menisci using the “Fit Circle” algorithm from Fiji, ImageJ. Fiji was also

used to measure the length of the meniscus beyond the fitted circle. The imaging of the meniscus was done with the collaboration of Dr. Xuegeng Yang, from the Institute of Fluid dynamics, at the Helmholtz-Zentrum Dresden-Rossendorf (HZDR).

7.3 The Effect of Piezoshearing on Stick-and-Slip Instabilities

For the following discussion, the “critical speed” is first established. It is the lowest speed for which the stick-and-slip instabilities cause the formation of wires instead of a continuous film.[146] In these experiments, a solution concentration of 5 mg ml^{-1} of the polymer DPP4DE-TT (Figure 7.2u) in chloroform is used, and the films are solution-sheared at room temperature.

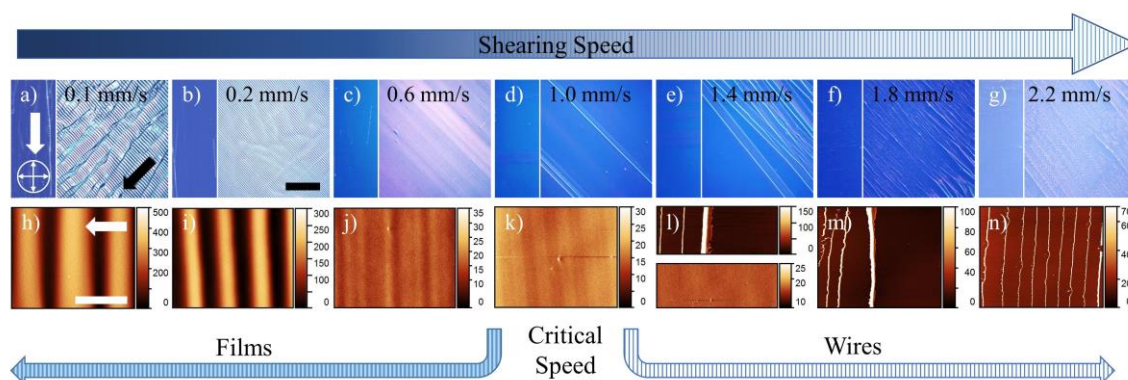


Figure 7.1: (a-g) Cross-polarized optical microscopy (CPOM) images of films of DPP4DE-TT in CF (5 mg ml^{-1}), coated at different shearing speeds. Black and white arrows in (a) indicate the solution shearing direction, and the crossed arrows indicate the orientation of the crossed polarizers – these also apply to (a-g). Scale bar in (b): $500 \mu\text{m}$. (h-n) Atomic force microscopy images of the surface of the respective films. Scale bar in (h): $40 \mu\text{m}$. Color bar at the side of AFM images have values given in nanometers. Image reproduced from Ref. [271].

7.3.1 Increasing Shearing Speed

The piezoshearing is used for several values of coating speed and voltage displacement to test whether it is possible to mitigate such instabilities. Figure 7.1 shows the results of piezoshearing deposition of DPP4DE-TT at different coating speeds using different applied voltages for the vibration. Films coated using the conventional solution shearing method are termed here “Reference”. AFM images of the various films are shown in Figure 7.7. The critical speed (transition speed from film to wire) of the DPP4DE-TT polymer in CF is 1 mm s^{-1} and can be more than doubled to over 2 mm s^{-1} when utilizing the piezoshearing. At speeds of 2.2 mm s^{-1} (Figure 7.2d), which would only provide wires without vibrations, a continuous uniform film can be deposited (Figure 7.2h). The films are challenging to image through cross-polarized microscopy due to their very low thickness (down to 7 nm ; see AFM results below for evidence that films are indeed formed), which is unusual for sheared films over an ODTs-treated substrate. The insets for Figure 7.2h and 7.5p are optical images of these films.

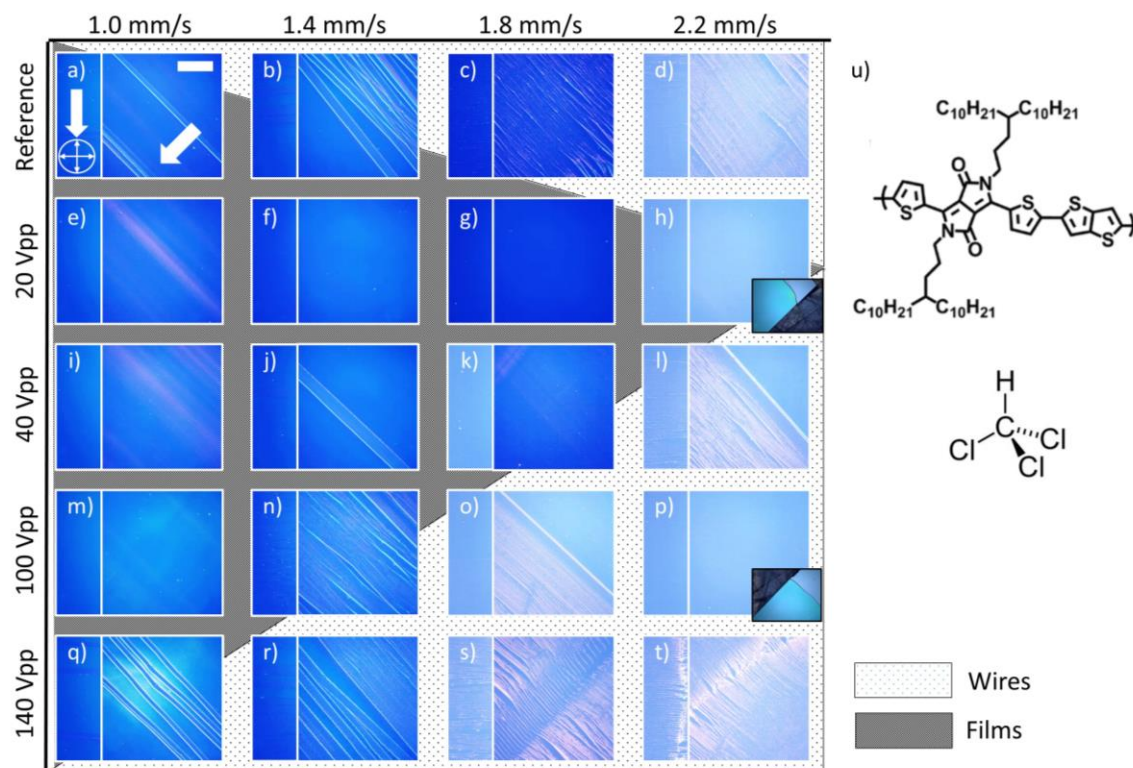


Figure 7.2: (a-t) CPOM diagram showing films at different shearing speeds and different vibration displacements (constant frequency of 1 kHz). The insets in (h) and (p) are non-polarized images that show the coating-start region and which are provided to illustrate that despite the uniform colors in (h) and (p) there are indeed thin films. White arrows in (a) indicate the solution shearing direction, and the crossed arrows indicate the orientation of the crossed polarizers. Scale bar: 500 μm . (u) Chemical structure of DPP4DE-TT and chloroform. Image reproduced from Ref. [271].

The piezoshearing method is also applied to the polymer PCDTPT (Figure 7.3u) to see if our approach can be applied to polymer semiconductors more generally. The solution shearing of PCDTPT is performed under two different sets of conditions: i) in chloroform at room temperature and ii) in chlorobenzene at a substrate temperature of 100 $^{\circ}\text{C}$. Although the latter conditions resulted in devices with the higher charge carrier mobilities, the experiments with chloroform are included in our discussion to have a direct comparison to the experiments using DPP4DE-TT.

For the shearing of the PCDTPT/CF solution (Figure 7.3), the critical speed is close to 1 mm s^{-1} (Figure 7.3a), which is similar to DPP4DE-TT. The vibration displacement required to yield continuous films is, however, higher than for the DPP4DE-TT solution. This is discussed further in this chapter.

For the PCDTPT/CB sheared solution, an improvement in film coverage is observed (at speeds of 1.2 mm s^{-1} and 1.4 mm s^{-1}) when the displacement of vibration is large enough. Here the critical speed is slightly higher, at 1.2 mm s^{-1} (Figure 7.4b). Moreover, the speed gap from the onset of wire occurrence to a wires-only morphology is smaller, meaning the system appears to be more unstable than the CF system. The different capillary characteristics of both systems are likely the reason for this. For the films with speed above the critical speed, full substrate coverage requires a higher displacement when increasing shearing speed. The gradual increase of displacement is shown in Figure 7.3 for the PCDTPT and in a further discussion for DPP4DE-TT. It shows that the higher the coating speed, the higher is the voltage necessary to mitigate the stick-and-slip completely.

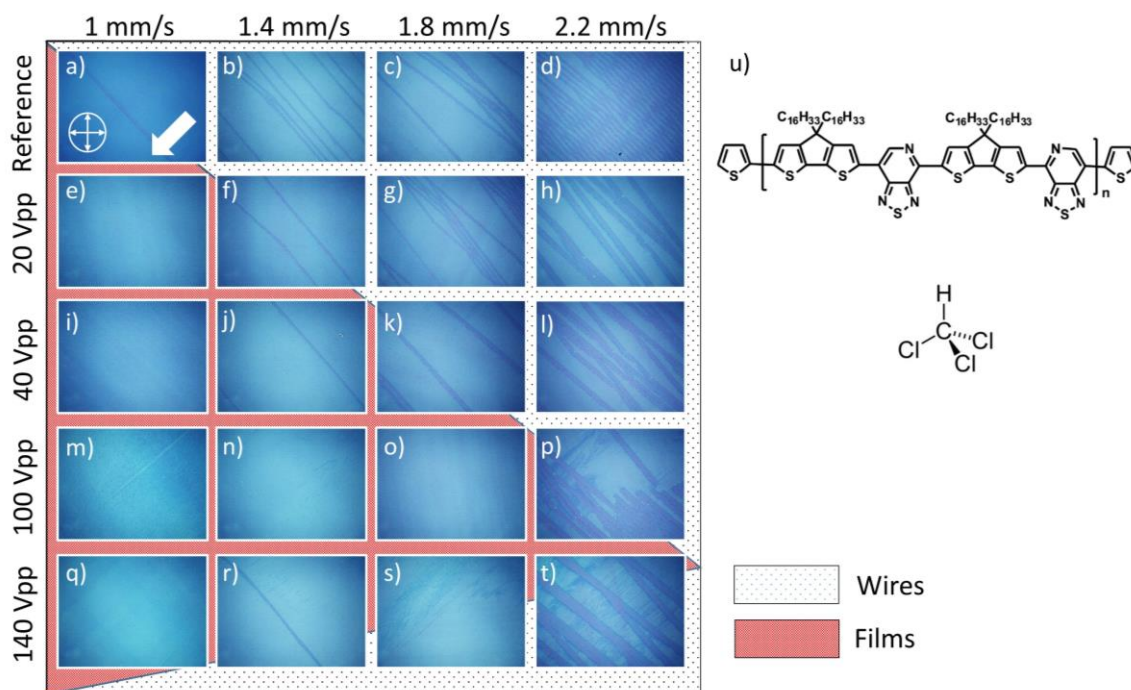


Figure 7.3: CPOM diagram showing films at different shearing speeds and different vibration displacements (constant frequency of 1 kHz). The white arrow in (a) indicates the solution shearing direction, and the crossed arrows indicate the orientation of the crossed polarizers. Scale bar: 500 μm . (u) Chemical structure of PCDTPT. Image reproduced from Ref. [271].

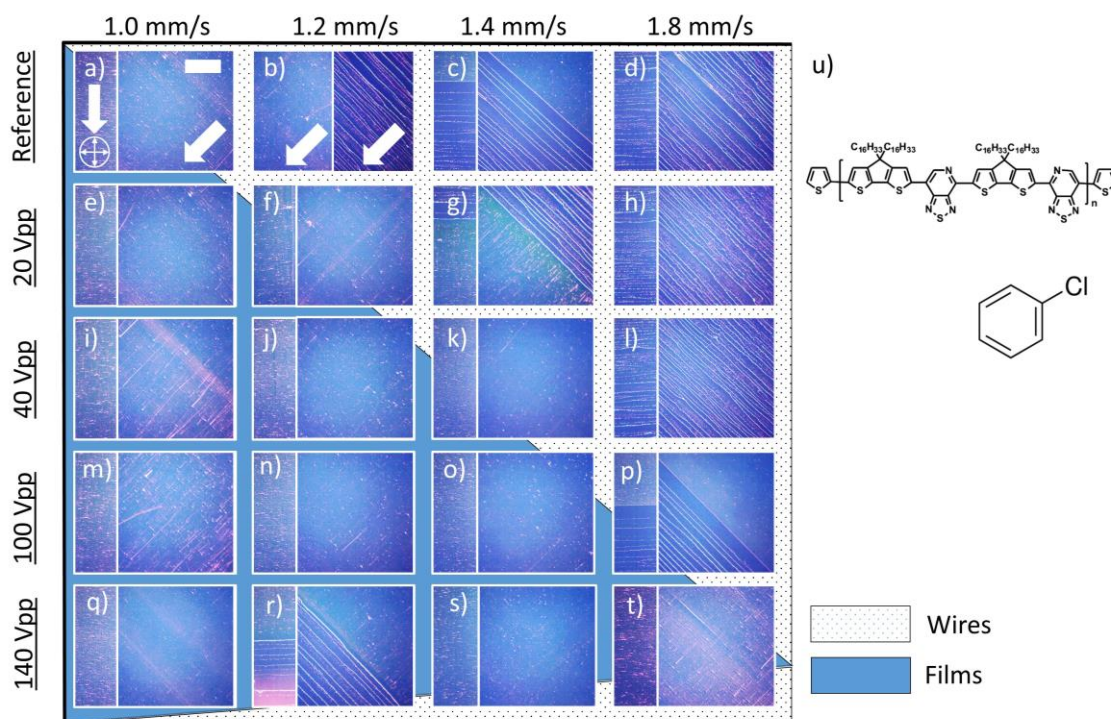


Figure 7.4: (a-t) Schematic of different shearing speeds and piezoshearing displacement amplitudes for the solution of (u) PCDTPT and chlorobenzene, coated at 100 $^{\circ}\text{C}$. White arrows in (a) indicate the solution shearing direction, and the crossed arrows indicate the orientation of the crossed polarizers. The white arrows in the image (b) indicate the coating direction, and that both wire and film morphology are observed at this shearing condition. Scale bar: 500 μm . Image reproduced from Ref. [271].

7.3.2 Thin-film Characterization

When utilizing piezoshearing, ultra-low film thicknesses are attainable, for example, DPP4DE-TT films solution sheared at 2.2 mm s^{-1} with a vibration displacement of 20 Vpp reached thicknesses of down to 7 nm. In contrast, for films fabricated without vibration, the thinnest films are around 25 nm (Figure 7.5a). This is a noticeable fact, considering that so far only films thicker than 20 nm have been reported for D-A polymers coated on ODTS substrates.[52], [54], [112], [134], [146] For the piezoshearing of PCDTPT/CF, the lowest thicknesses obtained for a complete film is again 7 nm, while for solution shearing without the vibrations, the minimum thickness is 21 nm (Figure 7.5b). The films realized by piezoshearing are some of the thinnest films reported for D-A materials for OFET devices and show that our method can successfully improve the adherence of polymer thin films to hydrophobic surfaces. It is worth pointing out that such a reduction in film thickness can not only improve contact resistance,[272]–[276] but also represents a significant degree of material savings. Mainly modern D-A polymers can still not easily be synthesized in large quantities and therefore represent a significant portion of the total costs of the electronic devices that they are employed in. Reducing the material volume that can generate a continuous film without a reduction in electrical performance is thus a significant cost saving factor.

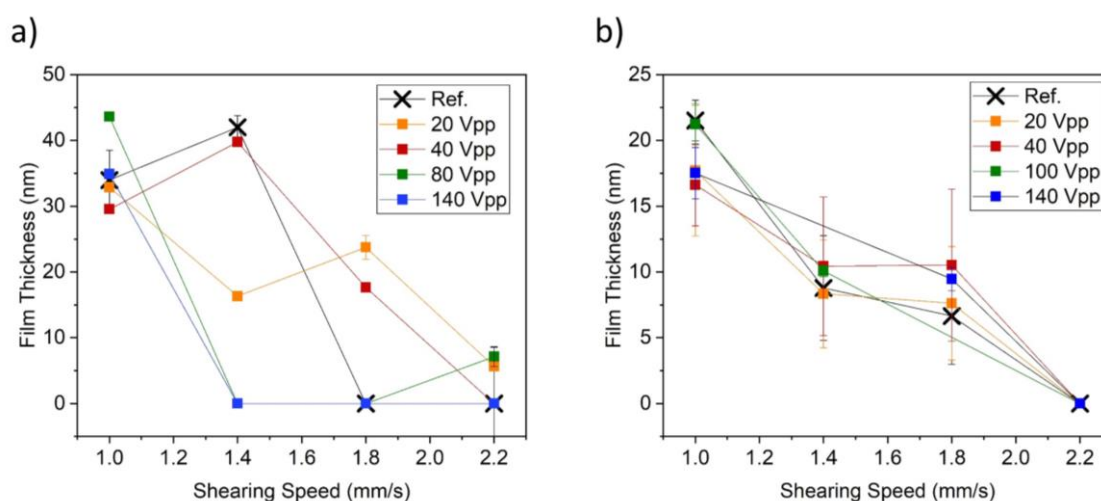


Figure 7.5: Film thickness for (a) DPP4DE-TT/CF solution and for (b) PCDTPT/CF solution, both solution-sheared at room temperature. Samples that consist mainly of wires are designated as thickness “zero”. Image reproduced from Ref. [271].

In the case of the very thin films of DPP4DE-TT (thickness $\sim 7 \text{ nm}$), such as the one coated at 2.2 mm s^{-1} (Figure 7.2h), it is possible to observe small holes in the film that reach down to the substrate level (Figure 7.7). From Figure 7.5a and 7.6, it can be concluded that the film thickness as measured from a scratch is similar to the apparent depth of gaps in the film. This means that although the film is completely covered on the macroscale, it might still exhibit some porosity on the microscale.

Due to incomplete coverage of the samples with wires, it is difficult to compare the evaporation rate of the films with and without piezoshearing. It is possible that the solute volume deposited is constant, but better distributed for continuous films.

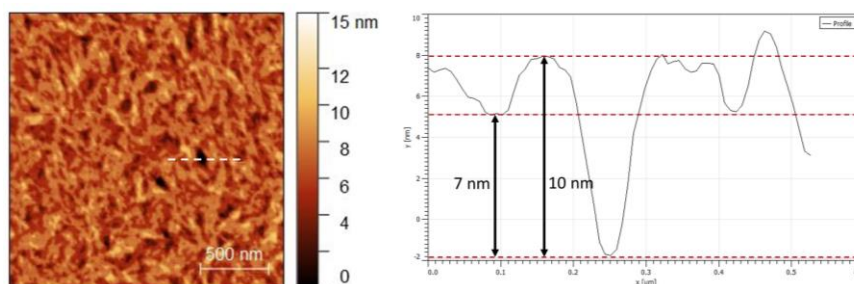


Figure 7.6: The surface of a piezosheared film at 2.2 mm s^{-1} and 20 Vpp (left) and cross-section of what seems to be a gap to the substrate (right). Image reproduced from Ref. [271].

From Figure 7.6 and Figure 7.7h, a detailed view of the surface of the films can be seen. Not only is the formation of wires suppressed by piezoshearing, but the degree of polymer agglomeration in fibrils seems to decrease when applying piezoshearing. From the AFM images (Figure 7.7f-h), the piezosheared samples do not present significant height variations in the deposit as the ones sheared in the conventional fashion (Figure 7.7b-d) and display less fibril formation, as observed from phase images in Figure 7.8. We attribute such fibril formation in the wires to the longer time span the polymer has to aggregate at the contact line while the latter is pinned. The lack of fibril formation for the piezosheared films is consistent with our hypothesis that piezoshearing prevents the contact line from getting pinned.

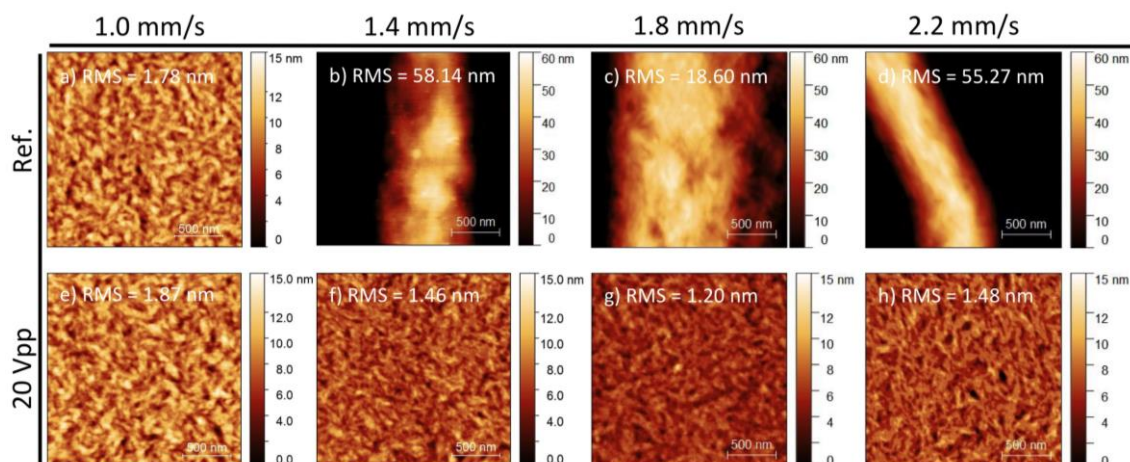


Figure 7.7: AFM topography images of (a-d) sheared samples and (e-h) piezosheared samples of DPP4DE-TT. Image reproduced from Ref. [271].

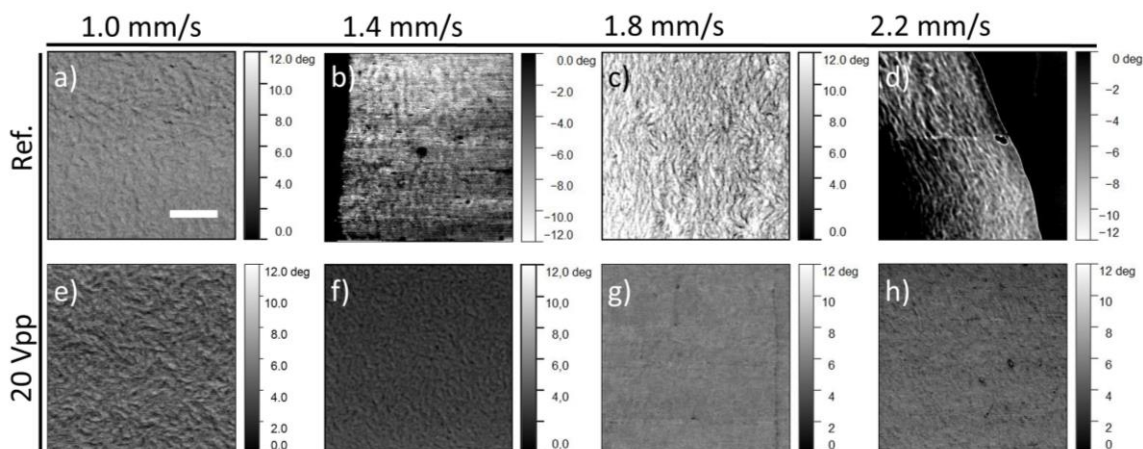


Figure 7.8: Phase images of (a-d) sheared samples and (e-h) piezosheared samples. These phase images are the ones corresponding to the z-axis images in Figure 5 in the main text. Scale bar in (a): 500 nm. Image reproduced from Ref. [271].

To check for changes in the molecular packing, grazing incidence wide-angle X-ray Scattering (GIWAXS) was performed in the parallel and perpendicular to the shearing direction for samples of DPP4DE-TT sheared at 1.4 mm s^{-1} (above the critical speed). From Figure 7.9 it is shown that all samples present a clear peak at 1.74 \AA^{-1} (corresponding to real space distance of 3.61 \AA), which can be attributed to the π - π stacking of the polymer backbones, something common in conjugated polymers.[64], [277] From this finding it can be concluded that the piezoshearing does not change the π - π stacking distance of the polymer backbones and thus does likely not impact the polymer chain packing on the nanoscale.

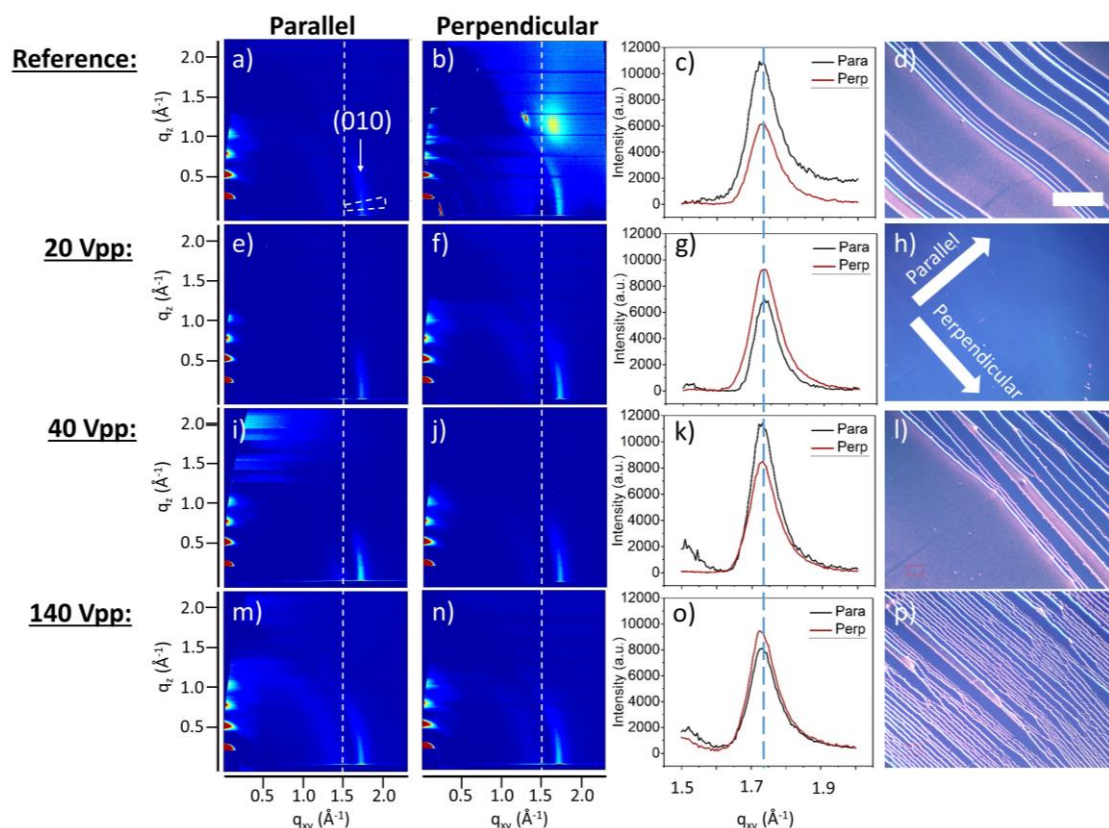


Figure 7.9: GIWAXS images with incident beam (a, e, i, m) parallel to coating direction, (b, f, j, n) perpendicular to coating direction, (c, g, k, o) integrated cake cuts, and (d, h, l, p) CPOM images for DPP4DE-TT coated at 1.4 mm s^{-1} . The cake cuts are obtained through integration of a 5° cake cut of the 2D image, from $1.5 \text{ \AA}^{-1} < q_{xy} < 2 \text{ \AA}^{-1}$ and from angles $82^\circ < \chi < 87^\circ$, as indicated by the white dashed line cake segment in (a). The vertical white dashed lines serve as a guide to the eye for comparison of the images. For these images, the ODTS peak (around 1.5 \AA^{-1}) is removed by subtracting the GIWAXS image of a sample with only ODTS on its surface. The blue dashed line (c, g, k, o) indicates where $q_{xy} = 1.74 \text{ \AA}^{-1}$ is. It can be observed from (d, h, l, p) that the coverage of the substrate is different; therefore the amount of material scanned by the beam varies, and the intensities in (c, g, k, o) cannot be directly compared. The directions parallel and perpendicular to the shearing direction are defined in (h) and valid for figures (d, h, l, p). Scale bar in (d): 500 \mu m . Image reproduced from Ref. [271].

7.3.3 Electrical Characterization

In Figure 7.10, the effective charge carrier mobility values, as suggested by Choi et al.,[12] are presented for devices where the channel direction is parallel to the shearing direction, as schematically shown in Figure 7.10d, with the channel parallel to the coating direction, with and without piezoshearing. The values are color-coded in mobility ranges to simplify the observation of a large quantity of data more efficiently. The absolute values for each coating condition are provided in Tables A.1, A.2, and A.3. For the calculation of

average charge carrier mobility values, around 5 devices are randomly chosen and measured. Both directions, parallel and perpendicular to the shearing direction, are characterized, and the values averaged. Therefore, the charge carrier mobility takes into account both the quality of molecular packing of the films and the coverage of the device's channels.

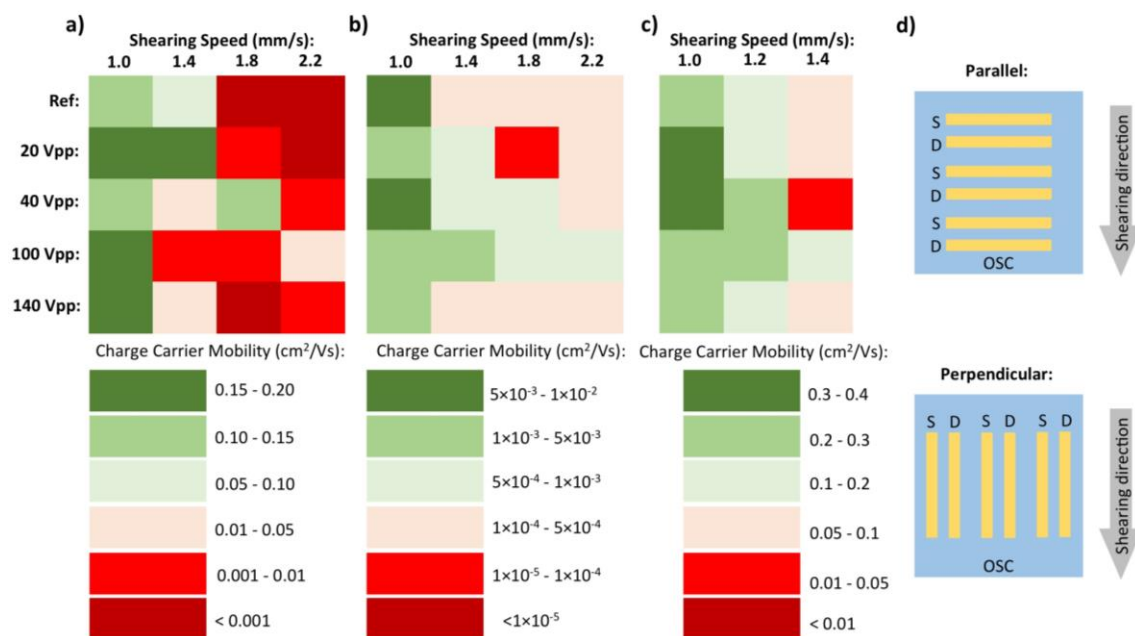


Figure 7.10: Charge carrier mobility values for the experiments with (a) DPP4DE-TT/CF, (b) PCDTPT/CF coated at room temperature, and (c) PCDTPT/CB coated at 100 °C. (d) Schematic of OFET electrodes in relation to the solution shearing direction. Image reproduced from Ref. [271].

Due to significantly better coverage of the substrates for the films above the critical speed, mobility along the shearing direction increases significantly. For example, from $4 \times 10^{-4} \text{ cm}^2 \text{ V}^{-1} \text{ s}^{-1}$ to $1.4 \times 10^{-1} \text{ cm}^2 \text{ V}^{-1} \text{ s}^{-1}$ at a coating speed of 1.8 mm s^{-1} when applying 40 Vpp to the piezo crystal (Figure 7.10a). In Figure 7.10, mobility improvements for both semiconductor materials are observed, in all setups tested. In general, the charge carrier mobility values with vibration are better than the ones without, until the point where the vibration amplitude is too high and makes the contact line more unstable, hindering solute deposition.

In Figure 7.12, the typical transfer curves of the DPP4DE-TT-based OFET devices are shown. Due to the occurrence of varying degrees of gate-voltage-dependent mobility, effective mobility as defined in the work of Choi et al. is reported.[12] PCDTPT OFET performance data for both coating setups can be seen in Figure 7.13 and Figure 7.14.

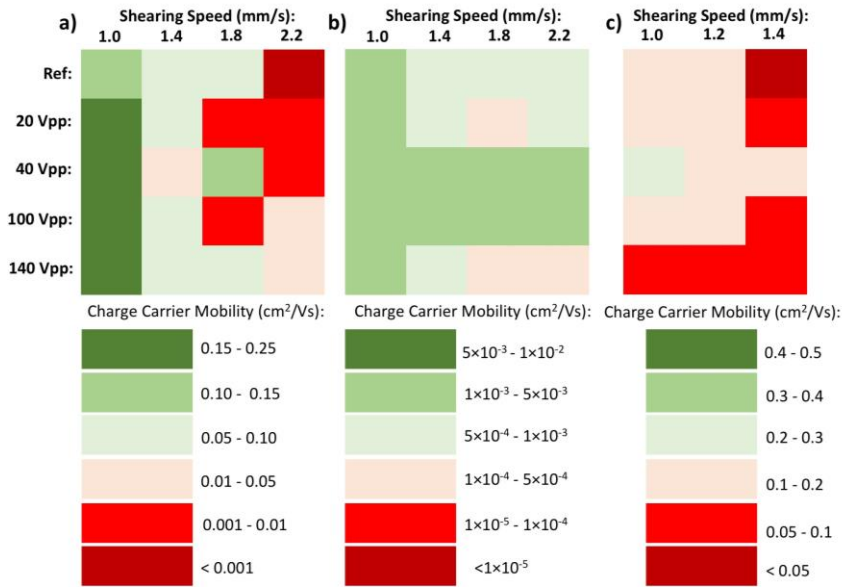


Figure 7.11: Effective charge carrier mobility for devices with transistors’ active channel perpendicular to the shearing direction. Shear coated from (a) DPP4DE-TT /CF at room temperature; (b) PCDTPT/CF at room temperature; (c) PCDTPT/CB coated at 100 °C. Image reproduced from Ref. [271].

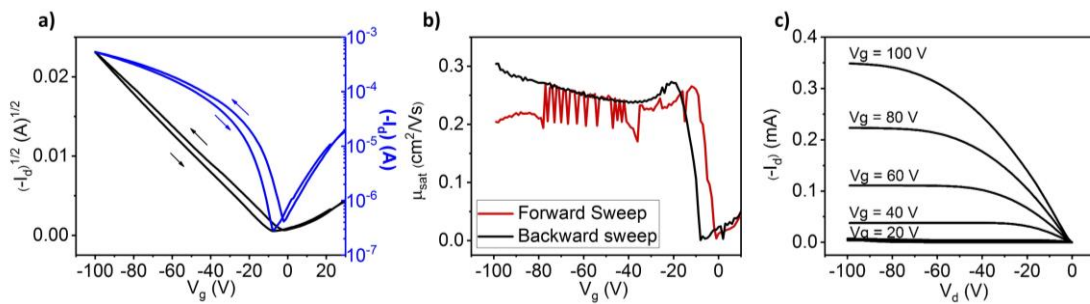


Figure 7.12: (a) Transfer curves, (b) mobility as a function of V_g, and (c) output curves for a typical device coated from the polymer DPP4DE-TT. Image reproduced from Ref. [271].

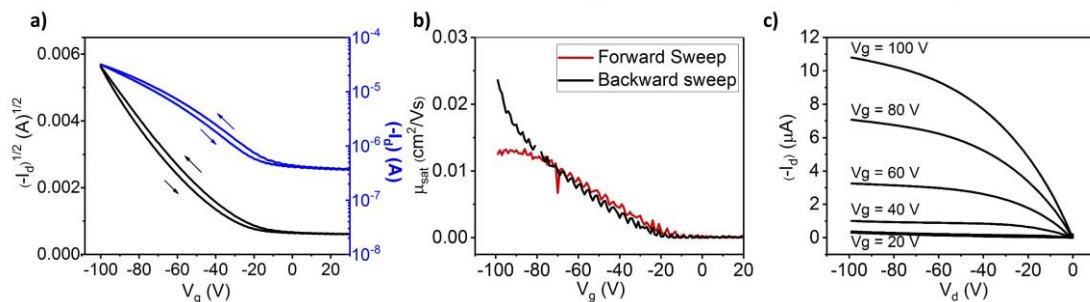


Figure 7.13: (a) Transfer curves, (b) saturation mobility dependent on V_g, and (c) output curves for a typical device coated from the solution of PCDTPT/CF at room temperature. Image reproduced from Ref. [271].

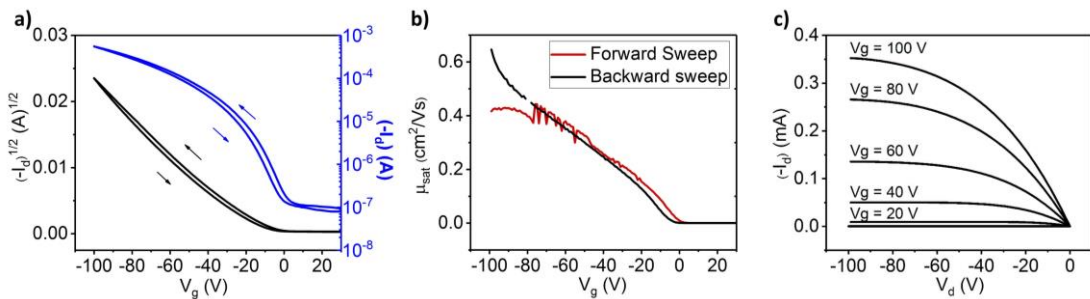


Figure 7.14: (a) Transfer curves, (b) saturation mobility dependent on V_g, and (c) output curves for a typical device coated from PCDTPT/CB. Image reproduced from Ref. [271].

In the case of charge carrier mobility for devices with the channel perpendicular to the shearing direction, some improvements are observed in Figure 7.11. It is worth pointing out here that for the mobility of devices with the channel in the perpendicular direction, the total electrode width of the device is used for calculation, and not only the effective electrode width as dictated by the semiconductor wires. Although the piezosheared films Figure 7.7(f-h) do not exhibit the fibril morphology Figure 7.7(b-d) that in other cases represents an electrically favorable morphology,[146] the better coverage of the film still produces higher mobility values when considering the full channel width of a device.

7.4 Energy Barriers and Overcoming them with Vibration

To gather visual evidence for the absence of stick-and-slip motion when using the piezoshearing conditions that lead to more continuous films, we attempt to image the stick-and-slip of the meniscus with a microscope camera setup (video S1 in Supporting Information for Ref. [271]) and are able to observe an evident variation in the length of the meniscus. Video S1 shows the meniscus during the shearing of a DPP4DE-TT film with a speed of 1.4 mm s^{-1} (0.4 mm s^{-1} over the critical speed). The white circle approximates the equilibrium meniscus position in all images to serve as a guide to the eye. It can be seen that during the “stick” position, the meniscus is prolonged beyond the white circle. A frame from video S1 is displayed in Figure 7.15c. The white line depicts the meniscus front at a position closer to equilibrium as is observed in the video, and the dashed red line shows the stretching of the meniscus during the sticking phase. When the meniscus “slips” it goes back to overlapping the marked white circle.

For a piezoshearing condition that leads to a continuous film, imaged at the same frame rate, no variation in the shape or length of the meniscus is detected (video S2) within the resolution of the data. This indicates that there is either no stick-and-slip or that it is either too fast and/or happens on a much smaller length scale than what can be resolved by the camera. In order to quantify the variation of the position of the meniscus, the distance D (Figure 7.15c) to which the meniscus stretches beyond the stable meniscus position is measured to compare samples sheared with and without vibration. From Figure 7.15a, it can be seen that the so-defined length of the meniscus increases during the pinning stage (stick stage) and goes back to zero when the slip occurs. In Figure 7.15b, there is little or almost no variation in the meniscus length.

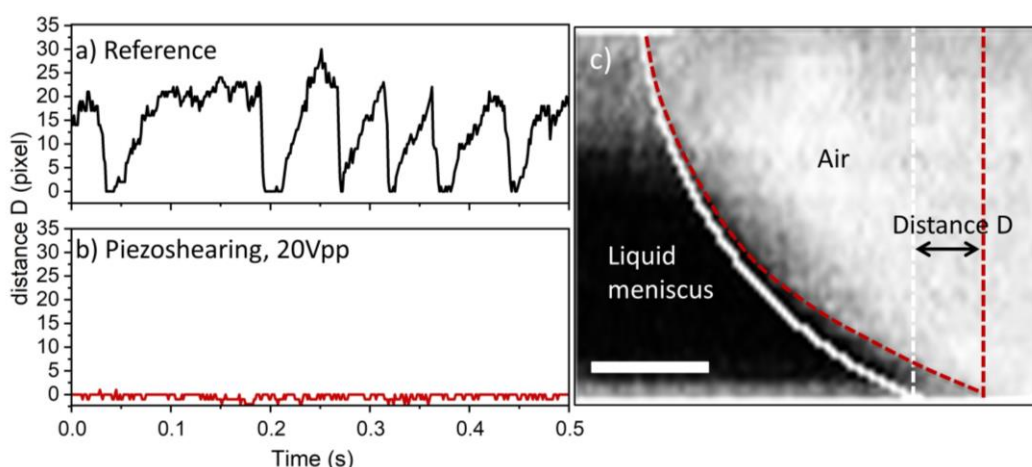


Figure 7.15: (a) Progress of variation of meniscus edge (distance D in pixels) with shearing over critical speed (1.4 mm s^{-1}); (b) progress of meniscus edge when using piezoshearing. (c) Image of meniscus illustrating how the distance D is calculated; the image is taken during a sticking stage. Scale bar in (c): $40 \mu\text{m}$. Image reproduced from Ref. [271].

Next, an experiment in which the displacement of the piezoshearing is gradually increased for a DPP4DE-TT/CF ink is performed, to see whether there is an equally gradual decrease in the occurrence of stick-and-slip instabilities. The displacement voltages used in this experiment are much lower than the voltages used for Figure 7.2. This is done so that the minimum voltage required to obtain a continuous film can be resolved in finer detail. In Figure 7.16, one can see that for constant speed, the higher the amplitude of the vibration, the more likely it is to obtain a film free of stick-and-slip instabilities. This is also observed for a drop of drying semiconductor under a static, non-moving, but vibrating coating blade (Figure 7.17 and Figure 7.18). A too low displacement (~ 2 Vpp) seems not to be enough to mitigate the stick-and-slip, and a too-high displacement (~ 40 Vpp) seems to hinder any pinning of the contact line, hampering any deposition. This suggests that there might be threshold energy values that need to be overcome to mitigate the stick-and-slip and formation of wires, similar to what is described when moving the contact angle for a sessile drop or a static meniscus with vibration.[263], [267] This is in agreement with the work of Decker and Garoff,[263] which relates the moving of the contact line to overcoming a local energy barrier to a lower energy state. The energy introduced by the vibrations is proportional to the square of the vibration amplitude (in our case, the piezo crystal's displacement), and thus overcoming a larger energy barrier requires larger vibration amplitudes.

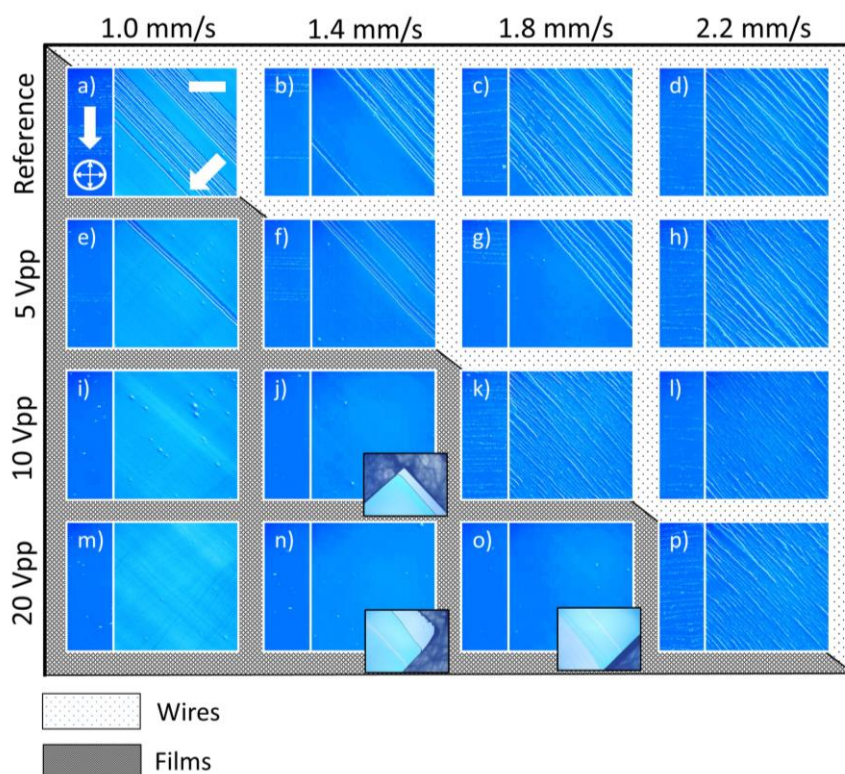


Figure 7.16: (a-p) Coating of DPP4DE-TT at different speeds with increasing vibration displacements, but in a reduced range and with finer steps than in Figure 7.2. White arrows in (a) indicate the solution shearing direction, and the crossed arrows indicate the orientation of the crossed polarizers. Insets in (j), (n), and (o) display optical images of the ultrathin films. Image reproduced from Ref. [271].

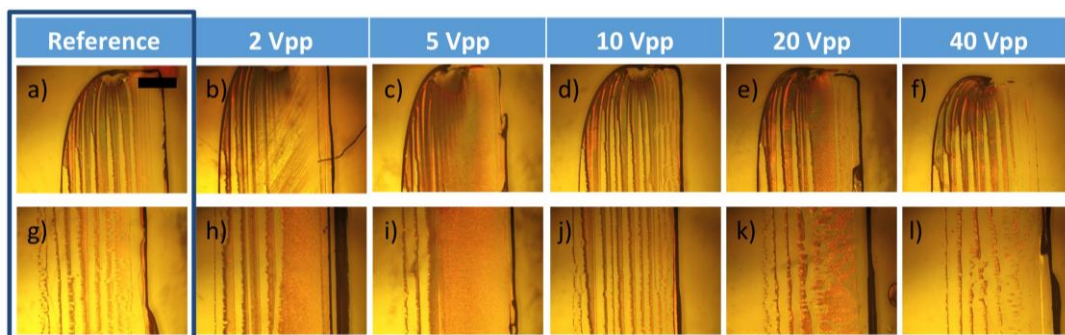


Figure 7.17: Experiment of a drop of DPP4DE-TT /CF placed under a static blade with and without vibration. (a, g): Drop without any vibration; (b, h) Vibration of 1 kHz with a displacement of 2Vpp; (c, i): 5 Vpp; (d, j): 10 Vpp; (e, k): 20 Vpp and (f, l): 40 Vpp. Scale bar: 500 μm . Image reproduced from Ref. [271].

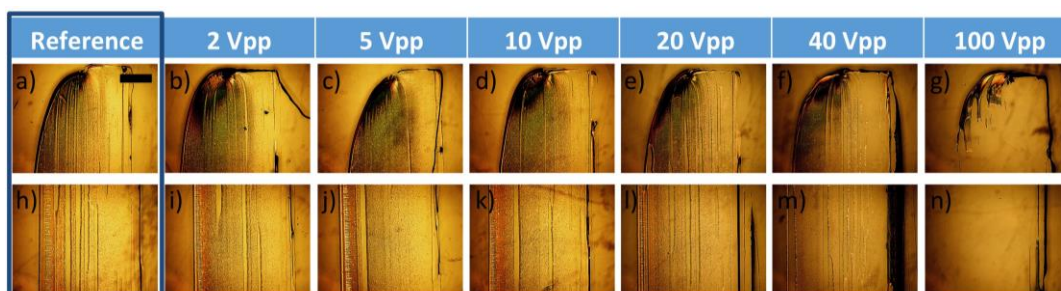


Figure 7.18: Experiment of a drop of PCDTPT/CF placed under a static blade with and without vibration. (a, h) Drop without any vibration; (b, i) Vibration of 1 kHz with a displacement of 2 Vpp; (c, j): 5 Vpp; (d, k): 10 Vpp; (e, l): 20 Vpp, (f, m): 40 Vpp, and (g, n): 100 Vpp. Scale bar: 500 μm . Image reproduced from Ref. [271].

It can also be observed that the higher the coating speed, the larger the displacement necessary to obtain a continuous film. Several works associate pinning at metastable positions and contact angle hysteresis to a local energy barrier model. These explain the metastable pinning behavior by analogy to the metastable states observed in thermal excitation.[162]–[164], [169], [263] Decker and Garoff[263] state that the potential barriers separating the metastable meniscus states depend on their distance from the global equilibrium position and become larger the closer they are to that global equilibrium position. However, in our situation, the moving meniscus represents a force (energy) that continually acts to stretch the meniscus further away from the equilibrium position, and this energy is increasing with the shearing speed. Therefore, at higher shearing speeds (e.g., 2.2 mm s^{-1}), the meniscus without vibrations is expected to be at a higher energy state since it is stretched out further than at lower speeds (e.g., 1.0 mm s^{-1}) due to viscous forces.[146] In order to relax to positions near the equilibrium (which is required for constant film deposition), the meniscus requires sufficient additional energy (see Figure 7.19 illustrating this hypothesis) to overcome the metastable states separating it from the equilibrium. At higher shearing speeds, the force that prevents this relaxation is, however also increasing, depleting the kinetic energy required to rapidly move from the starting meniscus position to the equilibrium position. This is, in our opinion, the reason why for an increasing shearing speed, an ever-increasing amount of external mechanical energy (vibrations) is needed to allow the meniscus to move rapidly enough to approach equilibrium while the blade motion is constantly countering that relaxation motion. Therefore, we find that in order to obtain continuous films, higher displacements are needed for increased shearing speeds.

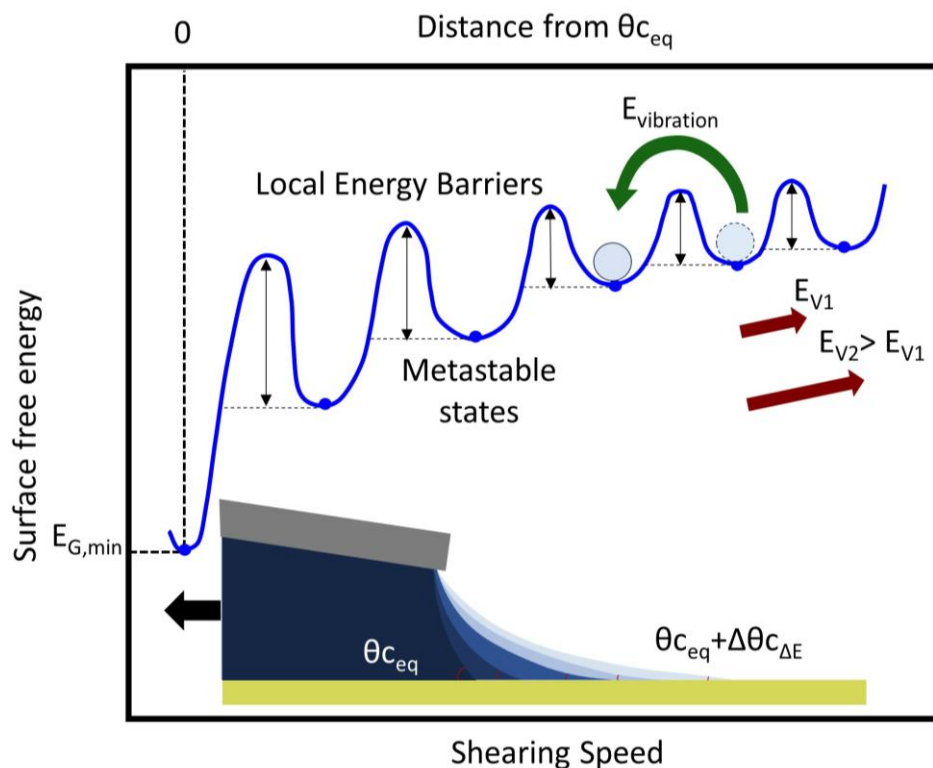


Figure 7.19: Schematic of a local energy barrier model for the shearing of OSC over the critical speed. The energy introduced by the vibration - $E_{\text{vibration}}$ - is counteracted by the kinetic energy of the moving blade - represented by E_{v1} and E_{v2} . Image reproduced from Ref. [271].

Regarding heating of the system, the possibility of continuous films due to a heating gradient induced by the piezo crystal is disregarded. The temperature of the blade when applying the frequency and amplitude parameters used in this work on the piezo crystal is measured and did not rise above room temperature.

During the initial stages of this study, the possibility of continuous films to be caused by Marangoni concentration flows induced by recirculation of the solute through the vibration was considered. One of the traces of such flow is very uniform instead of coffee rings.[86] Because the pinning de-pinning cycle of the meniscus appears to change significantly, the possibility is also discounted as the main reason for the ultrathin films.

7.5 Acceleration Threshold for Mitigating Stick-and-slip

This work demonstrates that it is possible to increase the shearing speed of films sheared for different materials, in different solvents and different shearing temperatures. However, the minimum vibration amplitude seems to vary from system to system. This can be explained by different inhomogeneities at the contact line, causing pinning at metastable states to be triggered under different shearing conditions.

Such inhomogeneities can arise from non-uniform evaporation at the contact line,[162], [163] which is not uncommon for polymeric solutions due to agglomeration.[137], [144], [278] Due to concentration and viscosity increase in localized regions, “fingers” can emerge, acting as localized defects and anchoring the contact line. Protuberances originated from a deformed contact line are observed in the wires deposited in Figure 7.20.[278] In the case of our polymeric system, the contact angle hysteresis during the coating of the polymer solution can be quite broad, considering that the concentration at the contact line changes with evaporation, and more defects tend to be formed there.

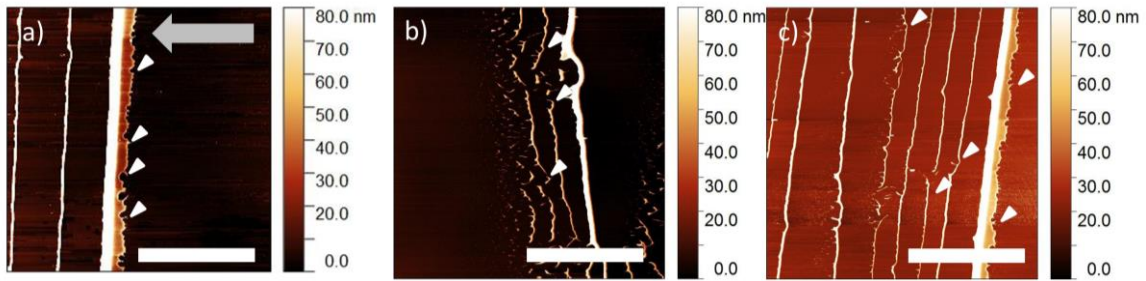


Figure 7.20: Inhomogeneities and fingering instabilities along the contact line for sheared DPP4DE-TT /CF samples coated at (a) 1.4 mm s⁻¹, (b) 1.8 mm s⁻¹, and (c) 2.2 mm s⁻¹ marked by white triangles. Scale bars: 40 μm. The small white arrows highlight a few very visible inhomogeneities that contribute for contact line pinning. The gray arrow in (a) denotes the solution shearing direction of the film. Image reproduced from Ref. [271].

It is challenging to directly compare what determines the onset of the moving of the contact line for the systems of DPP4DE-TT and PCDTPT due to the multiple different properties of the polymer solutions. A qualitative analysis, however, of which polymer system is more vulnerable to the effects of the piezoshearing and possible reasons for so can be done.

The work of Noblin et al., [208] as an example, calculates and analyzes the threshold acceleration experimentally to set the contact line of a sessile water drop in motion. When applying a large enough acceleration value of vibration, the contact line can be depinned. Using a solid friction oscillator model, the threshold for setting the contact line in motion is calculated. The acceleration threshold depends proportionally on the magnitude of the contact angle hysteresis and is inversely proportional to the cosine of the equilibrium contact angle (Equation (7.1)). Therefore, a liquid with a small contact angle hysteresis and low wettability requires less energy for de-pinning of the contact line.

$$\frac{a}{g} > \frac{H}{(1 - \cos \theta_E)} \quad (7.1)$$

H is the contact angle hysteresis and θ_E the equilibrium contact angle.

The acceleration threshold is mentioned earlier in Chapter 3 and is dependent on both frequency and displacement amplitude of the piezo actuator. We believe one can estimate the acceleration threshold for yielding a constant film for our setup, through thorough characterization of the liquid and with enough experiments. In case of an evaporating polymer solution though, the solution geometry and volume are continually changing during coating. This problem is significantly more complicated and would require extensive experiments and mathematical analyses of each case. In this discussion, we can only speculate about possible reasons for the different acceleration thresholds. In Figure 7.21, a graph with the apparent acceleration threshold for deposition of films is presented. It must be noted that these values are limited to the number of samples tested for each coating speed. For more accurate acceleration threshold values, smaller intervals of vibration displacement should be tested.

Considering that both the pinning during the “stick” phase of the cycle, and the mechanical de-pinning through vibration are dependent on the convolution of the likelihood of the contact line to pin and how much the meniscus can stretch before it “slips”, it is difficult to point to one aspect of the semiconductor solution that determines whether there will be wires or a film deposited under certain vibrating conditions. The dynamics of the receding contact line are quite complex, and a few reasons for the different onset point of de-pinning of the contact line for the different materials can only be suggested.

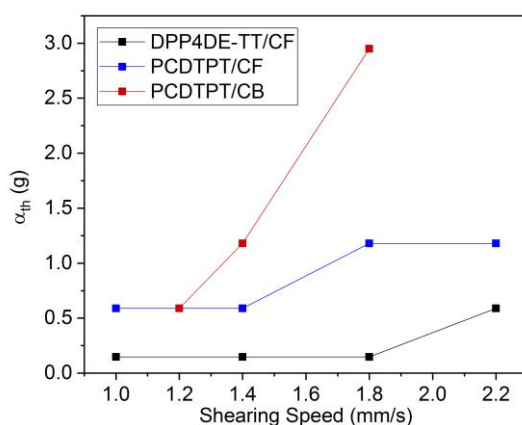


Figure 7.21: Acceleration threshold values required to obtain continuous film for the three experimental systems described here. These values are determined from Figure 7.3, Figure 7.4, and Figure 7.16.

Initially, one of the main reasons to which we attribute the different acceleration thresholds are the different capillary characteristics of the meniscus' contact line, requiring different vibration conditions to obtain a continuous film. We consider the capillary number $Ca = \eta V / \sigma$, [144], [279] where η is the solution viscosity, V the shearing speed, and σ the surface tension of the liquid. Since V is the same for both materials, such capillary number differences can emerge from different viscosity/surface tension ratios. These quantities are inherent to the semiconductor solution and can change due to differences in molecular weight, entanglement or polymer agglomeration; or due to the different surface tension of the polymeric solution in relation to the air and substrate interface. For materials that have a higher capillary number, the viscosity is expected to predominate over the surface tension factor of the pinned contact line and therefore require a higher amount of energy (higher displacement of the piezo crystal) to be depinned.

In the static case, however – a sessile drop drying under the vibrating blade – a continuous film is obtained at around ~ 5 Vpp (Figure 7.17 and Figure 7.18) for both materials. Therefore, the different constitution alone of both these materials does not seem to be the main factor determining the acceleration onset value of the moving contact line through vibration.

Because the main difference of the onset of continuous film growth is observed at higher coating speeds (ex: 1.8 mm s^{-1}), we believe the most significant difference to be in the pinning force and stretching limits of the meniscus once the contact line is pinned. We propose the contact line of the PCDTPT/CF to stretch to shorter lengths in comparison to the DPP4DE-TT. An indication of this is that there seems to be a more substantial area covered by semiconductor in the films of PCDTPT/CF in comparison to the DPP4DE-TT/CF. Examples are the films of Figure 7.4c and Figure 7.3c, where both films are coated at the same speed, and both are 0.8 mm s^{-1} above their critical speed (1 mm s^{-1}). For the DPP4DE-TT experiment, there are wires with considerable height and small width, indicating a longer pinning time. The PCDTPT/CF system has lower but wider wires, indicating the contact line stays pinned for a shorter time. This could be due to lower viscosity, higher surface tension, or a combination of both. The different evaporation rate for both materials is also likely to affect how these parameters vary during the coating process. If the contact line is pinned for a shorter amount of time, the contact line does also not reach a contact angle so far from its equilibrium position in comparison to the DPP4DE-TT system. Therefore, if some change in the deposited pattern of this polymer is to be seen, a higher amount of energy (higher voltage to the piezocrystal) is expected to be required.

Here are the multiple factors that we believe to influence the stretching mechanism of the meniscus: i) Free surface energy of the meniscus on the surrounding means, ii) Viscosity of the solution, iii) Resonance frequency of the semiconductor solution due to a different solution properties and various geometries, and iv) Concentration gradient at the contact line due to evaporation, agglomeration and crystallization processes.

The higher the surface tension of the liquid, the less prone it is to spreading and occupying a larger area.[280], [281] For the surface tension mentioned, the surface tension between the substrate and the liquid is accounted for as well and can vary for both systems. Therefore, a liquid with higher surface tension would be expected to be less prone to pinning, less likely to stretching, and its contact angle to be closer to an equilibrium position. Thus “stick-and-slip” effects are seen less prominently, and the contact line to require more energy to de-pinned.

Although higher viscosity decreases the spreading of liquids,[281] it increases the possibility of stretching the meniscus when applying extensional stress,[144], [282] and leads to more likely to more “fingers” that serve as anchors for contact line pinning [144], [278]. Therefore, higher viscosity could promote the occurrence of “stick-and-slip”, [144], [150], [278] and also make the mechanical de-pinning more difficult.

The viscosity and surface tension of the liquid have opposite effects on both the occurrence of “stick-and-slip” and the necessary energy to de-pin the contact line and obtain a continuous film. Considering an evaporating solution, both viscosity and surface tension of the liquid at the contact line are constantly changing with the build-up in concentration. Therefore, measuring only the viscosity and surface tension of the initial solution concentration is not enough for understanding the pinning/ depinning process. It is known that an increase of concentration in a polymer solution increases viscosity, and the polymer can act as a surfactant, changing the surface tension of the liquid depending on the concentration. In Figure 7.22, the contact angle values for varying concentrations of DPP4DE-TT and PCDTPT are shown. The increase of concentration increases wetting conditions for the polymer solution on the ODTS-treated substrate.

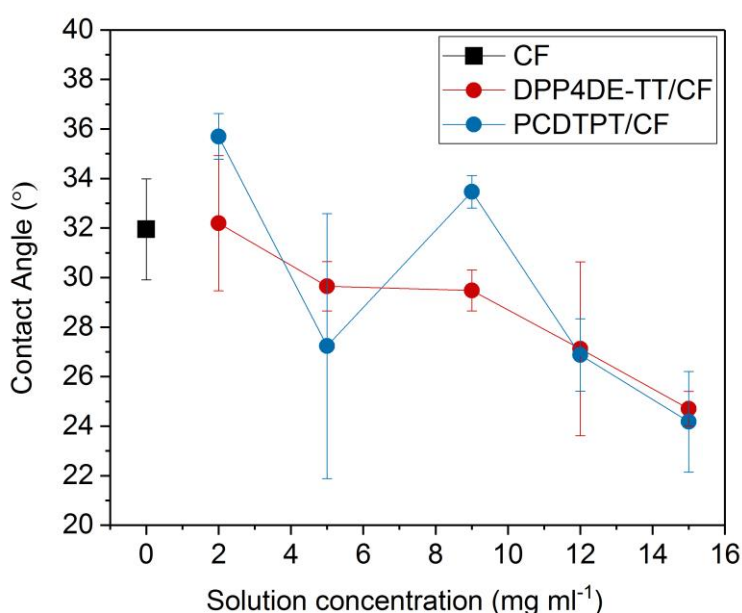


Figure 7.22: Contact angle values for the polymer solutions of DPP4DE-TT/CF and PCDTPT/CF with varying polymer concentrations.

The contact angle values displayed in Figure 7.22 are close to equilibrium for a sessile drop. The contact angle hysteresis is also expected to change with the change in polymer concentration. A more thorough characterization of surface tension and contact angle hysteresis for a broader range of polymer concentrations are required if quantitative comparisons are to be made between the two polymer systems.

The vibration frequency used in this system (1 kHz) could also be closer to the resonance frequency of the DPP4DE-TT/ CF system, making the threshold energy required for this material lower than for the PCDTPT/ CF system. Since the static drop does not present a significant difference in onset voltage, the resonance frequency could be different for both systems depending on the geometry of the meniscus, which varies continuously during the coating process.

The film formation, crystallization, and polymer aggregation could be different for both polymers and change the concentration gradient along the meniscus, causing different stretching characteristics for both materials.[140] The analysis of this is beyond our experimental setup and any experimental method known to us, and we can only speculate this to make a difference.

7.6 Summary

This study demonstrates the possibility of coating organic semiconductor solutions of donor-acceptor polymers on a partially wetting substrate with piezo crystal-generated vibrations at higher shearing speeds than would be possible without vibrations with a conventional blade coating setup. It is shown that the elimination of stick-and-slip effects produces an increase in the critical shearing speed of over 100% for two different polymer semiconductors and two different solvent-temperature conditions for one of the materials. Furthermore, the charge carrier mobility was shown to increase by 2 orders of magnitude due to better substrate coverage in films coated at increased speeds. It is also demonstrated that piezoshearing enables the deposition of ultra-thin films in applications in which uniformity and low material consumption are essential. Due to the high costs of semiconductor materials and often limited amounts, the reduction of material to a third of the quantity used without the vibration represents a significant contribution of the piezoshearing method to fabrication costs.

The piezoshearing can also be extendable to other applications which require ultrathin and uniform films, such as dielectrics in ultra-thin film capacitors,[38], [283], [284] transparent electrodes for photovoltaic applications,[285], [286] and strain sensors.[287], [288]

In previous works vibration has been used in several experiments for reaching the most stable contact angle of droplets,⁴³ for film spreading using acoustic streaming due to SAW (Surface Acoustic Waves)[289] or acoustic streaming.[290] However, to the best of our knowledge, the piezoshearing is the first so far reported solution shearing method to mechanically hinder stick-and-slip instabilities during meniscus-guided coating for the deposition of uniform thin films.

We believe it possible to extend this method to different materials and systems that need to be coated at higher speeds on hydrophobic surfaces and still yield excellent uniformity. It is a simple solution, which does not require any changes to the constitution of the deposit or the substrate. This mechanism is expected to be suitable to a wide range of deposition applications by adjusting vibration frequencies and displacement amplitudes to the coating system.

Chapter 8

8 Piezoshearing of Viscous Polymer Solutions

8.1 Introduction

As pointed out in Chapter 3, previous works have utilized ultrasonic vibration to induce aggregation in a polymer solution, yielding better-performance OFET devices. In this chapter, the liquid aggregation treatment is embedded directly in the deposition method through the piezoshearing, decreasing a processing step in a way that is favorable for large-scale fabrication. Because the vibration occurs on the meniscus and the OSC is still in a liquid state, it is expected that the polymer has enough freedom to self-organize during the shearing process. Low coating speeds ($500 \mu\text{m s}^{-1}$) are utilized, allowing the liquid to react to the vibration.

In this chapter, semicrystalline copolymers are used in an attempt to increase in-plane polymer alignment or change the degree of crystallinity during deposition utilizing the piezoshearing method. Polymers with higher molecular weight - over 100 kDa at high concentrations are used. Due to high viscosities in comparison to the solutions used in Chapter 7, higher vibration accelerations can be tested, without causing dewetting by stick-and-slip. It is observed in Chapter 7, that above a certain acceleration threshold, the piezoshearing can hinder film deposition. This limits the investigation of the effect of vibration on the morphology of films when full deposition occurs. The polymeric solution is expected to be susceptible to morphology changes if the flow is produced by vibration, without the de-wetting that can also be caused by the vibration.

In addition to permitting a broad range of frequencies and amplitudes to be tested, organic semiconductor solutions of high M_w polymers have the potential to yield high charge carrier mobility values if the polymer backbone can be aligned along the channel direction of a transistor.

It is also of general interest to be able to process a polymer solution with high- M_w polymers. Although the processing of viscous solutions by solution shearing can be quite challenging,[291]–[293] films of these materials can present a higher resistance to mechanical stress and cracking because of more chain entanglement. Another advantage of high molecular weight polymers is better substrate coverage. In the case of bottom contacts, where a smooth continuous film around the edges is desired, high molecular weight materials are advantageous.[294]

8.2 Device Fabrication

For these experiments, the polymers poly(diketopyrrolopyrrole-cothiophene-co-thieno[3,2-b]thiophene-co-thiophene) (**DPP4DE-TT**), Poly[2,5-(6-dodecyloctadecyl)-3,6-diketopyrrolopyrrole-alt-5,5-(2,5-di(thien-2-yl)thieno [3,2-b]thiophene)] (**DPP6DO-TT**), and poly{3-([2,2':5'2''-terthiophen]-5-yl)-2,5-bis(6-dodecyloctadecyl)-2,5-dihydropyrrolo[3,4-c]pyrrole-1,4-dione-6,5''-diyl} (**DPP6DO-T**) are utilized. The chemical structures are depicted in Figure 8.1, and physical properties of each polymer are summarized in Table 8.1. Unless specified otherwise, all the solutions utilized chloroform as the solvent. The concentration used for the polymer DPP4DE-TT is 20 mg ml⁻¹, for DPP6DO-TT 8 mg ml⁻¹, and for DPP6DO-T 16 mg ml⁻¹. The DPP4DE-TT polymer presents a lower M_w , but higher solute concentration, whilst the other two polymers present higher M_w and a lower concentration for the solution. Due to either high concentration or high molecular weight, the solutions used in this chapter are significantly viscous in comparison to the other solutions used throughout this work - this is a crucial factor, which enables the testing of higher piezoshearing frequencies and amplitudes. The polymer DPP4DE-TT was acquired from the Diao Research Group, from the University of Illinois at Urbana-Champaign. The polymers DPP6DP-TT and DPP6DP-T were acquired from the collaborating group of Dr. Anton Kiri (Leibniz-Institut für Polymerforschung Dresden (IPF)).

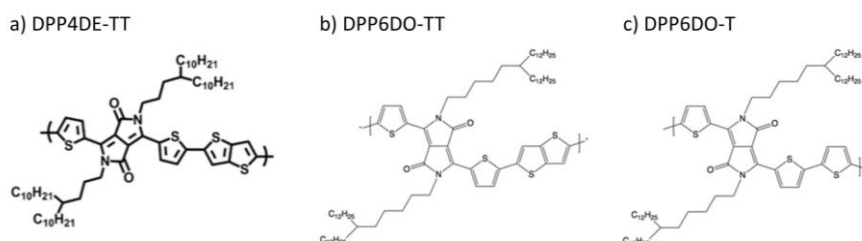


Figure 8.1: Chemical structures of the diketopyrrolopyrrole Polymers utilized in this chapter: (a) DPP4DE-TT, (b) DPP6DO-TT, and (c) DPP6DO-T.

	M_w	M_n	\bar{D}	Eluent for GPC
DPP4DE-TT	108	15.6	6.8	Chlorobenzene at 40 °C
DPP6DO-TT	298	98	3	Chloroform at 40 °C
DPP6DO-T	217	49.9	4.36	Chloroform at 40 °C

Table 8.1: Physical properties of the polymers us DPP4DE-TT, DPP6DO-TT, and DPP6DO-T.

The films were coated on ODTS-treated Si/SiO₂ substrates. The film deposition, the electrode evaporation, and the microscopic imaging of the DPP4DE-TT-based samples were done at the facilities of the Diao Research Group, at the University of Illinois at Urbana-Champaign.

The GIWAXS measurements for the DPP6DO-TT and DPP6DO-T-based samples were performed at the XRD-1 beamline at Elettra Sincrotrone facility. The grazing incidence angle for all measurements was 0.13°, and the beam exposure time onto the samples was around 270 seconds. The beam energy for the measurements was 12.4 keV. The GIWAXS measurements for the DPP4DE-TT were performed at ID 03 surface diffraction beamline of the European synchrotron radiation facility (ESRF), Grenoble. The

beam energy for the measurements was 12 keV. The grazing incidence angle for all measurements was 0.12° , and the beam exposure time onto the samples was around 600 seconds. A point detector was used to capture the scattering signal. Two-dimensional reciprocal maps were obtained by stitching together the point detector signal at all the scattering angles.

8.3 DPP4DE-TT and Film Morphology

In this section, the polymer DPP4DE-TT (Figure 8.1a) is utilized. It is a material that has been shown to have excellent charge carrier mobility, proper polymer alignment, and crystallinity.[19], [53], [134] The high polymer concentration and higher chain alignment at the top surface of the film makes us believe it possible to test a broad range of vibration conditions without hindering the film coverage and improve the surface morphology.[53]

A broad range of vibration frequencies is tested, and a trend of which frequencies have a stronger effect over the deposited films can be observed (Figure 8.2). The intensity of the birefringence contrast of the film is measured as the first test on whether there is any effect on the film quality or degree of chain alignment. Using a constant vibration displacement of 10 Vpp, Figure 8.2a shows that frequencies from 5 kHz to 20 kHz have a more significant effect on the resulting film. The average pixel intensity is measured to obtain a quantitative measurement of what frequencies are more likely to affect the morphology of the film. The pixel intensity is measured through the *Mean gray value* function in the ImageJ software. Figure 8.2b shows the average pixel intensity difference of the images for each film. The average pixel intensity is extracted from the images of the angles 45° and 0° in relation to the shearing direction, and the values subtracted from each other. The higher the pixel intensity difference, the more birefringent is the film. As mentioned in Chapter 4, the pixel intensity can change due to thickness, alignment, or crystalline quality of the film. Figure 8.2c displays the variation in intensity normalized by the thickness (intensity unit per nanometer of the film) of each film in comparison to the reference sample. The films with higher normalized intensity are expected to have a higher degree of alignment or crystallinity. These films serve as a reference to which vibration conditions should be further explored and could possibly be beneficial for device fabrication.

There is a significant difference in the morphology of the films coated at the frequency of 5 kHz, despite using a very low vibration displacement. We speculate this could be a frequency closer to the natural frequency of the material, and it could, therefore, have a significant effect on the film. There are large thickness variations and possibly different morphology domains. Although 10 Vpp is a considerably small displacement, it is enough to possibly cause deformation of the meniscus at the contact line and add the “fingering-like” macrostructures along the shearing direction. This effect is reported in other works for the vibrating of sessile drops when a high amplitude displacement is applied to the vibration of the substrate.[175], [179]

At the frequency of 10 kHz, a significant increase in the birefringence intensity is observed, and the film thickness seems to be uniform (Figure 8.2). Further investigation on the samples coated at such frequency is done for two different voltage values: 10 Vpp and 40 Vpp (Figure 8.3). The CPOM films indicate a higher degree of alignment and/or crystallinity in these films. These two features can possibly have a positive impact on charge carrier mobility. The far left column of Figure 8.3 shows that the normalized pixel intensity (units: a.u./nm) of the image increases when vibration is increased, although the thicknesses are quite similar.

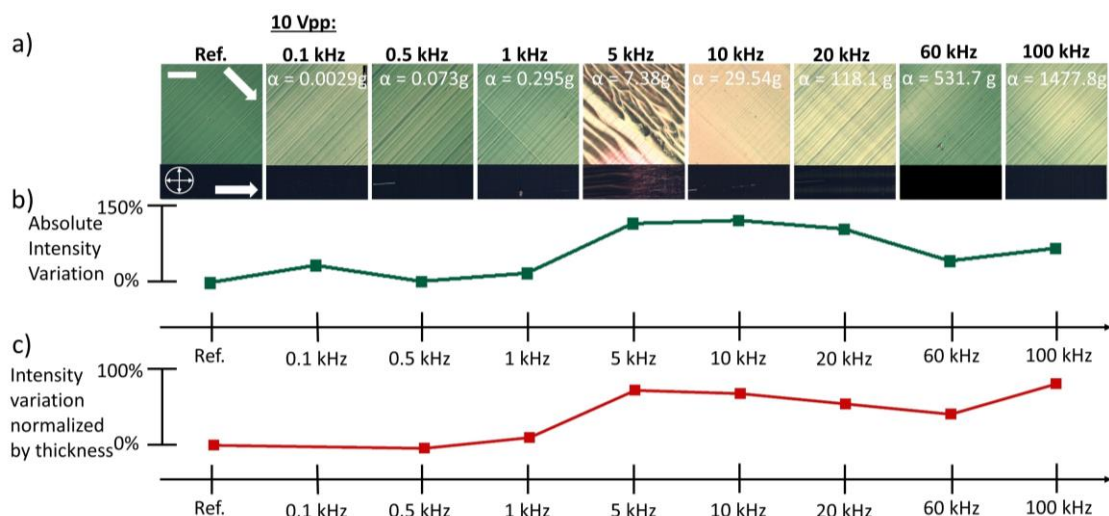


Figure 8.2: Cross-polarized microscopy images (CPOM) of the DPP4DE-TT films; (b) total intensity variation of the images of films coated at such frequencies; and (c) the respective pixel intensity normalized by thickness. White arrows in (a) denote the respective coating direction for the films, and the crossed arrows denote the direction of the crossed polarizers. Scale bar: 500 μm .

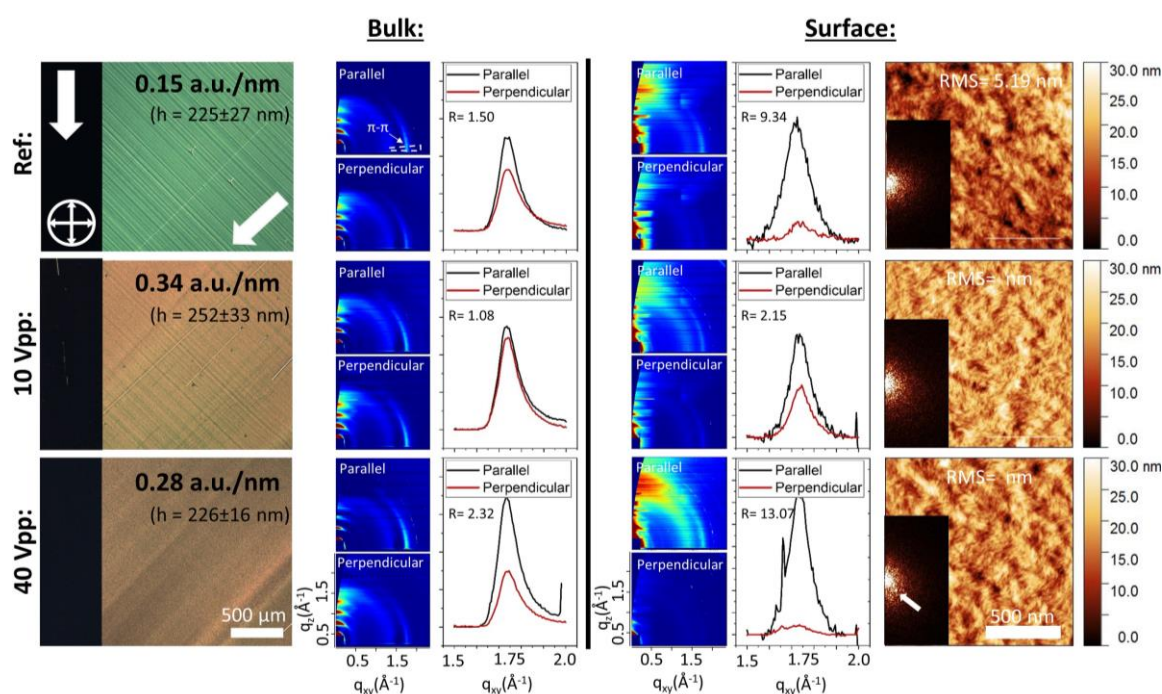


Figure 8.3: From the top to the bottom, is the reference film DPP4DE-TT, and then piezosheared samples with increasing displacement at a vibration frequency of 10 kHz. At the far left are cross-polarized images (CPOM), with their respective normalized pixel intensity and film thickness. In the middle section (Bulk, $\alpha = 0.12^\circ$), GIWAXS characterization for the bulk of the film is shown. In the section at the right (Surface), the GIWAXS characterization for a shallow incident angle ($\alpha = 0.04^\circ$) and AFM of the top surface of the film is depicted. The value R in the integrated cake segment graphs is the ratio of the integrated area of the parallel direction in relation to the perpendicular direction. Parallel and perpendicular are relative to the shearing direction.

In the left section of Figure 8.3, characterization results from the bulk of the film are displayed. The methods used are CPOM and GIWAXS. GIWAXS is used to determine whether there is a change in the polymer nanostructure morphology. Such changes can include both the in-plane degree of alignment of the polymer, volume of aligned crystallite populations in the polymer or a different degree of crystallinity – more uniform cofacial π -

π stack coupling. This is possible to investigate by GIWAXS due to the edge-on character of the material on such a substrate.[53] In the left part of the figure are the 2D images from the GIWAXS taken with an incident angle of 0.12° in relation to the substrate. At its right are the intensity counts of such images integrated from a cake segment from $82^\circ < \chi < 87^\circ$ for comparison of the degree of alignment. Such counts are normalized by film thickness and slight variations in the sample size to ensure intensity values are comparable among samples. From the cake segment integrations of the diffraction for the bulk, a degree of alignment favorable in the direction parallel to the shearing direction is detected. The in-plane π - π intensity anisotropy of each sample is displayed as “R” in the integrated cake segments, and consists of the ratio of the integrated area of the π - π peaks in the parallel direction in relation in the perpendicular direction. The integrated area is used instead of the maximum intensity to take into account slight changes in the Full-Width Half Maximum.

The degree of alignment decreases when using the piezoshearing at 10 kHz, 10 Vpp, and increases again when sheared at 10 kHz, 40 Vpp. The in-plane degree of alignment seems to change either due to an increase of crystalline structures in the perpendicular direction (10 Vpp), an increase in population in the parallel direction (40 Vpp), or both to different degrees. This could also be either due to crystallite structures aligning better in the parallel and perpendicular direction or due to the formation of a more significant number of crystallite populations induced by the piezoshearing. When integrating the areas of the peaks, which is proportional to the crystallite population, the values obtained for the piezosheared samples are higher. This is plotted further in Figure 8.4.

It has been shown that ultrasonic oscillation can induce aggregation and crystallinity for P3HT in a liquid state,[129], [198]–[200] and we believe it to be extendable to other semicrystalline polymer semiconductors. However, the possibility that the vibration could cause a different “flow” aspect at the surface of the liquid and could exert some torque on the crystalline populations, inducing them to align is not excluded. That seems, however, to be more unlikely.

A more accurate explanation of what occurs here would require the characterization of the film for a large number of φ angles (angle around the axis in the normal direction to the plane), or ideally, a full rotation of the sample while performing GIWAXS. If the integration of intensities around φ would be constant, this is an indication that the crystallite population does not change with vibration, but only have their orientation changed, and consequently their degree of alignment. If the total intensity of the diffraction over a rotation around φ would be higher, the vibration then is likely to have induced the formation of crystallites in the thin film.

From the UV-vis measurements performed (not shown), an anisotropic trend of the UV-vis can be observed, also favorable in the direction parallel to the coating. The wavelength used for comparison here is the peak close to 820 nm. The dichroic ratio does not seem to change for any of the displacements tested. The UV-vis measurements are also expected to show a change in alignment.[113] It should be noted that the UV-vis takes into account both the intensity counts from dipoles in the amorphous as well as dipoles in the crystalline regions.

Alignment gradients along the thickness of polymer films have been reported in recent works, and the surface of polymer films coated on smooth substrates has been observed to be significantly more aligned than the bulk or the bottom surface of the films. [53], [133], [295] Films with a large thickness/high concentration are prone to having an even more significant gradient.[53] This is believed to be due to the crystallization of the polymer solution to start from the liquid-air interface and grow from top-to-bottom until reaching the substrate. They argue polymeric material at the top surface to reach

supersaturation earlier, and therefore the region has a longer time to reorganize, aggregate, and align.[53], [133], [295] Due to the higher polymer alignment at the air surface of the thin film, top-gate devices have been demonstrated to have significantly higher anisotropy than bottom-gate devices.[53] We also expect the effect of the piezoshearing to be stronger at the film's top surface, considering that if a flow increase is provoked in the system, the solution closer to the coating blade would be the most likely portion of the liquid volume to be affected. This is significantly relevant for top-gate devices, for which the transistor's channel is the top surface of the active film.

At the right section of Figure 8.3 characterization methods focused on the surface of the film are shown. These are GIWAXS 2D data collected for an incident grazing angle of 0.04° . Due to the incident grazing angle below the critical angle of the thin film, more detail of the near-surface of the film is expected to be obtained. The anisotropy trend follows the same trend as observed for the GIWAXS of the bulk of the film, as can be concluded from the integration of the cake segments. However, the degree of in-plane alignment is significantly higher at the surface than at the bulk for all shearing conditions.

To the right of the GIWAXS images are AFM images of the surface. The roughness decreases slightly for the piezosheared samples, and films seem more uniform. The CPOM images also suggest that stick-and-slip decreases for the piezosheared samples, and thickness uniformity increases. This is in accordance with Chapter 7, where enough energy introduced to the meniscus mitigates stick-and-slip and thickness variations. To evaluate anisotropy of the surface morphology quantitatively, a Fast Fourier Transform (FFT) on the AFM images is performed. From the FFT images of the piezosheared samples, slight anisotropy is observed, and a stronger anisotropy for the sample coated with a vibration displacement of 40 Vpp.

To evaluate the relative degree of crystallinity (rDoC) of the films, the poles for the 2D images are calculated as described in Chapter 4 and are displayed in Figure 8.4. The pole calculations for both the parallel and perpendicular directions of the films and both incident angles were performed. The sample without vibration is used as the reference for the rDoC as well.

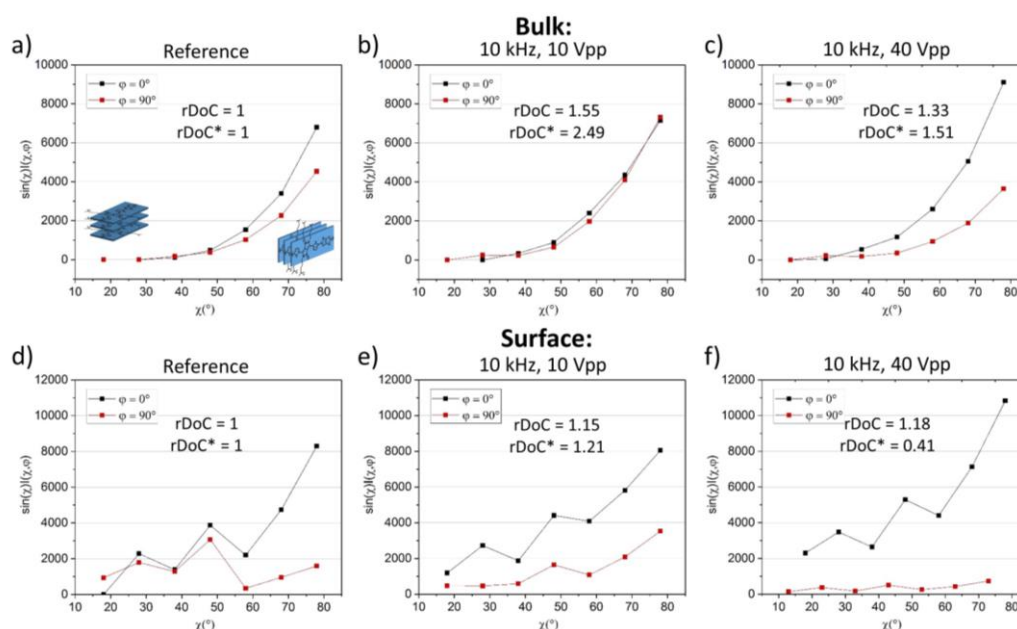


Figure 8.4: Pole figures for solution sheared samples of DPP4DE-TT of the (a-c) bulk of the film; and (d-f) of the near-surface. For calculation of the rDoC and rDoC*, the diffraction images from Figure 8.3 are used. Angle $\phi = 0^\circ$ is referent to the direction parallel to the solution shearing, and $\phi = 90^\circ$ is referent to the perpendicular direction.

From the CPOM results and previous works, the backbone of the polymer appears to be predominantly aligned parallel to the shearing direction. Hence the parallel and perpendicular directions represent the maximum and minimum degrees of in-plane alignment, and, the pole values for other φ angles should lie in between these two values. Summing the poles in both parallel and perpendicular directions, a relative degree of crystallinity for the films is obtained. These values are shown for the respective sample in Figure 8.4. However, for a more accurate calculation of the relative degree of crystallinity, a full rotation of $0^\circ < \varphi < 90^\circ$ would be necessary. If the alignment distribution of crystallite occurs gradually from the less aligned direction ($\varphi = 90^\circ$) to most aligned ($\varphi = 0^\circ$), as is likely to be the case, the density of crystallite populations in the film could be estimated. Considering the distribution of crystalline populations as a function of the angle φ , the distribution would resemble an ellipsoidal curve, and the integration of this area would be equivalent to the integration of the crystallite population. Given that the area of an ellipse is given by $\pi \cdot p \cdot q$, p and q the axis lengths, we define a degree of crystallinity rDoC* as the product of sums in both coating directions. These values are also displayed in Figure 8.4.

The piezosheared samples have a higher rDoC than the reference sample for the bulk of the films, and only a slight increase in the near-surface of the films. This increase in the rDoC difference could also be from either a larger crystalline population formed at the surface or a different alignment of a constant crystallite population. Table 8.2 sums up the values for the numerical figures calculated from Figure 8.3 and Figure 8.4. Although the data does not necessarily allow us to conclude what the piezoshearing does to the film formation precisely, the increased degree of alignment of the films and increased degree of crystallinity lets us believe there is a more favorable morphology for charge transport in the piezosheared films.

Sample	Bulk Characterization								Surface Characterization			
	CPOM int. (int. nm)	CPOM int. Variation	In-plane pi-pi anisotropy (Bulk)	In-plane pi-pi anisotropy Variation (Bulk)	rDoC (Bulk)	rDoC Variation (Bulk)	UV-vis anisotropy	UV-vis variation (Bulk)	In-plane pi-pi anisotropy (Surface)	In-plane pi-pi anisotropy Variation (Surface)	rDoC (Surface)	rDoC Variation (Surface)
Reference	0.15	0	1.5	0	1	0	1.32	0	9.34	0	1	0
10 kHz, 10 Vpp	0.34	+126%	1	-33%	1.55	+55%	1.29	-2.2%	2.15	-77%	1.15	+15
10 kHz, 40 Vpp	0.28	+86%	2.3	+53%	1.33	+33%	1.21	-8.3%	13.07	+39%	1.18	+18

Table 8.2: Numerical figures extracted from Figure 8.3 and Figure 8.4 for DPP4DE-TT.

Figure 8.5 displays the effective charge carrier mobility for DPP4DE-TT-based bottom-gate devices. From the effective mobility, little or no change in the charge carrier mobility is measured. The electrical characteristics of all the samples were measured under ambient conditions but under a constant flow of nitrogen. We believe a stronger effect to be observed in top-gate devices, but at the time of this study, top-gated devices were not fabricated.

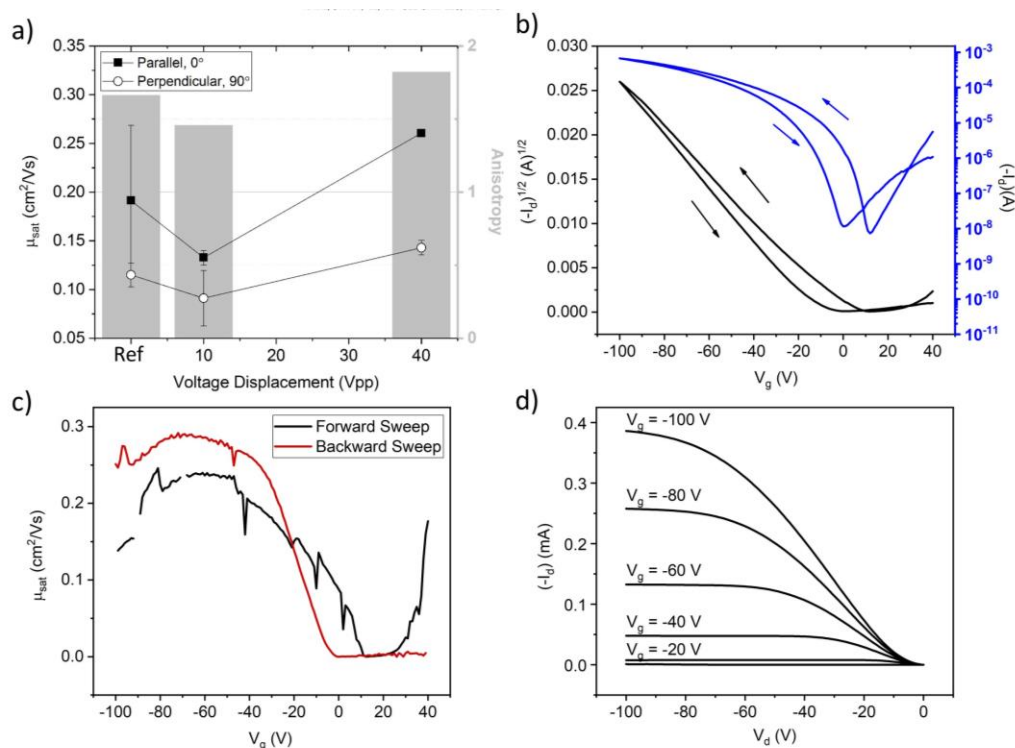


Figure 8.5: (a) Effective charge carrier mobility values for DPP4DE-TT, piezosheared at 10 kHz and varying displacement amplitudes. (b) Transfer curve, (c) gate-voltage-dependent mobility, and (d) output curves for devices coated at 10 kHz, 40 Vpp.

Different amplitude ranges and frequencies are tested, as limited by the piezoshearing setup. The results are shown in Figure 8.6. Figure 8.6t displays a color map of the percentual variation of the CPOM birefringence contrast in relation to the reference sample Figure 8.6a. Significant variation is observed for the films piezosheared at 5 kHz, likely due to the very non-uniform morphologies. For the frequencies higher than 5 kHz birefringence intensity increases. Like the samples analyzed for 10 kHz, these films could have favorable morphology for OFETs. Differences could be observed at frequencies greater than 5 kHz, possibly due to a higher acceleration (or energy) introduced into the system.

For samples coated at lower frequencies, such as 1 kHz, little differences, or even a decrease in birefringence intensity (for the higher voltages) are observed. From Figure 8.6, it can be concluded that frequencies above 5 kHz would be of higher interest for further exploration of the effects of piezoshearing on the coating of polymeric films. Our setup is, however, currently limited in displacement to the values tested in this study.

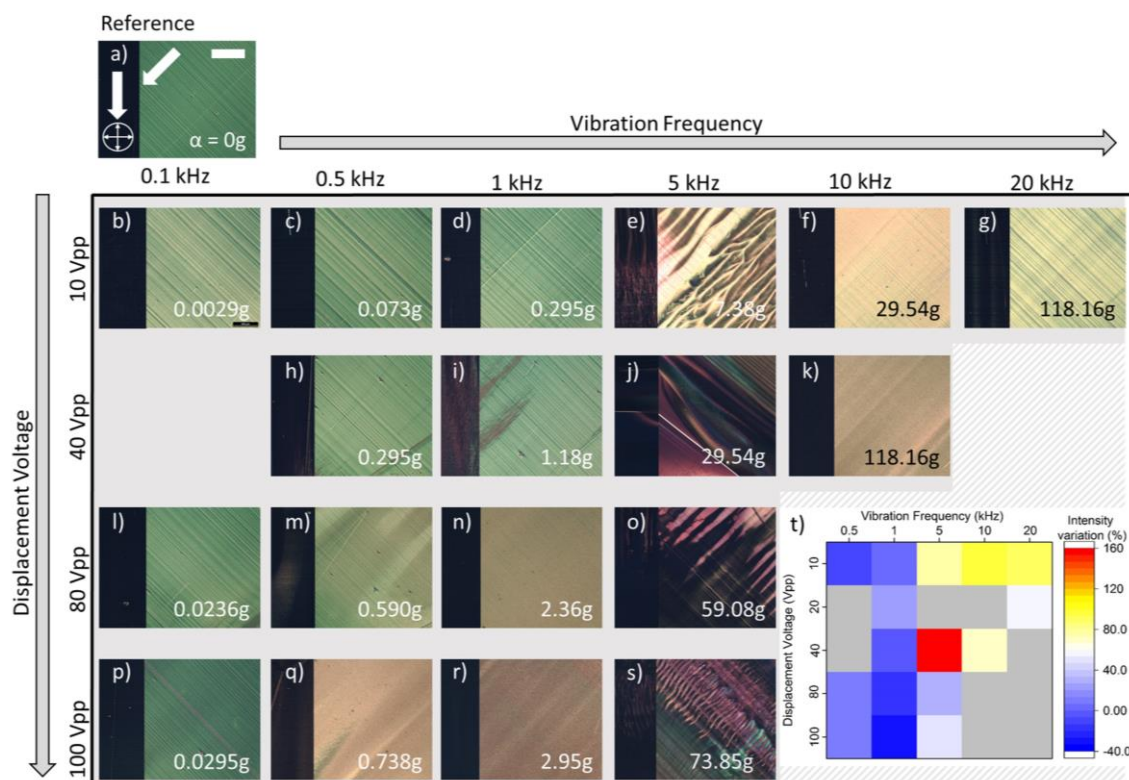


Figure 8.6: CPOM images of a solution-sheared DPP4DE-TT for (a) reference sample (scale bar: 500 μm), and (b-s) piezosheared samples at different vibration frequencies and amplitude displacements. The white arrows in (a) determine the shearing direction of the film, and crossed arrows indicated the direction of the crossed polarizers for (a-s). The acceleration for each piezoshearing condition is displayed at the right lower corner of the images. (t) Color map of the intensity variation normalized for the thickness of the respective films in relation to the reference sample in (a). The gray areas in (t) are missing data.

The resonance frequency of the liquid appears to be close to 5 kHz, and at low displacements, considerable differences in the film can be observed. In addition, Fast Fourier Transform (FFT) is performed on the optical intensity cross-sections of Figure 8.6e, o and s, and there are sharp intensity peaks at the frequency of 5 kHz (Figure 8.6s) and 2.5 kHz (Figure 8.6e and o). These are indicators of surface waves and Faraday instabilities, respectively. This is also a hint that the natural frequency of the system is around 5 kHz. The results of the FFT were not shown, and this is discussed again in a later section.

Using the vibration frequency of 1 kHz allows the testing of a broader range of displacement amplitudes. Figure 8.7 displays the CPOM images of the films piezosheared at 1 kHz, with their respective normalized intensity and thickness; and GIWAXS scans for both the bulk (above the critical angle of the film) and the near-surface (below critical angle of the film). The cake segments are integrated and normalized by film thickness and film length. The peaks for the piezosheared samples have higher intensity in the direction $\varphi = 0^\circ$ and a higher anisotropy than the reference sample for all the piezoshearing conditions.

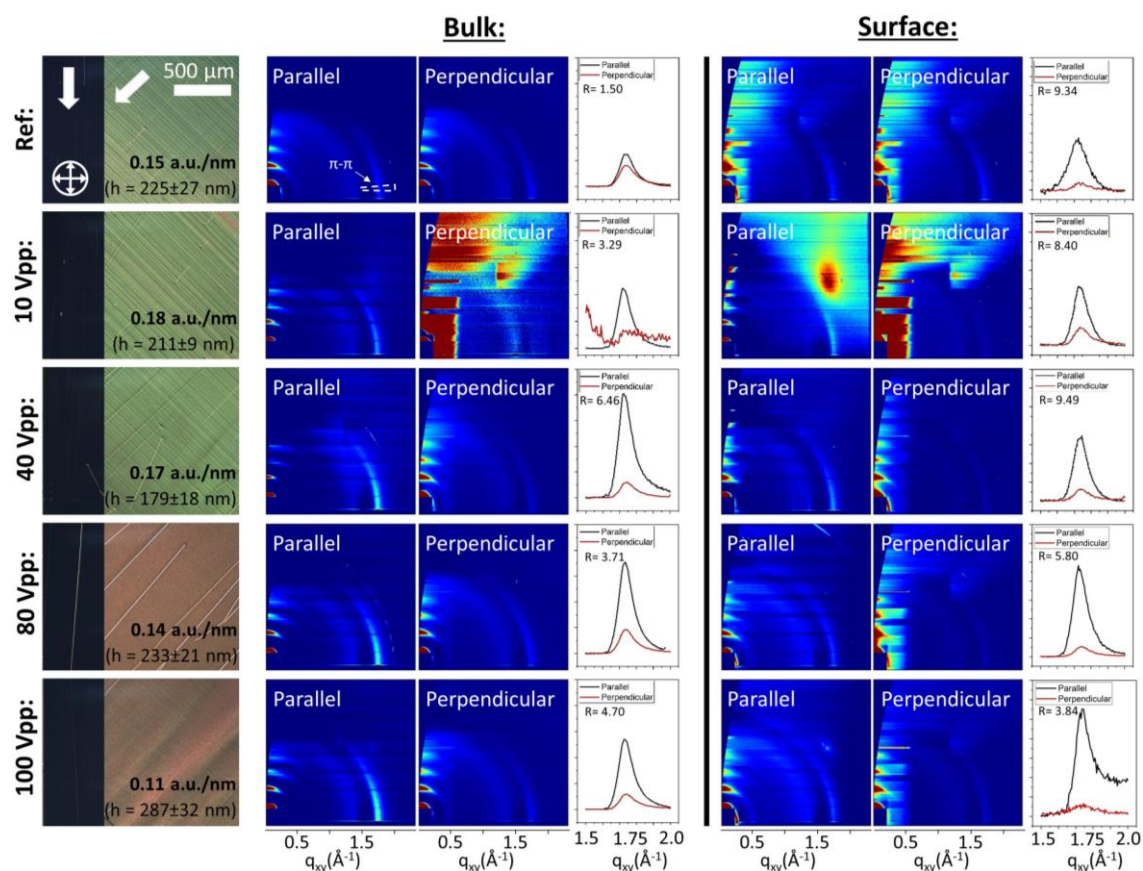


Figure 8.7: From top to bottom, there is a reference film of DPP4DE-TT, and following, piezosheared samples with increasing displacement at a vibration frequency of 1 kHz. At the far left are cross-polarized images (CPOM), with their respective normalized pixel intensity and film thickness. In the middle section (Bulk) is GIWAXS characterization for the bulk of the film. In the section at the right (Surface), is the GIWAXS characterization for a shallow incident angle.

The π - π stacking peak intensity anisotropy (at $\sim 1.74 \text{ \AA}^{-1}$) and the cake-integrated (integrated over q_{xy} and χ)[40] sum of the integrated π - π peaks are displayed in Figure 8.8a to facilitate visualization. Both the anisotropy of the π - π stacking and the sum of the intensity count are higher for the piezosheared samples than for the reference samples for any vibrating condition. This also supports the hypothesis that the piezoshearing can increase the crystallite population during film formation. Figure 8.8b displays the charge carrier mobility for these samples. A slight mobility improvement is observed for two of the samples, but no clear trend is visible, and the mobility does not correlate to the GIWAXS changes observed.

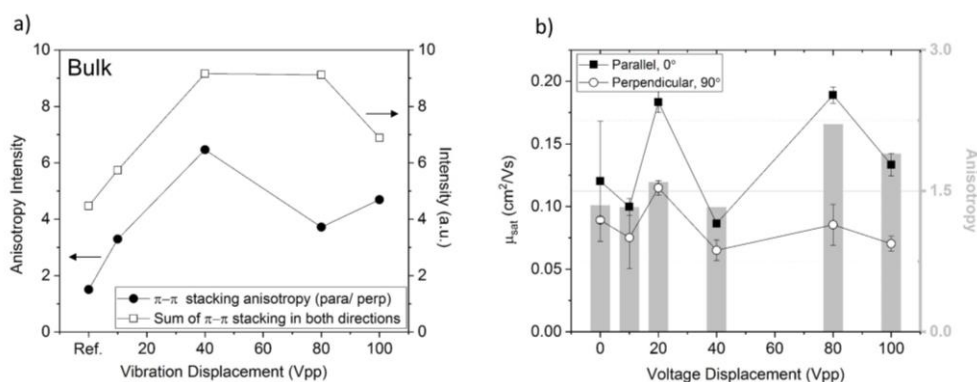


Figure 8.8: Charge carrier mobility for devices with films piezosheared at a vibration frequency of 1 kHz.

8.4 DPP6DO-TT, DPP6DO-T, and Faraday Instabilities

In this section, the effect of the piezoshearing on the polymers DPP6DO-TT and DPP6DO-T are studied. These have a high molecular weight and form very viscous solutions. From the handling of the solution, one can observe the viscosity is higher than that of DPP4DE-TT – at least visually.

Figure 8.9 displays CPOM images of the films solution-sheared from both these materials with a shearing speed of 0.5 mm s^{-1} at $25 \text{ }^\circ\text{C}$. Possibly due to the high viscosity of the solutions, the solution-sheared films tend to be very non-uniform, have significant thickness differences, and localized large crystallites and/or aggregates. The white parts of the films shown in Figure 8.9a and b are thicker parts of the film and appear to be white due to the high light intensity used for capturing the films. The insets show the optical images of the film without polarization. If the viscosity of the solution semiconductor is too high, it might overcome the capillary effect that maintains the solution under the shearing blade throughout the coating process, and large volumes of solute are left behind, forming the rough films observed.

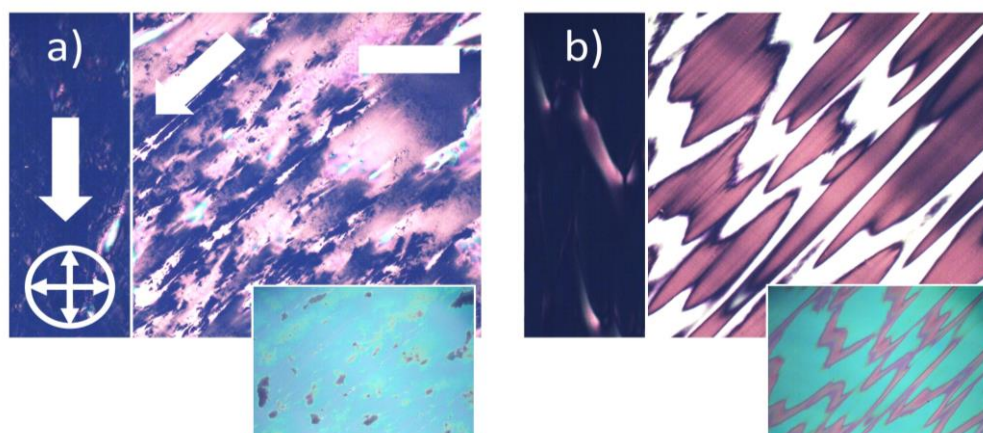


Figure 8.9: CPOM images of films coated at 0.5 mm s^{-1} at $25 \text{ }^\circ\text{C}$ for (a) DPP6DO-TT and (b) DPP6DO-T. The white arrows represent the coating direction, and the crossed arrows the direction of the crossed polarizers. The insets are the respective films without polarization. The different colors of the film are due to significant thickness differences. Scale bar: $500 \text{ }\mu\text{m}$.

The piezoshearing method is applied to the coating of the polymers with a wide range of vibration frequencies and amplitudes (up to what is possible with our setup). The diagram in Figure 8.10 displays the different film morphologies resulting from the piezoshearing. Different morphologies are separated by different background colors.

In Figure 8.10, different morphology regimes can be distinguished, and similar morphologies are grouped. For low amplitude displacements (20 Vpp), no significant change is visible (Figure 8.10b, c, d), and has a white background color. With the increase in displacement, apparent “crystalline formations” become smaller than for the reference sample, and are arranged in “lines” parallel to the coating directions. These line patterns that form in the coating direction, similar to fingering instabilities, are what will be called here “azimuthal instabilities” for reasons that will be further explained. This morphology is represented in Figure 8.10e-j, n, o q, r, and u, and have a light grey background.

When increasing the vibration displacement even more, patterns in the shearing direction appear, but without the crystalline formations. The films become smooth, and no crystalline chunks are present. This is observed in Figure 8.10k, m, p, s, and v, and have a dark grey background.

The last morphology observed is that of a partially wetted film, with stripes in the coating direction, but no solute deposited between the stripes. The semiconductor appears

to be ejected from the substrate. This is observed in Figure 8.10t, and the image has a black background. The liquid ejection (atomization) due to vibration often occurs from a pinch-off of the instabilities when vibration energy is increased, depends highly on the capillary number of the liquid.[180], [296]

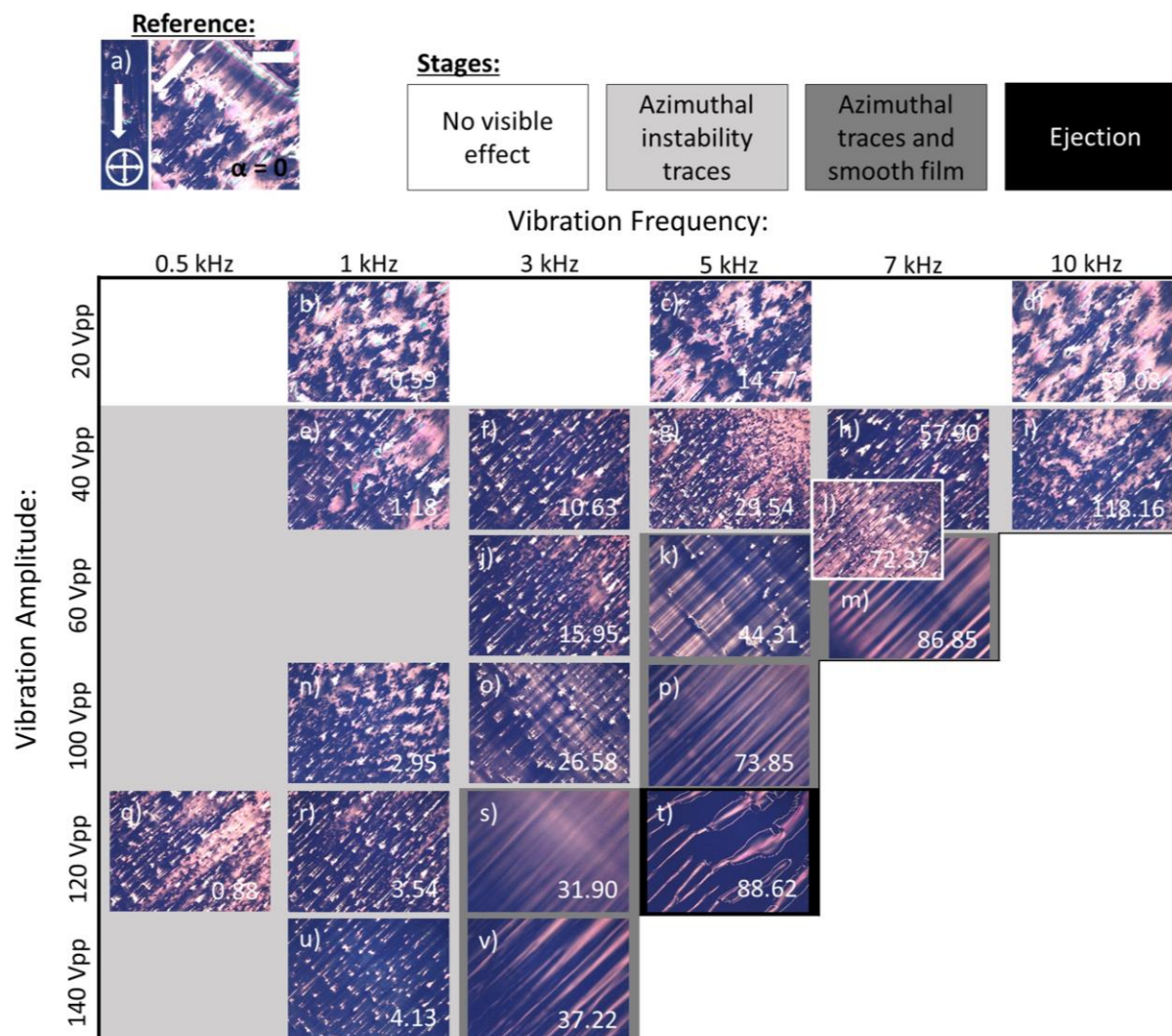


Figure 8.10: Films coated from DPP6DO-TT: (a) reference sample, and (b-v) piezosheared samples with varying vibration frequency and amplitude. The white arrows in (a) denote the coating direction of the film, and the crossed arrows denote the direction of the crossed polarizers. The values on the right bottom corners of the images are the acceleration values induced by the vibration of the piezo crystal. The background color of the images indicates in which regime the films are according to the legend on the top. Scale bar in (a): 500 μm .

The patterned lines in the shearing direction with a particular frequency, are “traces” that the instabilities are a product of parametric oscillation, caused by the vibration of the piezocrystal in resonance with the natural vibrating frequency of the meniscus. Several previous works have described the surface line of a drop submitted to the vibration of the substrate as a parametric oscillator.[175], [179], [208], [209]

The work of Vukasinovic et al. presents a detailed description of a process very similar to the one shown in Figure 8.10, but for a non-evaporative sessile drop system. They report the observations of a sessile drop, vibrated from the substrate, with gradual vibration amplitude increase. This work helps with a better understanding of what occurs during the piezoshearing. Figure 8.11 displays the side and top view of a sessile vibrating water drop when increasing the vibration amplitude.

Once the vibration is activated, a surface wave is created, as can be observed from the top and side view in Figure 8.11b and g and, respectively. This is similar to what is described in the works of Noblin et al.[208], [209] In these works, contact line movement can occur. This is consistent with the observation in Chapter 7, where the vibration deforms the contact line. In the work of Vukasinovic, however, no contact line movement is observed at this phase of vibration. When increasing vibration amplitude, protuberances appear at the contact line; these are what the authors call “azimuthal instabilities”. These are somewhat “fingers” that emerge from the contact line (Figure 8.11c and h). They are believed to be Faraday (or parametric) instabilities.

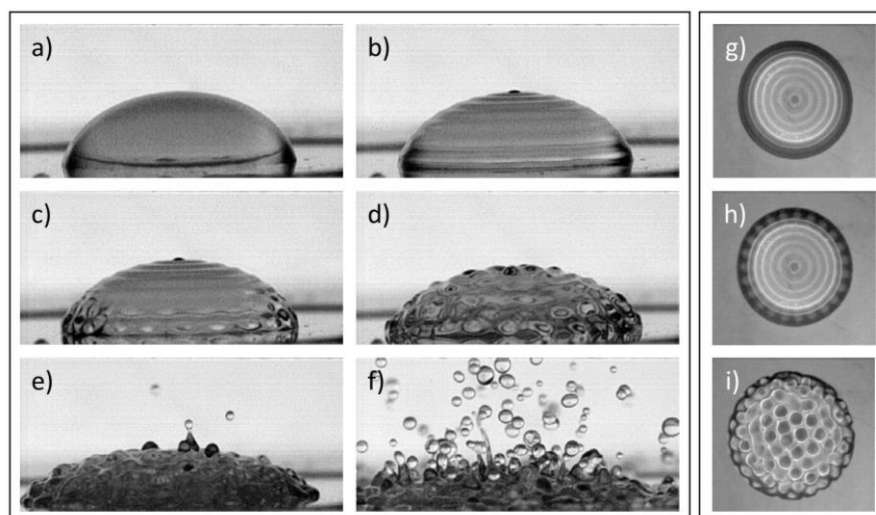


Figure 8.11: (a-f) Side view and the (g-i) top view of a vibrating sessile drop. Both sequences document the process the drop undergoes when vibration amplitude is increased. The images are reproduced and rearranged from the work of Vukasinovic et al.[179]

Faraday instabilities have been first observed in a vibrating sheet of water by Faraday,[170] and arise from a resonating condition in a parametric oscillator. It occurs when an oscillating movement is applied to another oscillating system, and resonance occurs. Standing waves at a particular frequency can occur, influencing the shape of that contact line, and therefore, influencing the pattern of the solute deposited. This is an effect that would enable the lines that appear in the shearing direction, as observed in Figure 8.10. Faraday instabilities are standing waves characterized for having a spacial frequency half of the frequency of the external driving frequency. The external driving frequency here is the frequency the piezo crystal vibrates at, and the natural frequency of the system is that of the receding meniscus. To check whether the instabilities occur at half of the driving frequency, FFT analysis is applied to the optical intensity profile of the films. The FFT will point out the most abundant frequencies in which the patterns appear. This method is usually used for in-situ experiments with high-speed imaging of the instabilities, but it is performed here on the deposited solute, considering the shape of the deposited film to resemble that of the contact line.[208], [297], [298]

Figure 8.12 displays the films from the gradual amplitude increase at a vibrating frequency of 5 kHz. The frequency 5 kHz was chosen because it enables the observation of all the morphology regimes at one driving frequency. Figure 8.12a-g display the CPOM images of the films, Figure 8.12h-n are the respective profile cross-sections as indicated in the CPOM figures, and Figure 8.12o-t are the resulting power spectra derived from the cross-sections. The power spectra are plotted as a function of f/f_d , where f_d is the driving frequency - in this case, $f_d = 5$ kHz. This way, it is easier to visualize the relation between the frequency of the instabilities and the driving frequency. The vertical lines in Figure

8.12o-t highlight the frequencies of $0.5 f_d$ and f_d . All the images are expected to have a peak at f_d due to a surface wave. The films with voltages sheared at 20 Vpp and 40 Vpp (Figure 8.12b and c) present a visible peak at $0.5 f_d$, which is not present for the reference sample. This frequency is due to the stripes along the shearing direction in which the small crystallites align. This is strong evidence that these are Faraday instabilities. By increasing the vibration amplitude, the $0.5 f_d$ peak decreases in comparison to the rest of the peaks, and f_d becomes very prominent at the higher vibrating amplitudes (100 Vpp and 120 Vpp). Instabilities with a frequency equal to the driving frequency are described by Bechshefer et al. as meniscus waves, which appear due to the reflection of waves at the wall of a container, and have no threshold acceleration. The driving frequency f_d is indeed observed in the FFT spectrum of all the samples in Figure 8.12. The patterns that remain when part of the solution is ejected (Figure 8.12) also have a predominant frequency of f_d .

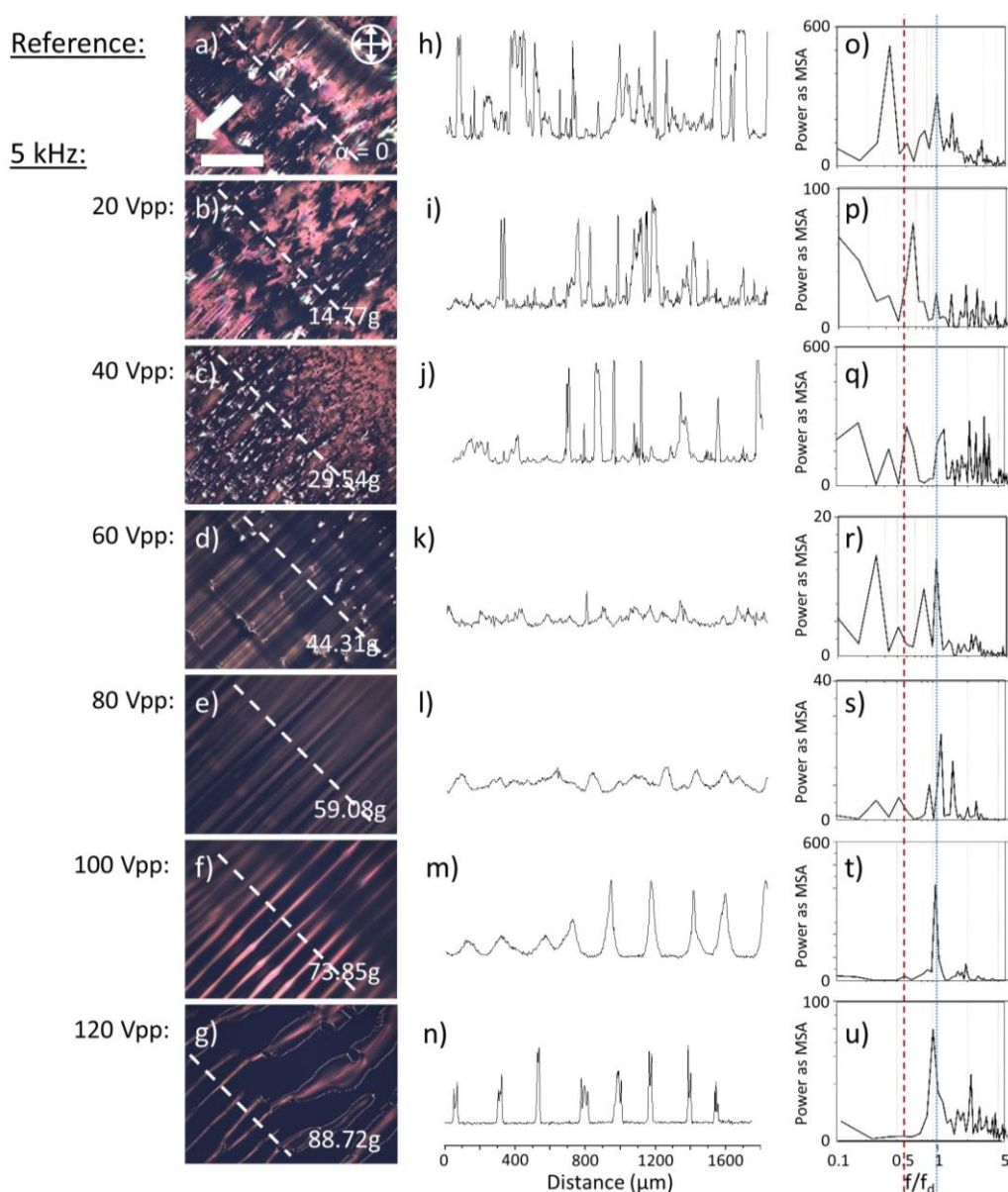


Figure 8.12: CPOM images of a DPP6DO-TT (a) sheared reference film, and (b-g) piezosheared films at a frequency of 5 kHz and varying vibration amplitude. (h-n) Intensity profile extracted from the cross-sections in figures (a-g). (o-u) Resulting Power Spectra of Fast Fourier Transform of the profiles in (h-n). The white arrow in (a) is the coating direction, and the white dashed line is where the intensity profile is extracted. The blue and red dashed lines on the images on the right of the figure are a guide to the eye of the frequency values $0.5 f_d$ and f_d , respectively. Scale bar in (a): 500 μm .

The displacement and the frequency at which such instabilities will arise depend on the resonance frequency of the system. The farther away from the resonance frequency, the larger the applied energy (acceleration) needed for the instabilities to occur. Several works have attempted to determine the threshold acceleration of Faraday instabilities for viscous fluids.[177], [189], [299] We believe it is possible to estimate the acceleration necessary for patterning solute depositions if the relation between the resonance frequency and the receding meniscus of an evaporating polymer system is investigated.

Similar effects are observed for the polymer DPP6DO-T coated from chloroform at room temperature, and for DPP6DO-TT coated with chlorobenzene at 100 °C (for better charge carrier mobility). The reference film is very non-uniform for both shearing conditions (Figure 8.13). The films coated from DPP6DO-TT/ CF present significant thickness variations in the direction along the contact line. These are apparently due to the stick-and-slip effect combined with the high viscosity of the semiconductor solution shown. In Figure 8.13, the effects of applying a vibration frequency of 5 kHz during the coating of the DPP6DO-T/CF and DPP6DO-TT/CB solutions are shown. In Figure 8.13b and c, the thickness pattern changes, possibly changing the stick-and-slip cycle of the receding meniscus. By increasing the vibration amplitude of the crystal, the stick-and-slip is completely mitigated, and smooth films are deposited (Figure 8.13d). For the highest amplitude (Figure 8.13e), Faraday Instabilities appear once more. This pattern indicates contact line depinning and appears at a lower acceleration value than the Faraday instabilities (at least for this material). For the DPP6DO-TT/CB system, films with a more uniform thickness can be achieved as well.

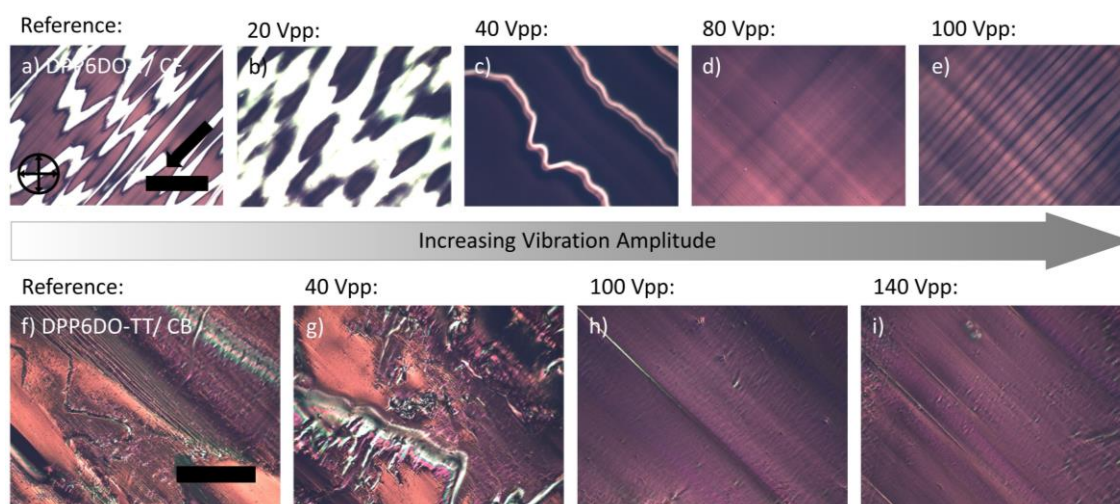


Figure 8.13: CPOM images of sheared and piezosheared films of (a-f) DPP6DO-T/CF coated at room temperature, and (g-j) DPP6DO-TT/CB coated at 100 °C. The vibration frequency used is 5 kHz for both materials. The black arrow indicates the coating direction, and the crossed arrows, the direction of the crossed polarizers. Scale bar: 500 μm .

8.4.1 Thin-film Characterization

In Figure 8.14a and b, CPOM images of the samples coated from DPP6DO-TT/CF are shown, and in Figure 8.14c to j, AFM images. It is believed that the smoother films could be a sign of chain disentanglement of the polymer and possibly more increased polymer aggregation, but the surface morphology does not seem to change or present a more fiber-like morphology. Although on a large scale the films are significantly smoother, at a microscale they do not present any perceptible change.

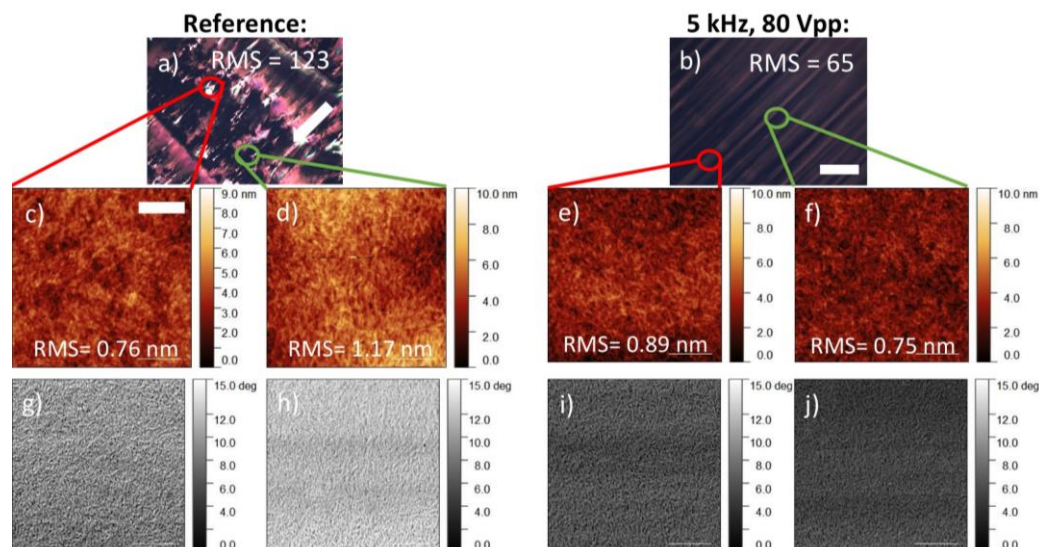


Figure 8.14: (a, b) CPOM images, (c-f) AFM topology images, and (g-j) AFM phase images of films sheared (left) and piezosheared (right) from DPP6DO-TT/CF. White arrows indicate the coating direction. Scale bar in (b): 500 μm . Scale bar in (c): 500 nm.

At the frequencies for which smooth films are obtained, an increase in the effective charge carrier mobility could be due to better alignment, more extended polymer chains, or less contact resistance. Figure 8.15a displays the values of the effective charge carrier mobility, as defined by Choi et al.,[12] for various frequencies of the piezosheared DPP6DO-TT/CF semiconductor solution. Typical curves for the electrical characteristics are displayed in Figure 8.15b-d. The effective charge carrier mobility, however, does not seem to be affected despite the different film morphology. We could imagine, however, that the smooth top surface is beneficial when a top-gate architecture is being used.

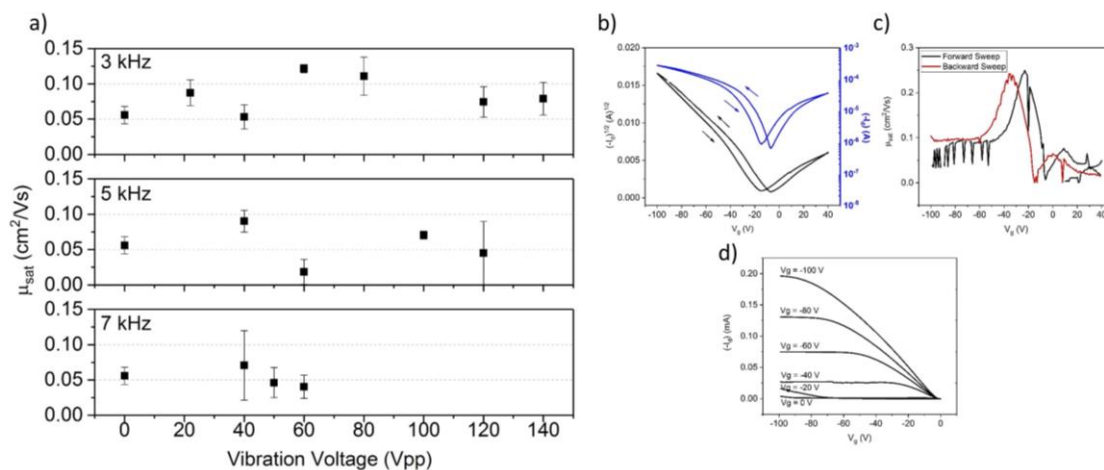


Figure 8.15: Electrical characteristics for films piezosheared from DPP6DO-TT/CF. (a) Effective charge carrier mobility values for vibration frequencies of 3, 5, and 7 kHz. (b) Transfer curve, (c) gate-voltage-dependent mobility, and (d) output curves for a typical device sheared from DPP6DO-TT/CF. The curves are those from the reference sample.

The DPP6DO-TT/CB polymer system (Figure 8.16f to i) is used to test whether the smoothing effect would be reproducible for different polymer systems, and the use of CB at a higher shearing temperature was expected to yield higher effective charge carrier mobility values. The average effective mobility improves only very slightly or does not improve at all, as is shown in Figure 8.16.

The films were also characterized by GIWAXS. In Figure 8.17, images for the DPP6DO-TT/CF and DPP6DO-T/CF polymer films are shown. In the films formed, the

polymer chains tend to align face-on. Although the chemical structure of the polymer is not so different from DPP4DE-TT/CF, the two differ in the preferred molecular alignment relative to the surface (DPP4DE-TT tends to pack mostly edge-on), and thus device performance. It has been reported in various works that different side-chain structures can yield different positioning of the backbone[65] and different π - π distances,[21] both influencing charge carrier mobility.

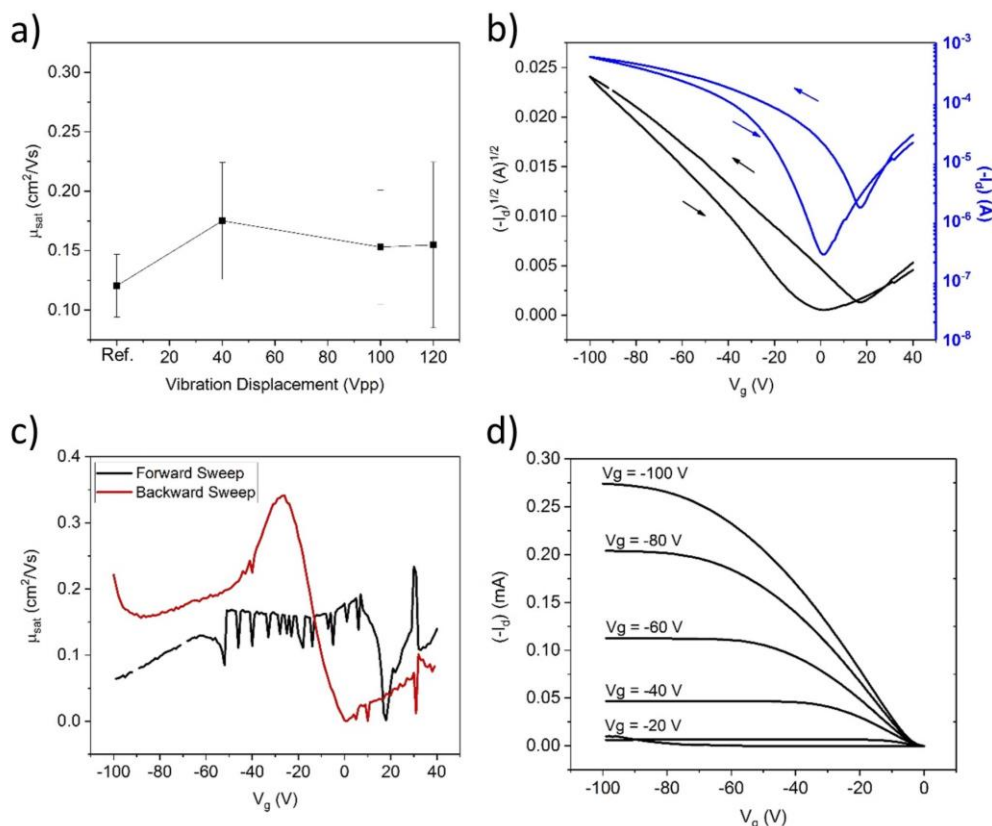


Figure 8.16: (a) Effective charge carrier mobility values for DPP4DE-TT/CB, piezosheared at 5 kHz and varying displacement amplitudes. (b) Transfer curve, (c) gate-voltage-dependent mobility, and (d) output curves for devices coated at 5 kHz, 40 Vpp.

No significant change is observed for the GIWAXS images for the films sheared with and without vibration. There is no change in the π - π stacking distance, and the peak intensity at $q_z \sim 1.74 \text{ \AA}^{-1}$ changes, but it has likely to do with the thickness change in the film. The out-of-plane tendency of stacking of the material also does not seem to change with the application of vibrations.

We speculate that the azimuthal instabilities along the contact line could change the degree of chain alignment during the solvent evaporation due to capillary forces. However, this cannot be evaluated because the reference films are highly non-uniform, and comparing intensities would not be possible. Figure 8.18a displays the effective charge carrier mobility values for the DPP6DO-T/CF polymer system. The charge carrier mobility also does not present any change.

For all the materials observed, films are significantly smoother and more uniform. It is believed that the amount of material used for coating the entire surfaces with the polymer is reduced by using the piezoshearing. Because most of the solution-sheared films are so rough and non-uniform, estimating thicknesses is challenging. For the DPP6DO-T/CF system, however, two thickness values seem predominant – that of the thin film, and that of stick-and-slip instabilities. In Figure 8.18b and Figure 8.18d, the reference film, and the film piezosheared at 5 kHz, 80 Vpp are compared. The film thicknesses are displayed

in the corresponding image. Through image treatment for detecting the thicker areas (Figure 8.18c), it is possible to estimate the volume of material used. It is fair to point out that, by using piezoshearing, 30% of the DPP6DO-T material was saved, compared to the conventional solution shearing.

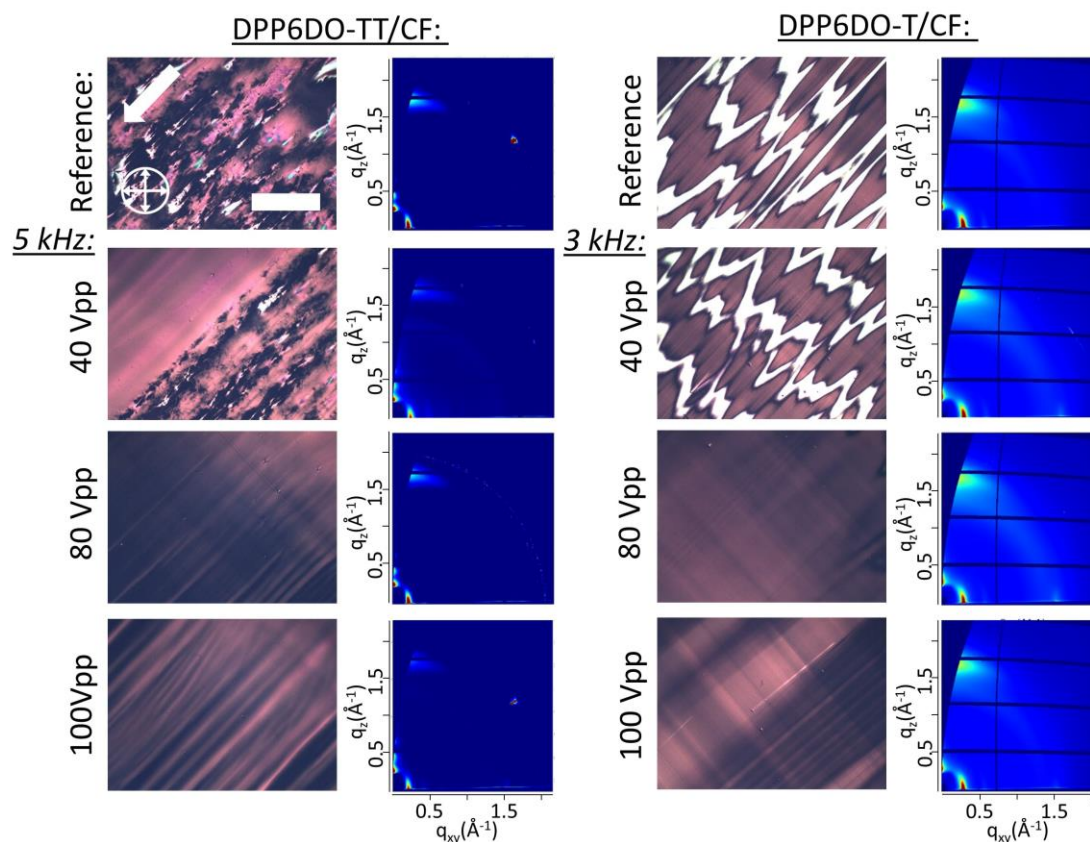


Figure 8.17: CPOM films for DPP6DO-TT/CF (left) and DPP6DO-T/CF (right), with the respective GIWAXS measurements. The beam is incident to the sample in the direction parallel to the coating direction. The frequency used for the piezoshearing of DPP6DO-TT/CF is of 5 kHz, and the one used for DPP6DO-T/CF is 3 kHz. Scale bar: 500 μm .

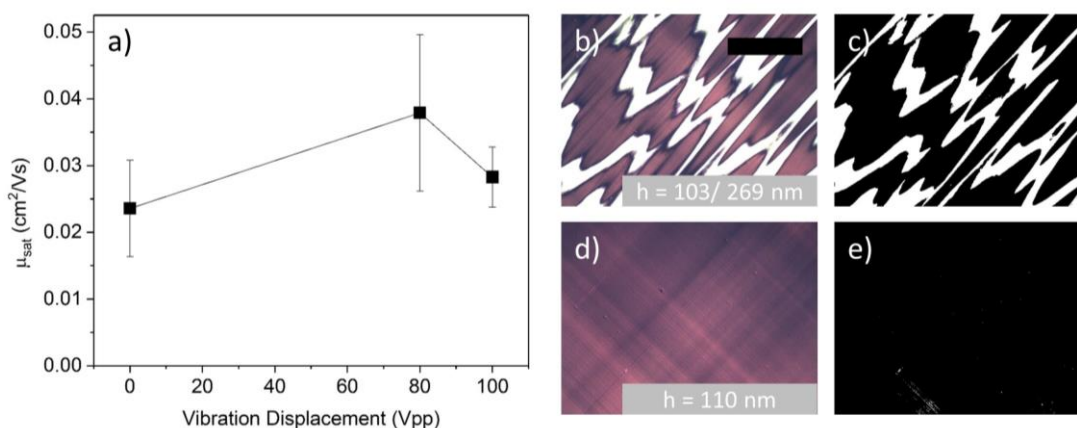


Figure 8.18: (a) Effective charge carrier mobility values for the DPP6DO-T/CF polymer system. The (b) reference sample has two film thicknesses (values for the thin and thick part of the film in the image are in the right bottom corner) and is treated with an intensity threshold algorithm for measuring the area covered by each film thickness. (c) The equivalent regions for the thick and the thin regions of the polymeric film. The black region is the area where the film is thin, and the white area is the area where the film is thick. (d) Piezosheared sample with a frequency of 5 kHz and 80 Vpp. (e) The same optical intensity threshold that was used for the reference sample is applied to this film for comparison. Scale bar: 500 μm .

8.5 Piezoshearing as a Parametric Oscillator System

In this study, one more aspect of the piezoshearing method is investigated. It has been observed that piezoshearing changes the pinning and de-pinning cycles, forms more continuous films, possibly changes crystalline formation, and provokes the appearance of instabilities parallel to the coating direction. The system is relatively complex, and it is challenging to describe what occurs during the piezoshearing process. Different effects have been observed for different materials and shearing conditions, but a comparison of different semiconductor systems is rather complicated. Different materials have several parameters that differ from each other, such as molecular structure, molecular weight, the tendency to aggregate, viscosity, and surface tension. Because of so many parameters, comparing our semiconductor systems is therefore not a trivial task, and to deconvolute how each characteristic affects the effect obtained from the piezoshearing is a challenge. Besides, due to the dynamic character of the method, effects taken into account are just the ones that somehow reflect on the solute deposit.

In the following, essential aspects to consider when approaching vibration in the shearing of liquids are introduced. We attempt to describe the piezoshearing setup as a parametric oscillating system, where existing equations can describe how the physical characteristics of the receding meniscus affect the total movement of the system. This is mostly for qualitative analysis and comparison between different semiconductor solutions, which have significantly different liquid properties and a discussion on why different effects are observed for different shearing conditions. If the piezoshearing setup is combined with the receding meniscus as a parametric oscillator, a schematic close to the one shown in Figure 8.19 can be drawn. The comparison has been made in previous works in an attempt to better understand the behavior of liquids submitted to vibration.[64], [177], [208], [209] The receding meniscus is an oscillating system, with elastic characteristics depending on the nature of the liquid and surface characteristics. The vibration induced by the piezo crystal is the external vibration source.

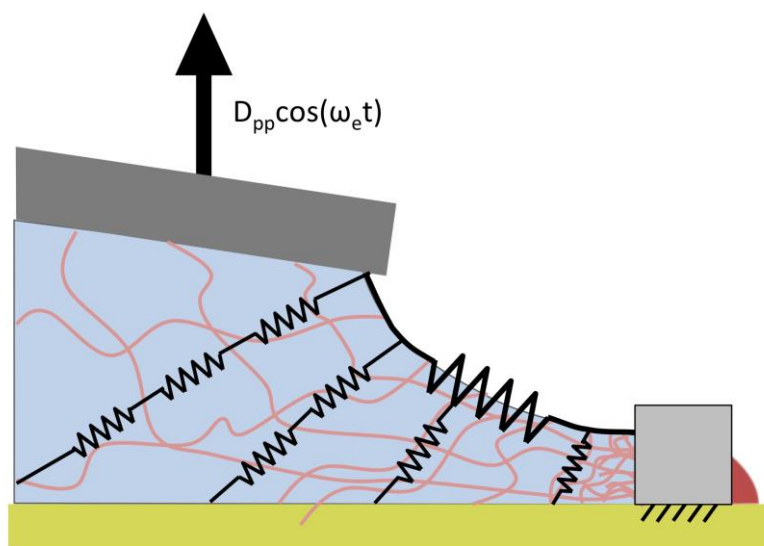


Figure 8.19: Schematic illustration of the piezoshearing setup as a parametric oscillator. The receding meniscus itself is an oscillating system, and the external vibration applied to the system is applied by the piezo actuator. The grey block at the contact line represents a friction element.

Therefore, the system can be considered to behave accordingly to the general parametric oscillator equation:[208], [209], [300]

$$\ddot{u} + \omega_m^2(1 + h \cos\omega_d t)u + \lambda\dot{u} + \mu \operatorname{sgn}(\dot{u}) = 0 \quad (8.1)$$

In Equation (8.1), u describes the displacement of the vibrating meniscus system, ω_m is the natural frequency of the system, ω_d is the driving external oscillation frequency, h is the amplitude of the external oscillating force, λ is the viscosity damping, and μ is the amplitude of the friction oscillator.

8.5.1 Solid Friction

The last term of Equation (8.1), the friction component, is what is mostly responsible for the behavior of the contact line. It is the reason for the stick-and-slip and determines the conditions under which the contact line can be de-pinned or not by a certain amount of energy introduced by the vibration movement.[301] Factors that determine the intensity of friction are gravity (tends to flatten the liquid), the surface tension of the liquid (tends to diminish the surface area of the liquid and prevents it from wetting the substrate), and the surface energy of the substrate.[208] Therefore, the intensity of the friction component will be dependent on the volume and concentration of the liquid, the surface tension of the liquid, the spreading on the surface, and the surface energy.

Noblin et al. make use of the solid friction in a parametric oscillator to attempt to predict the necessary acceleration to set the contact line into motion. They estimate the necessary acceleration threshold to depend on the equilibrium contact angle of the liquid on the substrate, and on the contact angle hysteresis, as mentioned in Chapter 7. The less likely the liquid is to spread on the surface, the easier it is to displace the CL; and the lower the contact angle hysteresis, the less flexible the contact line is to value changes and the lower the energy necessary to move it.[208]

We believe a moving contact line is present in the regime of the piezoshearing in Chapter 7, and that it is present in this Chapter as well. The accelerations at which the contact line moves is likely to be due to the very different liquid characteristics between the low concentrations used in Chapter 7, and the high concentrations and high M_w polymers in Chapter 8. We believe the contact line to move before the appearance of the Faraday instabilities for the DPP4DE-TT/ CF, and DPP6DO-T/CF polymeric semiconductor systems. Although there is no evidence of a moving contact line in the deposited solute for the polymer DPP6DO-TT, we do not discount that this may occur. As described in Chapter 7, the depinning of the contact line depends on the nature of the substrate, the surface tension of the liquid, and the dynamics of the contact line depending on the shearing speed.

8.5.2 Viscosity

The viscosity component μ determines the damping of the system when vibrations are applied to it. Both the bulk damping and the viscosity at the solid-liquid interface can act as damping sources. Therefore the viscosity of the liquid can lead to energy dissipation, and more energy is required to affect the liquid.[174], [177], [190]

Another effect of using a viscous liquid is that limited-size effects can be less pronounced. It has been shown that if the damping length of a liquid is smaller than a recipient, the system can be considered to have infinite size.[174]

8.5.3 Transition Between Regimes

As has been described by Noblin et al.,[209], there are two stages for a vibrating drop. To obtain a free contact line, an energy barrier (or acceleration threshold) has to be overcome; and for it to form Faraday instabilities, a second acceleration threshold should be overcome. This is similar to the effects observed in the experiments with polymer materials in this work. Therefore, two main regimes are observed: that of a moving contact line, and that of Faraday Instabilities. Once the acceleration increases, there is either ejection or dewetting.

When the acceleration threshold is overcome, the contact line of the meniscus acts as a source of dissipation for the system in addition to the liquid's viscosity. Pinned and depinned contact lines have different effects on the transmission of a surface wave on a liquid. Previous studies have shown that even a small meniscus at the edges of a flat liquid surface of a large container has an energy dissipation effect on the liquid and acceleration thresholds for observing Faraday instabilities increase.[174], [175]

Although different materials have different conditions under which they remain pinned, the sheared polymer solutions used in this work are vulnerable to dissipation through the contact line because of the stick-and-slip patterns observed in the films deposited. As has been observed in Chapter 7, the contact line of the meniscus can go through phases of pinning or depinning. We hypothesize the surface tension to be one of the defining factors of the pinning conditions, and speed and viscosity indirect factors. Although the contact line might be pinned under a specific condition, enough displacement from the vibration is enough to set it in motion and then trigger a new source of dissipation. So dissipation through the contact line is considered a source of energy loss for the piezoshearing setup.

The acceleration threshold value for the instabilities parallel to the shearing direction to occur will depend on the ratio of viscosity and dissipation of the system.[177]. As has been approached by several previous works, the acceleration threshold for occurrence of Faraday instabilities is significantly affected by the energy dissipation from the viscosity, the viscosity of the liquid-substrate line tension, or from the movement of the contact line.[177], [189], [299] When approaching a resonance frequency, if enough vibration displacement is applied, ejection of the ink occurs. This has been observed for numerous solutions systems, with different materials, concentrations, and shearing conditions.

8.6 Summary

In this study, the effect of the piezoshearing method on viscous polymers is investigated. The study was done as an attempt to modify film morphology and to increase in-plane chain alignment or crystallinity in the thin films.

Differences in the stick-and-slip pattern are observed, and smoother films are obtained, which was also observed in Chapter 7. Morphology changes at the microstructure level of the material occurred for the DPP4DE-TT-based thin films. It is, however, not wholly understood if chain alignment changes or if crystalline populations increase in the piezosheared samples. To clearly understand what happens to the polymer conformation clearly, more detailed GIWAXS measurements (e.g., full substrate rotation) would be needed. The difference in morphology does not improve the charge carrier mobility of bottom-gate OFETs. We believe the mobility differences to be more significant for top-gate devices since the top surface of the film is the part that seems to have the highest degree of alignment in the film and the region most influenced by the piezoshearing.

The piezoshearing of the high- M_w materials DPP6DO-TT and DPP6DO-T also presented different morphology patterns. The films coated are much smoother, uniform, and presented what appear to be Faraday instabilities, and the usage of semiconductor material is decreased due to the lack of blotches on the substrate. However, no significant charge carrier mobility change is observed for such films.

Although a few changes are observed, these are not significant enough to affirm they had a positive impact on device performance. A few reasons for this could be that the vibration of the blade does not produce flow with a large enough magnitude to promote polymer disentanglement, or that, there is not enough time during the solution shearing method for this to occur. It is also possible that due to the large film thickness, the effect of the vibration does not reach the bottom surface of the film, therefore not affecting mobility for bottom-gate devices. For the cases where ultrasonic vibrations are used, the flow produced by cavitation exerts a large amount of energy (as discussed in Chapter 4), and samples are left in sonication baths for periods of minutes. This is different from the application of vibration for seconds, as is the case for piezoshearing and possibly not enough vibration energy is inserted in the system to observe such significant morphology change.

Chapter 9

9 Conclusion and Outlook

Conclusion

The focus of this work is devoted to the improvement of the performance of Organic Field-Effect Transistors through a fabrication method scalable to large-scale deposition. The fabrication of high-performance OFETs, at a rate that is commercially feasible, is currently a challenge in the field of organic electronics. High-performance devices such as single-crystal materials are not feasible for mass production, and the materials that can be deposited at high coating speeds, such as amorphous polymers, have limited performance. The fabrication method that is considered the most realistic for commercialization of organic electronic materials is through solution deposition, which can be adapted to roll-to-roll processing methods. These enable a high printing speed on flexible and transparent substrates. In this work, modifications of the solution shearing process are applied for improving charge carrier mobility and improving fabrication conditions for semiconductors.

In the first part of this work, the blending of the small-molecule crystalline material TIPS-pentacene with an inert dielectric was optimized, and highly aligned crystalline structures were achieved through optimization of coating speed and ink formulation. The feasibility of such high performing devices for low-voltage applications was demonstrated by depositing the optimized blend on a very thin layer of a cross-linked polymer dielectric. For an optimized device, the effective charge carrier mobility reached was of $1.23 \text{ cm}^2 \text{ V}^{-1} \text{ s}^{-1}$, and an operating voltage of 1 V.

This work proposes a modification of the solution shearing process for enhancing crystal growth. Although the blended semiconductor formulation yields high charge carrier mobility devices, the films are far from being single-crystals, as a previous work had been able to achieve through intricate blade patterning. A vibrating mechanism for the shearing blade was implemented to attempt enhancing crystal growth. The vibrations were applied to the receding meniscus through the embedding of a piezo actuator to the shearing blade - the method was named “piezoshearing”. The vibrations applied to the receding meniscus were expected to stir the semiconductor solution at the contact line and delay supersaturation. This was expected to hinder secondary nucleation and enable single crystalline structures. No improvement was observed in the piezoshearing of the small-

molecule TIPS-pentacene, and the vibration was detrimental to crystal-growth in the small-molecule: polymer blend by inducing stick-and-slip. The piezoshearing showed, however, in preliminary results that it can form a more continuous film for the C₈-BTBT semiconductor small-molecule through increasing the area of coverage of the substrate.

After high-performance devices were obtained for the small-molecules TIPS-pentacene and C₈-BTBT, the focus of this work was shifted towards the solution shearing of polymer semiconductors. Proper control of polymer morphology for the field of semiconductors is still somewhat limited, and often high-performance polymer OFET fabrication methods require a long time for processing due to the time necessary for disentangling and self-assembling of ordered structures. In addition to that, the deposition procedure for polymeric materials can be quite challenging. For polymer FET devices, substrates with low surface energies are required for excellent electrical performance. This considerably limits the deposition speed of the semiconductor, an essential factor if upscaling of polymer OFETs is to happen. In this work we have demonstrated that the piezoshearing changes the pinning and depinning dynamic of the contact line during deposition, mitigates the stick-and-slip instabilities that occur from poor wetting, allowing ultrathin films to be deposited on a non-wetting substrate. Due to full substrate coverage with ultrathin films (~ 7nm), two-thirds of the semiconducting material can be spared. Because of significantly better coverage of the films, the shearing speeds can be doubled, and the charge carrier mobility has been improved by two orders of magnitude. This result is relevant for the coating of thin films in general. The stick-and-slip instability is observed to some extent in every deposition method that involves an evaporating contact line. The use of vibration for mitigating of pinning can be extended to numerous applications in different fields.

Finally, the piezoshearing method was used to investigate if polymer alignment or improvement in film crystallinity is possible through vibration. Viscous polymer solutions were used in this study to prevent dewetting that can also be caused by the piezoshearing. One of the polymers utilized in this work presented a change in morphology, which appears to be an increase in chain alignment or crystallite population. For the other two tested polymer materials, the film morphology changed significantly. Materials that presented very rough and non-uniform films due to the high viscosity without vibration yielded very smooth films, saving up to 70% in material for one of the materials. Although changes in morphology were attained, the charge carrier mobility was not changed for bottom-gate devices.

Outlook

Although improvements in the solution deposition of organic semiconductors have been made in this work, this is just an initial step to demonstrate the potential of adapting the solution shearing method for reaching further benefits. To better understand the piezoshearing and how to better controls its parameters, further study, and optimization is needed. In this section, aspects that need improving are suggested.

One of the main difficulties of this project was the wide range of frequency conditions that could be tested. While trying to approach a resonance frequency for the semiconductor material being used, a wide range of frequencies was tested, requiring a significant amount of material and time. A fast and straightforward method of testing the most effective frequency conditions was not available, and there are no existing works similar to our project. Calculating or modeling vibration conditions that would activate some result in the coating of films was very time-consuming, and would probably require a project of its own to be implemented. For example, due to the complex shape of the liquid

under the blade, and its constant changing volume due to solvent evaporation, calculating the resonance frequency of the system would be a lengthy task by itself.

For a better comprehension of the piezoshearing mechanism on the polymer solution, theoretical, and computational work needs to be done for the specific case of the receding meniscus. Due to the combination of multiple processes, such as the solvent evaporation, the dynamic contact line, boundaries of the meniscus, and the effect of different frequency conditions on different solutions, it is not a trivial task to fully unmask all the underlying processes during piezoshearing.

The solution shearing in its current setup is limited by the lack of constant material supply during the coating process. The resonance frequency of a liquid depends on the volume and the shape of the liquid. If the volume of the solution is changing, the response of the liquid to the vibration changes as well and evaluating the uniformity of films, or transient conditions can be challenging. Ideally, there should be a supply of solution that allows a constant amount of liquid to be present under the shearing blade. In terms of experimental improvements for further studies, the power the piezo actuator can transduce to the liquid can also be improved. The piezoshearing prototype built in this work was limited in terms of displacement. For higher frequencies, higher displacement can be achieved if a bigger piezo stack would be used, or if a more potent amplifier were used.

For a more detailed understanding of how strongly the polymer morphology is affected by the piezoshearing, a systematic study should be conducted for a polymeric system where polymer features - such as M_w or regioregularity- can be separately controlled. P3HT is the most commonly used polymer for such studies, and obtaining polymer materials with different conditions is more easily done than for other commercialized polymers.

The piezoshearing method can be extended to the general field of coatings for applications that require thin and uniform films. It is not uncommon that pinning stands as a hindrance for film deposition. We strongly believe the piezoshearing method is highly beneficial for the community in thin-film fabrication.

Appendix

A.1 OFET data for devices from Chapter 7

Coating Speed (mm/s)	Vibration Displacement (Vpp)	Channel Direction in relation to the coating direction	Mobility (cm ² /Vs)	V _{th} (V)	Ion/off	
1	none	Parallel	0.14 ± 0.035	-10.3 ± 4.05	6.22 × 10 ³	
		Perpendicular	0.11 ± 0.009	-16.4 ± 2.13	2.67 × 10 ³	
	20	Parallel	0.19 ± 0.029	-7.8 ± 3.26	1.84 × 10 ³	
		Perpendicular	0.22 ± 0.023	-2.6 ± 2.76	2.52 × 10 ³	
	40	Parallel	0.14 ± 0.019	-5.7 ± 6.94	4.84 × 10 ³	
		Perpendicular	0.15 ± 0.013	-11 ± 3.09	5.14 × 10 ³	
	100	Parallel	0.17 ± 0.031	-0.2 ± 3.52	7.93 × 10 ³	
		Perpendicular	0.19 ± 0.020	-1.5 ± 4.23	2.53 × 10 ³	
	140	Parallel	0.17 ± 0.057	-5.7 ± 5.65	5.50 × 10 ²	
		Perpendicular	0.21 ± 0.006	-12.8 ± 3.09	1.28 × 10 ³	
	1.4	none	Parallel	0.08 ± 0.052	-8 ± 4.88	1.20 × 10 ⁵

	20	Perpendicular	0.09 ± 0.013	-15.2 ± 2.42	1.15×10^5	
		Parallel	0.15 ± 0.026	-4.1 ± 5.98	1.81×10^4	
	40	Perpendicular	0.004 ± 0.003	-3.4 ± 2.70	1.91×10^5	
		Parallel	0.03 ± 0.030	-28.7 ± 13.67	4.49×10^4	
	100	Perpendicular	0.004 ± 0.003	-14 ± 1.51	1.05×10^4	
		Parallel	0.002 ± 0.005	-5.875 ± 6.44	3.73×10^3	
	140	Perpendicular	0.06 ± 0.018	3.25 ± 2.58	1.29×10^4	
		Parallel	0.03 ± 0.059	-3.25 ± 6.75	1.42×10^4	
		none	Perpendicular	0.05 ± 0.022	4.9 ± 2.83	4.27×10^3
			Parallel	0.0006 ± 0.0002	19.83 ± 5.42	2.25×10^3
	1.8	20	Perpendicular	0.0572 ± 0.0161	9.25 ± 3.45	1.53×10^4
			Parallel	0.002 ± 0.0024	-41.12 ± 4.56	2.09×10^4
		40	Perpendicular	0.0090 ± 0.0088	-41.12 ± 4.56	2.36×10^3
			Parallel	0.10 ± 0.0098	-15.2 ± 1.12	1.29×10^5
100		Perpendicular	0.1318 ± 0.0039	-11.4 ± 0.37	1.29×10^4	
		Parallel	0.0015 ± 0.0013	-40 ± 5	1.81×10^3	
140		Perpendicular	0.0582 ± 0.0245	-37.5 ± 9.26	1.47×10^3	
		Parallel	0.0009 ± 0.0015	2.12 ± 5.54	2.70×10^2	
		none	Perpendicular	0.0582 ± 0.0245	-12.00 ± 4.71	4.51×10^5
			Parallel	0.0009 ± 0.0015	2.12 ± 5.54	2.70×10^2

2.2	none	Parallel	0.00001 ± 0.000013	15 ± 3	6.78×10^1
		Perpendicular	0.0007 ± 0.0001	-7.33 ± 9.33	6.50×10^3
	20	Parallel	0.00011 ± 0.00022	-62.1 ± 5.96	3.12×10^2
		Perpendicular	0.0035 ± 0.0062	-39.25 ± 6.45	5.76×10^3
	40	Parallel	0.0063 ± 0.0093	-35.66 ± 12.42	2.06×10^4
		Perpendicular	0.0088 ± 0.0010	3 ± 0.81	3.98×10^4
	100	Parallel	0.0238 ± 0.0246	-15.37 ± 3.50	1.71×10^5
		Perpendicular	0.0150 ± 0.0105	-16.87 ± 2.96	2.83×10^4
	140	Parallel	0.0034 ± 0.0025	5 ± 0.70	2.77×10^4
		Perpendicular	0.0166 ± 0.0043	3.83 ± 6.19	9.86×10^4

Table A.1: Mobility, threshold voltage, and on/off ratio for devices coated from DPP4DE-TT /CF.

Coating Speed (mm/s)	Vibration Displacement (Vpp)	Channel Direction in relation to the coating direction	Mobility (cm ² /Vs)	V _{th} (V)	I _{on/off}	
1	none	Parallel	0.00537 ± 0.00047	-20.33 ± 0.57	1.91 × 10 ²	
		Perpendicular	0.00339 ± 0.00029	-16.5 ± 0.5	8.82 × 10 ²	
	20	Parallel	0.00360 ± 0.00017	-20.83 ± 0.62	7.77 × 10 ²	
		Perpendicular	0.00246 ± 0.00054	-15.33 ± 0.23	2.30 × 10 ²	
	40	Parallel	0.00785 ± 0.00135	-14.16 ± 1.02	1.37 × 10 ²	
		Perpendicular	0.00278 ± 0.00037	-8.5 ± 1.08	9.24 × 10 ¹	
	100	Parallel	0.00409 ± 0.00024	-15.16 ± 0.62	1.55 × 10 ²	
		Perpendicular	0.00422 ± 0.00179	-10 ± 0.81	6.9 × 10 ¹	
	140	Parallel	0.00288 ± 0.0057	3.5 ± 12.72	1.05 × 10 ²	
		Perpendicular	0.00212 ± 0.0079	9.16 ± 12.14	6.70 × 10 ¹	
	1.4	none	Parallel	0.00017 ± 0.00005	11.66 ± 3.40	4.18 × 10 ³
			Perpendicular	0.00083 ± 0.00013	-9 ± 12.27	1.23 × 10 ³
		20	Parallel	0.00055 ± 0.00009	-28.16 ± 1.31	7.42 × 10 ²
			Perpendicular	0.00056 ± 0.00010	-28 ± 1.08	8.66 × 10 ²
40		Parallel	0.00065 ± 0.000051	4.16 ± 0.62	7.87 × 10 ²	
		Perpendicular	0.00173 ± 0.00021	15.33 ± 0.23	3.64 × 10 ²	

	100	Parallel	0.00187 ± 0.00039	-16.5 ± 1.41	1.37×10^2	
		Perpendicular	0.00118 ± 0.00019	-15.16 ± 1.64	1.10×10^2	
	140	Parallel	0.00031 ± 0.00003	-20.66 ± 0.47	2.22×10^1	
		Perpendicular	0.00025 ± 0.00003	-11.83 ± 12.97	4.54×10^1	
1.8	none	Parallel	0.00016 ± 0.00008	-32.66 ± 2.02	1.74×10^4	
		Perpendicular	0.00076 ± 0.0006	-10.33 ± 1.25	6.99×10^2	
	20	Parallel	0.00008 ± 0.00005	-34.5 ± 2.12	5.76×10^2	
		Perpendicular	0.00041 ± 0.00012	-21 ± 2.27	5.48×10^2	
	40	Parallel	0.00077 ± 0.00069	-11 ± 15.23	3.28×10^2	
		Perpendicular	0.00063 ± 0.00045	-9.66 ± 1.69	2.72×10^2	
	100	Parallel	0.00094 ± 0.00043	-20.66 ± 1.43	7.68×10^2	
		Perpendicular	0.00074 ± 0.00029	-16.5 ± 1.63	2.26×10^2	
	140	Parallel	0.00027 ± 0.00004	-23.6 ± 2.24	6.14×10^1	
		Perpendicular	0.00017 ± 0.00004	-24.25 ± 1.25	5.34×10^1	
	2.2	none	Parallel	0.00022 ± 0.00009	-36.33 ± 1.52	8.49×10^2
			Perpendicular	0.00051 ± 0.00008	-22.5 ± 1.5	2.25×10^3
20		Parallel	0.00038 ± 0.00003	-29.33 ± 1.31	8.76×10^2	
		Perpendicular	0.00073 ± 0.00030	-17 ± 1.08	1.67×10^3	
40		Parallel	0.00037 ± 0.00008	-26 ± 1.87	1.22×10^3	

	100	Perpendicular	0.00176 ± 0.00040	-5.16 ± 0.47	2.72×10^2
		Parallel	0.00278 ± 0.00219	-7 ± 7.25	1.59×10^2
	140	Perpendicular	0.00219 ± 0.00110	-14.66 ± 1.17	6.49×10^2
		Parallel	0.00071 ± 0.00058	-1 ± 2.16	5.02×10^2
		Perpendicular	0.00079 ± 0.00034	-3.16 ± 1.24	1.47×10^3

Table A.2: Mobility, threshold voltage, and on/off ratio for devices coated from PCDTPT/CF.

Coating Speed (mm/s)	Vibration Displacement (V _{pp})	Channel Direction in relation to the coating direction	Mobility (cm ² /Vs)	V _{th} (V)	I _{on/off}	
1	none	Parallel	0.223 ± 0.0688	-16 ± 0.5	4.74 × 10 ³	
		Perpendicular	0.163 ± 0.0088	-8.33 ± 1.25	2.89 × 10 ³	
	20	Parallel	0.328 ± 0.0586	-10.83 ± 2.84	1.86 × 10 ³	
		Perpendicular	0.157 ± 0.0048	-7.83 ± 0.57	1.41 × 10 ³	
	40	Parallel	0.332 ± 0.0910	-10.1 ± 2.63	8.87 × 10 ²	
		Perpendicular	0.205 ± 0.0926	-10.16 ± 1.60	5.90 × 10 ²	
	100	Parallel	0.278 ± 0.0634	-10.33 ± 3.01	6.92 × 10 ²	
		Perpendicular	0.100 ± 0.0302	-1.16 ± 3.32	5.52 × 10 ²	
	140	Parallel	0.142 ± 0.0231	-13.66 ± 1.25	4.19 × 10 ²	
		Perpendicular	0.069 ± 0.0023	-14.33 ± 0.57	1.88 × 10 ²	
	1.2	none	Parallel	0.199 ± 0.0341	-12.83 ± 3.01	8.93 × 10 ²
			Perpendicular	0.102 ± 0.0072	-12.83 ± 1.04	7.27 × 10 ²
20		Parallel	0.180 ± 0.0603	-13.16 ± 3.88	4.91 × 10 ³	
		Perpendicular	0.106 ± 0.0234	-14 ± 0.5	2.43 × 10 ³	
40		Parallel	0.263 ± 0.0216	-6.33 ± 7.68	3.06 × 10 ³	
		Perpendicular	0.105 ± 0.0050	-11.33 ± 1.44	2.52 × 10 ³	

	100	Parallel	0.287 ± 0.0399	-13 ± 0.5	1.60×10^3
		Perpendicular	0.133 ± 0.0177	-9.83 ± 3.32	1.34×10^3
	140	Parallel	0.136 ± 0.0172	-16.33 ± 1.15	6.13×10^2
		Perpendicular	0.076 ± 0.0032	-13.66 ± 0.28	5.02×10^2
1.4	none	Parallel	0.058 ± 0.0575	-16 ± 2.78	9.65×10^2
		Perpendicular	0.048 ± 0.0016	-1.5 ± 12.61	7.51×10^2
	20	Parallel	0.074 ± 0.0700	-13.5 ± 4.44	6.06×10^2
		Perpendicular	0.063 ± 0.0172	3.16 ± 15.82	6.86×10^2
	40	Parallel	0.046 ± 0.0153	-16.75 ± 0.35	3.48×10^3
		Perpendicular	0.152 ± 0.0018	-13.66 ± 0.28	1.87×10^4
	100	Parallel	0.115 ± 0.0414	-18.5 ± 1.80	1.59×10^4
		Perpendicular	0.062 ± 0.0055	-17 ± 1	6.08×10^3
	140	Parallel	0.084 ± 0.0138	-18 ± 2.17	2.63×10^3
		Perpendicular	0.057 ± 0.0052	-15.5 ± 1.32	2.09×10^3

Table A.3: Mobility, threshold voltage, and on/off ratio for devices coated from PCDTPT/CB.

Bibliography

- [1] J. Kang, J. B.-H. Tok, and Z. Bao, "Self-healing soft electronics," *Nat. Electron.*, vol. 2, no. 4, pp. 144–150, Apr. 2019, doi: 10.1038/s41928-019-0235-0.
- [2] D. Son *et al.*, "An integrated self-healable electronic skin system fabricated via dynamic reconstruction of a nanostructured conducting network," *Nat. Nanotechnol.*, vol. 13, no. 11, pp. 1057–1065, Nov. 2018, doi: 10.1038/s41565-018-0244-6.
- [3] B. Razavi, *Fundamentals of microelectronics*, Second edition. Hoboken, NJ: Wiley, John Wiley & Sons, Inc, 2014.
- [4] J. Nitta *et al.*, "The actual electronic band structure of a rubrene single crystal," *Sci. Rep.*, vol. 9, no. 1, p. 9645, Dec. 2019, doi: 10.1038/s41598-019-46080-4.
- [5] K. Haase, C. Teixeira da Rocha, C. Hauenstein, Y. Zheng, M. Hamsch, and S. C. B. Mannsfeld, "High-Mobility, Solution-Processed Organic Field-Effect Transistors from C8-BTBT:Polystyrene Blends," *Adv. Electron. Mater.*, vol. 4, no. 8, p. 1800076, Aug. 2018, doi: 10.1002/aelm.201800076.
- [6] G. C. Schmidt *et al.*, "Fully printed flexible audio system on the basis of low-voltage polymeric organic field effect transistors with three layer dielectric," *J. Polym. Sci. Part B Polym. Phys.*, vol. 53, no. 20, pp. 1409–1415, Oct. 2015, doi: 10.1002/polb.23778.
- [7] Z. Bao and J. J. Locklin, Eds., *Organic field-effect transistors*. Boca Raton: CRC Press, 2007.
- [8] A. Köhler and H. Bässler, *Electronic Processes in Organic Semiconductors: An Introduction*. John Wiley & Sons, 2015.
- [9] H. Phan, M. J. Ford, A. T. Lill, M. Wang, G. C. Bazan, and T.-Q. Nguyen, "Electrical Double-Slope Nonideality in Organic Field-Effect Transistors," *Adv. Funct. Mater.*, p. 1707221, Feb. 2018, doi: 10.1002/adfm.201707221.
- [10] H. Sirringhaus, "Device Physics of Solution-Processed Organic Field-Effect Transistors," *Adv. Mater.*, vol. 17, no. 20, pp. 2411–2425, Oct. 2005, doi: 10.1002/adma.200501152.
- [11] A. Troisi, "Charge transport in high mobility molecular semiconductors: classical models and new theories," *Chem. Soc. Rev.*, vol. 40, no. 5, p. 2347, 2011, doi: 10.1039/c0cs00198h.
- [12] H. H. Choi, K. Cho, C. D. Frisbie, H. Sirringhaus, and V. Podzorov, "Critical assessment of charge mobility extraction in FETs," *Nat. Mater.*, vol. 17, no. 1, p. 2, 2017.
- [13] L. Giraudet and O. Simonetti, "Threshold voltage and turn-on voltage in organic transistors: Sensitivity to contact parasitics," *Org. Electron.*, vol. 12, no. 1, pp. 219–225, Jan. 2011, doi: 10.1016/j.orgel.2010.11.002.

- [14] C. Liu, Y. Xu, and Y.-Y. Noh, "Contact engineering in organic field-effect transistors," *Mater. Today*, vol. 18, no. 2, pp. 79–96, Mar. 2015, doi: 10.1016/j.mattod.2014.08.037.
- [15] A. Kahn, "Fermi level, work function and vacuum level," *Mater. Horiz.*, vol. 3, no. 1, pp. 7–10, 2016, doi: 10.1039/C5MH00160A.
- [16] S. J. Lee *et al.*, "Analysis of charge injection and contact resistance as a function of electrode surface treatment in ambipolar polymer transistors," *Electron. Mater. Lett.*, vol. 14, no. 1, pp. 1–6, Jan. 2018, doi: 10.1007/s13391-017-6414-0.
- [17] I. Kaur *et al.*, "Substituent Effects in Pentacenes: Gaining Control over HOMO–LUMO Gaps and Photooxidative Resistances," *J. Am. Chem. Soc.*, vol. 130, no. 48, pp. 16274–16286, Dec. 2008, doi: 10.1021/ja804515y.
- [18] H. Kobayashi *et al.*, "Hopping and band mobilities of pentacene, rubrene, and 2,7-dioctyl[1]benzothieno[3,2-*b*][1]benzothiophene (C₈-BTBT) from first principle calculations," *J. Chem. Phys.*, vol. 139, no. 1, p. 014707, Jul. 2013, doi: 10.1063/1.4812389.
- [19] Z. Chen *et al.*, "High-Performance Ambipolar Diketopyrrolopyrrole-Thieno[3,2-*b*]thiophene Copolymer Field-Effect Transistors with Balanced Hole and Electron Mobilities," *Adv. Mater.*, vol. 24, no. 5, pp. 647–652, Feb. 2012, doi: 10.1002/adma.201102786.
- [20] L. Ying *et al.*, "Regioregular Pyridal[2,1,3]thiadiazole π -Conjugated Copolymers," *J. Am. Chem. Soc.*, vol. 133, no. 46, pp. 18538–18541, Nov. 2011, doi: 10.1021/ja207543g.
- [21] M. Hamsch *et al.*, "Increased charge carrier mobility and molecular packing of a solution sheared diketopyrrolopyrrole-based donor–acceptor copolymer by alkyl side chain modification," *J. Mater. Chem. C*, 2019, doi: 10.1039/C8TC06255B.
- [22] S. Lee *et al.*, "Enhanced Charge Injection in Pentacene Field-Effect Transistors with Graphene Electrodes," *Adv. Mater.*, vol. 23, no. 1, pp. 100–105, Jan. 2011, doi: 10.1002/adma.201003165.
- [23] B. J. Worfolk *et al.*, "Ultrahigh electrical conductivity in solution-sheared polymeric transparent films," *Proc. Natl. Acad. Sci.*, vol. 112, no. 46, pp. 14138–14143, Nov. 2015, doi: 10.1073/pnas.1509958112.
- [24] N. Kim *et al.*, "Highly Conductive PEDOT:PSS Nanofibrils Induced by Solution-Processed Crystallization," *Adv. Mater.*, vol. 26, no. 14, pp. 2268–2272, Apr. 2014, doi: 10.1002/adma.201304611.
- [25] M. Kano, T. Minari, and K. Tsukagoshi, "Improvement of subthreshold current transport by contact interface modification in p-type organic field-effect transistors," *Appl. Phys. Lett.*, vol. 94, no. 14, p. 143304, Apr. 2009, doi: 10.1063/1.3115826.
- [26] T. Uemura *et al.*, "On the Extraction of Charge Carrier Mobility in High-Mobility Organic Transistors," *Adv. Mater.*, vol. 28, no. 1, pp. 151–155, Jan. 2016, doi: 10.1002/adma.201503133.
- [27] L.-L. Chua, P. K. H. Ho, H. Sirringhaus, and R. H. Friend, "Observation of Field-Effect Transistor Behavior at Self-Organized Interfaces," *Adv. Mater.*, vol. 16, no. 18, pp. 1609–1615, Sep. 2004, doi: 10.1002/adma.200400392.
- [28] S. Y. Park, M. Park, and H. H. Lee, "Cooperative polymer gate dielectrics in organic thin-film transistors," *Appl. Phys. Lett.*, vol. 85, no. 12, pp. 2283–2285, Sep. 2004, doi: 10.1063/1.1794857.
- [29] U. Zschieschang *et al.*, "Flexible low-voltage organic thin-film transistors and circuits based on C₁₀-DNTT," *J Mater Chem*, vol. 22, no. 10, pp. 4273–4277, 2012, doi: 10.1039/C1JM14917B.

- [30] U. Zschieschang *et al.*, “Megahertz operation of flexible low-voltage organic thin-film transistors,” *Org. Electron.*, vol. 14, no. 6, pp. 1516–1520, Jun. 2013, doi: 10.1016/j.orgel.2013.03.021.
- [31] G. Grau and V. Subramanian, “Fully High-Speed Gravure Printed, Low-Variability, High-Performance Organic Polymer Transistors with Sub-5 V Operation,” *Adv. Electron. Mater.*, vol. 2, no. 4, p. 1500328, Apr. 2016, doi: 10.1002/aelm.201500328.
- [32] S. Conti, S. Lai, P. Cosseddu, and A. Bonfiglio, “An Inkjet-Printed, Ultralow Voltage, Flexible Organic Field Effect Transistor,” *Adv. Mater. Technol.*, vol. 2, no. 2, p. 1600212, Feb. 2017, doi: 10.1002/admt.201600212.
- [33] L. Feng, C. Jiang, H. Ma, X. Guo, and A. Nathan, “All ink-jet printed low-voltage organic field-effect transistors on flexible substrate,” *Org. Electron.*, vol. 38, pp. 186–192, Nov. 2016, doi: 10.1016/j.orgel.2016.08.019.
- [34] A. Facchetti, “Semiconductors for organic transistors,” *Mater. Today*, vol. 10, no. 3, pp. 28–37, 2007.
- [35] K. B. R. Teja and N. Gupta, “Low-k polymer gate dielectric selection for organic thin-film transistors (OTFTs) using material selection methodologies,” *J. Comput. Electron.*, May 2019, doi: 10.1007/s10825-019-01343-1.
- [36] J. Veres, S. Ogier, G. Lloyd, and D. de Leeuw, “Gate Insulators in Organic Field-Effect Transistors,” *Chem. Mater.*, vol. 16, no. 23, pp. 4543–4555, 2004, doi: 10.1021/cm049598q.
- [37] M.-H. Yoon, H. Yan, A. Facchetti, and T. J. Marks, “Low-Voltage Organic Field-Effect Transistors and Inverters Enabled by Ultrathin Cross-Linked Polymers as Gate Dielectrics,” *J. Am. Chem. Soc.*, vol. 127, no. 29, pp. 10388–10395, Jul. 2005, doi: 10.1021/ja052488f.
- [38] K. Haase, J. Zessin, K. Zouboulis, M. Müller, M. Hamsch, and S. C. B. Mannsfeld, “Solution Shearing of a High-Capacitance Polymer Dielectric for Low-Voltage Organic Transistors,” *Adv. Electron. Mater.*, p. 1900067, Apr. 2019, doi: 10.1002/aelm.201900067.
- [39] D. Knipp, R. A. Street, B. Krusor, J. Ho, and R. B. Apte, “Influence of The Dielectric on The Growth and Performance of Pentacene Thin Film Transistors,” *MRS Proc.*, vol. 708, p. BB8.10, 2001, doi: 10.1557/PROC-708-BB8.10.
- [40] J. Rivnay, S. C. B. Mannsfeld, C. E. Miller, A. Salleo, and M. F. Toney, “Quantitative Determination of Organic Semiconductor Microstructure from the Molecular to Device Scale,” *Chem. Rev.*, vol. 112, no. 10, pp. 5488–5519, Oct. 2012, doi: 10.1021/cr3001109.
- [41] S. S. Lee *et al.*, “Controlling Nucleation and Crystallization in Solution-Processed Organic Semiconductors for Thin-Film Transistors,” *Adv. Mater.*, vol. 21, no. 35, pp. 3605–3609, Sep. 2009, doi: 10.1002/adma.200900705.
- [42] J. Rivnay *et al.*, “Large modulation of carrier transport by grain-boundary molecular packing and microstructure in organic thin films,” *Nat. Mater.*, vol. 8, no. 12, pp. 952–958, Dec. 2009, doi: 10.1038/nmat2570.
- [43] S. C. B. Mannsfeld, M. L. Tang, and Z. Bao, “Thin Film Structure of Triisopropylsilylethynyl-Functionalized Pentacene and Tetraceno[2,3-b]thiophene from Grazing Incidence X-Ray Diffraction,” *Adv. Mater.*, vol. 23, no. 1, pp. 127–131, Jan. 2011, doi: 10.1002/adma.201003135.
- [44] O. D. Jurchescu *et al.*, “Effects of polymorphism on charge transport in organic semiconductors,” *Phys. Rev. B*, vol. 80, no. 8, Aug. 2009, doi: 10.1103/PhysRevB.80.085201.
- [45] S. Illig *et al.*, “Reducing dynamic disorder in small-molecule organic semiconductors by suppressing large-amplitude thermal motions,” *Nat. Commun.*, vol. 7, no. 1, p. 10736, Apr. 2016, doi: 10.1038/ncomms10736.

- [46] T. Uemura *et al.*, “Band-like transport in solution-crystallized organic transistors,” *Curr. Appl. Phys.*, vol. 12, pp. S87–S91, Dec. 2012, doi: 10.1016/j.cap.2012.05.046.
- [47] F. V. Farmakis, J. Brini, G. Kamarinos, C. T. Angelis, C. A. Dimitriadis, and M. Miyasaka, “On-current modeling of large-grain polycrystalline silicon thin-film transistors,” *IEEE Trans. Electron Devices*, vol. 48, no. 4, pp. 701–706, 2001.
- [48] G. Horowitz, “Organic thin film transistors: From theory to real devices,” *J. Mater. Res.*, vol. 19, no. 7, pp. 1946–1962, Jul. 2004, doi: 10.1557/JMR.2004.0266.
- [49] V. Coropceanu, J. Cornil, D. A. da Silva Filho, Y. Olivier, R. Silbey, and J.-L. Brédas, “Charge Transport in Organic Semiconductors,” *Chem. Rev.*, vol. 107, no. 4, pp. 926–952, Apr. 2007, doi: 10.1021/cr050140x.
- [50] A. R. Chew *et al.*, “Unraveling the Effect of Conformational and Electronic Disorder in the Charge Transport Processes of Semiconducting Polymers,” *Adv. Funct. Mater.*, vol. 28, no. 41, p. 1804142, Oct. 2018, doi: 10.1002/adfm.201804142.
- [51] R. Noriega *et al.*, “A general relationship between disorder, aggregation and charge transport in conjugated polymers,” *Nat. Mater.*, vol. 12, no. 11, pp. 1038–1044, Aug. 2013, doi: 10.1038/nmat3722.
- [52] D. Wu *et al.*, “Blade Coating Aligned, High-Performance, Semiconducting-Polymer Transistors,” *Chem. Mater.*, Feb. 2018, doi: 10.1021/acs.chemmater.7b04835.
- [53] G. Qu *et al.*, “Understanding Interfacial Alignment in Solution Coated Conjugated Polymer Thin Films,” *ACS Appl. Mater. Interfaces*, vol. 9, no. 33, pp. 27863–27874, Aug. 2017, doi: 10.1021/acsami.7b08133.
- [54] F.-J. Lin *et al.*, “Directional Solution Coating by the Chinese Brush: A Facile Approach to Improving Molecular Alignment for High-Performance Polymer TFTs,” *Adv. Mater.*, p. 1606987, Jul. 2017, doi: 10.1002/adma.201606987.
- [55] K. Müllen and W. Pisula, “Donor–Acceptor Polymers,” *J. Am. Chem. Soc.*, vol. 137, no. 30, pp. 9503–9505, Aug. 2015, doi: 10.1021/jacs.5b07015.
- [56] D. Venkateshvaran *et al.*, “Approaching disorder-free transport in high-mobility conjugated polymers,” *Nature*, vol. 515, no. 7527, pp. 384–388, Nov. 2014, doi: 10.1038/nature13854.
- [57] Y. Zhao *et al.*, “Complementary Semiconducting Polymer Blends for Efficient Charge Transport,” *Chem. Mater.*, vol. 27, no. 20, pp. 7164–7170, Oct. 2015, doi: 10.1021/acs.chemmater.5b03349.
- [58] X. Zhao *et al.*, “Complementary Semiconducting Polymer Blends: The Influence of Conjugation-Break Spacer Length in Matrix Polymers,” *Macromolecules*, vol. 49, no. 7, pp. 2601–2608, Apr. 2016, doi: 10.1021/acs.macromol.6b00050.
- [59] K. S. Park *et al.*, “Tuning conformation, assembly, and charge transport properties of conjugated polymers by printing flow,” *Sci. Adv.*, vol. 5, no. 8, p. eaaw7757, Aug. 2019, doi: 10.1126/sciadv.aaw7757.
- [60] K. Zhao, H. U. Khan, R. Li, Y. Su, and A. Amassian, “Entanglement of Conjugated Polymer Chains Influences Molecular Self-Assembly and Carrier Transport,” *Adv. Funct. Mater.*, vol. 23, no. 48, pp. 6024–6035, Dec. 2013, doi: 10.1002/adfm.201301007.
- [61] F. C. Grozema and L. D. A. Siebbeles, “Charge Mobilities in Conjugated Polymers Measured by Pulse Radiolysis Time-Resolved Microwave Conductivity: From Single Chains to Solids,” *J. Phys. Chem. Lett.*, vol. 2, no. 23, pp. 2951–2958, Dec. 2011, doi: 10.1021/jz201229a.
- [62] A. R. Aiyar, J.-I. Hong, R. Nambiar, D. M. Collard, and E. Reichmanis, “Tunable Crystallinity in Regioregular Poly(3-Hexylthiophene) Thin Films and Its Impact on Field Effect Mobility,” *Adv. Funct. Mater.*, vol. 21, no. 14, pp. 2652–2659, Jul. 2011, doi: 10.1002/adfm.201002729.

- [63] H.-R. Tseng *et al.*, “High-Mobility Field-Effect Transistors Fabricated with Macroscopic Aligned Semiconducting Polymers,” *Adv. Mater.*, vol. 26, no. 19, pp. 2993–2998, May 2014, doi: 10.1002/adma.201305084.
- [64] H. Sirringhaus *et al.*, “Two-dimensional charge transport in self-organized, high-mobility conjugated polymers,” *Nature*, vol. 401, no. 6754, pp. 685–688, Oct. 1999, doi: 10.1038/44359.
- [65] M. Saito, T. Koganezawa, and I. Osaka, “Understanding Comparable Charge Transport Between Edge-on and Face-on Polymers in a Thiazolothiazole Polymer System,” *ACS Appl. Polym. Mater.*, vol. 1, no. 6, pp. 1257–1262, Jun. 2019, doi: 10.1021/acsapm.8b00111.
- [66] R. R. Søndergaard, M. Hösel, and F. C. Krebs, “Roll-to-Roll fabrication of large area functional organic materials,” *J. Polym. Sci. Part B Polym. Phys.*, vol. 51, no. 1, pp. 16–34, Jan. 2013, doi: 10.1002/polb.23192.
- [67] X. Gu *et al.*, “Roll-to-Roll Printed Large-Area All-Polymer Solar Cells with 5% Efficiency Based on a Low Crystallinity Conjugated Polymer Blend,” *Adv. Energy Mater.*, vol. 7, no. 14, p. 1602742, Jul. 2017, doi: 10.1002/aenm.201602742.
- [68] J. Xu *et al.*, “Multi-scale ordering in highly stretchable polymer semiconducting films,” *Nat. Mater.*, vol. 18, no. 6, pp. 594–601, Jun. 2019, doi: 10.1038/s41563-019-0340-5.
- [69] D. H. Kim, J. A. Lim, W. Cha, J. H. Lee, H. Kim, and J. H. Cho, “Directed self-assembly of organic semiconductors via confined evaporative capillary flows for use in organic field-effect transistors,” *Org. Electron.*, vol. 15, no. 10, pp. 2322–2327, Oct. 2014, doi: 10.1016/j.orgel.2014.06.022.
- [70] H. S. Lee, D. Kwak, W. H. Lee, J. H. Cho, and K. Cho, “Self-Organization Characteristics of Soluble Pentacene on Wettability-Controlled Patterned Substrate for Organic Field-Effect Transistors,” *J. Phys. Chem. C*, vol. 114, no. 5, pp. 2329–2333, Feb. 2010, doi: 10.1021/jp909227b.
- [71] H. Minemawari *et al.*, “Inkjet printing of single-crystal films,” *Nature*, vol. 475, no. 7356, pp. 364–367, Jul. 2011, doi: 10.1038/nature10313.
- [72] E. L. Paul, H.-H. Tung, and M. Midler, “Organic crystallization processes,” *Powder Technol.*, vol. 150, no. 2, pp. 133–143, Feb. 2005, doi: 10.1016/j.powtec.2004.11.040.
- [73] Y. Diao, L. Shaw, Z. Bao, and S. C. B. Mannsfeld, “Morphology control strategies for solution-processed organic semiconductor thin films,” *Energy Env. Sci.*, vol. 7, no. 7, pp. 2145–2159, May 2014, doi: 10.1039/C4EE00688G.
- [74] H. A. Becerril, M. E. Roberts, Z. Liu, J. Locklin, and Z. Bao, “High-Performance Organic Thin-Film Transistors through Solution-Sheared Deposition of Small-Molecule Organic Semiconductors,” *Adv. Mater.*, vol. 20, no. 13, pp. 2588–2594, Jul. 2008, doi: 10.1002/adma.200703120.
- [75] M. Le Berre, Y. Chen, and D. Baigl, “From Convective Assembly to Landau–Levich Deposition of Multilayered Phospholipid Films of Controlled Thickness,” *Langmuir*, vol. 25, no. 5, pp. 2554–2557, Mar. 2009, doi: 10.1021/la803646e.
- [76] S. Galindo, A. Tamayo, F. Leonardi, and M. Mas-Torrent, “Control of Polymorphism and Morphology in Solution Sheared Organic Field-Effect Transistors,” *Adv. Funct. Mater.*, p. 1700526, Apr. 2017, doi: 10.1002/adfm.201700526.
- [77] H. W. Ro *et al.*, “Morphology changes upon scaling a high-efficiency, solution-processed solar cell,” *Energy Environ. Sci.*, vol. 9, no. 9, pp. 2835–2846, 2016, doi: 10.1039/C6EE01623E.
- [78] J. Wan *et al.*, “Transient phases during fast crystallization of organic thin films from solution,” *APL Mater.*, vol. 4, no. 1, p. 016103, Jan. 2016, doi: 10.1063/1.4939464.

- [79] R. D. Deegan, O. Bakajin, T. F. Dupont, G. Huber, S. R. Nagel, and T. A. Witten, "Capillary flow as the cause of ring stains from dried liquid drops," *Nature*, vol. 389, p. 3, 1997, doi: 10.1038/39827.
- [80] R. D. Deegan, O. Bakajin, T. F. Dupont, G. Huber, S. R. Nagel, and T. A. Witten, "Contact line deposits in an evaporating drop," *Phys. Rev. E*, vol. 62, no. 1, p. 756, 2000.
- [81] L. E. Scriven and C. V. Sternling, "The marangoni effects," *Nature*, vol. 187, no. 4733, p. 186, 1960.
- [82] M. Kaneda, K. Hyakuta, H. Ishizuka, and J. Fukai, "Effect of the Initial Solute Concentration on the Flow Pattern Inside an Evaporating Polymer Solution Droplet on a Substrate," in *ASME/JSME 2007 Thermal Engineering Heat Transfer Summer Conference collocated with the ASME 2007 InterPACK Conference*, 2007, pp. 1091–1097.
- [83] P. J. Yunker, T. Still, M. A. Lohr, and A. G. Yodh, "Suppression of the coffee-ring effect by shape-dependent capillary interactions," *Nature*, vol. 476, no. 7360, pp. 308–311, Aug. 2011, doi: 10.1038/nature10344.
- [84] X. Fanton and A. M. Cazabat, "Spreading and instabilities induced by a solutal Marangoni effect," *Langmuir*, vol. 14, no. 9, pp. 2554–2561, 1998.
- [85] B. B. Patel and Y. Diao, "Multiscale assembly of solution-processed organic electronics: the critical roles of confinement, fluid flow, and interfaces," *Nanotechnology*, vol. 29, no. 4, p. 044004, Jan. 2018, doi: 10.1088/1361-6528/aa9d7c.
- [86] M. Majumder *et al.*, "Overcoming the 'Coffee-Stain' Effect by Compositional Marangoni-Flow-Assisted Drop-Drying," *J. Phys. Chem. B*, vol. 116, no. 22, pp. 6536–6542, Jun. 2012, doi: 10.1021/jp3009628.
- [87] H. J. Park, M.-G. Kang, S. H. Ahn, and L. J. Guo, "A Facile Route to Polymer Solar Cells with Optimum Morphology Readily Applicable to a Roll-to-Roll Process without Sacrificing High Device Performances," *Adv. Mater.*, vol. 22, no. 35, pp. E247–E253, Sep. 2010, doi: 10.1002/adma.201000250.
- [88] Z. Wang, Z. Ma, and L. Li, "Flow-Induced Crystallization of Polymers: Molecular and Thermodynamic Considerations," *Macromolecules*, vol. 49, no. 5, pp. 1505–1517, Mar. 2016, doi: 10.1021/acs.macromol.5b02688.
- [89] R. J. Davey, S. L. M. Schroeder, and J. H. ter Horst, "Nucleation of Organic Crystals-A Molecular Perspective," *Angew. Chem. Int. Ed.*, vol. 52, no. 8, pp. 2166–2179, Feb. 2013, doi: 10.1002/anie.201204824.
- [90] J. Xu *et al.*, "Probing the interfacial molecular packing in TIPS-pentacene organic semiconductors by surface enhanced Raman scattering," *J Mater Chem C*, vol. 2, no. 16, pp. 2985–2991, 2014, doi: 10.1039/C3TC32581D.
- [91] G. Giri *et al.*, "Tuning charge transport in solution-sheared organic semiconductors using lattice strain," *Nature*, vol. 480, no. 7378, pp. 504–508, Dec. 2011, doi: 10.1038/nature10683.
- [92] Y. Diao *et al.*, "Solution coating of large-area organic semiconductor thin films with aligned single-crystalline domains," *Nat Mater*, vol. 12, no. 7, pp. 665–671, Jul. 2013.
- [93] H. Chung and Y. Diao, "Polymorphism as an emerging design strategy for high performance organic electronics," *J Mater Chem C*, vol. 4, no. 18, pp. 3915–3933, 2016, doi: 10.1039/C5TC04390E.
- [94] G. Giri *et al.*, "One-dimensional self-confinement promotes polymorph selection in large-area organic semiconductor thin films," *Nat. Commun.*, vol. 5, Apr. 2014, doi: 10.1038/ncomms4573.

- [95] Y. Diao *et al.*, “Understanding Polymorphism in Organic Semiconductor Thin Films through Nanoconfinement,” *J. Am. Chem. Soc.*, vol. 136, no. 49, pp. 17046–17057, Dec. 2014, doi: 10.1021/ja507179d.
- [96] J. Chen *et al.*, “Conjugated Polymer-Mediated Polymorphism of a High Performance, Small-Molecule Organic Semiconductor with Tuned Intermolecular Interactions, Enhanced Long-Range Order, and Charge Transport,” *Chem. Mater.*, vol. 25, no. 21, pp. 4378–4386, Nov. 2013, doi: 10.1021/cm403039y.
- [97] Y. Yuan *et al.*, “Ultra-high mobility transparent organic thin film transistors grown by an off-centre spin-coating method,” *Nat. Commun.*, vol. 5, Jan. 2014, doi: 10.1038/ncomms4005.
- [98] F. Molina-Lopez, H. Yan, X. Gu, Y. Kim, M. F. Toney, and Z. Bao, “Electric Field Tuning Molecular Packing and Electrical Properties of Solution-Shearing Coated Organic Semiconducting Thin Films,” *Adv. Funct. Mater.*, vol. 27, no. 8, p. 1605503, Feb. 2017, doi: 10.1002/adfm.201605503.
- [99] R. Janneck, F. Vercesi, P. Heremans, J. Genoe, and C. Rolin, “Predictive Model for the Meniscus-Guided Coating of High-Quality Organic Single-Crystalline Thin Films,” *Adv. Mater.*, vol. 28, no. 36, pp. 8007–8013, Sep. 2016, doi: 10.1002/adma.201602377.
- [100] J.-O. Kim *et al.*, “Inorganic Polymer Micropillar-Based Solution Shearing of Large-Area Organic Semiconductor Thin Films with Pillar-Size-Dependent Crystal Size,” *Adv. Mater.*, vol. 30, no. 29, p. 1800647, Jul. 2018, doi: 10.1002/adma.201800647.
- [101] C. Xiao *et al.*, “Controlled formation of large-area single-crystalline TIPS-pentacene arrays through superhydrophobic micropillar flow-coating,” *J Mater Chem C*, vol. 5, no. 10, pp. 2702–2707, 2017, doi: 10.1039/C6TC04704A.
- [102] G. Giri, S. Park, M. Vosgueritchian, M. M. Shulaker, and Z. Bao, “High-Mobility, Aligned Crystalline Domains of TIPS-Pentacene with Metastable Polymorphs Through Lateral Confinement of Crystal Growth,” *Adv. Mater.*, vol. 26, no. 3, pp. 487–493, Jan. 2014, doi: 10.1002/adma.201302439.
- [103] M. R. Niazi *et al.*, “Solution-printed organic semiconductor blends exhibiting transport properties on par with single crystals,” *Nat. Commun.*, vol. 6, p. 8598, Nov. 2015, doi: 10.1038/ncomms9598.
- [104] M. R. Niazi *et al.*, “Contact-Induced Nucleation in High-Performance Bottom-Contact Organic Thin Film Transistors Manufactured by Large-Area Compatible Solution Processing,” *Adv. Funct. Mater.*, vol. 26, no. 14, pp. 2371–2378, Apr. 2016, doi: 10.1002/adfm.201502428.
- [105] A. F. Paterson *et al.*, “Small Molecule/Polymer Blend Organic Transistors with Hole Mobility Exceeding $13 \text{ cm}^2 \text{ V}^{-1} \text{ s}^{-1}$,” *Adv. Mater.*, vol. 28, no. 35, pp. 7791–7798, Sep. 2016, doi: 10.1002/adma.201601075.
- [106] J. Smith *et al.*, “Solution-Processed Small Molecule-Polymer Blend Organic Thin-Film Transistors with Hole Mobility Greater than $5 \text{ cm}^2/\text{Vs}$,” *Adv. Mater.*, vol. 24, no. 18, pp. 2441–2446, May 2012, doi: 10.1002/adma.201200088.
- [107] Z. Zhang, B. Peng, X. Ji, K. Pei, and P. K. L. Chan, “Marangoni-Effect-Assisted Bar-Coating Method for High-Quality Organic Crystals with Compressive and Tensile Strains,” *Adv. Funct. Mater.*, vol. 27, no. 37, p. 1703443, Oct. 2017, doi: 10.1002/adfm.201703443.
- [108] M. Muthukumar and P. Welch, “Modeling polymer crystallization from solutions,” *Polymer*, vol. 41, no. 25, pp. 8833–8837, Dec. 2000, doi: 10.1016/S0032-3861(00)00226-3.
- [109] P. Welch and M. Muthukumar, “Molecular Mechanisms of Polymer Crystallization from Solution,” *Phys. Rev. Lett.*, vol. 87, no. 21, p. 218302, Nov. 2001, doi: 10.1103/PhysRevLett.87.218302.

- [110] Y.-K. Lan and A.-C. Su, "Nucleation of Polymer Crystals: The 'δ Mystery,'" *Macromolecules*, vol. 43, no. 19, pp. 7908–7912, Oct. 2010, doi: 10.1021/ma101078a.
- [111] X. Gu, L. Shaw, K. Gu, M. F. Toney, and Z. Bao, "The meniscus-guided deposition of semiconducting polymers," *Nat. Commun.*, vol. 9, no. 1, Dec. 2018, doi: 10.1038/s41467-018-02833-9.
- [112] J. Chang *et al.*, "Controlling aggregation and crystallization of solution processed diketopyrrolopyrrole based polymer for high performance thin film transistors by pre-metered slot die coating process," *Org. Electron.*, vol. 36, pp. 113–119, Sep. 2016, doi: 10.1016/j.orgel.2016.06.003.
- [113] F. Molina-Lopez *et al.*, "Enhancing Molecular Alignment and Charge Transport of Solution-Sheared Semiconducting Polymer Films by the Electrical-Blade Effect," *Adv. Electron. Mater.*, vol. 4, no. 7, p. 1800110, Jul. 2018, doi: 10.1002/aelm.201800110.
- [114] Y. D. Park, J. K. Park, W. H. Lee, B. Kang, K. Cho, and G. C. Bazan, "Post-deposition dipping method for improving the electronic properties of a narrow bandgap conjugated polymer," *J. Mater. Chem.*, vol. 22, no. 23, p. 11462, 2012, doi: 10.1039/c2jm31183f.
- [115] S. Kim *et al.*, "Sequential solvent casting for improving the structural ordering and electrical characteristics of polythiophene thin films," *RSC Adv*, vol. 4, no. 77, pp. 41159–41163, 2014, doi: 10.1039/C4RA06311B.
- [116] I. M. Ward, *Structure and Properties of Oriented Polymers*. Dordrecht: Springer Netherlands, 1997.
- [117] P. Dyreklev, G. Gustafsson, O. Inganäs, and H. Stubb, "Aligned polymer chain field effect transistors," *Solid State Commun.*, vol. 82, no. 5, pp. 317–320, May 1992, doi: 10.1016/0038-1098(92)90359-H.
- [118] P. Dyreklev, G. Gustafsson, O. Inganäs, and H. Stubb, "Polymeric field effect transistors using oriented polymers," *Synth. Met.*, vol. 57, no. 1, pp. 4093–4098, Apr. 1993, doi: 10.1016/0379-6779(93)90563-C.
- [119] B. O'Connor *et al.*, "Anisotropic Structure and Charge Transport in Highly Strain-Aligned Regioregular Poly(3-hexylthiophene)," *Adv. Funct. Mater.*, vol. 21, no. 19, pp. 3697–3705, Oct. 2011, doi: 10.1002/adfm.201100904.
- [120] J. Lee, A.-R. Han, J. Kim, Y. Kim, J. H. Oh, and C. Yang, "Solution-Processable Ambipolar Diketopyrrolopyrrole–Selenophene Polymer with Unprecedentedly High Hole and Electron Mobilities," *J. Am. Chem. Soc.*, vol. 134, no. 51, pp. 20713–20721, Dec. 2012, doi: 10.1021/ja308927g.
- [121] J. Lee, A.-R. Han, H. Yu, T. J. Shin, C. Yang, and J. H. Oh, "Boosting the Ambipolar Performance of Solution-Processable Polymer Semiconductors via Hybrid Side-Chain Engineering," *J. Am. Chem. Soc.*, vol. 135, no. 25, pp. 9540–9547, Jun. 2013, doi: 10.1021/ja403949g.
- [122] H.-R. Tseng *et al.*, "High Mobility Field Effect Transistors Based on Macroscopically Oriented Regioregular Copolymers," *Nano Lett.*, vol. 12, no. 12, pp. 6353–6357, Dec. 2012, doi: 10.1021/nl303612z.
- [123] M. J. Ford *et al.*, "High Mobility Organic Field-Effect Transistors from Majority Insulator Blends," *Chem. Mater.*, vol. 28, no. 5, pp. 1256–1260, Mar. 2016, doi: 10.1021/acs.chemmater.5b04774.
- [124] Y. Wang *et al.*, "Organic crystalline materials in flexible electronics," *Chem. Soc. Rev.*, vol. 48, no. 6, pp. 1492–1530, 2019, doi: 10.1039/C8CS00406D.
- [125] U. Bielecka, P. Lutsyk, K. Janus, J. Sworakowski, and W. Bartkowiak, "Effect of solution aging on morphology and electrical characteristics of regioregular P3HT

- FETs fabricated by spin coating and spray coating,” *Org. Electron.*, vol. 12, no. 11, pp. 1768–1776, Nov. 2011, doi: 10.1016/j.orgel.2011.06.027.
- [126] P.-H. Chu *et al.*, “Toward Precision Control of Nanofiber Orientation in Conjugated Polymer Thin Films: Impact on Charge Transport,” *Chem. Mater.*, vol. 28, no. 24, pp. 9099–9109, Dec. 2016, doi: 10.1021/acs.chemmater.6b04202.
- [127] M. Chang, J. Lee, N. Kleinhenz, B. Fu, and E. Reichmanis, “Photoinduced Anisotropic Supramolecular Assembly and Enhanced Charge Transport of Poly(3-hexylthiophene) Thin Films,” *Adv. Funct. Mater.*, vol. 24, no. 28, pp. 4457–4465, Jul. 2014, doi: 10.1002/adfm.201400523.
- [128] M. Chang, Z. Su, and E. Egan, “Alignment and Charge Transport of One-Dimensional Conjugated Polymer Nanowires in Insulating Polymer Blends,” *Macromolecules*, vol. 49, no. 24, pp. 9449–9456, Dec. 2016, doi: 10.1021/acs.macromol.6b01721.
- [129] A. R. Aiyar, J.-I. Hong, J. Izumi, D. Choi, N. Kleinhenz, and E. Reichmanis, “Ultrasound-Induced Ordering in Poly(3-hexylthiophene): Role of Molecular and Process Parameters on Morphology and Charge Transport,” *ACS Appl. Mater. Interfaces*, vol. 5, no. 7, pp. 2368–2377, Apr. 2013, doi: 10.1021/am3027822.
- [130] D. Khim *et al.*, “Uniaxial Alignment of Conjugated Polymer Films for High-Performance Organic Field-Effect Transistors,” *Adv. Mater.*, p. 1705463, Mar. 2018, doi: 10.1002/adma.201705463.
- [131] Y. D. Park *et al.*, “Solubility-Induced Ordered Polythiophene Precursors for High-Performance Organic Thin-Film Transistors,” *Adv. Funct. Mater.*, vol. 19, no. 8, pp. 1200–1206, Apr. 2009, doi: 10.1002/adfm.200801763.
- [132] Z. Bao, A. Dodabalapur, and A. J. Lovinger, “Soluble and processable regioregular poly(3-hexylthiophene) for thin film field-effect transistor applications with high mobility,” *Appl. Phys. Lett.*, vol. 69, no. 26, pp. 4108–4110, 1996, doi: <http://dx.doi.org/10.1063/1.117834>.
- [133] S. N. Patel *et al.*, “NEXAFS Spectroscopy Reveals the Molecular Orientation in Blade-Coated Pyridal[2,1,3]thiadiazole-Containing Conjugated Polymer Thin Films,” *Macromolecules*, vol. 48, no. 18, pp. 6606–6616, Sep. 2015, doi: 10.1021/acs.macromol.5b01647.
- [134] E. Mohammadi *et al.*, “Dynamic-template-directed multiscale assembly for large-area coating of highly-aligned conjugated polymer thin films,” *Nat. Commun.*, vol. 8, p. 16070, Jul. 2017, doi: 10.1038/ncomms16070.
- [135] Y. Diao *et al.*, “Flow-enhanced solution printing of all-polymer solar cells,” *Nat. Commun.*, vol. 6, p. 7955, Aug. 2015, doi: 10.1038/ncomms8955.
- [136] S. Schott *et al.*, “Charge-Transport Anisotropy in a Uniaxially Aligned Diketopyrrolopyrrole-Based Copolymer,” *Adv. Mater.*, vol. 27, no. 45, pp. 7356–7364, Dec. 2015, doi: 10.1002/adma.201502437.
- [137] H. Yabu and M. Shimomura, “Preparation of Self-Organized Mesoscale Polymer Patterns on a Solid Substrate: Continuous Pattern Formation from a Receding Meniscus,” *Adv. Funct. Mater.*, vol. 15, no. 4, pp. 575–581, Apr. 2005, doi: 10.1002/adfm.200400315.
- [138] U. Thiele, “Patterned deposition at moving contact lines,” *Adv. Colloid Interface Sci.*, vol. 206, pp. 399–413, Apr. 2014, doi: 10.1016/j.cis.2013.11.002.
- [139] H. S. Kim, C. H. Lee, P. K. Sudeep, T. Emrick, and A. J. Crosby, “Nanoparticle Stripes, Grids, and Ribbons Produced by Flow Coating,” *Adv. Mater.*, vol. 22, no. 41, pp. 4600–4604, Nov. 2010, doi: 10.1002/adma.201001892.
- [140] Y. Liu, D. Y. Lee, C. Monteux, and A. J. Crosby, “Hyperbranched polymer structures via flexible blade flow coating,” *J. Polym. Sci. Part B Polym. Phys.*, vol. 54, no. 1, pp. 32–37, Jan. 2016, doi: 10.1002/polb.23952.

- [141] H. Bodiguel, F. Doumenc, and B. Guerrier, "Stick-Slip Patterning at Low Capillary Numbers for an Evaporating Colloidal Suspension," *Langmuir*, vol. 26, no. 13, pp. 10758–10763, Jul. 2010, doi: 10.1021/la100547j.
- [142] S. Li *et al.*, "High-resolution patterning of solution-processable materials via externally engineered pinning of capillary bridges," *Nat. Commun.*, vol. 9, no. 1, Dec. 2018, doi: 10.1038/s41467-018-02835-7.
- [143] S. Watanabe, K. Inukai, S. Mizuta, and M. T. Miyahara, "Mechanism for Stripe Pattern Formation on Hydrophilic Surfaces by Using Convective Self-Assembly," *Langmuir*, vol. 25, no. 13, pp. 7287–7295, Jul. 2009, doi: 10.1021/la900315h.
- [144] A. Deblais, R. Harich, A. Colin, and H. Kellay, "Taming contact line instability for pattern formation," *Nat. Commun.*, vol. 7, p. 12458, Aug. 2016, doi: 10.1038/ncomms12458.
- [145] D. D. Brewer, T. Shibuta, L. Francis, S. Kumar, and M. Tsapatsis, "Coating Process Regimes in Particulate Film Production by Forced-Convection-Assisted Drag-Out," *Langmuir*, vol. 27, no. 18, pp. 11660–11670, Sep. 2011, doi: 10.1021/la202040x.
- [146] G. Qu, J. J. Kwok, E. Mohammadi, F. Zhang, and Y. Diao, "Understanding Film-to-Stripe Transition of Conjugated Polymers Driven by Meniscus Instability," *ACS Appl. Mater. Interfaces*, Oct. 2018, doi: 10.1021/acsami.8b13790.
- [147] M. Byun, S. W. Hong, L. Zhu, and Z. Lin, "Self-Assembling Semicrystalline Polymer into Highly Ordered, Microscopic Concentric Rings by Evaporation," *Langmuir*, vol. 24, no. 7, pp. 3525–3531, Apr. 2008, doi: 10.1021/la703270c.
- [148] M. E. R. Shanahan, "Simple Theory of 'Stick-Slip' Wetting Hysteresis," *Langmuir*, vol. 11, no. 3, pp. 1041–1043, Mar. 1995, doi: 10.1021/la00003a057.
- [149] M. E. R. Shanahan, "Effects of surface flaws on the wettability of solids," *J. Adhes. Sci. Technol.*, vol. 6, no. 4, pp. 489–501, Jan. 1992, doi: 10.1163/156856192X00818.
- [150] S. Maheshwari, L. Zhang, Y. Zhu, and H.-C. Chang, "Coupling Between Precipitation and Contact-Line Dynamics: Multiring Stains and Stick-Slip Motion," *Phys. Rev. Lett.*, vol. 100, no. 4, Jan. 2008, doi: 10.1103/PhysRevLett.100.044503.
- [151] K. P. Pernstich *et al.*, "Threshold voltage shift in organic field effect transistors by dipole monolayers on the gate insulator," *J. Appl. Phys.*, vol. 96, no. 11, pp. 6431–6438, Dec. 2004, doi: 10.1063/1.1810205.
- [152] S. Kobayashi *et al.*, "Control of carrier density by self-assembled monolayers in organic field-effect transistors," *Nat. Mater.*, vol. 3, no. 5, pp. 317–322, May 2004, doi: 10.1038/nmat1105.
- [153] F. Zhang, E. Mohammadi, X. Luo, J. Strzalka, J. Mei, and Y. Diao, "Critical Role of Surface Energy in Guiding Crystallization of Solution-Coated Conjugated Polymer Thin Films," *Langmuir*, Oct. 2017, doi: 10.1021/acs.langmuir.7b02807.
- [154] H. A. Um, J. Shin, T. W. Lee, M. J. Cho, and D. H. Choi, "Modulation of carrier mobility of diketopyrrolopyrrole and quaterthiophene containing copolymer with self-assembled monolayers on gate dielectrics of thin film transistors," *Synth. Met.*, vol. 184, pp. 61–67, Nov. 2013, doi: 10.1016/j.synthmet.2013.09.020.
- [155] A. Virkar *et al.*, "The Role of OTS Density on Pentacene and C₆₀ Nucleation, Thin Film Growth, and Transistor Performance," *Adv. Funct. Mater.*, vol. 19, no. 12, pp. 1962–1970, Jun. 2009, doi: 10.1002/adfm.200801727.
- [156] Y. Ito *et al.*, "Crystalline Ultrasoother Self-Assembled Monolayers of Alkylsilanes for Organic Field-Effect Transistors," *J. Am. Chem. Soc.*, vol. 131, no. 26, pp. 9396–9404, Jul. 2009, doi: 10.1021/ja9029957.
- [157] L.-L. Chua *et al.*, "General observation of n-type field-effect behaviour in organic semiconductors," *Nature*, vol. 434, no. 7030, pp. 194–199, Mar. 2005, doi: 10.1038/nature03376.

- [158] G. Sauv e *et al.*, “Well-defined, high molecular weight poly(3-alkylthiophene)s in thin-film transistors: side chain invariance in field-effect mobility,” *J. Mater. Chem.*, vol. 20, no. 16, p. 3195, 2010, doi: 10.1039/c000172d.
- [159] L. Fra tia, A. J. Archer, and U. Thiele, “Modelling the formation of structured deposits at receding contact lines of evaporating solutions and suspensions,” *Soft Matter*, vol. 8, no. 44, p. 11363, 2012, doi: 10.1039/c2sm26574e.
- [160] C. Monteux, Y. Elmaallem, T. Narita, and F. Lequeux, “Advancing-drying droplets of polymer solutions: Local increase of the viscosity at the contact line,” *EPL Europhys. Lett.*, vol. 83, no. 3, p. 34005, Aug. 2008, doi: 10.1209/0295-5075/83/34005.
- [161] D. Orejon, K. Sefiane, and M. E. R. Shanahan, “Stick–Slip of Evaporating Droplets: Substrate Hydrophobicity and Nanoparticle Concentration,” *Langmuir*, vol. 27, no. 21, pp. 12834–12843, Nov. 2011, doi: 10.1021/la2026736.
- [162] J. F. Joanny, “A model for contact angle hysteresis,” vol. 81, p. 12, 1984.
- [163] A. Marmur, “Wetting on real surfaces,” *J. Imaging Sci. Technol.*, vol. 44, no. 5, pp. 406–409, 2000.
- [164] R. E. Johnson, R. H. Dettre, and D. A. Brandreth, “Dynamic contact angles and contact angle hysteresis,” *J. Colloid Interface Sci.*, vol. 62, no. 2, pp. 205–212, Nov. 1977, doi: 10.1016/0021-9797(77)90114-X.
- [165] E. L. Decker, B. Frank, Y. Suo, and S. Garoff, “Physics of contact angle measurement,” *Colloids Surf. Physicochem. Eng. Asp.*, vol. 156, no. 1–3, pp. 177–189, 1999, doi: [https://doi.org/10.1016/S0927-7757\(99\)00069-2](https://doi.org/10.1016/S0927-7757(99)00069-2).
- [166] T. S. Meiron, A. Marmur, and I. S. Saguy, “Contact angle measurement on rough surfaces,” *J. Colloid Interface Sci.*, vol. 274, no. 2, pp. 637–644, Jun. 2004, doi: 10.1016/j.jcis.2004.02.036.
- [167] H. B. Eral, D. J. C. M. ’t Mannetje, and J. M. Oh, “Contact angle hysteresis: a review of fundamentals and applications,” *Colloid Polym. Sci.*, vol. 291, no. 2, pp. 247–260, Feb. 2013, doi: 10.1007/s00396-012-2796-6.
- [168] P. Lenz, “Wetting phenomena on structured surfaces,” *Adv. Mater.*, vol. 11, no. 18, pp. 1531–1534, 1999.
- [169] C. Della Volpe, D. Maniglio, S. Siboni, and M. Morra, “An experimental procedure to obtain the equilibrium contact angle from the Wilhelmy method,” *Oil Gas Sci. Technol.*, vol. 56, no. 1, pp. 9–22, 2001.
- [170] M. Faraday, “XVII. On a peculiar class of acoustical figures; and on certain forms assumed by groups of particles upon vibrating elastic surfaces,” *Philos. Trans. R. Soc. Lond.*, no. 121, pp. 299–340, 1831.
- [171] Lord Rayleigh, “VII. *On the crispations of fluid resting upon a vibrating support*,” *Lond. Edinb. Dublin Philos. Mag. J. Sci.*, vol. 16, no. 97, pp. 50–58, Jul. 1883, doi: 10.1080/14786448308627392.
- [172] M. Eslamian, “Excitation by acoustic vibration as an effective tool for improving the characteristics of the solution-processed coatings and thin films,” *Prog. Org. Coat.*, vol. 113, pp. 60–73, Dec. 2017, doi: 10.1016/j.porgcoat.2017.08.008.
- [173] G. Michel, F. P tr elis, and S. Fauve, “Acoustic Measurement of Surface Wave Damping by a Meniscus,” *Phys. Rev. Lett.*, vol. 116, no. 17, p. 174301, Apr. 2016, doi: 10.1103/PhysRevLett.116.174301.
- [174] J. Bechhoefer, V. Ego, S. Manneville, and B. Johnson, “An experimental study of the onset of parametrically pumped surface waves in viscous fluids,” *J. Fluid Mech.*, vol. 288, pp. 325–350, 1995.
- [175] S. Douady, “Experimental study of the Faraday instability,” *J. Fluid Mech.*, vol. 221, pp. 383–409, 1990.
- [176] J. Miles, “On faraday waves,” *J. Fluid Mech.*, vol. 248, pp. 671–683, 1993.

- [177] E. A. Cerda and E. L. Tirapegui, "Faraday's instability in viscous fluid," *J. Fluid Mech.*, vol. 368, pp. 195–228, 1998.
- [178] J. Miles and D. Henderson, "Parametrically Forced Surface Waves," p. 23.
- [179] B. Vukasinovic, M. K. Smith, and A. Glezer, "Dynamics of a sessile drop in forced vibration," *J. Fluid Mech.*, vol. 587, Sep. 2007, doi: 10.1017/S0022112007007379.
- [180] B. Vukasinovic, M. K. Smith, and A. Glezer, "Mechanisms of free-surface breakup in vibration-induced liquid atomization," *Phys. Fluids*, vol. 19, no. 1, p. 012104, Jan. 2007, doi: 10.1063/1.2434799.
- [181] R. W. Wood and A. L. Loomis, "XXXVIII. *The physical and biological effects of high-frequency sound-waves of great intensity*," *Lond. Edinb. Dublin Philos. Mag. J. Sci.*, vol. 4, no. 22, pp. 417–436, Sep. 1927, doi: 10.1080/14786440908564348.
- [182] S. Nii, "Ultrasonic Atomization," in *Handbook of Ultrasonics and Sonochemistry*, M. Ashokkumar, Ed. Singapore: Springer Singapore, 2015, pp. 1–19.
- [183] R. Manasseh, "Acoustic Bubbles, Acoustic Streaming, and Cavitation Microstreaming," in *Handbook of Ultrasonics and Sonochemistry*, Singapore: Springer Singapore, 2016, pp. 33–68.
- [184] C. Eckart, "Vortices and Streams Caused by Sound Waves," *Phys. Rev.*, vol. 73, no. 1, pp. 68–76, Jan. 1948, doi: 10.1103/PhysRev.73.68.
- [185] Lord Rayleigh, "On the Circulation of Air Observed in Kundt's Tubes, and on Some Allied Acoustical Problems," p. 22.
- [186] H. Lamb, *Hydrodynamics*, 6. ed., 1. Cambridge Univ. Press paperback ed. Cambridge: Cambridge Univ. Press, 1993.
- [187] M. Strani and F. Sabetta, "Free vibrations of a drop in partial contact with a solid support," *J. Fluid Mech.*, vol. 141, pp. 233–247, 1984.
- [188] C. Picard and L. Davoust, "Resonance Frequencies of Meniscus Waves as a Physical Mechanism for a DNA Biosensor," *Langmuir*, vol. 23, no. 3, pp. 1394–1402, Jan. 2007, doi: 10.1021/la0624236.
- [189] F. Raynal, S. Kumar, and S. Fauve, "Faraday instability with a polymer solution," *Eur. Phys. J. B-Condens. Matter Complex Syst.*, vol. 9, no. 2, pp. 175–178, 1999.
- [190] K. Kumar and L. S. Tuckerman, "Parametric instability of the interface between two fluids," *J. Fluid Mech.*, vol. 279, no. 1, p. 49, Nov. 1994, doi: 10.1017/S0022112094003812.
- [191] C. A. Miller and L. E. Scriven, "The oscillations of a fluid droplet immersed in another fluid," *J. Fluid Mech.*, vol. 32, no. 3, pp. 417–435, 1968.
- [192] Q. Wang and M. Eslamian, "Improving uniformity and nanostructure of solution-processed thin films using ultrasonic substrate vibration post treatment (SVPT)," *Ultrasonics*, vol. 67, pp. 55–64, Apr. 2016, doi: 10.1016/j.ultras.2015.12.012.
- [193] F. Zabihi and M. Eslamian, "Substrate vibration-assisted spray coating (SVASC): significant improvement in nano-structure, uniformity, and conductivity of PEDOT:PSS thin films for organic solar cells," *J. Coat. Technol. Res.*, vol. 12, no. 4, pp. 711–719, Jul. 2015, doi: 10.1007/s11998-015-9682-3.
- [194] Q. Chen, F. Zabihi, and M. Eslamian, "Improved functionality of PEDOT:PSS thin films via graphene doping, fabricated by ultrasonic substrate vibration-assisted spray coating," *Synth. Met.*, vol. 222, pp. 309–317, Dec. 2016, doi: 10.1016/j.synthmet.2016.11.009.
- [195] A. Rahimzadeh and M. Eslamian, "On evaporation of thin liquid films subjected to ultrasonic substrate vibration," *Int. Commun. Heat Mass Transf.*, vol. 83, pp. 15–22, Apr. 2017, doi: 10.1016/j.icheatmasstransfer.2017.03.004.
- [196] M. Habibi, M. Eslamian, F. Soltani-Kordshuli, and F. Zabihi, "Controlled wetting/dewetting through substrate vibration-assisted spray coating (SVASC)," *J.*

- Coat. Technol. Res.*, vol. 13, no. 2, pp. 211–225, Mar. 2016, doi: 10.1007/s11998-015-9748-2.
- [197] P. J. Diemer *et al.*, “Vibration-Assisted Crystallization Improves Organic/Dielectric Interface in Organic Thin-Film Transistors,” *Adv. Mater.*, vol. 25, no. 48, pp. 6956–6962, Dec. 2013, doi: 10.1002/adma.201302838.
- [198] B.-G. Kim, M.-S. Kim, and J. Kim, “Ultrasonic-Assisted Nanodimensional Self-Assembly of Poly-3-hexylthiophene for Organic Photovoltaic Cells,” *ACS Nano*, vol. 4, no. 4, pp. 2160–2166, Apr. 2010, doi: 10.1021/nn901568w.
- [199] K. Zhao *et al.*, “A New Method to Improve Poly(3-hexyl thiophene) (P3HT) Crystalline Behavior: Decreasing Chains Entanglement To Promote Order–Disorder Transformation in Solution,” *Langmuir*, vol. 26, no. 1, pp. 471–477, Jan. 2010, doi: 10.1021/la903381f.
- [200] Y. Kondo, T. Hiraki, Y. Suenaga, T. Hanasaki, and I. Fujieda, “Vibration-induced mobility enhancement for a polymer transistor,” Feb. 2012, p. 82581A, doi: 10.1117/12.906567.
- [201] W. Lauterborn and C.-D. Ohl, “Cavitation bubble dynamics,” *Ultrason. Sonochem.*, vol. 4, no. 2, pp. 65–75, Apr. 1997, doi: 10.1016/S1350-4177(97)00009-6.
- [202] M. Habibi and M. Eslamian, “Facile and low-cost mechanical techniques for the fabrication of solution-processed polymer and perovskite thin film transistors,” *J. Phys. Commun.*, vol. 2, no. 7, p. 075018, Jul. 2018, doi: 10.1088/2399-6528/aad3a6.
- [203] S. Daniel, M. K. Chaudhury, and P.-G. de Gennes, “Vibration-Actuated Drop Motion on Surfaces for Batch Microfluidic Processes,” *Langmuir*, vol. 21, no. 9, pp. 4240–4248, Apr. 2005, doi: 10.1021/la046886s.
- [204] S. Oberti, A. Neild, and T. Wah Ng, “Microfluidic mixing under low frequency vibration,” *Lab. Chip*, vol. 9, no. 10, p. 1435, 2009, doi: 10.1039/b819739c.
- [205] M. K. Araz and A. Lal, “Acoustic mixing and chromatography in a PZT driven silicon microfluidic actuator,” in *2010 IEEE 23rd International Conference on Micro Electro Mechanical Systems (MEMS)*, Wanchai, Hong Kong, China, Jan. 2010, pp. 1111–1114, doi: 10.1109/MEMSYS.2010.5442405.
- [206] G. G. Yaralioglu, I. O. Wygant, T. C. Marentis, and B. T. Khuri-Yakub, “Ultrasonic Mixing in Microfluidic Channels Using Integrated Transducers,” *Anal. Chem.*, vol. 76, no. 13, pp. 3694–3698, Jul. 2004, doi: 10.1021/ac035220k.
- [207] A. Rahimzadeh and M. Eslamian, “Stability of thin liquid films subjected to ultrasonic vibration and characteristics of the resulting thin solid films,” *Chem. Eng. Sci.*, vol. 158, pp. 587–598, Feb. 2017, doi: 10.1016/j.ces.2016.11.006.
- [208] X. Noblin, A. Buguin, and F. Brochard-Wyart, “Vibrated sessile drops: Transition between pinned and mobile contact line oscillations,” *Eur. Phys. J. E*, vol. 14, no. 4, pp. 395–404, Aug. 2004, doi: 10.1140/epje/i2004-10021-5.
- [209] X. Noblin, A. Buguin, and F. Brochard-Wyart, “Triplon Modes of Puddles,” *Phys. Rev. Lett.*, vol. 94, no. 16, Apr. 2005, doi: 10.1103/PhysRevLett.94.166102.
- [210] M. Gilbert, *Brydson’s plastics materials*. Boston, MA: Elsevier, 2016.
- [211] D. B. Murphy and M. W. Davidson, *Fundamentals of light microscopy and electronic imaging*, 2nd ed. Hoboken, N.J: Wiley-Blackwell, 2013.
- [212] S. Liu, W. M. Wang, A. L. Briseno, S. C. B. Mannsfeld, and Z. Bao, “Controlled Deposition of Crystalline Organic Semiconductors for Field-Effect-Transistor Applications,” *Adv. Mater.*, vol. 21, no. 12, pp. 1217–1232, Mar. 2009, doi: 10.1002/adma.200802202.
- [213] P. Fesenko *et al.*, “Determination of crystal orientation in organic thin films using optical microscopy,” *Org. Electron.*, vol. 37, pp. 100–107, Oct. 2016, doi: 10.1016/j.orgel.2016.06.011.

- [214] F. J. Padden and H. D. Keith, "Spherulitic Crystallization in Polypropylene," *J. Appl. Phys.*, vol. 30, no. 10, pp. 1479–1484, Oct. 1959, doi: 10.1063/1.1734985.
- [215] R. R. Lagasse and B. Maxwell, "An experimental study of the kinetics of polymer crystallization during shear flow," *Polym. Eng. Sci.*, vol. 16, no. 3, pp. 189–199, 1976.
- [216] M. Gilbert, "States of Aggregation in Polymers," in *Brydson's Plastics Materials*, Elsevier, 2017, pp. 39–57.
- [217] G. Wang *et al.*, "Microfluidic Crystal Engineering of π -Conjugated Polymers," *ACS Nano*, vol. 9, no. 8, pp. 8220–8230, Aug. 2015, doi: 10.1021/acsnano.5b02582.
- [218] C. Müller *et al.*, "One-Step Macroscopic Alignment of Conjugated Polymer Systems by Epitaxial Crystallization during Spin-Coating," *Adv. Funct. Mater.*, vol. 23, no. 19, pp. 2368–2377, May 2013, doi: 10.1002/adfm.201202983.
- [219] P. Fesenko *et al.*, "Determination of crystal orientation in organic thin films using optical microscopy," *Org. Electron.*, vol. 37, pp. 100–107, Oct. 2016, doi: 10.1016/j.orgel.2016.06.011.
- [220] E. Cho *et al.*, "Three-Dimensional Packing Structure and Electronic Properties of Biaxially Oriented Poly(2,5-bis(3-alkylthiophene-2-yl)thieno[3,2-*b*]thiophene) Films," *J. Am. Chem. Soc.*, vol. 134, no. 14, pp. 6177–6190, Apr. 2012, doi: 10.1021/ja210272z.
- [221] H. Sirringhaus *et al.*, "Two-dimensional charge transport in self-organized, high-mobility conjugated polymers," *Nature*, vol. 401, no. 6754, pp. 685–688, 1999.
- [222] J. J. Beaudoin, Ed., *Handbook of analytical techniques in concrete science and technology*. Park Ridge, NJ: Norwich, NY: Noyes Publications; William Andrew Pub, 2001.
- [223] L. H. Jimison, M. F. Toney, I. McCulloch, M. Heeney, and A. Salleo, "Charge-Transport Anisotropy Due to Grain Boundaries in Directionally Crystallized Thin Films of Regioregular Poly(3-hexylthiophene)," *Adv. Mater.*, vol. 21, no. 16, pp. 1568–1572, Apr. 2009, doi: 10.1002/adma.200802722.
- [224] M. Tolan, *X-ray scattering from soft-matter thin films: materials science and basic research*. Berlin; New York: Springer, 1999.
- [225] T. Schuettfort, L. Thomsen, and C. R. McNeill, "Observation of a Distinct Surface Molecular Orientation in Films of a High Mobility Conjugated Polymer," *J. Am. Chem. Soc.*, vol. 135, no. 3, pp. 1092–1101, Jan. 2013, doi: 10.1021/ja310240q.
- [226] Q. Yuan, S. C. B. Mannsfeld, M. L. Tang, M. F. Toney, J. Lüning, and Z. Bao, "Thin Film Structure of Tetraceno[2,3-*b*]thiophene Characterized by Grazing Incidence X-ray Scattering and Near-Edge X-ray Absorption Fine Structure Analysis," *J. Am. Chem. Soc.*, vol. 130, no. 11, pp. 3502–3508, Mar. 2008, doi: 10.1021/ja0773002.
- [227] G. Horowitz, "Field-effect transistors based on short organic molecules," *J. Mater. Chem.*, vol. 9, no. 9, pp. 2021–2026, 1999, doi: 10.1039/a902242b.
- [228] A. R. Brown, C. P. Jarrett, D. M. de Leeuw, and M. Matters, "Field-effect transistors made from solution-processed organic semiconductors," *Synth. Met.*, vol. 88, no. 1, pp. 37–55, Apr. 1997, doi: 10.1016/S0379-6779(97)80881-8.
- [229] H. Phan, M. Wang, G. C. Bazan, and T.-Q. Nguyen, "Electrical Instability Induced by Electron Trapping in Low-Bandgap Donor-Acceptor Polymer Field-Effect Transistors," *Adv. Mater.*, vol. 27, no. 43, pp. 7004–7009, Nov. 2015, doi: 10.1002/adma.201501757.
- [230] J. Kang, N. Shin, D. Y. Jang, V. M. Prabhu, and D. Y. Yoon, "Structure and Properties of Small Molecule–Polymer Blend Semiconductors for Organic Thin Film Transistors," *J. Am. Chem. Soc.*, vol. 130, no. 37, pp. 12273–12275, Sep. 2008, doi: 10.1021/ja804013n.

- [231] J. Smith *et al.*, “Solution-processed organic transistors based on semiconducting blends,” *J. Mater. Chem.*, vol. 20, no. 13, p. 2562, 2010, doi: 10.1039/b921674j.
- [232] D. K. Hwang *et al.*, “Solvent and polymer matrix effects on TIPS-pentacene/polymer blend organic field-effect transistors,” *J. Mater. Chem.*, vol. 22, no. 12, p. 5531, 2012, doi: 10.1039/c2jm16487f.
- [233] R. Hamilton *et al.*, “High-Performance Polymer-Small Molecule Blend Organic Transistors,” *Adv. Mater.*, vol. 21, no. 10–11, pp. 1166–1171, Mar. 2009, doi: 10.1002/adma.200801725.
- [234] C. Teixeira da Rocha, K. Haase, Y. Zheng, M. Löffler, M. Hamsch, and S. C. B. Mannsfeld, “Solution Coating of Small Molecule/Polymer Blends Enabling Ultralow Voltage and High-Mobility Organic Transistors,” *Adv. Electron. Mater.*, p. 1800141, May 2018, doi: 10.1002/aelm.201800141.
- [235] M. Egginger, S. Bauer, R. Schwödiauer, H. Neugebauer, and N. S. Sariciftci, “Current versus gate voltage hysteresis in organic field effect transistors,” *Monatshefte Für Chem. - Chem. Mon.*, vol. 140, no. 7, pp. 735–750, Jul. 2009, doi: 10.1007/s00706-009-0149-z.
- [236] S. Lai *et al.*, “Morphology Influence on the Mechanical Stress Response in Bendable Organic Field-Effect Transistors with Solution-Processed Semiconductors,” *Adv. Electron. Mater.*, p. 1700271, Sep. 2017, doi: 10.1002/aelm.201700271.
- [237] Y. S. Chung *et al.*, “Zone-Refinement Effect in Small Molecule–Polymer Blend Semiconductors for Organic Thin-Film Transistors,” *J. Am. Chem. Soc.*, vol. 133, no. 3, pp. 412–415, Jan. 2011, doi: 10.1021/ja108772q.
- [238] N. Shin *et al.*, “Vertically Segregated Structure and Properties of Small Molecule-Polymer Blend Semiconductors for Organic Thin-Film Transistors,” *Adv. Funct. Mater.*, vol. 23, no. 3, pp. 366–376, Jan. 2013, doi: 10.1002/adfm.201201389.
- [239] W. H. Lee *et al.*, “The Influence of the Solvent Evaporation Rate on the Phase Separation and Electrical Performances of Soluble Acene-Polymer Blend Semiconductors,” *Adv. Funct. Mater.*, vol. 22, no. 2, pp. 267–281, Jan. 2012, doi: 10.1002/adfm.201101159.
- [240] Z. He, D. Li, D. K. Hensley, A. J. Rondinone, and J. Chen, “Switching phase separation mode by varying the hydrophobicity of polymer additives in solution-processed semiconducting small-molecule/polymer blends,” *Appl. Phys. Lett.*, vol. 103, no. 11, p. 113301, Sep. 2013, doi: 10.1063/1.4820588.
- [241] K. Zhao *et al.*, “Vertical Phase Separation in Small Molecule:Polymer Blend Organic Thin Film Transistors Can Be Dynamically Controlled,” *Adv. Funct. Mater.*, vol. 26, no. 11, pp. 1737–1746, Mar. 2016, doi: 10.1002/adfm.201503943.
- [242] F. G. del Pozo *et al.*, “Single Crystal-Like Performance in Solution-Coated Thin-Film Organic Field-Effect Transistors,” *Adv. Funct. Mater.*, vol. 26, no. 14, pp. 2379–2386, Apr. 2016, doi: 10.1002/adfm.201502274.
- [243] J. Chen, C. K. Tee, M. Shtein, D. C. Martin, and J. Anthony, “Controlled solution deposition and systematic study of charge-transport anisotropy in single crystal and single-crystal textured TIPS pentacene thin films,” *Org. Electron.*, vol. 10, no. 4, pp. 696–703, Jul. 2009, doi: 10.1016/j.orgel.2009.03.007.
- [244] M. Le Berre, Y. Chen, and D. Baigl, “From Convective Assembly to Landau–Levich Deposition of Multilayered Phospholipid Films of Controlled Thickness,” *Langmuir*, vol. 25, no. 5, pp. 2554–2557, Mar. 2009, doi: 10.1021/la803646e.
- [245] M. E. Roberts, N. Queraltó, S. C. B. Mannsfeld, B. N. Reinecke, W. Knoll, and Z. Bao, “Cross-Linked Polymer Gate Dielectric Films for Low-Voltage Organic Transistors,” *Chem. Mater.*, vol. 21, no. 11, pp. 2292–2299, Jun. 2009, doi: 10.1021/cm900637p.

- [246] M. E. Roberts *et al.*, “Water-stable organic transistors and their application in chemical and biological sensors,” *Proc. Natl. Acad. Sci.*, vol. 105, no. 34, pp. 12134–12139, 2008.
- [247] G. Schwabegger *et al.*, “High mobility, low voltage operating C60 based n-type organic field effect transistors,” *Synth. Met.*, vol. 161, no. 19–20, pp. 2058–2062, Oct. 2011, doi: 10.1016/j.synthmet.2011.06.042.
- [248] V. Pecunia *et al.*, “Trap Healing for High-Performance Low-Voltage Polymer Transistors and Solution-Based Analog Amplifiers on Foil,” *Adv. Mater.*, vol. 29, no. 23, p. 1606938, Jun. 2017, doi: 10.1002/adma.201606938.
- [249] G. Houin *et al.*, “Device engineering for high-performance, low-voltage operating organic field effect transistor on plastic substrate,” *Flex. Print. Electron.*, vol. 2, no. 4, p. 045004, Dec. 2017, doi: 10.1088/2058-8585/aa8cb1.
- [250] U. Kraft *et al.*, “Detailed analysis and contact properties of low-voltage organic thin-film transistors based on dinaphtho[2,3- b :2',3'- f]thieno[3,2- b]thiophene (DNNT) and its didecyl and diphenyl derivatives,” *Org. Electron.*, vol. 35, pp. 33–40, Aug. 2016, doi: 10.1016/j.orgel.2016.04.038.
- [251] L. Feng, J. Zhao, W. Tang, X. Xu, and X. Guo, “Solution Processed Organic Thin-Film Transistors With Hybrid Low/High Voltage Operation,” *J. Disp. Technol.*, vol. 10, no. 11, pp. 971–974, Nov. 2014, doi: 10.1109/JDT.2014.2344040.
- [252] T. Yokota *et al.*, “Flexible Low-Voltage Organic Transistors with High Thermal Stability at 250 °C,” *Adv. Mater.*, vol. 25, no. 27, pp. 3639–3644, Jul. 2013, doi: 10.1002/adma.201300941.
- [253] J. H. Cho *et al.*, “Printable ion-gel gate dielectrics for low-voltage polymer thin-film transistors on plastic,” *Nat. Mater.*, vol. 7, no. 11, pp. 900–906, Nov. 2008, doi: 10.1038/nmat2291.
- [254] Y. Jang, D. H. Kim, Y. D. Park, J. H. Cho, M. Hwang, and K. Cho, “Low-voltage and high-field-effect mobility organic transistors with a polymer insulator,” *Appl. Phys. Lett.*, vol. 88, no. 7, p. 072101, Feb. 2006, doi: 10.1063/1.2173633.
- [255] E. G. Bittle, J. I. Basham, T. N. Jackson, O. D. Jurchescu, and D. J. Gundlach, “Mobility overestimation due to gated contacts in organic field-effect transistors,” *Nat. Commun.*, vol. 7, p. 10908, Mar. 2016, doi: 10.1038/ncomms10908.
- [256] S. Oberti, A. Neild, and T. Wah Ng, “Microfluidic mixing under low frequency vibration,” *Lab. Chip*, vol. 9, no. 10, p. 1435, 2009, doi: 10.1039/b819739c.
- [257] Z. Yang, H. Goto, M. Matsumoto, and R. Maeda, “Active micromixer for microfluidic systems using lead-zirconate-titanate (PZT)-generated ultrasonic vibration,” *Electrophor. Int. J.*, vol. 21, no. 1, pp. 116–119, 2000.
- [258] R. F. Jakubowicz and J. J. Porte, “Ribbed mechanism for mixing sample by vibration,” Nov. 1994.
- [259] M. Woodmansee, P. Zsiga, J. Rayner, and R. Shampine, “Vibration Enhanced Mixing Process,” Jun. 2010.
- [260] T. Asano, “Inkjet device including ultrasonic vibrator for applying ultrasonic vibration to ink,” Feb. 2004.
- [261] E. Kougoulos, A. G. Jones, and M. W. Wood-Kaczmar, “Process Modelling Tools for Continuous and Batch Organic Crystallization Processes Including Application to Scale-Up,” p. 12.
- [262] R. Janneck *et al.*, “Highly Crystalline C8-BTBT Thin-Film Transistors by Lateral Homo-Epitaxial Growth on Printed Templates,” *Adv. Mater.*, vol. 29, no. 44, p. 1703864, Nov. 2017, doi: 10.1002/adma.201703864.
- [263] E. L. Decker and S. Garoff, “Using vibrational noise to probe energy barriers producing contact angle hysteresis,” *langmuir*, vol. 12, no. 8, pp. 2100–2110, 1996, doi: <https://doi.org/10.1021/la951021n>.

- [264] J. P. Stokes, M. J. Higgins, A. P. Kushnick, S. Bhattacharya, and M. O. Robbins, "Harmonic generation as a probe of dissipation at a moving contact line," *Phys. Rev. Lett.*, vol. 65, no. 15, p. 1885, 1990, doi: <https://doi.org/10.1103/PhysRevLett.65.1885>.
- [265] C. Andrieu, C. Sykes, and F. Brochard, "Average spreading parameter on heterogeneous surfaces," *Langmuir*, vol. 10, no. 7, pp. 2077–2080, 1994, doi: <https://doi.org/10.1021/la00019a010>.
- [266] T. Young, "III. An essay on the cohesion of fluids," p. 24.
- [267] M. A. Rodríguez-Valverde, F. J. Montes Ruiz-Cabello, and M. A. Cabrerizo-Vílchez, "A new method for evaluating the most-stable contact angle using mechanical vibration," *Soft Matter*, vol. 7, no. 1, pp. 53–56, 2011, doi: [10.1039/C0SM00939C](https://doi.org/10.1039/C0SM00939C).
- [268] F. J. M. Ruiz-Cabello, M. A. Rodríguez-Valverde, and M. Cabrerizo-Vílchez, "A new method for evaluating the most stable contact angle using tilting plate experiments," *Soft Matter*, vol. 7, no. 21, p. 10457, 2011, doi: [10.1039/c1sm06196h](https://doi.org/10.1039/c1sm06196h).
- [269] F. J. Montes Ruiz-Cabello, M. A. Rodríguez-Valverde, and M. A. Cabrerizo-Vílchez, "Comparison of the Relaxation of Sessile Drops Driven by Harmonic and Stochastic Mechanical Excitations," *Langmuir*, vol. 27, no. 14, pp. 8748–8752, Jul. 2011, doi: [10.1021/la2010858](https://doi.org/10.1021/la2010858).
- [270] C. D. Volpe, D. Maniglio, M. Morra, and S. Siboni, "The determination of a 'stable-equilibrium' contact angle on heterogeneous and rough surfaces," *Colloids Surf. Physicochem. Eng. Asp.*, vol. 206, no. 1–3, pp. 47–67, Jul. 2002, doi: [10.1016/S0927-7757\(02\)00072-9](https://doi.org/10.1016/S0927-7757(02)00072-9).
- [271] C. Teixeira da Rocha *et al.*, "Mitigating Meniscus Instabilities in Solution-Sheared Polymer Films for Organic Field-Effect Transistors," *ACS Appl. Mater. Interfaces*, p. acsami.9b07832, Aug. 2019, doi: [10.1021/acsami.9b07832](https://doi.org/10.1021/acsami.9b07832).
- [272] T. Matsumoto, W. Ou-Yang, K. Miyake, T. Uemura, and J. Takeya, "Study of contact resistance of high-mobility organic transistors through comparisons," *Org. Electron.*, vol. 14, no. 10, pp. 2590–2595, Oct. 2013, doi: [10.1016/j.orgel.2013.06.032](https://doi.org/10.1016/j.orgel.2013.06.032).
- [273] P. V. Pesavento, K. P. Puntambekar, C. D. Frisbie, J. C. McKeen, and P. P. Ruden, "Film and contact resistance in pentacene thin-film transistors: Dependence on film thickness, electrode geometry, and correlation with hole mobility," *J. Appl. Phys.*, vol. 99, no. 9, p. 094504, May 2006, doi: [10.1063/1.2197033](https://doi.org/10.1063/1.2197033).
- [274] T. J. Richards and H. Sirringhaus, "Analysis of the contact resistance in staggered, top-gate organic field-effect transistors," *J. Appl. Phys.*, vol. 102, no. 9, p. 094510, Nov. 2007, doi: [10.1063/1.2804288](https://doi.org/10.1063/1.2804288).
- [275] A. Yamamura *et al.*, "Wafer-scale, layer-controlled organic single crystals for high-speed circuit operation," *Sci. Adv.*, vol. 4, no. 2, p. eaao5758, Feb. 2018, doi: [10.1126/sciadv.aao5758](https://doi.org/10.1126/sciadv.aao5758).
- [276] D. He *et al.*, "Ultra-high mobility and efficient charge injection in monolayer organic thin-film transistors on boron nitride," *Sci. Adv.*, vol. 3, no. 9, p. e1701186, Sep. 2017, doi: [10.1126/sciadv.1701186](https://doi.org/10.1126/sciadv.1701186).
- [277] J. Rivnay, S. C. B. Mannsfeld, C. E. Miller, A. Salleo, and M. F. Toney, "Quantitative Determination of Organic Semiconductor Microstructure from the Molecular to Device Scale," *Chem. Rev.*, vol. 112, no. 10, pp. 5488–5519, Oct. 2012, doi: [10.1021/cr3001109](https://doi.org/10.1021/cr3001109).
- [278] O. Karthaus, L. Gråsjö, N. Maruyama, and M. Shimomura, "Formation of ordered mesoscopic polymer arrays by dewetting," *Chaos Interdiscip. J. Nonlinear Sci.*, vol. 9, no. 2, pp. 308–314, Jun. 1999, doi: [10.1063/1.166407](https://doi.org/10.1063/1.166407).
- [279] R. G. Larson, "Transport and deposition patterns in drying sessile droplets," *AIChE J.*, vol. 60, no. 5, pp. 1538–1571, May 2014, doi: [10.1002/aic.14338](https://doi.org/10.1002/aic.14338).

- [280] J. L. Plawsky, M. Ojha, A. Chatterjee, and P. C. Wayner, "REVIEW OF THE EFFECTS OF SURFACE TOPOGRAPHY, SURFACE CHEMISTRY, AND FLUID PHYSICS ON EVAPORATION AT THE CONTACT LINE," *Chem. Eng. Commun.*, vol. 196, no. 5, pp. 658–696, Dec. 2008, doi: 10.1080/00986440802569679.
- [281] G. Kumar and K. N. Prabhu, "Review of non-reactive and reactive wetting of liquids on surfaces," *Adv. Colloid Interface Sci.*, vol. 133, no. 2, pp. 61–89, Jun. 2007, doi: 10.1016/j.cis.2007.04.009.
- [282] V. Bertola, "Dynamic wetting of dilute polymer solutions: The case of impacting droplets," *Adv. Colloid Interface Sci.*, vol. 193–194, pp. 1–11, Jun. 2013, doi: 10.1016/j.cis.2013.03.001.
- [283] M. Halik *et al.*, "Low-voltage organic transistors with an amorphous molecular gate dielectric," *Nature*, vol. 431, no. 7011, pp. 963–966, Oct. 2004, doi: 10.1038/nature02987.
- [284] S. Y. Yang, S. H. Kim, K. Shin, H. Jeon, and C. E. Park, "Low-voltage pentacene field-effect transistors with ultrathin polymer gate dielectrics," *Appl. Phys. Lett.*, vol. 88, no. 17, p. 173507, Apr. 2006, doi: 10.1063/1.2199592.
- [285] A. Yu, I. Roes, A. Davies, and Z. Chen, "Ultrathin, transparent, and flexible graphene films for supercapacitor application," *Appl. Phys. Lett.*, vol. 96, no. 25, p. 253105, Jun. 2010, doi: 10.1063/1.3455879.
- [286] Z. Liu, K. Parvez, R. Li, R. Dong, X. Feng, and K. Müllen, "Transparent Conductive Electrodes from Graphene/PEDOT:PSS Hybrid Inks for Ultrathin Organic Photodetectors," *Adv. Mater.*, vol. 27, no. 4, pp. 669–675, Jan. 2015, doi: 10.1002/adma.201403826.
- [287] X. Li *et al.*, "Large-Area Ultrathin Graphene Films by Single-Step Marangoni Self-Assembly for Highly Sensitive Strain Sensing Application," *Adv. Funct. Mater.*, vol. 26, no. 9, pp. 1322–1329, Mar. 2016, doi: 10.1002/adfm.201504717.
- [288] S. Gong *et al.*, "A wearable and highly sensitive pressure sensor with ultrathin gold nanowires," *Nat. Commun.*, vol. 5, no. 1, Dec. 2014, doi: 10.1038/ncomms4132.
- [289] G. Altshuler and O. Manor, "Spreading dynamics of a partially wetting water film atop a MHz substrate vibration," *Phys. Fluids*, vol. 27, no. 10, p. 102103, Oct. 2015, doi: 10.1063/1.4932086.
- [290] A. R. Rezk, O. Manor, J. R. Friend, and L. Y. Yeo, "Unique fingering instabilities and soliton-like wave propagation in thin acoustowetting films," *Nat. Commun.*, vol. 3, no. 1, Jan. 2012, doi: 10.1038/ncomms2168.
- [291] L. Wengeler, M. Schmitt, K. Peters, P. Scharfer, and W. Schabel, "Comparison of large scale coating techniques for organic and hybrid films in polymer based solar cells," *Chem. Eng. Process. Process Intensif.*, vol. 68, pp. 38–44, Jun. 2013, doi: 10.1016/j.cep.2012.03.004.
- [292] F. C. Krebs, "Polymer solar cell modules prepared using roll-to-roll methods: Knife-over-edge coating, slot-die coating and screen printing," *Sol. Energy Mater. Sol. Cells*, vol. 93, no. 4, pp. 465–475, Apr. 2009, doi: 10.1016/j.solmat.2008.12.012.
- [293] S. Schmatloch, H. Bach, R. A. T. M. van Benthem, and U. S. Schubert, "High-Throughput Experimentation in Organic Coating and Thin Film Research: State-of-the-Art and Future Perspectives," *Macromol. Rapid Commun.*, vol. 25, no. 1, pp. 95–107, Jan. 2004, doi: 10.1002/marc.200300146.
- [294] A. Armin *et al.*, "Efficient, Large Area, and Thick Junction Polymer Solar Cells with Balanced Mobilities and Low Defect Densities," *Adv. Energy Mater.*, vol. 5, no. 3, p. 1401221, Feb. 2015, doi: 10.1002/aenm.201401221.
- [295] D. Wu *et al.*, "Blade Coating Aligned, High-Performance, Semiconducting-Polymer Transistors," *Chem. Mater.*, Mar. 2018, doi: 10.1021/acs.chemmater.7b04835.

- [296] S. SUDO, A. GOTO, H. KUWANO, Y. HAMATE, T. YANO, and K. HOSHIKA, “The Dynamic Behavior of Liquid Droplets on Vibrating Plate.” The Japanese Society for Experimental Mechanics, 2010, Accessed: Aug. 06, 2019. [Online]. Available: <https://doi.org/10.11395/jjsem.10.s38>.
- [297] “Vukasinovic et al. - 2007 - Dynamics of a sessile drop in forced vibration.pdf.” .
- [298] L. Jiang, C.-L. Ting, M. Perlin, and W. W. Schultz, “Moderate and steep Faraday waves: instabilities, modulation and temporal asymmetries,” *J. Fluid Mech.*, vol. 329, pp. 275–307, 1996.
- [299] K. Kumar, “Linear Theory of Faraday Instability in Viscous Liquids,” *Proc. Math. Phys. Eng. Sci.*, vol. 452, no. 1948, pp. 1113–1126, 1996.
- [300] S. V. Diwakar, V. Jajoo, S. Amiroudine, S. Matsumoto, R. Narayanan, and F. Zoueshtiagh, “Influence of capillarity and gravity on confined Faraday waves,” *Phys. Rev. Fluids*, vol. 3, no. 7, Jul. 2018, doi: 10.1103/PhysRevFluids.3.073902.
- [301] P. N. V. Kluge, D. K. Germaine, and K. T. Crépin, “Dry Friction with Various Frictions Laws: From Wave Modulated Orbit to Stick-Slip Modulated,” *Mod. Mech. Eng.*, vol. 05, no. 02, pp. 28–40, 2015, doi: 10.4236/mme.2015.52004.

List of Figures

- Figure 2.1: (a) Self-healable electronic skin device for health monitoring. Image reproduced from Ref.[2]. (b) Flexible solar panels from Heliatek on a windmill; (c) a flexible e-reader developed by Plastic Logic, and (d) a prototype of a flexible screen, by Samsung. 14
- Figure 2.2: (a) The atomic s orbital and (b) p orbital. (c) The molecular σ orbital and (d) π orbitals resultant from the atomic overlap. (e) A simplified energetic diagram of σ and π orbitals for ethene. π corresponds to the bonding band and π^* to the antibonding. Images reproduced from Ref. [8]. 15
- Figure 2.3: (a) Widely used small-molecule semiconductors. (b) A HOMO-LUMO representation of the donor and acceptor moieties in a D-A polymer, (c) a schematic representing how both moieties organize in a chain, and (d) the most used donor and acceptor units used for polymer synthesis. Figure reproduced from Ref. [9]. 16
- Figure 2.4: (a) Wavefunction of the HOMO and LUMO of tetracene; (b) the consequences of the electronic splitting when the distance between two cofacial tetracene dimers is increased. (c) Consequences of the increasing intermolecular distance on the charge carrier mobility. Image reproduced from Ref. [7]. 17
- Figure 2.5: (a) Schematic a field-effect transistor. Schematics of (b) charge accumulated in the channel of the semiconductor when a gate voltage is applied; (c) drain current flowing in the transistor channel. 19
- Figure 2.6: (a) Schematic of a bottom-gate, top contact architecture with a gradual charge channel. Schematics of (b) bottom-gate, bottom-contact, (c) top-gate, bottom-contact, and (d) top-gate, top-contact. 20
- Figure 2.7: Example of (a) a transfer curve in the linear regime of a transistor, (b) the transfer curve of a transistor in saturation and the equivalent square root for mobility calculation, and (c) the output curve of a transistor with increasing V_g -value-steps of +10 V. Image reproduced from Ref. [9]. 21
- Figure 2.8: Schematic of the behavior of a metal-semiconductor junction for a p-type semiconductor. (a) The energy levels of a metal and a semiconductor interface when the interfaces are apart. Φ_m is the work function of the metal, EA the electron affinity of the semiconductor, IP the ionization potential, E_C the conductance band, E_V the valence band, and E_F the Fermi level. (b) When both surfaces are in contact, band bending occurs to maintain the Fermi level of the semiconductor at the same level of the metal's work function at the contact region. Therefore, a potential barrier of height Φ_b is formed. When a negative voltage is applied to the junction, the barrier is lowered by a factor dependent on the voltage applied. 23

- Figure 2.9: Schematic of the energy levels for an (a) Ohmic contact, and a (b) Schottky contact. (c) Schematic of the potential barrier lowering due to the insertion of an intermediate dipole layer. (d) The thinning of the depletion layer of a Schottky barrier through interface doping. 24
- Figure 2.10: Work function for gold (Au) reported in different publications and under different cleaning condition. HOMO-LUMO values for semiconductors used in this work. The values from this image are taken from published works that utilize the same materials.[14], [16]–[21] 24
- Figure 2.11: (a) Different scales and morphology features for organic crystalline thin films. Image reproduced from Ref. [40]. (b) Study of the influence of crystalline grains and boundaries of the small-molecule PDI8 on the charge carrier mobility of the transistors. The schematics to the right show the orientation of the crystal structures in a film. Images reproduced from Ref. [42]. 28
- Figure 2.12: Typical charge carrier paths in semicrystalline polymer semiconductors. Image reproduced and adjusted from Ref. [51]..... 29
- Figure 2.13: (a) Potential charge carrier mobilities depending on the degree of disorder of a polymer semiconductor. Image reproduced from Ref. [Grozema].41 (b) A semicrystalline polymer, (c) small disordered aggregates, and a (d) completely amorphous polymer. The ordered regions are highlighted by orange, the entangled black lines are the amorphous regions of the polymer, and the red chains are connecting ordered regions. Image reproduced from Ref. [51]. 30
- Figure 3.1: Schematic illustrations of solution deposition methods. Image reproduced from Ref. [73]. 34
- Figure 3.2: Schematic of the (a) evaporation regime and the (b) the Landau-Levich regime. (c) Graph of the film thickness as a function of the shearing speed, showing both the evaporation n and Landau-Levich regimes. The Figures (a) and (b) are adapted, and (c) are reproduced from Ref. [75]..... 35
- Figure 3.3: (a) The coffee ring effect: a higher concentration of solute is deposited at the borders of the evaporating drop. (b)The stronger evaporating flux at the edges of the drop and the pinned contact line promotes an outwards flow close to the substrate, and carry the solute from the center of the drop to the contact line. Images reproduced from Ref. [79]. 36
- Figure 3.4: (a) Capillaries and Marangoni flows in a sessile evaporation droplet. Image reproduced from Ref. [85]. (b) An evaporating drop with its natural flow and the (d) consequent coffee ring effect. (c) An induced Marangoni flow (e) resulting in a uniform deposit. Images (b-e) are reproduced from Ref. [86]. 37
- Figure 3.5: Simulation of shear flow in a receding meniscus at the different solution shearing regimes. The top row shows the evaporation flux and flow field. The middle row, the flow field and corresponding coating speeds; and the bottom row corresponds to the strain rate applied. The image is reproduced from Ref. [59]. 38
- Figure 3.6: Schematics of the two crystal nucleation models in solution. Image reproduced from Ref. [89]..... 39
- Figure 3.7: (a) Solution shearing method from the work of Giri et al. and (b-f) the respective films sheared with varying speed. (g) The corresponding polymorphs present in the films. These images are reproduced from Ref. [91]. (h) Schematic of the formation of TIPS-Pentacene polymorphs in the films through vertical confinement during the solution shearing process. This image is reproduced from Ref. [94]. 41

- Figure 3.8: (a) The solution shearing setup for the FLUENCE method with the microstructured blade and patterned substrate. The images are reproduced from Ref. [92] (b) The flexible patterned blade from Kim et al. and details of the multiple menisci. Images reproduced from Ref. [100]. (c) A schematic showing the micropillar, and the single-crystal arrays from the work of Xiao et al. Images reproduced from Ref. [101]. 42
- Figure 3.9: The meniscus at the top left is the simulated backward flow Marangoni from the thermal gradient of the substrate. The meniscus at the top right is the expected Marangoni flow towards the contact line, believed to be caused by the solvent blending. (a-e) Are the resulting polarized optical microscopy images of the films deposited by using the solvent blend, and (f-j) are the corresponding atomic force microscopy (AFM) images. The images above are reproduced from Ref. [107]. 43
- Figure 3.10: (a) Schematic of the crystal growth process in homopolymers in solution. (b) Illustration of the aggregation phase; (b) the extension – or coalescence – phase, and (c) the crystal growth phase. Illustration adapted from Ref. [111]. 44
- Figure 3.11: Schematic of flow fluid transport mechanism, such as flows; and polymer conformation mechanisms during solution shearing. Image reproduced from Ref. [111]. 45
- Figure 3.12: (a-c) UV-light exposure and aging process of the P3HT solution slot-die coated. Image reproduced from Ref. [125]. (d) Effect of UV radiation on the P3HT solution, charge carrier mobility, and birefringence of the P3HT film as a function of the time exposed to UV-light. Image reproduced from Ref. [126]. 47
- Figure 3.13: (a) The solution shearing of PCDTPT on a nanogrooved substrate promotes alignment on the film surface, which is detected by NEFAXS. Image reproduced from Ref. [132]. (b) An in-situ study of the polymer alignment during the solution shearing over nanogrooves unravels the change in alignment for different depths of the film. They show significant charge carrier mobility differences and suggest what causes such a mobility boost. Images reproduced from Ref. [52]. (c) A dynamic template allows the higher crystalline quality of polymeric films, improving charge carrier mobility of OFET devices. Images reproduced from Ref. [133]. 48
- Figure 3.14: (a) Illustration of the FLUENCE method: a shearing blade with micropillars is used for enhancing the crystallinity of all-polymer solar cells. Images reproduced from Ref. [Diao].[92] (b) The coating method using a flexible lamella for a higher shear force during the deposition of the co-polymer DPP-BTz, resulting in highly anisotropic thin films. Images are reproduced from Ref. [135]. (c) The CONPHINE method for aligning polymer lamellas for stretchable semiconducting films. Images are reproduced from Ref. [68]. 49
- Figure 3.15: (a) DNA stain patterns formed from aqueous solution at a concentration of $50 \mu\text{g ml}^{-1}$ (left) and $20 \mu\text{g ml}^{-1}$. (b) Polystyrene patterns formed from the shearing of a chloroform solution at different shearing speeds. (c) Method for manipulating stick-and-slip for nanoparticle deposition; scale bar: $200 \mu\text{m}$. (d) Deposition of silica particles through dip-coating of a colloidal suspension. Images reproduced from Refs. [136], [138], [140], [149], respectively. 51
- Figure 3.16: Schematic of the stick-and-slip motion of the contact line. (a) Initial evaporation condition; (b) contact angle and drop height decrease due to evaporation until reaching a limit contact angle; (c) slip occurs due to high free surface energy; (d) new pinned contact line. Schematic adapted from Ref. [147]. (e) the equivalent pinned contact line (“stick”) for a receding meniscus during solution coating; (f) a deposited wire and the meniscus after the “slip” process. 52

- Figure 3.17: (a) A drop stuck at its critical advancing contact angle (θ_A) and critical receding contact angle (θ_R). In addition to tilting a drop, (b) slowly pumping liquid in or out of a drop enables the measurement of the critical contact angles. Images are reproduced from Ref. [166]. (c) A qualitative graph representing the apparent contact angles of a meniscus and its metastable states. Image (c) is reproduced from Ref. [168]..... 52
- Figure 3.18: (a) Surface waves and microstreaming induced by a vibrating substrate and (b) acoustic streaming caused by an ultrasonic probe. Figures are reproduced from Ref. [171]. . 54
- Figure 3.19: Depictions of solutions for flow, counterflow, and vorticity caused by acoustic oscillations. These are the intensity of flows expected when (a) the sound beam is narrow in relation to the width of the liquid (distance from center to the wall); (b) the beam is approximately half of the width, and when the (c) beam occupies a significantly large portion of the width. Images reproduced from [183]..... 56
- Figure 3.20: (a) The setup with speakers used in the work of Diemer et al. Image is reproduced from Ref. [196]. (b) The setup used in the work of Zabihi et al. for vibration during spray-coating deposition. (c) The profile and (d) AFM images of the films PEDOT:PSS films deposited with and without vibration of the substrate. Images reproduced from Ref. [192]... 59
- Figure 3.21: (a) At the left, AFM images of films coated through drop-casting (DC), spin-coating (SC), for a P3HT/chloroform solution with (Sonic) and without (Pristine) ultrasonication before the deposition. At the right are the charge carrier mobility values for the corresponding OFETs. Images reproduced from Ref. [128]. (b) Schematic shown in the work of Kondo et al., for the expected self-assembly behavior of P3HT when the solution is vibrated during solvent evaporation, after drop-casting. At the right are the resulting charge carrier mobility values for devices with different solution concentrations fabricated using this method. The images are reproduced from Ref. [199]. 60
- Figure 3.22: (a) Schematic of the experiment for comparing the vibration of the spin-coated film and the vibration of the solution before spin-coating. (b) Resulting AFM surfaces. (c) X-ray diffraction patterns, the roughness of film, and conductivity for the experiment in (a). ... 61
- Figure 4.1: Fabrication process of OFET devices for this work: (a) a Si/SiO₂ wafer is used as the substrate, (b) the surface is cleaned and treated with SAMs, (c) the organic semiconductor is deposited through solution shearing – or piezoshearing, (d) the electrodes are deposited through thermal evaporation, and (e) the final device has a bottom-gate top-contact architecture. 63
- Figure 4.2: Figure 4.2: (a) Schematic of how the piezo crystal is embedded in the solution shearing system, and a figure of the PA4GE model, used throughout this work; (b) maximum displacement applicable to the piezo actuator, depending on the frequency applied. These include both the nominal value, which is calculated from the nominal I_{ave} and nominal capacitance of the piezo actuator, and the maximum voltage reached experimentally with our setup..... 65
- Figure 4.3: (a) The amplifier MX200, from PiezoDrive; (b) schematic of the circuit configuration used for our setup; (c) output voltage configuration options for the MX200 amplifier and its respective current values. The output voltage configurations of 100 V and 150 V are used to calculate the maximum displacement of the crystal displayed in Figure 4.2b... 67
- Figure 4.4: Circuit Schematic for the Piezoshearing setup. 67
- Figure 4.5: (a) Final experimental setup for the piezoshearing. (b) Piezoshearing blade. 68
- Figure 4.6: (a) Representation of light as an electromagnetic wave. The electrical (E) and magnetic (B) components are orthogonal to each other, with the same amplitude and phase, and

oscillate in time and space. For simplicity, only the electrical component is shown for schematics of light rays. (b) Schematic of light transmission when crossed polarizers are overlapped with different angles between the respective transmission axis. The larger the angle between the axis', the least light is transmitted. Both images reproduced from Ref. [210]. ... 69

Figure 4.7: Illustration of ray splitting on a crystal structure, with different incident angles in relation to the optic axis of the crystal. The optic axis of the crystal is the black double arrows; the O rays are the pink arrows, and the E rays are the blue arrows. The incident ray is (a) oblique, (b) perpendicular, and (c) parallel to the optic axis. This image is reproduced from Ref. [210]. 70

Figure 4.8: Schematic of cross-polarized microscopy and a crystal sample. From the different optical colors observed after passing through the analyzer, it can be concluded there is birefringence. This figure is reproduced from Ref. [218]. 71

Figure 4.9: Schematic illustration of the different lengths scales of X-ray characterization and the particular traits that can be detected in the thin-film morphology analysis. The top row shows a system for a blended material, such as used in photovoltaic systems, and the bottom row shows a one material system, such as used in OFETs. Image reproduced from Ref. [40]. 72

Figure 4.10: (a) 2D-detector GIWAXS setup, as utilized for the characterization of our films. Image reproduced from Ref. [40]. (b) Incident beam on atomic planes when Bragg's law is fulfilled, and diffraction occurs. Image reproduced from Ref. [221]. 72

Figure 4.11: Different out-of-plane stacking preferences for the polymer P3HT and the respective diffraction imprints. For the edge-on (a) stacking preference, a strong (010) peak is observed at q_{xy} , and a strong (100) peak is observed close to the q_z axis. For the face-on stacking preference, a strong (010) peak is present close to q_z , and a strong (001) peak is close to the q_{xy} . Image reproduced from Ref. [220]. 74

Figure 4.12: (a) Films with randomly oriented crystallites tend to have a diffraction pattern of rings. When the out-of-plane alignment of crystallite populations is increased, rings are limited to arches, as displayed in (b) and (c). The images displayed in the bottom row are for the polymer PBTBT and are the resulting diffraction patterns from processing through a solid-state press (a), spin coating (b) and annealing after spin coating (c). The image is reproduced from Ref. [40]. 75

Figure 4.13: Illustration of the top view of films and their respective diffraction patterns for varying ϕ for (a) isotropic films and (b) anisotropic films. (c) Resulting peaks for (001) and (010) peaks in an aligned film. 75

Figure 4.14: Common plots of transfer functions for OFET devices. The Ideal model is in (f). The black dashed lines are the equivalent plot, and the red lines are the values often reported and that are considered to be overestimated. The green lines in (d-f) are the suggested values and the respective reliability factor r . The black dot represents the origin and the red dot the maximum current. Image reproduced from Ref. [12]. 78

Figure 5.1: (a) Shearing speed-dependent maximum saturation charge carrier mobility of neat TIPS-pentacene and blends with different molecular weight polystyrene (blend ratio 1:1 by volume). The inset shows the molecular weight dependent mobility of the blends at a shearing speed of 2 mm s^{-1} . (b) Transfer characteristics of a typical device with TIPS-pentacene:PS blend ($M_w = 20 \text{ kDa}$ and ratio 1:1). Image reproduced from Ref. [233]. 84

Figure 5.2: (a) The threshold voltage, (b) Ion/off ratio and (c) maximum values of drain current for TIPS-pentacene:PS blend films (ratio 1:1) with different polystyrene molecular weights

- sheared at different speeds. The large error bars in (b) are omitted. Image reproduced from Ref. [233]. 84
- Figure 5.3: (a) Transfer curve for a typical device sheared at 2 mm s^{-1} with a 20 kDa blend. (b) minimum mobility values for backward sweep measurement, (c) maximum values of mobility for the forward sweep measurements, and (d) minimum values of mobility for the forward sweep. Image reproduced from Ref. [233]. 85
- Figure 5.4: Top row: neat TIPS-pentacene films with increasing speed from left to right; and lower row: blended films of TIPS-pentacene:PS 2000 kDa with increasing shearing speeds. The size of the hysteresis for each plot is given by ΔV_g 86
- Figure 5.5: Optical microscope images of (a-d) pristine TIPS-pentacene and blends with polystyrene with a molecular weight of (e-g) 2 kDa, (i-l) 20 kDa, (m-p) 200 kDa, and (q-t) 2000 kDa. The white arrow indicates the shearing direction. Scale bar: $200 \mu\text{m}$. Image reproduced from Ref. [233]. 87
- Figure 5.6: Shear-rate dependent viscosities for PS:toluene solutions, with the equivalent PS concentration as in the semiconducting solution. Measurements are carried out at $90 \text{ }^\circ\text{C}$, to resemble as much as possible the solution shearing process. 88
- Figure 5.7: Atomic force microscopy images of film surfaces for (a) neat TIPS-pentacene films (shearing speed of 2.6 mm s^{-1}), films blended with (b) PS $M_w = 2 \text{ kDa}$ (2 mm s^{-1}), (c) PS $M_w = 20 \text{ kDa}$ (2 mm s^{-1}), (d) PS $M_w = 200 \text{ kDa}$ (2 mm s^{-1}), and (e) PS $M_w = 2000 \text{ kDa}$ (2.6 mm s^{-1}). Scale bar: $5 \mu\text{m}$. Image reproduced from Ref. [233]. 89
- Figure 5.8: AFM scan for a film of neat TIPS-pentacene. The cross-section shows gaps with the same height as the nominal film thickness, $16.6 \pm 3.4 \text{ nm}$, and indicating exposed substrate between crystallite formations. 89
- Figure 5.9: (a) Charge carrier mobility of TIPS-pentacene:PS with different blending ratios at a shearing speed of 2.2 s^{-1} . Microscopy images for blends containing (b) 33%, (c) 36%, (d) 40%, (e) 42%, (f) 44%, (g) 47%, (h) 50%, (i) 55%, (j) 63%, (k) 66% weight of polystyrene. Scale bar: $500 \mu\text{m}$. Image reproduced from Ref. [233]. 90
- Figure 5.10: Scanning electron microscopy image of the cross-section of a TIPS-pentacene:PS blended films of ($M_w = 20 \text{ kDa}$ and shearing speed of 2 mm s^{-1}). Image reproduced from Ref. [233]. 91
- Figure 5.11: Optical microscopy images of the film before (left) and after (right) removing the TIPS-pentacene with hexane for blends of polystyrene of (a) 2 kDa, (b) 20 kDa, (c) 200 kDa and (d) 2000 kDa. Scale bar: $500 \mu\text{m}$. Images reproduced from Ref. [233]. 91
- Figure 5.12: (a) Phase image from sample blended with 2 kDa and a (b) SEM image of the film surface. The scale bar applies to both images and has a length of $4 \mu\text{m}$. Image reproduced from Ref. [233]. 92
- Figure 5.13: (a) Shearing speed-dependent film thickness of TIPS-pentacene:PS blends with different molecular weights. (b) The thickness of the PS layer buried in the film (measured after dissolving the TIPS-pentacene layer with hexane); (c) thickness of the TIPS-pentacene layer formed at the interface of air due to phase separation. This thickness was obtained from subtracting the thickness of the buried PS layer from the total film thickness. Image reproduced from Ref. [233]. 93
- Figure 5.14: Film thicknesses of TIPS-pentacene:PS blends with (a) $M_w = 20 \text{ kDa}$, (b) $M_w = 200 \text{ kDa}$, and (c) $M_w = 2000 \text{ kDa}$ sheared at different speeds. The thicknesses for the blends and polystyrene are measured, and the TIPS-pentacene thicknesses are calculated by subtracting the other two. Images reproduced from Ref. [233]. 94

- Figure 5.15: GIWAXS data for films (background-subtracted, Gaussian fits, scaled and offset) of (a) neat semiconductor and (b) blend of $M_w = 200$ kDa films. The peaks are background-corrected, noise filtered, and Gaussian fitted. The colors in the legends represent the ranges of the peak positions for the different polymorphs forms of TIPS-pentacene mapped out in previous works.[92], [95] One can observe the more visible peak shift of the 200 kDa films starting at 2 mm s^{-1} due to the significant thickness difference between the neat films and the films of high molecular weight. This is consistent with previous observations of the nanoconfinement effect for TIPS-pentacene.[92], [94], [95] Image reproduced from Ref. [233].
..... 95
- Figure 5.16: Maximum saturation charge carrier mobility as a function of orientation for the best sample of each blend. The inset shows the electrode geometry and the shearing direction. Image reproduced from Ref. [233].
..... 96
- Figure 5.17: (a) Optical micrograph of TIPS-pentacene:PS (20 kDa) sheared over the PVP:HDA dielectric layer. Scale bar: $200 \mu\text{m}$; (b) transfer and (c) output characteristics of low voltage operating devices. The films are sheared with a blend of TIPS- pentacene:PS (20 kDa) at a speed of 2 mm s^{-1} . Image reproduced from Ref. [233].
..... 97
- Figure 5.18: (a) Optical microscopy image and (b) transfer characteristics of the neat TIPS-pentacene sheared over the PVP:HDA dielectric layer. Scale bar: $200 \mu\text{m}$. Image reproduced from Ref. [233].
..... 97
- Figure 5.19: Mobility plots extracted from data from the works of (a) Giri et al. (2011),[91] (b) Diao et al. (2013),[92] (c) Niazi et al.(2016),[104] (d) Molina-Lopez et al. (2017)[98] (e) Xiao et al. (2017),[101] (f) and from our group (2018).
..... 98
- Figure 5.20: Graph depicting the charge carrier mobility of OFETs and their respective operation voltages. The year in brackets corresponds to the year of publication..... 99
- Figure 6.1: Microscopy images of TIPS-pentacene films coated from a toluene solution with a substrate temperature of 90°C with the (a-e) standard shearing method; and with vibration with a constant amplitude, and frequencies of (f-j) 5 kHz, (k-o) of 15 kHz, and (p-s) of 25 kHz, and a constant displacement voltage of 20 Vpp. Scale bar in (a): $100 \mu\text{m}$. Size of AFM images in insets (r) and (s) is of $40 \mu\text{m}$.
..... 103
- Figure 6.2: Thickness for the shearing conditions displayed in Figure 6.1..... 103
- Figure 6.3: (a-f) Microscopy images from films sheared without vibration, and with vibration at 15 kHz; and (g-i) their corresponding charge carrier mobility as a function of the gate voltage. The effective saturation charge carrier mobility is also displayed. The black arrow represents the shearing direction. Scale bar in (a): $100 \mu\text{m}$.
..... 104
- Figure 6.4: (a) Reference film for TIPS-pentacene:PS blend, and (b-g) piezosheared samples. The white arrow indicates the shearing direction. Scale bar: $100 \mu\text{m}$.
..... 105
- Figure 6.5: (a) Microscopy image of a reference film and (b) of a film piezosheared at a frequency of 60 kHz and a displacement of 8 Vpp. The white arrow indicates the shearing direction. (c) Effective saturation charge carrier mobility values are equivalent to film in (a) and (b). Scale bar in (a) is $500 \mu\text{m}$, and in the inset is $100 \mu\text{m}$.
..... 106
- Figure 6.6: (a) Reference film for $\text{C}_8\text{-BTBT}$, and (b) piezosheared sample with at a frequency of 60 kHz, and an amplitude of 8 Vpp. The white arrow indicated the shearing speed. (c) and (d) are the cross-sections of the dashed white line indicated in (a) and (b), respectively. Scale bar: $100 \mu\text{m}$.
..... 106

- Figure 7.1: (a-g) Cross-polarized optical microscopy (CPOM) images of films of DPP4DE-TT in CF (5 mg ml^{-1}), coated at different shearing speeds. Black and white arrows in (a) indicate the solution shearing direction, and the crossed arrows indicate the orientation of the crossed polarizers – these also apply to (a-g). Scale bar in (b): $500 \mu\text{m}$. (h-n) Atomic force microscopy images of the surface of the respective films. Scale bar in (h): $40 \mu\text{m}$. Color bar at the side of AFM images have values given in nanometers. Image reproduced from Ref. [270]..... 111
- Figure 7.2: (a-t) CPOM diagram showing films at different shearing speeds and different vibration displacements (constant frequency of 1 kHz). The insets in (h) and (p) are non-polarized images that show the coating-start region and which are provided to illustrate that despite the uniform colors in (h) and (p) there are indeed thin films. White arrows in (a) indicate the solution shearing direction, and the crossed arrows indicate the orientation of the crossed polarizers. Scale bar: $500 \mu\text{m}$. (u) Chemical structure of DPP4DE-TT and chloroform. Image reproduced from Ref. [270]..... 112
- Figure 7.3: CPOM diagram showing films at different shearing speeds and different vibration displacements (constant frequency of 1 kHz). The white arrow in (a) indicates the solution shearing direction, and the crossed arrows indicate the orientation of the crossed polarizers. Scale bar: $500 \mu\text{m}$. (u) Chemical structure of PCDTPT. Image reproduced from Ref. [270]. 113
- Figure 7.4: (a-t) Schematic of different shearing speeds and piezoshearing displacement amplitudes for the solution of (u) PCDTPT and chlorobenzene, coated at 100°C . White arrows in (a) indicate the solution shearing direction, and the crossed arrows indicate the orientation of the crossed polarizers. The white arrows in the image (b) indicate the coating direction, and that both wire and film morphology are observed at this shearing condition. Scale bar: $500 \mu\text{m}$. Image reproduced from Ref. [270]..... 113
- Figure 7.5: Film thickness for (a) DPP4DE-TT /CF solution and for (b) PCDTPT/CF solution, both solution-sheared at room temperature. Samples that consist mainly of wires are designated as thickness “zero”. Image reproduced from Ref. [270]. 114
- Figure 7.6: The surface of a piezosheared film at 2.2 mm s^{-1} and 20 Vpp (left) and cross-section of what seems to be a gap to the substrate (right). Image reproduced from Ref. [270]. 115
- Figure 7.7: AFM topography images of (a-d) sheared samples and (e-h) piezosheared samples of DPP4DE-TT. Image reproduced from Ref. [270]..... 115
- Figure 7.8: Phase images of (a-d) sheared samples and (e-h) piezosheared samples. These phase images are the ones corresponding to the z-axis images in Figure 5 in the main text. Scale bar in (a): 500 nm . Image reproduced from Ref. [270]. 115
- Figure 7.9: GIWAXS images with incident beam (a, e, i, m) parallel to coating direction, (b, f, j, n) perpendicular to coating direction, (c, g, k, o) integrated cake cuts, and (d, h, l, p) CPOM images for DPP4DE-TT coated at 1.4 mm s^{-1} . The cake cuts are obtained through integration of a 5° cake cut of the 2D image, from $1.5 \text{ \AA}^{-1} < q_{xy} < 2 \text{ \AA}^{-1}$ and from angles $82^\circ < \chi < 87^\circ$, as indicated by the white dashed line cake segment in (a). The vertical white dashed lines serve as a guide to the eye for comparison of the images. For these images, the ODTs peak (around 1.5 \AA^{-1}) is removed by subtracting the GIWAXS image of a sample with only ODTs on its surface. The blue dashed line (c, g, k, o) indicates where $q_{xy} = 1.74 \text{ \AA}^{-1}$ is. It can be observed from (d, h, l, p) that the coverage of the films is different; therefore the amount of material scanned by the beam varies, and the intensities in (c, g, k, o) cannot be directly compared. The directions parallel and perpendicular to the shearing direction are defined in (h) and valid for figures (d, h, l, p). Scale bar in (d): $500 \mu\text{m}$. Image reproduced from Ref. [270]. 116

- Figure 7.10: Charge carrier mobility values for the experiments with (a) DPP4DE-TT /CF, (b) PCDTPT/CF coated at room temperature, and (c) PCDTPT/CB coated at 100 °C. (d) Schematic of OFET electrodes in relation to the solution shearing direction. Image reproduced from Ref. [270]. 117
- Figure 7.11: Effective charge carrier mobility for devices with transistors' active channel perpendicular to the shearing direction. Shear coated from (a) DPP4DE-TT /CF at room temperature; (b) PCDTPT/CF at room temperature; (c) PCDTPT/CB coated at 100 °C. Image reproduced from Ref. [270]. 118
- Figure 7.12: (a) Transfer curves, (b) mobility as a function of V_g , and (c) output curves for a typical device coated from the polymer DPP4DE-TT. Image reproduced from Ref. [270]. . 118
- Figure 7.13: (a) Transfer curves, (b) saturation mobility dependent on V_g , and (c) output curves for a typical device coated from the solution of PCDTPT/CF at room temperature. Image reproduced from Ref. [270]. 118
- Figure 7.14: (a) Transfer curves, (b) saturation mobility dependent on V_g , and (c) output curves for a typical device coated from PCDTPT/CB. Image reproduced from Ref. [270]. 118
- Figure 7.15: (a) Progress of variation of meniscus edge (distance D in pixels) with shearing over critical speed (1.4 mm s^{-1}); (b) progress of meniscus edge when using piezoshearing. (c) Image of meniscus illustrating how the distance D is calculated; the image is taken during a sticking stage. Scale bar in (c): $40 \mu\text{m}$. Image reproduced from Ref. [270]. 119
- Figure 7.16: (a-p) Coating of DPP4DE-TT at different speeds with increasing vibration displacements, but in a reduced range and with finer steps than in Figure 7.2. White arrows in (a) indicate the solution shearing direction, and the crossed arrows indicate the orientation of the crossed polarizers. Insets in (j), (n), and (o) display optical images of the ultrathin films. Image reproduced from Ref. [270]. 120
- Figure 7.17: Experiment of a drop of DPP4DE-TT /CF placed under a static blade with and without vibration. (a, g): Drop without any vibration; (b, h) Vibration of 1 kHz with a displacement of 2Vpp; (c, i): 5 Vpp; (d, j): 10 Vpp; (e, k): 20 Vpp and (f, l): 40 Vpp. Scale bar: $500 \mu\text{m}$. Image reproduced from Ref. [270]. 121
- Figure 7.18: Experiment of a drop of PCDTPT/CF placed under a static blade with and without vibration. (a, g) Drop without any vibration; (b, h) Vibration of 1 kHz with a displacement of 2 Vpp; (c, i): 5 Vpp; (d, j): 10 Vpp; (e, k): 20 Vpp and (f- l): 40 Vpp. Scale bar: $500 \mu\text{m}$. Image reproduced from Ref. [270]. 121
- Figure 7.19: Schematic of a local energy barrier model for the shearing of OSC over the critical speed. The energy introduced by the vibration - $E_{\text{vibration}}$ - is counteracted by the kinetic energy of the moving blade - represented by E_{v1} and E_{v2} . Image reproduced from Ref. [270]. 122
- Figure 7.20: Inhomogeneities and fingering instabilities along the contact line for sheared DPP4DE-TT /CF samples coated at (a) 1.4 mm s^{-1} , (b) 1.8 mm s^{-1} , and (c) 2.2 mm s^{-1} marked by white triangles. Scale bars: $40 \mu\text{m}$. The small white arrows highlight a few very visible inhomogeneities that contribute for contact line pinning. The gray arrow in (a) denotes the solution shearing direction of the film. Image reproduced from Ref. [270]. 123
- Figure 7.21: Acceleration threshold values required to obtain continuous film for the three experimental systems described here. These values are determined from Figure 7.3, Figure 7.4, and Figure 7.16. 124
- Figure 7.22: Contact angle values for the polymer solutions of DPP4DE-TT/CF and PCDTPT/CF with varying polymer concentrations. 125

- Figure 8.1: Chemical structures of the diketopyrrolopyrrole Polymers utilized in this chapter: (a) DPP4DE-TT, (b) DPP6DO-TT, and (c) DPP6DO-T..... 128
- Figure 8.2: Cross-polarized microscopy images (CPOM) of the DPP4DE-TT films; (b) total intensity variation of the images of films coated at such frequencies; and (c) the respective pixel intensity normalized by thickness. White arrows in (a) denote the respective coating direction for the films, and the crossed arrows denote the direction of the crossed polarizers. Scale bar: 500 μm 130
- Figure 8.3: From the top to bottom, is the reference film DPP4DE-TT, and then piezosheared samples with increasing displacement at a vibration frequency of 10 kHz. At the far left are cross-polarized images (CPOM), with their respective normalized pixel intensity and film thickness. In the middle section (Bulk, $\alpha = 0.12^\circ$), GIWAXS characterization for the bulk of the film is shown. In the section at the right (Surface), the GIWAXS characterization for a shallow incident angle ($\alpha = 0.04^\circ$) and AFM of the top surface of the film is depicted. The value R in the integrated cake segment graphs is the ratio of the integrated area of the parallel direction in relation to the perpendicular direction. Parallel and perpendicular are relative to the shearing direction..... 130
- Figure 8.4: Pole figures for solution sheared samples of DPP4DE-TT of the (a-c) bulk of the film; and (d-f) of the near-surface. For calculation of the rDoC and rDoC*, the diffraction images from Figure 8.3 are used. Angle $\varphi = 0^\circ$ is referent to the direction parallel to the solution shearing, and $\varphi = 90^\circ$ is referent to the perpendicular direction. 132
- Figure 8.5: (a) Effective charge carrier mobility values for DPP4DE-TT, piezosheared at 10 kHz and varying displacement amplitudes. (b) Transfer curve, (c) gate-voltage-dependent mobility, and (d) output curves for devices coated at 10 kHz, 40 Vpp..... 134
- Figure 8.6: CPOM images of a solution-sheared DPP4DE-TT for (a) reference sample (scale bar: 500 μm), and (b-s) piezosheared samples at different vibration frequencies and amplitude displacements. The white arrows in (a) determine the shearing direction of the film, and crossed arrows indicated the direction of the crossed polarizers for (a-s). The acceleration for each piezoshearing condition is displayed at the right lower corner of the images. (t) Color map of the intensity variation normalized for the thickness of the respective films in relation to the reference sample in (a). The gray areas in (t) are missing data..... 135
- Figure 8.7: From top to bottom, there is a reference film of DPP4DE-TT, and following, piezosheared samples with increasing displacement at a vibration frequency of 1 kHz. At the far left are cross-polarized images (CPOM), with their respective normalized pixel intensity and film thickness. In the middle section (Bulk) is GIWAXS characterization for the bulk of the film. In the section at the right (Surface), is the GIWAXS characterization for a shallow incident angle. 136
- Figure 8.8: Charge carrier mobility for devices with films piezosheared at a vibration frequency of 1 kHz. 136
- Figure 8.9: CPOM images of films coated at 0.5 mm s⁻¹ at 25 °C for (a) DPP6DO-TT and (b) DPP6DO-T. The white arrows represent the coating direction, and the crossed arrows the direction of the crossed polarizers. The insets are the respective films without polarization. The different colors of the film are due to significant thickness differences. Scale bar: 500 μm . 137
- Figure 8.10: Films coated from DPP6DO-TT: (a) reference sample, and (b-v) piezosheared samples with varying vibration frequency and amplitude. The white arrows in (a) denote the coating direction of the film, and the crossed arrows denote the direction of the crossed polarizers. The values on the right bottom corners of the images are the acceleration values

induced by the vibration of the piezo crystal. The background color of the images indicates in which regime the films are according to the legend on the top. Scale bar in (a): 500 μm 138

Figure 8.11: (a-f) Side view and the (g-i) top view of a vibrating sessile drop. Both sequences document the process the drop undergoes when vibration amplitude is increased. The images are reproduced and rearranged from the work of Vukasinovic et al.[178] 139

Figure 8.12: CPOM images of a DPP6DO-TT (a) sheared reference film, and (b-g) piezosheared films at a frequency of 5 kHz and varying vibration amplitude. (h-n) Intensity profile extracted from the cross-sections in figures (a-g). (o-u) Resulting Power Spectra of Fast Fourier Transform of the profiles in (h-n). The white arrow in (a) is the coating direction, and the white dashed line is where the intensity profile is extracted. The blue and red dashed lines on the images on the right of the figure are a guide to the eye of the frequency values $0.5 f_d$ and f_d , respectively. Scale bar in (a): 500 μm 140

Figure 8.13: CPOM images of sheared and piezosheared films of (a-f) DPP6DO-T/CF coated at room temperature, and (g-j) DPP6DO-TT/CB coated at 100 °C. The vibration frequency used is 5 kHz for both materials. The black arrow indicates the coating direction, and the crossed arrows, the direction of the crossed polarizers. Scale bar: 500 μm 141

Figure 8.14: (a, b) CPOM images, (c-f) AFM topology images, and (g-j) AFM phase images of films sheared (left) and piezosheared (right) from DPP6DO-TT/CF. White arrows indicate the coating direction. Scale bar in (b): 500 μm . Scale bar in (c): 500 nm. 142

Figure 8.15: Electrical characteristics for films piezosheared from DPP6DO-TT/CF. (a) Effective charge carrier mobility values for vibration frequencies of 3, 5, and 7 kHz. (b) Transfer curve, (c) gate-voltage-dependent mobility, and (d) output curves for a typical device sheared from DPP6DO-TT/CF. The curves are those from the reference sample. 142

Figure 8.16: (a) Effective charge carrier mobility values for DPP4DE-TT/CB, piezosheared at 5 kHz and varying displacement amplitudes. (b) Transfer curve, (c) gate-voltage-dependent mobility, and (d) output curves for devices coated at 5 kHz, 40 Vpp. 143

Figure 8.17: CPOM films for DPP6DO-TT/CF (left) and DPP6DO-T/CF (right), with the respective GIWAXS measurements. The beam is incident to the sample in the direction parallel to the coating direction. The frequency used for the piezoshearing of DPP6DO-TT/CF is of 5 kHz, and the one used for DPP6DO-T/CF is 3 kHz. Scale bar: 500 μm 144

Figure 8.18: (a) Effective charge carrier mobility values for the DPP6DO-T/CF polymer system. The (b) reference sample has two film thicknesses (values for the thin and thick part of the film in the image are in the right bottom corner) and is treated with an intensity threshold algorithm for measuring the area covered by each film thickness. (c) The equivalent regions for the thick and the thin regions of the polymeric film. The black region is the area where the film is thin, and the white area is the area where the film is thick. (d) Piezosheared sample with a frequency of 5 kHz and 80 Vpp. (e) The same optical intensity threshold that was used for the reference sample is applied to this film for comparison. Scale bar: 500 μm 144

Figure 8.19: Schematic illustration of the piezoshearing setup as a parametric oscillator. The receding meniscus itself is an oscillating system, and the external vibration applied to the system is applied by the piezo actuator. The grey block at the contact line represents a friction element. 145

List of Tables

Table 5.1: Electrical characteristics of shear-coated TIPS-pentacene:PS devices	86
Table 8.1: Physical properties of the polymers us DPP4DE-TT, DPP6DO-TT, and DPP6DO-T.	128
Table 8.2: Numerical figures extracted from Figure 8.3 and Figure 8.4 for DPP4DE-TT....	133

List of Abbreviations

AFM	atomic force microscopy
BGTC	bottom gate top contact
C ₈ -BTBT	2,7-Dioctyl[1]benzothieno[3,2-b][1]benzothiophene
C ₁₀ -DNNT	2,9-didicyldinaphtho[2,3-b:20,30-f]thieno[3,2-b]thiophene
CB	chlorobenzene
CF	chloroform
D-A	donor-acceptor
diF-TES-ADT	2,8-Difluoro-5,11-bis(triethylsilylethynyl)anthradithiophene
DPP4DE-TT	poly(diketopyrrolopyrrole-cothiophene-co-thieno[3,2-b]thiophene-co-thiophene)
DPP6DO-T	poly{3-([2,2':5'2''-terthiophen]-5-yl)-2,5-bis(6-dodecyloctadecyl)-2,5-dihydropyrrolo[3,4-c]pyrrole-1,4-dione-6,5''-diyl}
DPP6DO-TT	poly[2,5-(6-dodecyloctadecyl)-3,6-diketopyrrolopyrrole-alt-5,5-(2,5-di(thien-2-yl)thieno [3,2-b]thiophene)]
FET	field-effect transistor
FFT	fast Fourier transform
FWHM	full-width half maximum
GIWAXS	grazing incident wide-angle x-ray scattering
HDA	4,4'-(hexafluoroisopropylidene) diphthalic anhydride
HOMO	highest occupied molecular orbital
LUMO	lowest occupied molecular orbital
MGC	meniscus guided coating
MOSFET	metal-oxide-semiconductor field-effect transistor
M _w	molecular weight
ODTS	octadecyltrimethoxysilane
OFET	organic field-effect transistor
OSC	organic semiconductor
P3HT	poly(3-hexylthiophene-2,5-diyl)
PEDOT	poly(3,4-ethylenedioxythiophene)
PS	polystyrene
PSS	polystyrene sulfonate
PTCS	phenyltrichlorosilane
PVP	poly(4-vinylphenol)
rDoC	relative degree of crystallinity
SAM	self-assembled monolayer
SEM	scanning electron microscopy

TIPS-pentacene	6,13-bis(triisopropylsilylethynyl)pentacene
UV	ultraviolet
VIS	visible

Acknowledgment

I would like to express my deepest gratitude to all of those who have accompanied me throughout the last four years, and that made the completion of this work possible. These years were challenging, but also full of support and companionship. I am very grateful for being able to finish this work, but I am also very grateful for the great time I had while doing so.

I am immensely grateful to Prof. Stefan Mannsfeld for giving me the opportunity to join the group and trusted me with such an exciting topic. I am deeply grateful for all the support, time, and energy received from him during the last four years. I am grateful for the discussions, the constant encouragement, and for the freedom to look into different topics. I would also like to thank him for the first review of this thesis.

Moreover, I would like to thank Prof. Sebastian Reineke for investing his time in preparing the second review of this thesis.

I would like to thank Dr. Mike Hambsch, for all the help received throughout the last four years, and making himself available for any discussion. A special thanks for coming through with last-minute things that had to be done, or reviews that I needed. A very special thank you to Anne Schulze, which has supported me with all the paperwork of the last years, always very fast, prompt and with a great disposition. Thank you to Knut Range for the support and maintenance in the laboratory.

I would like to thank my current and previous colleagues, Katherina Haase, Yichu Zheng, Jakob Zessin, Jonathan Perez, Felix Talnack, Rishi Shivhare, Tianyu Tang, Nara Shin, and Zhe Zhang for all the help, companionship, and patience of the last years. I'm very grateful for you all; your company made everything much more enjoyable. A special thanks to Katherina, Jakob, Jonathan, Felix, and Yichu, who took some of their own time to go over parts of my thesis. I would like to thank Luigi Castriotta, Christoph Hauenstein, Konstantinos Zoumboulis, Zhe Zhang, and Zheng Xu, for all the help with measurements and disposition.

I would like to thank Prof. Ying Diao, for welcoming me to do a research stay at her group, and making herself available for discussions. I would also like to thank her group members, who have helped me immensely during my stay there.

Thank you to Prof. Stefan Blawid for introducing me to the field of organic electronic materials and promptly helping me with documentation and translations before I started my doctorate studies. Thank you also to Dr. Martin Claus for showing me the possibility of doing my doctorate at the TU Dresden when I was considering pursuing a Ph.D.

I would like to acknowledge the Graduate Academy for financial support, enabling me to continue my work for a few months. I would also like to acknowledge financial support from the Center for Advancing Electronics Dresden for enabling my stay abroad, which was very enriching for my work.

Thank you to all friends who have been a part of my life in the last years, and have somehow helped me and supported me.

Lastly, I would like to thank my family. I am forever in debt to my parents, sister, grandparents, and aunts, who have always made everything possible and have always been there for me when I needed it.

Erklärung zur Eröffnung des Promotionsverfahrens

Hiermit versichere ich, dass ich die vorliegende Arbeit ohne unzulässige Hilfe Dritter und ohne Benutzung anderer als der angegebenen Hilfsmittel angefertigt habe; die aus fremden Quellen direkt oder indirekt übernommenen Gedanken sind als solche kenntlich gemacht.

Weitere Personen waren an der geistigen Herstellung der vorliegenden Arbeit nicht beteiligt. Insbesondere habe ich nicht die Hilfe eines kommerziellen Promotionsberaters in Anspruch genommen. Dritte haben von mir weder unmittelbar noch mittelbar geldwerte Leistungen für Arbeiten erhalten, die im Zusammenhang mit dem Inhalt der vorgelegten Dissertationen stehen.

Die Arbeit wurde bisher weder im Inland noch im Ausland in gleicher oder ähnlicher Form einer anderen Prüfungsbehörde vorgelegt und ist auch noch nicht veröffentlicht worden.

Mir ist bekannt, dass die Nichteinhaltung dieser Erklärung zum nachträglichen Entzug des Dokortitels führen kann.

Ich bestätige, dass ich die Promotionsordnung der Fakultät Elektrotechnik und Informationstechnik vom 12.05.2012 der Technischen Universität Dresden anerkenne.

Cecilia Teixeira da Rocha

Dresden, 12.09.2019